UNIVERSIDAD DE SANTIAGO DE COMPOSTELA

FACULTAD DE FISICA

Departamento de Física de Partículas

QUALITY CONTROL AND PREPARATION OF THE PWO CRYSTALS FOR THE ELECTROMAGNETIC CALORIMETER OF CMS

CERN-THESIS-2011-113
//2011

Memoria presentada por:
PABLO SEMPERE ROLDAN
para optar al
Grado de Doctor en Física
Noviembre 2001

UNIVERSIDAD DE SANTIAGO DE COMPOSTELA

JUAN A. GARZON HEYDT, PROFESOR TITULAR DEL DEPARTAMENTO DE FISICA DE PARTICULAS DE LA UNIVERSIDAD DE SANTIAGO DE COMPOSTELA,

CERTIFICA:

que la memoria titulada **QUALITY CONTROL AND PREPARATION OF THE PWO CRYSTALS FOR THE ELECTROMAGNETIC CALORIMETER OF CMS** ha sido realizada por **D. Pablo Sempere Roldán** en el **Departamento de Física de Partículas de la Universidad de Santiago de Compostela** y en el **Laboratorio Europeo de Física de Partículas (CERN)** bajo la dirección de los profesores **Juan A. Garzón** (U. Santiago de Compostela) y **Paul Lecoq** (CERN) y constituye el trabajo de **tesis** que presenta para optar al **Grado de Doctor en Física.**

Ginebra, 11 de Octubre de 2001

Juan A. Garzón Heydt	Paul Lecoq	Pablo Sempere Roldán
Dpto. de Física de Partículas	EP/CMA (CERN)	Estudiante de Doctorado

A mi familia y amigos

Acknowledgements

I would first like to thank my two supervisors during this Doctoral Student stage who were Dr. Paul Lecoq from CERN (Switzerland) and Dr. Juan Antonio Garzón Heydt from the University of Santiago de Compostela (Spain). Both gave always a kind treat to me and besides, they offered me the possibility of performing this studying stage, thus I am indebted to them.

In addition, I would like to thank Etiennette Auffray and Marc Schneegans, for their friendly treat in the daily work, for their wise advices and, of course, for their unvaluable collaboration in the writing of this thesis.

I am also grateful to the Lab 27 colleagues I had during these three years. Among them, I would like to mention Huguette Cabel, Francesca Cavallari, Antonio Conde García, Gavin Davies, Susan Gascon, Michel Lebeau and Jean Marie Le-Goff. I also thank warmly the students I worked with: Roger Marcos, Laura Perez and Claudia Kuntner.

Je voudrais aussi remercier chaleureusement pour leur aide et amitié à Bruno Buisson, Herve Cornet, Armando de Forni, Eric Gitton, Alain Machard et René Morino.

Además quisiera dar las gracias a mis compañeros y amigos del CERN (demasiados para mencionarlos, pero ellos saben quienes son); a mis amigos de la facultad de Física y a mis amigos de Santiago por su cariño y amistad.

También quería dedicar un agradecimiento especial a mi madre y hermanos e igualmente a Virginia por su apoyo y comprensión durante los no pocos momentos difíciles que ha generado la escritura de esta tesis.

Y a ti, porque sé que esta vez también me has ayudado.

Contents

List of Figures

List of Tables

Chapter 1

INTRODUCTION

The Standard Model of Particle Physics describes the electromagnetic, weak and strong interactions among particles. In this model, the strong force is described by Quantum Chromodynamics (QCD), a theory in which eight different kinds of gluons carry the force between quarks. The other two forces can be described by the electroweak theory, which in a similar way, is characterized by the existence of a neutral carrier of force (Z^0) as well as charged carriers (W^+ and W^-). This electroweak theory was formulated in the late 1960's by Glashow, Salam and Weinberg and it predicted not only the existence of the bosons W^+, W^-, and Z^0 but also the existence of weak neutral current interactions. In 1973 the first neutral currents were observed at the European Centre for Nuclear Research (CERN), and 10 years later, the existence of the three bosons mentioned above was proved again at CERN. This confirmed the electroweak theory but, however, the mechanism that causes the force carriers to differ in mass (bosons W and Z are very massive and photon is massless) still today has no explanation. The possible solution arising from the "Higgs mechanism" can solve the problem but it has a consequence: the existence of a new particle known as Higgs boson (H^0) which has not been yet observed and is only known to have a mass in the range: 100 GeV $< m_H <$ 1000 GeV. Nowadays, the discovery of this particle is one of the main objectives of particle physicists.

The Large Hadron Collider (LHC) is an instrument that will explore new Physics at the higher energies ever achieved, aiming to find the Higgs boson.

The LHC is being built at CERN and by 2005 it will be ready to produce head-on collisions of protons at a centre-of-mass energy of 14 TeV. Several spectrometers will be installed along the 27 km LHC ring. One of them, the Compact Muon Solenoid (CMS) will have its electromagnetic calorimeter composed of Lead Tungstate crystals ($PbWO_4$). This homogeneous calorimeter will play an essential role in the potential discovery of a light Higgs, the main decay of which is given by the $H \rightarrow \gamma\gamma$ channel, characterized by an enormous diphotonic background. This thesis will be mainly focused on the quality control performed on those crystals, in order to achieve a high precision electromagnetic calorimeter with an optimum energy resolution allowing the light Higgs to be detected.

Chapter 2 will firstly explain what is CERN and which are the characteristics and aims of the LHC project. This will be followed by a brief overview of the Standard Model, the Higgs mechanism mentioned above and the possible discovery channels of H^0 at LHC, focusing on the difficulties existing on the channel $H \rightarrow \gamma\gamma$. Then, a short description of the CMS collaboration, will be followed by some notions about calorimeters that will help to introduce the CMS electromagnetic calorimeter (CMS ECAL). Its general characteristics and the constraints imposed to crystals performances will be discussed. To finish, we will discuss the important role of the CMS ECAL Regional Centres, and the different steps that constitute the whole characterization procedure applied in them.

In chapter 3, we will perform a detailed description of $PbWO_4$ crystal properties. First, we will explain the reasons for the choice of this scintillating crystal, together with its basic properties, which will be compared to other scintillating crystals widely used in Particle Physics. Then, we will describe lead tungstate crystals growing methods used by the existing producers and later, we will discuss its scintillating and optical properties. An overview of the different crystal geometries used at the CMS Electromagnetic Calorimeter will be then presented. To finish, we will list and discuss the existing specifications for CMS ECAL barrel crystals.

Chapter 4 will describe in detail the characterization of the $PbWO_4$ crystals. We will first perform a detailed description of all the measuring devices employed for such a characterization: the "classical benches" (old devices measuring generally only a characteristic of the crystals), and the Automatic Crystal Control System (ACCOS) devices. To finish, we will place a special emphasis on the stability and inter-calibrations studies performed for these

devices.

The importance of the light collection uniformity and the methods to achieve it will be the main topics discussed in chapter 5. First of all, we will show Monte Carlo simulations to show that the energy resolution strongly depends on this uniformity. Then we will illustrate how non-uniform the CMS ECAL barrel crystals are naturally, thus forcing us to find a suitable uniformization method. The final method chosen will be then explained and the result from its application to several thousands of barrel crystals will be presented. Later, we will discuss about a previously unknown parameter influencing the light collection uniformity and to finish, we will discuss the importance of the crystal wrapping on the uniformity and the light yield losses induced with our uniformization method.

In chapter 6 we will explain all the processes involved in the light extraction from $PbWO_4$ crystals. First, we will describe the photodetectors chosen as readout system for the CMS ECAL barrel, that are the Avalanche Photodiodes. Then, we will focus on the importance of the optical glue that must couple crystals and photodetectors. We will discuss the considered glue candidates, evaluating their advantages and drawbacks. Then, we will describe the different tools developed at CERN Regional Center in order to ease this gluing task and we will finish by summarizing the results achieved up to summer 2001, focusing on the problems found for each considered glue.

Finally, chapter 7 will present the results from two different test beams where some interesting performances of $PbWO_4$ crystals were analyzed. In the first part of this chapter, we will show a comparison between the uniformity curves measured at CERN Regional Center laboratories and the ones measured at Paul Scherrer Institute (PSI) under beam conditions (i.e. high-energy particles hitting into crystals, and readout performed with final Avalanche Photodiodes). Then, we will present the results of the second test-beam performed at CERN H4 area, where we will confirm the importance of achieving a uniform light collection for our crystals in order to improve the energy resolution of our detector.

Chapter 2

SCIENTIFIC CONTEXT

2.1 CERN

Particle Physics studies the basic constituents of matter and their fundamental interactions. The interest on this subject dates from the Greeks philosophers time. The ideas of these philosophers were developed and formalized in the early nineteenth century, with the development of chemistry and the molecular theories.

Already in the first half of the twentieth century many progresses were made like, for example, the discovery of the electron, the atomic nucleus and its constituents and the formulation of special relativity theory and quantum mechanics. Most of these progresses were achieved in Europe, however, the military conflicts in the end of this first half of the century reduced enormously the European capabilities. Besides, at that time, the Americans understood the importance of investment in science and started to build powerful accelerators whereas European scientists were still relying on their simple equipment. To redress the balance and restore European science to its former prestige, at the European Cultural Conference at Lausanne, the French physicist and Nobel prize-winner Louis de Broglie proposes the creation of a European science Laboratory in 1949. Only one year later, at the 5th General Conference of UNESCO in Florence, the idea of de Broglie is retaken by Isidore Rabi (American

Physicist and Nobel prize-winner) who asks UNESCO to assist and encourage the formation and organization of regional centres and laboratories, to make more fruitful the collaboration of scientists. In 1952, 11 European governments agree to set up a provisional "Conseil Europeen pour la Recherche Nucleaire" (CERN). At a meeting of this new CERN council, a site near Geneva is selected for the planned laboratory. The European Organization for Nuclear Research (still CERN, as in spite of being dissolved the "provisional" council, the easy acronym is retained) borns on 29 September of 1954, after the ratification of the Convention by its 12 member states.

Nowadays, CERN is composed of 20 member states: Austria, Belgium, Bulgaria, Czech Republic, Denmark, Finland, France, Germany, Greece, Hungary, Italy, Netherlands, Norway, Poland, Portugal, Slovak Republic, Spain, Sweden, Switzerland, and the United Kingdom. There are also some non-european countries that take part of CERN as observers. Some of them are: Israel, Japan, the Russian Federation, Turkey and the United States of America.

CERN provides European physicists with accelerator facilities allowing them to take an active part in investigations at the frontiers of human knowledge. The need of higher interaction energies to explore new physics has been understood by CERN, hence, the laboratory has played a leading role in developing colliding beam machines: The world's first proton collider was the Intersecting Storage Rings (ISR), which started working in 1971; In same year was approved the construction of a 7-kilometre Super Proton Synchrotron (SPS), which started operation in 1976. With the SPS adapted as a proton-antiproton collider in 1981, starts an important research period that leads to the discovery, two years later, of the massive W and Z bosons, confirming the unified theory of electromagnetic and weak forces.

Since November 1989 to November 2000 the Large Electron-Positron collider (LEP) has been the main colliding machine working at CERN. The LEP installations are located in an annular 27 km long tunnel, at a variable depth between 50 and 170 meters (see figure 2.1). In LEP, electrons and positrons were accelerated up to an energy of initially 50 GeV per beam, and then, they were made to collide in any of its detection experiments (ALEPH, OPAL, DELPHI and L3). By 1996, LEP energy was increased up to 90 GeV per beam in what was called LEP II, and finally, by 1999 it was increased to 103 GeV per beam. At those energies LEP registered what seems to be the first signatures of a Higgs boson decay, at a mass $m_H \sim 115$ GeV. After LEP

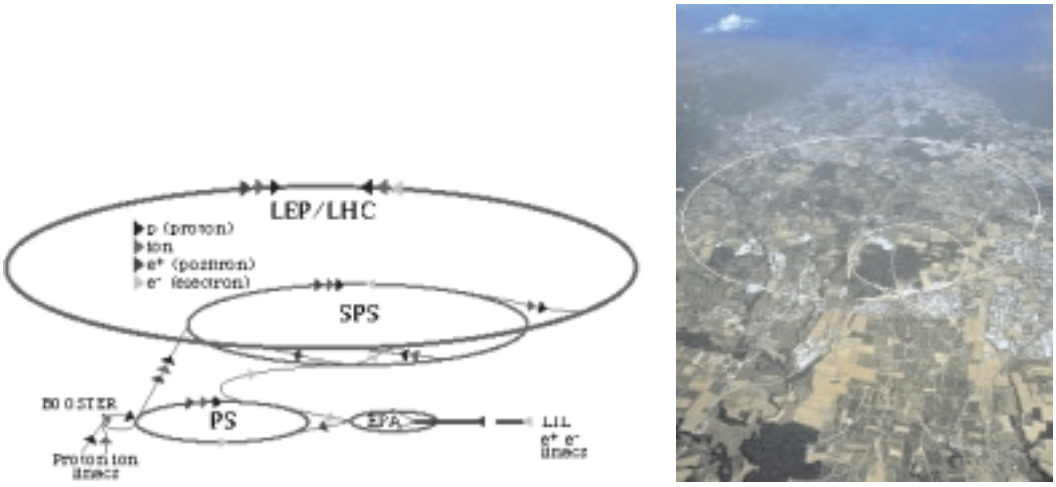

(a) CERN Accelerators (b) CERN site view

Figure 2.1: *The existing accelerators at CERN and the real view from above of CERN site.*

shutdown, the new colliding machine that will be developed at CERN is the Large Hadron Collider (LHC). The new physics, that lay at energies $\gtrsim$1 TeV, will be the exciting domain explored by LHC, and of course, the quest of Higgs boson is one of its main objectives.

2.2 LHC

2.2.1 The LHC project

The Large Hadron Collider (LHC) project [1] was approved by the CERN Council in December 1994. The machine will provide proton-proton collisions with a centre-of-mass energy of 14 TeV and a luminosity of 10^{34} cm^{-2}s^{-1}. The main performance parameters for proton-proton operation are shown in table 2.1. In addition to p-p operation, the LHC will be able to collide heavy nuclei (Pb-Pb) produced in the existing CERN accelerator complex, giving an ion centre-of-mass energy of 1148 TeV (equivalent to 574 TeV/ion, i.e. 2.76 TeV/u and 7.0 TeV per charge) and a luminosity of 10^{27} cm^{-2}s^{-1}. In keeping CERN's cost effective strategy of building on previous investments, it

is designed to share the 27-kilometre LEP tunnel, and to be fed by existing particle sources and preaccelerators. This LEP/LHC tunnel (see figure 2.1) is located at the Franco-Swiss border west of Geneva, at the foot of the Jura mountains, in front of the Alps.

Table 2.1: *LHC Performance Parameters.*

Parameter	*Unit*	*Value*
Beam energy	[TeV]	7.0
Injection energy	[GeV]	450
Luminosity	[$cm^{-1}s^{-1}$]	10^{34}
Ring circumference	[m]	26658.9
RF Frequency	[MHz]	400.8
Number of bunches		2835
Particles per bunch		10^{11}
Bunch spacing	[ns]	25
Normalized transverse emittance	[μm.rad]	3.75
Dipole field	[T]	8.4
Number of bending dipoles		1232
Bending Radius	[m]	2784.3
Circulating current per beam	[A]	0.54
Energy loss per turn	[keV]	6.7
Critical photon energy	[eV]	44.1
Total radiated power per beam	[kW]	3.6

The basic layout of the LHC (see figure 2.2) mirrors the one from LEP, with eight straight sections each one approximately 528 m long, available for experimental insertions or utilities. The two high-luminosity insertions are located at diametrically opposite straight sections, point 1 (ATLAS) and point 5 (CMS). Two more experimental insertions are located at point 2 (Alice Pb ions) and point 8 (B physics). These latter straight sections also contain the injection systems (T12 and T18 in figure 2.2). The beams cross from one ring to the other only at these four interaction points. The remaining four straight sections do not have beam crossings: insertions 3 and 7 are designed to be robust against the inevitable beam loss on the primary collimators; insertion 4 contains the RF systems, which are separated for the two beams; finally, point 6 contains the beam dump insertion (the beams are extracted vertically from the machine using a combination of horizontally-deflecting fast-pulse magnets and vertically-deflecting double-steel septum magnets).

There are some other important aspects of LHC that should be pointed out although here we will only do an overview of them. One of those as-

Figure 2.2: *Schematic Layout of the LHC.*

pects is the injection process: the existing accelerator chain consisting of Linac/Booster/PS/SPS (see figure 2.1) will be used for the LHC injection. In the former, the proton beam will achieve an energy of 50 MeV. Then it will be boosted up to 1.4 GeV. Later, in the Proton Synchrotron (PS), it will be accelerated up to 25 GeV and then injected in the Super Proton Synchrotron (SPS), where the protons will acquire an energy of 450 GeV. After that, two transfer lines will drive protons to the LHC rings.

Another interesting aspect is related to the magnets: high energy LHC beams need high magnetic bending fields, because the machine radius was not a parameter which could have been increased to provide gentle curves. We can deduce the magnetic field needed to bend 7 TeV particles to a radius like the one from LHC (see bending radius parameter in table 2.1), just by knowing that momentum (p), magnetic field (B) and bending radius (R) are related by the following equation

$$p = 0.3BR \tag{2.1}$$

where p is expressed in GeV/c, B in Tesla, and R in meters. Taking in account that for ultrarelativistic particles E $\simeq$ pc, 7 TeV particles have a p=7000 GeV/c, and hence, we get B $\sim$ 8.4 T (which is the magnetic field specified in table 2.1). Such magnetic fields (over 5 times those used a few years ago at the SPS proton-antiproton collider) are only achievable using superconducting magnets. Examples of other high fields superconducting magnets are the ones

used at Tevatron (Fermilab, USA), with a maximum magnetic field of 4 T and also the ones used at HERA (Desy, Germany), with a maximum magnetic field of 4.7 T, both sensibly lower than LHC maximum magnetic fields. In spite of that difference, the LHC will retain the well-proven fabrication of cables and coils made of NbTi superconductors used in both accelerators mentioned above, but in order to achieve the high magnetic fields needed, the magnets will be cooled down to 1.9 K (Tevatron and Hera cool down to a temperature slightly above 4.2 K). This is done by using super-fluid helium, which has unusually efficient heat transfer properties, allowing kilowatts of refrigeration to be transported over more than a kilometer with a temperature drop of less than 0.1 K.

In spite of being talking about LHC, a proton collider, the synchrotron radiation can not be neglected as the energy loss of a particle with mass m, per charge unit and per turn due to synchrotron radiation is given by

$$U_0 = 88.5\frac{E^4}{\rho}\Big(\frac{m_e}{m}\Big)^4 \tag{2.2}$$

where U_0 is in KeV, E in GeV, and ρ in meters. Clearly, in case of protons, the energy loss will be much smaller than in case of electrons, due to mass ratio in equation 2.2. In fact, with the energy of particles and bending radius of LHC mentioned in Table 2.1, we can estimate the LHC energy loss per turn to be $U_0 \sim 6.6$ KeV. We can estimate as well the total synchrotron radiation power, P_T, emitted using

$$P_T = I_0 U_0 \tag{2.3}$$

where P_T is in Watt, I_0 is expressed in Amps and stands for the maximum circulating current per beam (see its value in table 2.1), and U_0 is the already calculated energy loss per turn and is expressed in eV. This yields a power emitted per beam due to synchrotron radiation losses of around 3.6 kW (as appears in table 2.1). Such a power would be an excessive heat load for the 1.9 K system mentioned in previous paragraph. Therefore there is a special protection called beam-screen, maintained at a temperature between 5K and 20K by gaseous helium flow which is inserted inside the magnet cold bore to intercept this power.

2.2.2 Physics at LHC

Standard Model and Higgs Mechanism

The Standard Model (SM) attempts to explain all the phenomena of particle physics in terms of the properties and interactions of a small number of particles of three distinct types. The first two are called *leptons* and *quarks* and are spin 1/2 fermions. The third is a set of spin 1 bosons called *gauge bosons*, which act as "force carriers" in the theory. In the Standard Model all these particles are assumed to be elementary, i.e. they are treated as point particles, without internal structure or excited states. The most familiar example of a lepton is the electron, which is bound in atoms by the **electromagnetic** interaction, one of the four fundamental forces of nature. Another example of lepton is the neutrino, which is a light, neutral particle observed in the decay of some unstable nuclei (β-decay). The force responsible for this β-decay of nuclei is called the **weak** interaction. The two interactions mentioned up to now (electromagnetic and weak), are both described by the electroweak model in the Standard Model of Particle Physics. In addition to leptons, another class of particles called *hadrons* is also observed in nature. Familiar examples are neutron and proton. In the SM, these are not considered to be elementary, but made of quarks bound together by the third force of nature, the **strong** interaction, which is described by quantum chromodynamics. Apart from the strong, weak and electromagnetic interactions between quarks and leptons, there is a fourth force of nature, the **gravity**. However, the gravitational interaction between elementary particles is so small compared with the other three that we neglect it in particle physics and usually refer to the "three forces of nature".

These forces are associated with elementary spin 1 bosons. In the case of electromagnetic interaction, the quantum theory says that the interaction is transmitted discontinuously by a exchange of massless spin 1 photons. The weak and strong forces are also associated with the exchange of spin 1 particles. In the case of the weak interaction, they are called W and Z bosons, and are very massive. The equivalent particles for strong interactions are called gluons, and are massless like the photon. In the Standard Model, the main actors are the leptons and quarks, which are the basic constituents of matter (see the Fundamental Particles in table 2.2) and the force carriers (i.e. the gauge bosons like the photon, the W and Z bosons and the gluons) which mediate interactions between them (see Interactions in table 2.2). In addition,

because not all these particles are directly observable, the quark bound states (or hadrons) are also very important in the Standard Model.

Table 2.2: *The fundamental particles and interactions in the Standard Model.*

Fundamental Particles			
Fermions (Spin 1/2)			
Leptons	e^-	μ^-	τ^-
	ν_e	ν_μ	ν_τ
Quarks	u	c	t
	d	s	b
+ their antiparticles			
Gauge Bosons (Spin 1)			
Massless electroweak boson		γ	
Massive electroweak bosons	W^+	W^-	Z^0
Coloured gluons		g	
Higgs Boson (Spin 0)			
Higgs boson		H^0	

Interaction	Mediator
Electromagnetic interaction	γ
Weak interaction	W^+,$W^-$and Z^0
Strong interaction	g

The Standard Model describes the fundamental interactions of particles on the basis of local gauge invariance. The principle of gauge invariance says that the Lagrangian density of a system must be invariant under a gauge transformation. If the Lagrangian density is invariant under a global gauge transformation, it follows from Noether's theorem, that there is a conserved current and also an associated conserved charge. In the Standard Model, the three fundamental interactions are described by three different gauge groups: $SU(3)_C$, $SU(2)_L$ and $U(1)_Y$. If the invariance is still maintained when going from a global gauge transformation to a local one, we are moving from a theory with only free particles to a theory with interactions. The reason is that, in order to obtain invariance under local gauge transformation, one has to introduce a gauge field to compensate the additional terms in the lagrangian density, which would spoil the invariance. As many massless gauge bosons have

to be introduced as there are generators in the group.

The simplest gauge group is the $U(1)_{em}$ gauge group, which describes quantum electrodynamics (QED). This group can be taken to show how local gauge invariance works: a free electron is described by its field ψ, which transforms under the U(1) local gauge transformation like

$$\psi \rightarrow \psi' = e^{ief(x)}\psi \tag{2.4}$$

The importance of a local gauge transformation is that the parameter f is a function of its space-time point x, whereas for a global transformation, f would be a constant. The lagrangian density $L = T - V$, can be written as:

$$L = i\overline{\psi}\gamma^{\mu}\partial_{\mu}\psi - m\overline{\psi}\psi \tag{2.5}$$

where the first term corresponds to electron's kinetic energy and the second to its mass. This lagrangian density is not invariant under a local gauge transformation (equation 2.4), due to the action of the partial derivative on $f(x)$. In order to remove the extra term coming from $\partial_{\mu}f(x)$, we can introduce a gauge field A_{μ}, and substitute the partial derivative ∂_{μ} with the covariant derivative D_{μ} that can be expressed as:

$$D_{\mu} = \partial_{\mu} - ieA_{\mu}(x) \tag{2.6}$$

If we require the covariant derivative $D_{\mu}\psi$ to undergo the same transformation as the field itself ψ:

$$D_{\mu}\psi \rightarrow (D_{\mu}\psi)' = e^{ief(x)}D_{\mu}\psi \tag{2.7}$$

then the lagrangian density becomes locally invariant, provided that the gauge field transforms like:

$$A_{\mu}(x) \rightarrow A'_{\mu}(x) = A_{\mu}(x) + \partial f(x) \tag{2.8}$$

The obtained invariant lagrangian density is, hence:

$$\begin{aligned} L &= i\overline{\psi}\gamma^{\mu}D_{\mu}\psi - m\overline{\psi}\psi \\ &= i\overline{\psi}\gamma^{\mu}\partial_{\mu}\psi - m\overline{\psi}\psi - eA_{\mu}\overline{\psi}\gamma^{\mu}\psi \end{aligned} \tag{2.9}$$

Comparing expression above to equation 2.5, we see that there is an additional term which is given by the interaction between the gauge field A_{μ} and the electromagnetic current $J^{\mu} = e\overline{\psi}\gamma^{\mu}\psi$. The introduced field is in fact the photon and the interaction term describes the electromagnetic interactions mediated through photons, like $\gamma \rightarrow e^{+}e^{-}$. In the lagrangian density expressed in equation 2.9 there is no kinetic term for the photon. This term is given by

the invariant tensor $F_{\mu\nu} = \partial_\mu A_\nu - \partial_\nu A_\mu$, and by adding it we get the full QED lagrangian density:

$$L = i\overline{\psi}(i\gamma^\mu \partial_\mu - m)\psi - J^\mu A_\mu - \frac{1}{4} F_{\mu\nu} F^{\mu\nu} \tag{2.10}$$

Summarizing, local gauge invariance under the $U(1)_{em}$ transformation given in equation 2.4 requires the existence of a gauge boson, which is the photon. It is a massless boson as the introduction of a mass term in the lagrangian density from equation 2.10 would spoil the invariance under the local gauge transformation. It is important to remark that the single generator of this $U(1)_{em}$ group is the electric charge e.

Similarly, the strong interaction of quarks can be described by the non-abelian group SU(3). There are three possible colour states, and therefore quarks are in the fundamental representation of a group having three dimensions. The gauge transformations are those of the quark colour fields. The number of bosons which have to be introduced is eight. Those are the corresponding eight gluons, which are also massless bosons, as required by the local gauge principle. The only difference to photon is that self-interactions between gluons are allowed, as they mediate the force between colour charged objects but also carry the colour charge themselves (photons are chargeless but couple only to electrically charged particles). This causes the phenomenological difference between the electromagnetic and strong interactions.

Historically, the weak interactions were thought to be described by the SU(2) gauge group. At the time, physicists only observed charged weak currents, coupling electrically charged with electrically neutral particles. The fermions experiencing the charged weak force were grouped in weak isospin doublets and the group was denoted by $SU(2)_L$ since it seemed that the bosons associated with this group coupled only to left-handed particles. However, this gauge group requires a third gauge boson, which was not yet identified. From global gauge invariance and Noether's theorem, we get the three conserved currents (the weak isospin currents):

$$J_i^\mu = \frac{1}{2} \overline{\Psi}_l^L \gamma^\mu \tau_i \Psi_l^L \quad , \quad i = 1, 2, 3. \tag{2.11}$$

and the three weak isospin charges :

$$I_i^W = \frac{1}{2} \tau_i \quad , \quad i = 1, 2, 3. \tag{2.12}$$

The term τ_i stands for the Pauli matrices, which are generators of the group SU(2), and Ψ_l^L is the isospin spinor, which is the two-component field, consisting of the two left-handed lepton fields $\psi_{\nu_l}^L$ and ψ_l^L. With linear combinations

of the first two currents, the charged currents were obtained. The third current should couple either two electrically neutral leptons or, like the electromagnetic current J^{μ}, two electrically charged leptons with each other (this neutral weak current was discovered in 1973).

However, the sensitivity to the electric charge indicates that the $SU(2)_L$ group will have to be combined with the $U(1)_{em}$ group. In order to keep local gauge invariance, the $SU(2)_L$ group requires three massless bosons, W_i^{μ}, with i=1,2,3. Two of these bosons are electrically charged and hence, is evident that the $U(1)_{em}$ group will not leave the $SU(2)_L$ group undisturbed. In consequence, a new group has to be introduced. The new group is the weak hypercharge group $U(1)_Y$ with the generator Y that conmutes with the three $SU(2)_L$ generators. This procedure is called **electroweak unification** since the $U(1)_{em}$ is a subgroup of the total electroweak gauge group: $U(1)_{em} \subset SU(2)_L \times U(1)_Y$. With the $U(1)_Y$ group, the weak hypercharge current

$$J_{\mu}^{Y} = \overline{\Psi}_l^L \gamma_{\mu} Y \Psi_l^L + \overline{\psi}_l^R \gamma_{\mu} Y \psi_l^R \tag{2.13}$$

and the conserved weak hypercharge

$$Y = 2(Q - I_3^W) \tag{2.14}$$

are associated. Applying the principle of local gauge invariance leads to the introduction of an additional gauge boson B^{μ}. The $SU(2)_L \times U(1)_Y$ Lagrangian is then given by:

$$L^{EW} = i[\overline{\Psi}_l^L \gamma^{\mu} D_{\mu} \Psi_l^L + \overline{\psi}_l^R \gamma^{\mu} D_{\mu} \psi_l^R] - \frac{1}{4} F_{\mu\nu}^i F_i^{\mu\nu} - \frac{1}{4} B_{\mu\nu} B^{\mu\nu}. \tag{2.15}$$

The covariant derivative, D_{μ}, has a different form for left-handed spinors Ψ_l^L, consisting of leptons and neutrinos, as for right-handed spinors ψ_l^R since the charged weak interaction (see its associated charge in equation 2.12) only couples to left-handed particles:

$$\begin{aligned} D_{\mu} \Psi_l^L &= [\partial_{\mu} + ig \frac{\tau^i}{2} W_{\mu}^i + i \frac{g'}{2} Y B_{\mu}] \Psi_l^L \\ D_{\mu} \psi_l^R &= [\partial_{\mu} + i \frac{g'}{2} Y B_{\mu}] \psi_l^R \end{aligned} \tag{2.16}$$

where g' and g are the U(1) and SU(2) coupling constants respectively. The second and third terms of equation 2.15 are the kinetic terms for the bosons, looking similar to the one corresponding to photon in equation 2.10:

$$\begin{aligned} F_{\mu\nu}^i &= \partial_{\mu} W_{\nu}^i - \partial_{\nu} W_{\mu}^i + g \epsilon^{ijk} W_{\mu}^j W_{\nu}^k \\ B_{\mu\nu} &= \partial_{\mu} B_{\nu} - \partial_{\nu} B_{\mu}. \end{aligned} \tag{2.17}$$

The vector bosons W^1, W^2, W^3 and B are directly associated to physical particles. A linear combination of the neutral gauge particles W^3 and B gives the physical particles mediating the weak neutral interactions (Z^0) and the electromagnetic interactions (the photon, A_μ) as can be seen in the following equations:

$$\begin{aligned} A_\mu &= B_\mu \cos\theta_W + W^3_\mu \sin\theta_W \\ Z_\mu &= -B_\mu \sin\theta_W + W^3_\mu \cos\theta_W. \end{aligned} \tag{2.18}$$

where θ_W is the so called Weinberg angle, defined as:

$$\sin\theta_W = \frac{g'}{\sqrt{g^2 + g'^2}}. \tag{2.19}$$

Similarly, the observed charged vector bosons ($W^+$and W^-) are linear combinations of the gauge particles W^1 and W^2:

$$W^\pm_\mu = \frac{W^1_\mu \mp W^2_\mu}{\sqrt{2}}. \tag{2.20}$$

The mixing of the gauge fields to give the physical particles is a consequence of the unification of the two gauge groups $SU(2)_L \times U(1)_Y$. This unification is represented by the Weinberg angle (equation 2.19) which contains the coupling constants of each group.

The obtained vector bosons γ, W^+, W^- and Z^0 were assumed to be massless since introducing mass terms in the lagrangian density would spoil the invariance under $SU(2)_L \times U(1)_Y$ transformations. However, from experiments it is known that the W and Z bosons are very massive. In the ground state or vacuum, only $U(1)_{em}$ is an exact symmetry that leads to the observed effect (i.e. the massless photon). Therefore, we speak of the $SU(2)_L \times U(1)_Y$ spontaneous symmetry breaking. In the case of the electroweak Standard Model, the Higgs mechanism is implemented by a weak isodoublet scalar field ϕ, which is given by:

$$\phi = \begin{pmatrix} \phi^+ \\ \phi^0 \end{pmatrix} = \frac{1}{\sqrt{2}} \begin{pmatrix} \phi_1 + i\phi_2 \\ \phi_3 + i\phi_4 \end{pmatrix} \tag{2.21}$$

and with a Lagrangian density given by:

$$L_{Higgs} = (D_\mu \phi)^\dagger (D^\mu \phi) - \mu^2 \phi^\dagger \phi - \lambda (\phi^\dagger \phi)^2 \tag{2.22}$$

where last two terms correspond to the Higgs potential $V(\phi)$, with $\mu^2 < 0$ and $\lambda > 0$. The minima of the Higgs potential can be shown to be found when:

$$\frac{\partial V}{\partial \phi^\dagger \phi} = 0 \qquad \Rightarrow \qquad \phi^\dagger \phi = -\frac{\mu^2}{2\lambda} = \eta^2 \tag{2.23}$$

what can be rewritten, taking in account equation 2.21, in this way:

$$\phi^\dagger\phi = \frac{1}{2}(\phi_1^2 + \phi_2^2 + \phi_3^2 + \phi_4^2) = \eta^2 \tag{2.24}$$

in consequence, a set of values that can verify the minimum condition and therefore that can characterize a ground state is $\phi_1 = \phi_2 = \phi_4 = 0$, $\phi_3 = \sqrt{-\mu^2/\lambda} = \sqrt{2}\eta$. Introducing this ϕ_3 in equation 2.21, and recalling the definition of η from equation 2.23, the ground state can be also written, in terms of η, as follows:

$$\phi_0 = \begin{pmatrix} 0 \\ \eta \end{pmatrix}. \tag{2.25}$$

As the potential has a nonzero minimum value, it is reasonable to describe the field itself as deviations ($H(x)$) from its value at the minimum in this manner:

$$\phi_0 = \begin{pmatrix} 0 \\ \eta + \frac{H(x)}{\sqrt{2}} \end{pmatrix}. \tag{2.26}$$

Introducing this in the Lagrangian density from equation 2.22 we get:

$$\begin{aligned} L = & \frac{1}{2}(\partial_\mu H \partial^\mu H + 2\mu^2 H^2) \\ & - \frac{1}{4} W^1_{\mu\nu} W_1^{\mu\nu} + \frac{1}{2}\frac{g^2\eta^2}{2} W^1_\mu W_1^\mu \\ & - \frac{1}{4} W^2_{\mu\nu} W_2^{\mu\nu} + \frac{1}{2}\frac{g^2\eta^2}{2} W^2_\mu W_2^\mu \\ & - \frac{1}{4} Z_{\mu\nu} Z^{\mu\nu} + \frac{1}{2}\frac{g^2\eta^2}{2\cos\theta_W{}^2} Z_\mu Z^\mu \\ & - \frac{1}{4} A_{\mu\nu} A^{\mu\nu} \end{aligned} \tag{2.27}$$

where Z_μ and A_μ are as defined in equation 2.18, being g and g' the coupling constants appearing in equation 2.16. Each one of the lines appearing in equation 2.27 represents the kinetic energy and the mass of each one of the 5 fields H, W^1, W^2, Z and A. Therefore, mass terms can be read from the Lagrangian density:

a) A new boson appears, called Higgs boson, with mass:

$$m_H = \sqrt{-2\mu^2} \tag{2.28}$$

b) The gauge bosons associated to fields W^1_μ and W^2_μ have the same mass:

$$m_W = \frac{g\eta}{\sqrt{2}} \tag{2.29}$$

c) Another gauge field Z_μ appeared as a linear combination of gauge fields W_μ^3 and B_μ, with mass:

$$m_Z = \frac{g\eta}{\sqrt{2}\cos\theta_W} \tag{2.30}$$

d) The gauge field A_μ corresponds to photons, and hence, no mass term is associated.

As we have seen, the Higgs mechanism gives the $W^\pm$ and the Z^0 bosons their masses but introduces as well a new boson (the Higgs boson, H) of which the mass is unknown. The existence of this Higgs boson is the most important prediction of the Standard Model, and the searches for it are a high priority at most accelerators, although unfortunately the model does not allow to predict its mass precisely, and hence the search is extremely difficult. However, the model allow to do some other important predictions: in 1981, the experimental determination of Weinberg angle, allowed to predict the $W^\pm$ and the Z^0 masses before they were discovered. The resulting values of this prediction were:

$$\begin{aligned} M_Z &= 89.0 \pm 2.0 GeV \\ M_W &= 78.3 \pm 2.4 GeV \end{aligned} \tag{2.31}$$

One of the greatest triumphs of the unified theory was the agreement between the predicted masses for the W and Z bosons and their experimental values found at CERN in 1983 which are the following:

$$\begin{aligned} M_Z &= 91.187 \pm 0.007 GeV \\ M_W &= 80.33 \pm 0.15 GeV \end{aligned} \tag{2.32}$$

The small disagreement between them is due to: 1) the use of a Weinberg angle value for the estimations which was not so accurate at that time and 2) the fact of only considering the lower order diagrams contribution for the calculations performed, whereas strictly speaking higher order contributions should have been included. Taking in account the higher order diagrams and a more accurate value for θ_W, the agreement between experimental and predicted values becomes excellent.

Higgs production mechanisms and discovery channels at the LHC

The production mechanisms of the Higgs boson in an hadron collider like LHC are the following [2]:

gluon fusion	:	$gg \to H$
WW, ZZ fusion	:	$W^+W^-, ZZ \to H$
W, Z bremsstrahlung	:	$q\bar{q} \to W, Z \to W, Z + H$
$t\bar{t}$ fusion	:	$q\bar{q}, gg \to t\bar{t} + H$

The lowest order diagrams of these processes are depicted in figure 2.3. An overview of the production cross sections for the Higgs particles at the LHC is shown in figure 2.4. We can clearly distinguish three classes of channels:

a) The Higgs production from a top quark loop generated in a gluon-gluon fusion is a universal process, dominant over the entire Standard Model Higgs mass range. It is furthermore amplified by the higher order QCD processes (contributions included in the cross section shown in figure 2.4), i.e. virtual contributions to the $gg \to H$ process and contributions with an additional parton in the final state.

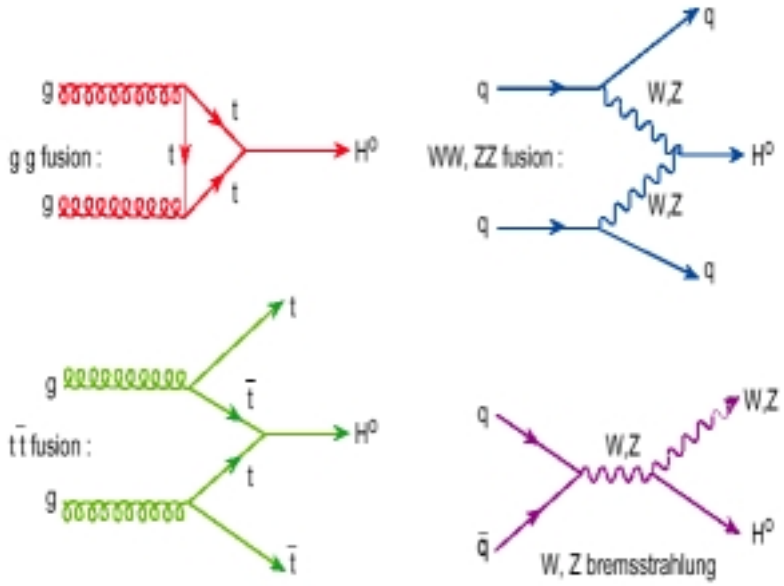

Figure 2.3: *Standard Model Higgs production mechanisms at LHC*

b) The WW or ZZ fusion (labeled in figure 2.4 as $qq \to Hqq$, which in fact corresponds to the process: $qq \to VVqq \to Hqq$, with $V = W, Z$) gives a significant contribution as at $m_H \approx 100$ GeV, its cross-section is one order of magnitude smaller than the gluon-gluon fusion one, but its relative

contribution increases with the Higgs mass, becoming as important as the gluon-gluon fusion process at $m_H \approx 1$ TeV. The QCD corrections are less relevant in this case, although are also taken in account in the figure.

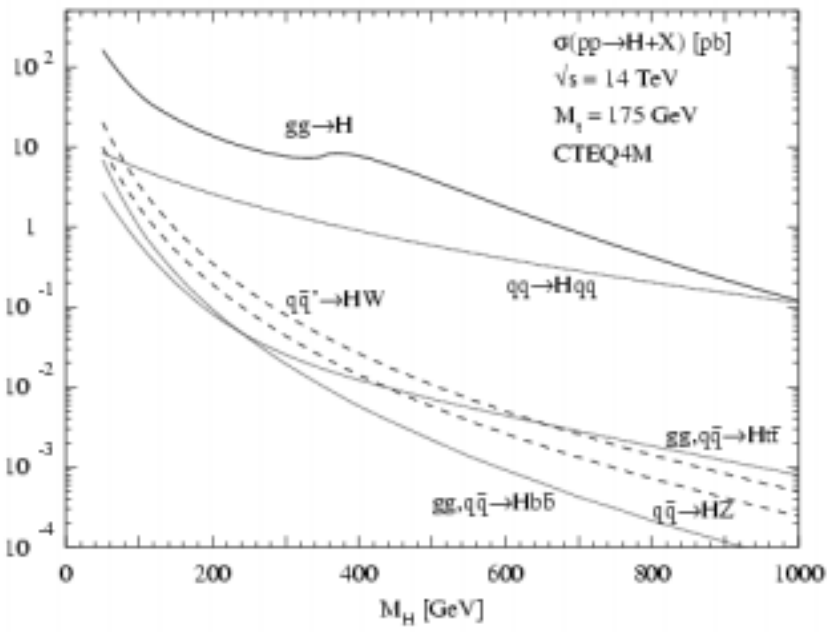

Figure 2.4: *Higgs production cross sections at the LHC for various production mechanisms as a function of the Higgs mass.*

c) The processes with an associated production of W, Z (corresponding to $q\bar{q} \to V^* \to VH$, and labeled in figure 2.4 as $q\bar{q} \to VH$, with $V = W, Z$) or a $t\bar{t}$ pair (corresponding to $gg \to t\bar{t}H$) are prominent for light Higgs bosons ($m_H < 120$ GeV). The QCD corrections for the Higgs radiation from a W or Z are included in figure 2.4, however, corrections to the Higgs radiation from a $t\bar{t}$ fusion are unknown.

We will discuss now which are the Higgs boson main decay modes and its widths. The Higgs decays are determined by the coupling to the fermions (f) and gauge bosons ($V = W, Z$), resulting in couplings proportional to fermions masses and to the square of gauge bosons masses:

$$\begin{aligned} g_{Hff} &= [\sqrt{2}G_F]^{1/2} m_f \\ g_{HVV} &= 2[\sqrt{2}G_F]^{1/2} {M_V}^2 \end{aligned} \tag{2.33}$$

The total decay width and lifetime, as well as the branching ratios for specific decay channels are determined by these parameters. By adding up all possible

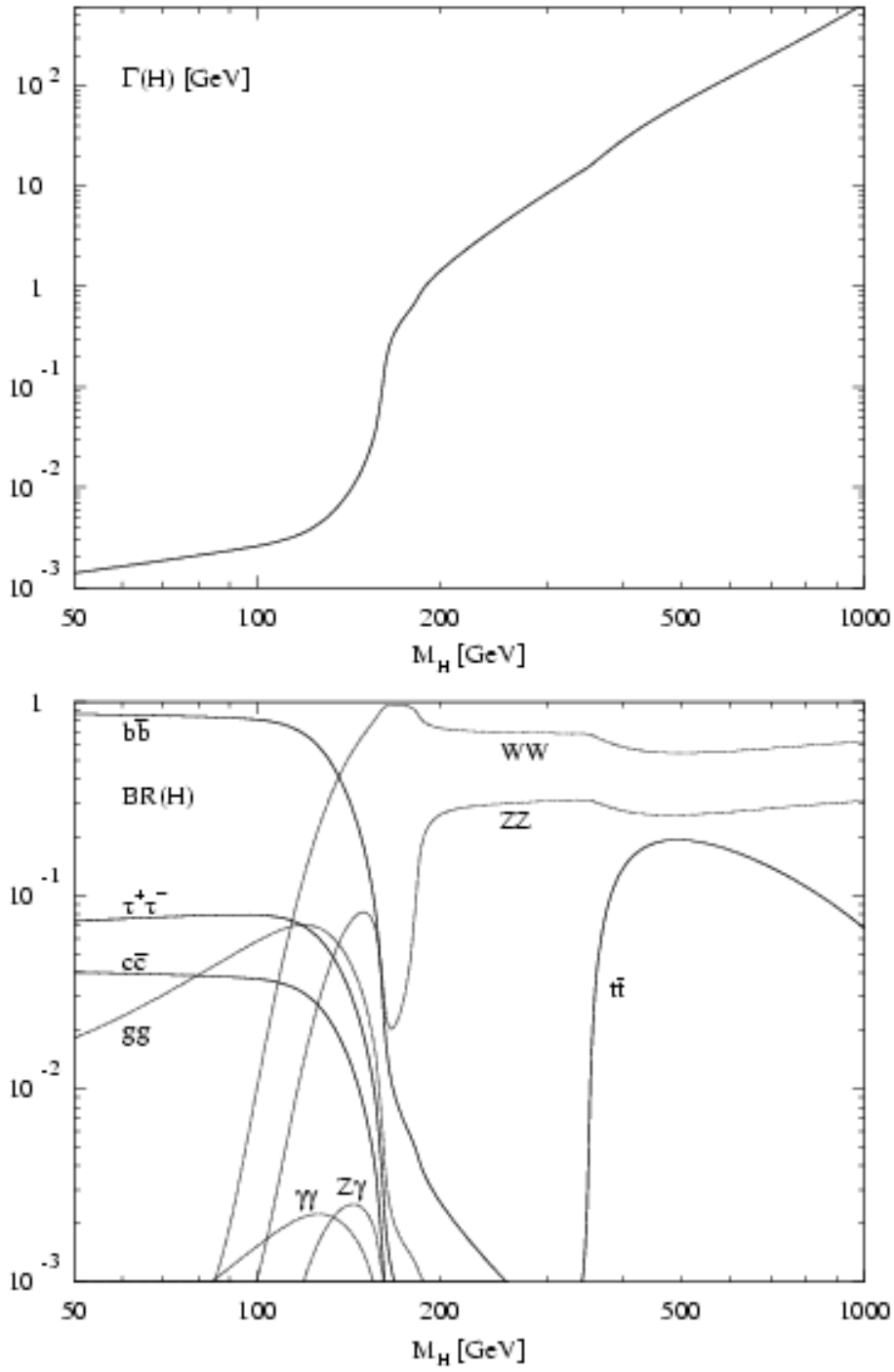

Figure 2.5: *(a) Total decay width (in GeV) of the SM Higgs boson as a function of its mass. (b) Branching ratios of the dominant decay modes of the SM Higgs particle.*

decay channels, we obtain the total width ($\Gamma = \Sigma\Gamma_i$) shown in figure 2.5a. As is shown in the figure, the width remains extremely narrow at low Higgs masses (few MeV at m_H=100 GeV, and $\approx$ 1 GeV at m_H=200 GeV) becoming much broader at higher Higgs masses.
The branching ratio of a decay channel i is defined by $BR_i = \Gamma_i/\Gamma$. The branching ratios of the channels as a function of the Higgs mass are shown in figure 2.5b. In this plot it can be seen that for Higgs particles in the intermediate mass range ($m_Z < m_H < 2m_Z$) the main decay modes are into $b\bar{b}$ pairs and WW,ZZ pairs, one of the gauge bosons being virtual below the respective threshold. Above the WW,ZZ pair thresholds, the Higgs particles decay almost exclusively into these two channels, with a small contribution of top decays near the $t\bar{t}$ threshold. Below 140 GeV, the decays $H \to \tau^+\tau^-$, $c\bar{c}$ and gg are also important besides the clearly dominating $b\bar{b}$ channel. However, not all the decay modes provide experimentally distinguishable signatures and the amount of detectable signal is reduced. For example, the abundant decay channels at low Higgs masses ($b\bar{b}$,$\tau^+\tau^-$) are believed not to be exploitable due to the large background present in hadron colliders. Therefore, not all Higgs decay channels are expected to be exploited in the LHC. In spite of that, there is another decay channel which will become relevant at low Higgs masses: the decay of the Higgs into a photon pair. This channel and the other most promising channels for the Higgs discovery at LHC are shown in figure 2.6.

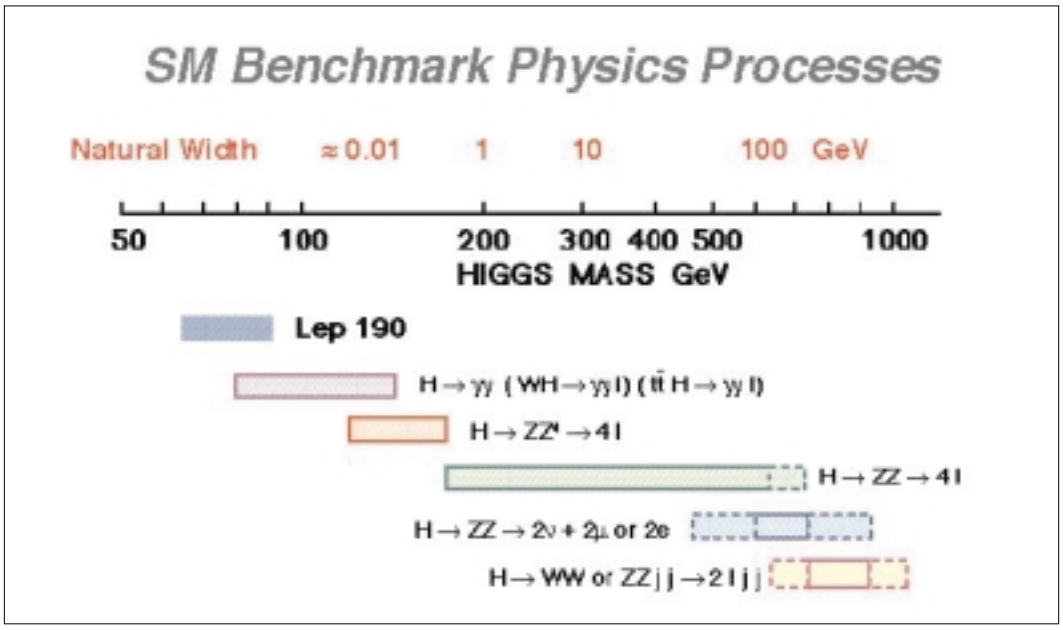

Figure 2.6: *The most important decay channels for Higgs discovery at LHC.*

In figure 2.6 we can see that between the lowest Higgs mass possible, which is the limit imposed by LEP2 (not 90 GeV as in the figure, but $\approx$ 110 GeV at

the end of LEP running) and $m_H \approx 150$ GeV, the main discovery channel is $H \to \gamma\gamma$, which gives a signal of two electromagnetic clusters. This channel is strongly suppressed by its small branching ratio (see figure 2.5b, where BR $\approx 10^{-3}$) but, as shown in figure 2.5a, the natural width of the Higgs boson at this mass range is extremely narrow, being in consequence possible to detect this channel over the enormous diphotonic background if we count on an extremely precise detector for measuring the mass peak. Below $m_H \approx 2m_Z$ an important signal is the decay of the Higgs boson to one real and one virtual Z boson, with both, Z and Z^* decaying into leptons. With masses larger than $2m_Z$, the decays into two real Z can be exploited, giving a clean signature if the two Z decay into electrons or muons. The Higgs production cross-section decreases with the increasing Higgs mass (see figure 2.4) and therefore the four lepton mode of the $H \to ZZ$ becomes complicated when $m_H > 600$ GeV. At those values some other decays are more relevant, such as: $H \to ZZ \to \nu\bar{\nu}ll$ (l stands for lepton), or the channel $H \to WW \to l\nu jj$.

2.3 CMS

2.3.1 General overview of the CMS Experiment

The concept of a compact detector for the LHC based on a solenoid, the Compact Muon Solenoid (CMS) detector, was presented in October 1990 at the LHC workshop in Aachen. For a high luminosity proton-proton machine it is natural to optimize first the muon detection system. All types of magnetic configurations were studied [3]. The requirement for a compact design led to the choice of a strong magnetic field. The only practical magnet that can generate a very strong magnetic field is a solenoid. A long (about 14 m) superconducting solenoid of large radius (about 3m) generating a magnetic field of 4 T guarantees good momentum resolution for high momentum (≈ 1 TeV) muons up to rapidities of 2.5, without strong demands on the chamber space resolution. The large radius of the solenoid allows the full calorimetry to be located inside it. Therefore, the coil does not affect the calorimeter performance. As was mentioned in previous section, the efficient detection of an intermediate mass Higgs boson via its two photon decay would require a very precise electromagnetic calorimeter. Such a precise electromagnetic calorimeter fits naturally in the CMS design.

The design goals of CMS are the following:

a) A very good muon identification and momentum measurement even in the most difficult experimental conditions.

b) A high resolution electromagnetic calorimeter for the energy measurements of photons and electrons.

c) A powerful inner tracking system that allows reconstruction of particle tracks and precise momentum measurement to reach the two criteria mentioned above.

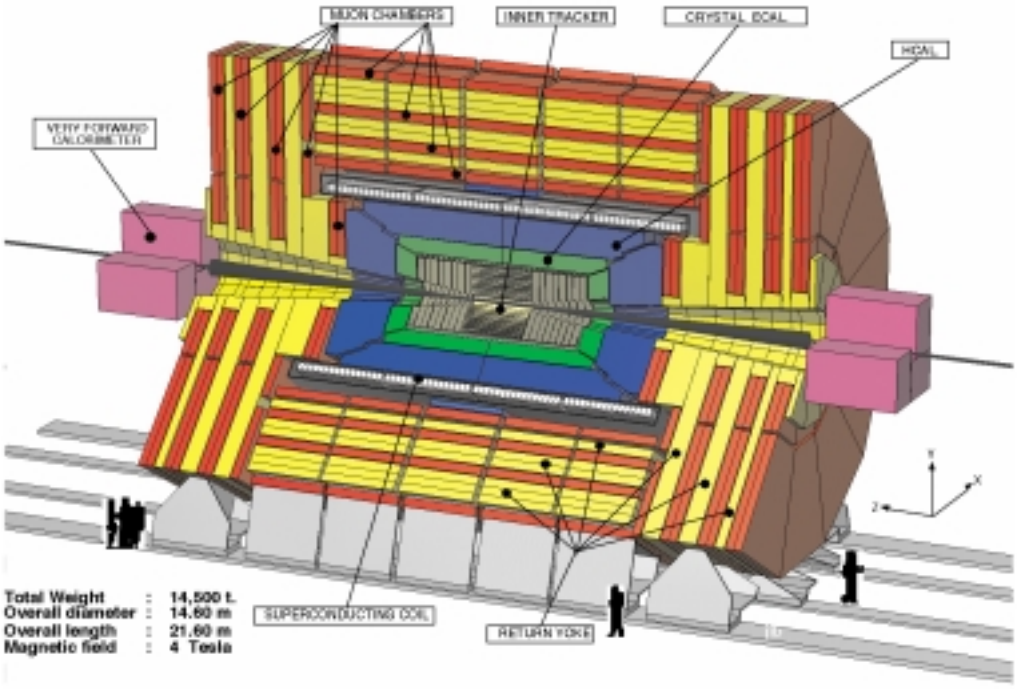

Figure 2.7: *Three dimensional view of the CMS detector.*

A general 3D view of the CMS detector is shown in figure 2.7, whereas the transversal section of it is what depicts figure 2.8. In both pictures we clearly see which are the main parts of CMS detector: going from the interaction point outwards we find the inner tracker, then the calorimetry system (consisting of two parts, the electromagnetic and the hadronic calorimeter), then the superconducting coil and after that, the muon system which is composed by four muon stations integrated in the iron return yoke of the magnet. All CMS sub-detectors will be briefly described in the following subsections, whereas only some generalities will be pointed out in this overview.

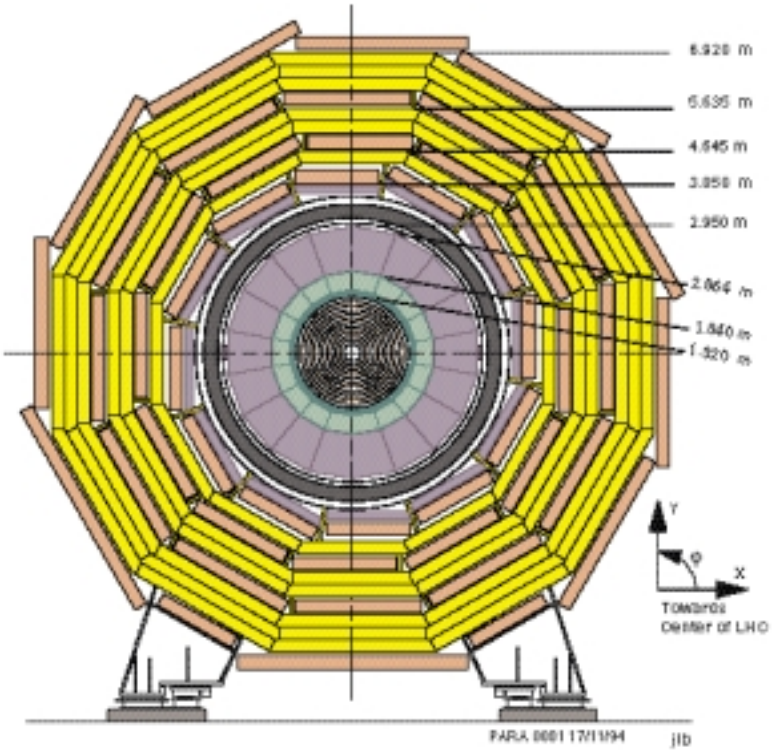

Figure 2.8: *Transversal view of the CMS detector.*

The strong magnetic field chosen (4 T) will be parallel to the beam line, bending therefore the charged particle tracks in the transverse plane. Such a magnetic field will clean the environment in the region between the interaction point and the electromagnetic calorimeter by confining low momentum charged particles in helicoidal trajectories around the beam line. This will strongly reduce the charged particle multiplicity in the electromagnetic calorimeter barrel. However in the inner tracker there will be an enormous particle density due to the confining of low momentum particles. This implies that the inner tracker must have a very high granularity. It is important to mention that outside the superconducting coil, the magnetic field keeps the same direction than inside but with an opposite sense, due to the action of the return yoke. This produces the typical S-shape muon tracks characteristic from CMS that are part of its logotype.

Another interesting aspect is that the calorimeters are located inside the solenoid which has technical size limits. In consequence, the calorimeter system must be compact and besides provide enough material to avoid hadronic cascades leaking into the muon system. The first constraint played an im-

portant role in the choice of an homogeneous $PbWO_4$ crystal electromagnetic calorimeter (the high radiation length of the $PbWO_4$ allows a very compact detector) and the second was very important in the choice of an hadronic sampling calorimeter consisting of active scintillator plates and copper absorbers.

2.3.2 The inner tracker

The tracker system [4] must be as light as possible to minimize the number of secondary interactions produced in the tracker material by the primary particles. With that aim, the inner tracking system is representing in average only a 30% of a single radiation length (X_0).

The inner tracking will provide the momentum measurements for all Higgs signals with decay products being charged leptons. It will allow to establish which are the leptons and photons that are isolated and therefore will allow to suppress the background in most of the Higgs discovery channels mentioned in previous section. It will be also used for the vertex location in the $H \rightarrow \gamma\gamma$ channel. The design goal of the inner tracker is to reconstruct isolated high p_t tracks with an efficiency better than 95%, and high p_t tracks within jets with an efficiency better than 90% over the pseudorapidity range $|\eta| < 2.6$. It will provide a tool for frequent in situ calibration of every cell of the crystal electromagnetic calorimeter, needed to maintain the high energy resolution of the calorimeter. It will also help to tag the presence of b-quarks at the highest luminosities.

The CMS tracker is divided in two regions: barrel and forward parts, meeting at η=2. The barrel part, going from the inside to the outside, consists of 2 layers of silicon pixel detectors, and 3 layers of silicon microstrip devices. In the forward part we find 3 layers of silicon pixel detectors, also 3 layers of the silicon microstrip devices and in the outer part, the MSGC are placed in an intermediate region with 5 detection layers and in the endcap region with 9 detection layers. The cell size pixel detectors is 150×150 μm^2, and the expected hit resolution is 15μm. For the silicon microstrip detectors, the strip length is 12.5 and the pitch ranges from 61 to 244 μm, depending on the type of device. The hit resolution varies from 15 to 70 μm.

Existing simulations confirm that isolated muon tracks with a p_t=1 GeV can be reconstructed with an efficiency better than 98% over the full pseudorapidity range. High energy electrons (with $p_t > 10$ GeV) can be reconstructed with an efficiency above 90%. Besides, the b quark tagging efficiency in the central pseudorapidity region is 50% or better (a slightly lower efficiency is found in the forward region: 40%).

2.3.3 The electromagnetic calorimeter

The role of this part of the CMS detector is to measure the energy of electrons, positrons and photons produced in collisions. It will also be used in particle identification (specifically electron/charged pion separation in conjunction with the inner tracker) and will also help to measure the energy of high energy hadrons (in conjunction with the hadron calorimeter). The CMS electromagnetic calorimeter (ECAL) will be described in detail in section 2.4.

2.3.4 The hadronic calorimeter

The CMS Hadron Calorimeter (HCAL) will be used to measure quark, gluon and neutrino directions and energies by measuring the energy and direction of particle jets and of the missing transverse energy flow. It will be the combined response of the ECAL and the HCAL what will provide the raw data needed for the reconstruction of particle jets and missing energy mentioned previously. The HCAL will also help in the identification of electrons, photons, and muons in conjunction with the ECAL and the muon system.

The CMS HCAL [5] is a sampling calorimeter (see subsection 2.4.1) with active plastic scintillators layers and brass absorber layers. The absorber plates are 5 cm thick in the barrel and 8 cm thick in the endcap. The active elements of the entire central HCAL are 4mm thick plastic scintillator tiles read out by using wavelength-shifting plastic fibers. The HCAL is placed inside the solenoidal magnet starting at a radius of 1.806 m and ending at 2.95 m in the barrel region ($|\eta|$ <1.3), whereas in the endcap region ($1.3 < |\eta| < 3$) it is placed in the region $3.88 < |z| < 5.70$ m (see figures 2.7 and 2.8). To ensure

and adequate sampling depth in the barrel and endcap region of the HCAL, the first muon absorber layer is instrumented with scintillator tiles forming the so called outer hadronic calorimeter. A separated forward calorimeter, composed of quartz fibers as active medium embedded in a copper absorber matrix, will be placed in the region $3.0 < |\eta| < 5.0$ in order to extend the hermeticity of the HCAL (as required to perform precise missing transverse energy measurements).

Test beam results and simulation studies confirm that the CMS HCAL will be able to reconstruct single pions with an energy resolution of $(\sigma/E) = (110\%/\sqrt{E}) \oplus (5\%)$. Some other tests and simulations show that the decay into two jets of a W boson coming from a Higgs with mass 800 GeV can be reconstructed with a good resolution (FWHM≈20 GeV).

2.3.5 The muon system

Muon detection is the most natural and powerful tool to detect interesting events over the background. As mentioned previously, a very important decay of the Higgs boson is given by $H \rightarrow ZZ^{(*)} \rightarrow 4l^{\pm}$ (see figure 2.6). The four lepton channel is crucial for the discovery of the Higgs boson in the mass range from ≈130 GeV up to ≈750 GeV. If the leptons are muons, the best 4-particle mass resolution can be achieved, and muons are much less affected by radiative losses in tracker material than electrons due to its higher mass.

The muon system [6] has three main purposes: muon identification, muon trigger and muon momentum measurement. The muon identification at the highest luminosities reachable can be ensured thanks to presence of a sufficient amount of material in front of the muon system. The combination of precise muon chambers and fast dedicated trigger detectors provide unambiguous beam crossing identification and trigger on single and multimuon events with well defined p_t thresholds from a few GeV to 100 GeV up to η=2.1. The momentum measurements can be made in standalone mode (only the muon system) or in global mode (after matching muon system information with the Central Tracker data).

The CMS muon system consists of five wheels surrounding the magnet

and two endcaps. The four muon stations present in both the barrel and the endcaps are integrated in the iron return yoke of the magnet. The muon system provides coverage in the range $0 < |\eta| < 2.4$. The active parts of the system use different devices: drift tubes are used in the barrel and cathod strip chambers in the endcaps. Besides, resistive plate chambers are used in both the endcap and barrel regions.

The momentum resolution in the standalone mode goes from 8 to 30% for $p_t = 100$ GeV and from 15 to 35 % for p_t=1 TeV, always at pseudorapidity values below 2. When the momentum measurement is made in global mode (combining with Inner Tracker data) momentum resolution can be improved: 2 to 6 % for p_t= 100 GeV and 6 to 17 % for p_t=1 TeV, in the full pseudorapidity range covered by the muon system (0 to 2.4), matching the performance requirements.

2.4 The CMS Electromagnetic Calorimeter

2.4.1 General notions about calorimeters

A calorimeter is a composite detector using total absorption of particles to measure the energy and position of incident particles or jets. In the process of absorption showers are generated by cascades of interactions, hence the occasionally used name "shower counter" for a calorimeter. In the course of showering, eventually, most of the incident particle energy will be converted into "heat" what explains the name calorimeter ("calor" is the Latin term for heat) for this kind of detector. However, no temperature is measured in practical calorimeters but characteristic interactions with matter are used to generate a detectable effect, via particle charges: neutral and charged particles incident on a block of matter will deposit their energy through creation and destruction processes. The deposited energy is rendered measurable by ionisaton or excitation of the atoms of matter in the active medium. According to the active medium we can distinguish between totally active or **homogeneous calorimeters**, when the active medium is a block itself, combining in a single material the functions of passive particle absorption and active signal generation, and **sampling calorimeters**, when the particle absorption function is separated from the active signal readout, being these calorimeters usually

built as sandwichs of a dense absorber and a light active plane. An example of the cascade of interactions or shower generated in a bubble chamber in a 3 T magnetic field due to the incidence of a 50 GeV electron is shown in figure 2.9.

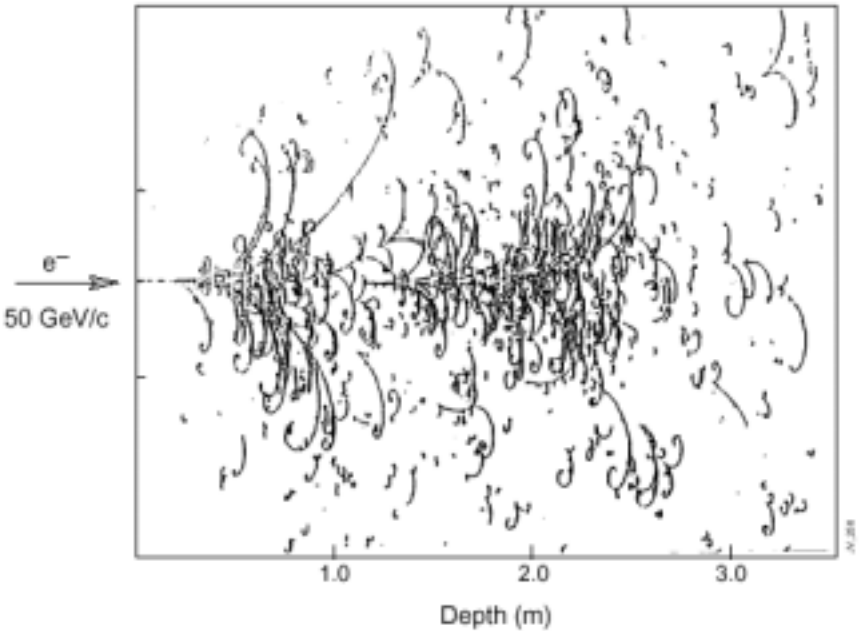

Figure 2.9: *Shower generated in a bubble chamber with radiation length 34 cm by a 50 GeV electron.*

Calorimeters are extremely important in nowadays physics for the following reasons [7]:

a) Calorimeters can measure energies of both neutral and charged particles.

b) The absorption of energy of incident particle is made via a cascade process that leads to a number of secondary particles, n, where n is proportional to the incident energy. The cascade development is statistical in nature and the uncertainty on the measurement of energy (σ) is governed by the statistical fluctuation on n, and hence the relative energy resolution σ/E improves with energy as $1/\sqrt{n} \approx E^{-1/2}$. This contrasts with momentum measurement of charged particles with tracking devices, where relative momentum resolution worsens when p increases.

c) The longitudinal depth required to contain the cascades scales logarithmically with particle energy whereas for magnetic spectrometers the size

scales with momentum p as $\sqrt{p}$ for a given momentum resolution $\delta p/p$.

d) Calorimeters are essentially the only devices that can measure the energy of jets.

e) Full geometric coverage enables the determination of missing transverse energy which, if significant, signals the presence of weakly interacting particles such as neutrinos.

f) The cascade develops differently longitudinally and laterally, for electrons or photons, hadrons and muons. This difference can be exploited for particle identification.

g) Calorimeters are devices with potentially fast response, allowing operation at high particle rates.

h) The pattern of energy deposit in a calorimeter with good lateral and longitudinal segmentation allows fast, efficient and very selective triggering on electrons or photons, jets and missing transverse energy.

Energy loss in matter

Moderately relativistic particles other than electrons loose energy in matter through the Coulomb interaction with atomic electrons. There is an energy transfer to these electrons that can make them to be ejected from the parent atom (this process is called ionisation) or to be excited to a higher level (process called excitation). The energy loss is given by the well known Bethe-Bloch equation:

$$-\frac{dE}{dx} = N_A \frac{Z}{A} \frac{4\pi\alpha^2(hc)^2}{m_e c^2} \frac{Z_i^2}{\beta^2} \left[ln \frac{2m_e c^2 \gamma^2 \beta^2}{I} - \beta^2 - \frac{\delta}{2} \right] \tag{2.34}$$

where E is the kinetic energy of the incident particle with velocity β and charge Z_i and I ($\approx 10 \times Z$ eV) is the mean ionization potential in a medium with atomic number Z.

In the case of electrons the radiative processes dominate energy loss for energies above 1 GeV. In the intense electric field of nuclei relativistic electrons radiate photons by bremsstrahlung and photons are converted into electron-positron pairs (see figure 2.10). When talking about electrons or photons striking on a material it is convenient to measure the depth and radial extent of the resulting cascades in terms of the so called radiation length (X_0) and the Moliere radius (R_M), which will be defined later. The photons loose energy through photoelectric effect and Compton scattering at low energies and by pair production at relativistic energies (see figure 2.11).

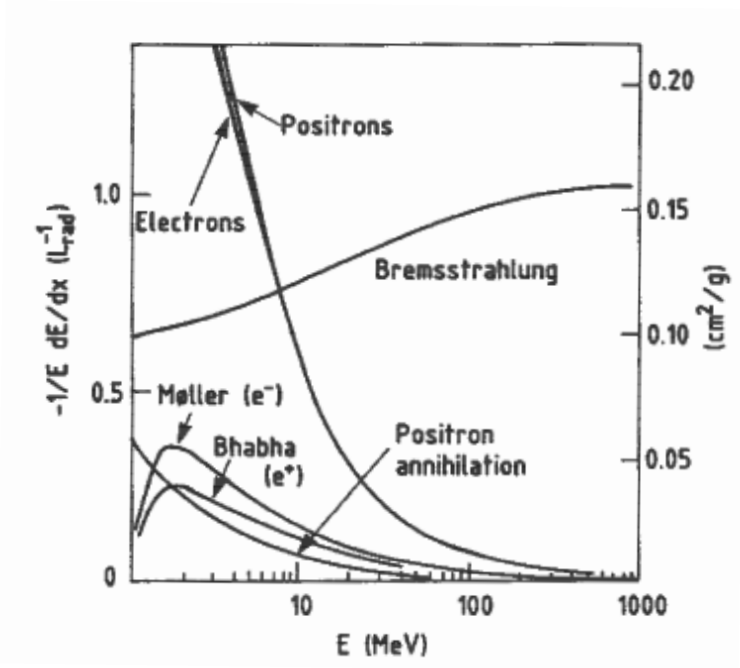

Figure 2.10: *Fractional energy loss per radiation length in lead as a function of electron energy.*

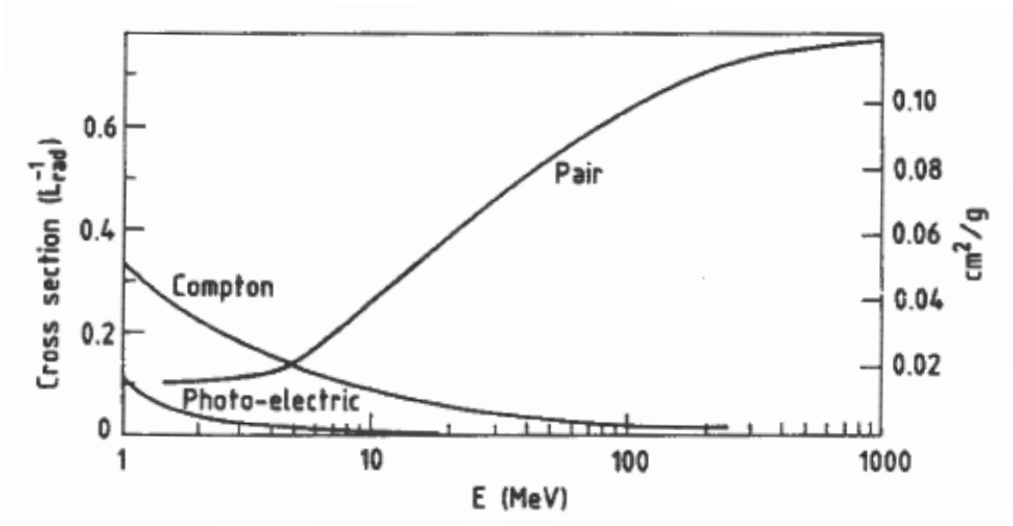

Figure 2.11: *Photon cross section in lead as a function of photon energy.*

Electromagnetic cascades

In the development of electromagnetic cascades there are some important parameters to be defined. The first of them, already mentioned, is the *radiation length* (X_0) that can be defined as the mean distance traveled by a high-energy electron until its energy has been reduced to a fraction 1/e of the initial energy. It is very important also to define the *critical energy* (ε), or the energy at which the losses due to ionisation and radiation are equal. It is often defined in terms of proton as the value of its energy below which the energy loss for ionisation starts dominating the energy loss for bremsstrahlung. Another important parameter already mentioned is the *Moliere radius* (R_M) that can be understood as the radius of an infinite cylinder containing 90% of the shower energy, or, in terms of the *critical energy* the average lateral deflection of electrons with energy ε after traversal of 1 X_0.

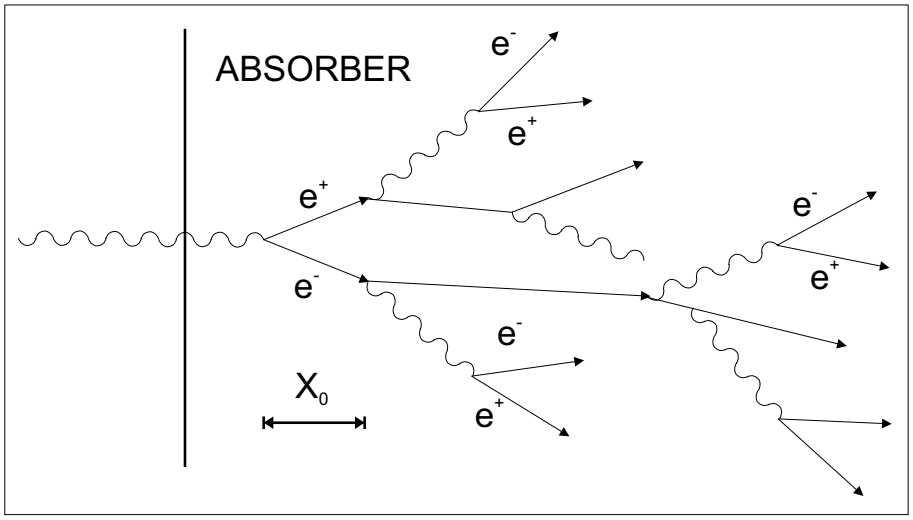

Figure 2.12: *Schematic development of an electromagnetic shower.*

A high energy electron or photon incident on a thick absorber initiates a cascade of secondary electrons and photons via bremsstrahlung and pair production as is illustrated in figure 2.12. With increasing depth, the number of secondary particles increases although their mean energy decreases. This multiplication process goes on until the energies are so degraded that fall below the critical energy ε. Then, ionization and excitation rather than generation of more particles dominate the dissipation of energy.

Longitudinal development of electromagnetic showers is usually assumed to be contained in a distance of $26X_0$, being the shower maximum at a depth

typically between 3 and $10X_0$, depending on the atomic number Z of the material (e.g. $PbWO_4$ crystals present the shower maximum at a depth $\approx 8X_0$ for 100 GeV incident electrons), and on the energy of incident particles. Lateral development of and electromagnetic cascade is determined by the multiple scattering of electrons away from the shower longitudinal axis. There is also an influence of low energy photons that deposit its energy far away from their emission point, especially when electrons that generated them also traveled far from the original longitudinal axis. Lateral extent of electromagnetic showers scales accurately with R_M for different materials.

Energy resolution

The energy resolution of calorimeters is usually expressed in terms of three parameters a, b and c as follows [8]:

$$\frac{\sigma}{E} = \frac{a}{\sqrt{E}} \oplus \frac{b}{E} \oplus c \tag{2.35}$$

where $\oplus$ stands for quadratic sum, i.e. the square of the energy resolution σ/E is equal to the sum of the square of terms in a, b and c.

The first term, with parameter a is usually called the *stochastic* or *sampling* term and accounts for the statistical fluctuation in the number of primary and independent signal generating processes, or any further process that may limit this number. An example of one of these processes is the conversion of light into photoelectrons by a photo-device.

The second term, with parameter b is called the *noise* term and includes the energy equivalent of the electronics noise and the fluctuation in energy carried by particles other than the ones of interest entering in the measurement area. This phenomenon is usually called *pileup*. This term is normally negligible at energies higher than hundred GeV.

The third term, with parameter c is usually called *constant* term and takes in account:

- Quality imperfections in the construction of the calorimeter,

- Non-uniformity effects of the signal generation and/or collection.
- Cell to cell intercalibration error,
- Fluctuations in the amount of energy leakage from the front, the rear and the sides of the volume used for the energy measurement,
- Fluctuations in the amount of energy deposited in dead areas in front or inside the calorimeter.

The typical values of the energy resolution parameters for homogeneous and sampling electromagnetic calorimeters used in high energy physics are the following:

$$\begin{aligned} Sampling \qquad &\Rightarrow \qquad \frac{\sigma}{E} \approx \frac{10\%}{\sqrt{E}} + 1\% \\ Homogeneous \qquad &\Rightarrow \qquad \frac{\sigma}{E} \approx \frac{2\%}{\sqrt{E}} + 0.5\% \end{aligned} \tag{2.36}$$

where the noise term b is not included because is negligible at the energies at which these calorimeters usually operate.

2.4.2 CMS Electromagnetic Calorimeter physical objectives and requirements

The main tasks of the CMS Electromagnetic Calorimeter (ECAL) are to measure the energy and location of the electromagnetic showers and to contribute to the measurement of hadron showers and missing energy in collaboration with the hadron calorimeter [9]. The ECAL will provide very helpful information for the Higgs search at LHC by measuring the two-photon decay mode for $m_H \leq 150$ GeV, and by measuring the electrons and positrons from the decay of W's and Z's originating from $H \rightarrow ZZ^{(*)}$ and $H \rightarrow WW$ decay chain for a Higgs with mass between 140 and 700 GeV. However, all these physical processes that we would like to see in the CMS ECAL are very exigent and require special performances, in particular for the detection of the decay $H \rightarrow \gamma\gamma$ of a light Higgs. The natural width of H in this mass range is very narrow (see figure 2.5a) therefore, the width of the mass spectra will be entirely dominated by the calorimeter energy resolution. In consequence,

some of the special performances needed are an excellent energy resolution and an excellent angular resolution to measure the two photons produced in the light Higgs decay. The mass of the Higgs boson will be reconstructed from the energy of the two photons and the angle between their trajectories according to:

$$M_H = 2\sqrt{E_1 E_2}\sin\frac{\theta}{2} \tag{2.37}$$

Obviously, the mass resolution will depend on the energy resolution for each one of the two photons and on the resolution of the measurement of θ. Hence, mass resolution is given by:

$$\frac{\sigma_M}{M} = \frac{1}{2}\left[\frac{\sigma_{E_1}}{E_1} \oplus \frac{\sigma_{E_2}}{E_2} \oplus \frac{\sigma_\theta}{\tan(\theta/2)}\right] \tag{2.38}$$

where E is in GeV and θ is in radians. Angular resolution in the barrel is expected to be ≈ 40 mrad$/\sqrt{E}$, whereas energy resolution for each photon is described in equation 2.35.

In order to show how important a good energy resolution is for CMS ECAL physics lets analyze the signal significance. Significance is giving as a comparison of the signal S respect to background B according to $S/\sqrt{S+B}$ which in our case ($B \gg S$) can be expressed as $S/\sqrt{B}$. Simulations have shown that for a Higgs with mass 100 GeV, the significance of the signal varies from 10.5 to 7.5 when the stochastic term a varies from 2%to 10%, for a given constant term b=0.5%. Taking in account the typical values for sampling and homogeneous calorimeters for parameter a expressed in equation 2.36 we understand why the CMS ECAL was chosen to be an homogeneous calorimeter. Besides, when varying c from 0.5% to 1% for an homogeneous calorimeter, the significance worsens from 10.5 to 8. By knowing that a signal only has a serious chance to be recognized when significance is 5 or bigger, then we realize that the constant term c needs to be as low as possible.

The most important requirements for the CMS ECAL are due to two factors: the strict LHC operation conditions and the very challenging performances needed for the light Higgs decay detection already mentioned. They can be summarized as follows:

- An excellent energy resolution with $a \lesssim 3\%$ and $c \lesssim 0.5\%$ is required.

- An optimum granularity is also required. Simulations have shown that a segmentation as $\Delta\eta \times \Delta\phi \lesssim 0.02 \times 0.02$ should be enough to limit pileup.

- An important angular covering is important to maximize the significance of events. It is foreseen that $0 \leq |\eta| \leq 3.0$ and $0^\circ \leq \phi \leq 360^\circ$.

- A fast response is required as the detector has to work at the same frequency than the given by bunch crosses every 25 ns. Response time for ECAL crystals and electronics should be between 25 and 100 ns.

- A optimum resistance to radiation is mandatory: all the elements in the ECAL must resist radiation levels up to values around 5 kGy per year in the barrel and 70 kGy per year in the endcaps (calculated for the first 10 years of LHC operation).

2.4.3 Considerations on the CMS Electromagnetic Calorimeter design

After establishing in previous section which are the CMS ECAL requirements, it is clear that the right choice for the ECAL is an homogeneous calorimeter, providing high granularity and resolution. Scintillating crystal calorimeters are known to provide an optimum performance for energy resolution, so this kind of calorimeter was considered as a strong candidate for the ECAL since the very beginning [a]. However, the type of crystal to be used was something that took some more time to decide. After an intensive R&D program, lead tungstate crystals ($PbWO_4$) were chosen because they offer the best prospects to meet the requirements for LHC operation: it has a short radiation length and a small Moliere radius (allowing a compact calorimeter), it is relatively fast and it is easy to produce at two different plants (a detailed description of the so called PWO crystals can be found in chapter 3).

As some other CMS subdetectors, the ECAL will be composed of a barrel and two endcaps. Both are shown in figure 2.13.

[a] Another possibility was a sampling electromagnetic calorimeter composed of a sandwich of lead and scintillator plates read out by orthogonal wavelength shifting fibers, called "Shashlik" calorimeter.

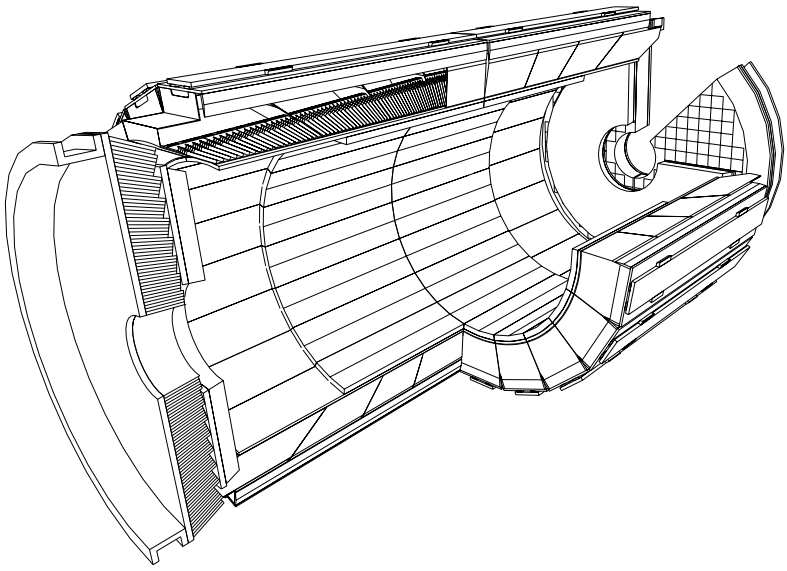

Figure 2.13: *A 3-D view of the CMS electromagnetic calorimeter.*

ECAL barrel calorimeter

It will cover the pseudorapidity range $|\eta| < 1.479$. The front face of $PbWO_4$ crystals will be at radius 1.29m, each crystal having a square cross-section of $\approx 22 \times 22$ mm^2 and a length of 230 mm (25.8 X_0). The truncated pyramid-shaped crystals are mounted in a geometry which is off pointing with respect to the mean position of the primary interaction vertex, with a 3° tilt in both ϕ and in η. The crystal cross-section corresponds to $\Delta\eta \times \Delta\phi = 0.0175 \times 0.0175$. The total amount of crystals in the barrel will be 61200, with a total crystal volume of 8.14 m^3 and with weight 67.4 tons. Crystals for each half barrel will be grouped in 18 supermodules (1700 crystals each). Each one of them will comprise four modules with 500 crystals in the first and 400 in the other three. For simplicity of construction and assembly, crystals have been grouped in arrays of 2×5 crystals which form a submodule (see ECAL barrel elements in figure 2.15). The shape of crystals varies with η in the barrel part, thus demanding initially 85 different types of crystals. However, in order to simplify things, these 85 types have been rearranged into 17 groups. For each group, 5 crystals with the same size are located at successive η values (see figure 2.14). These 17 different types of geometries will be discussed later (see section 3.5). These main ECAL barrel elements are depicted in figure 2.15 and their composition is briefly explained in table 2.3.

Figure 2.14: *View of the 17 different types of submodules present in the ECAL barrel.*

The 10 crystals forming a submodule are inserted into an alveolar structure which is constructed using a low-density two-layer composite material. The first layer (closest to crystal) is a 25 μm aluminium foil with quartz deposited, which acts as a reflector for the light produced in the crystal and also provides mechanical rigidity. The second layer is a glass fiber epoxy resin composite 75 μm thick. Although the walls of the alveola are very thin, the composite structure is very strong. It enables a small inter-crystal gap of 0.4mm to be achieved within a submodule. The alveolar unit is closed by a ferule holder, into which fibers for the optical calibration system are mounted.

The light emitted by the PWO crystals will be detected with silicon avalanche photodiodes (APD). There will be two APD's glued to the rear face of the barrel crystals, covering 50mm^2 of the surface. They operate at a gain of 50 and have quantum efficiency of $\approx 80\%$ for PWO crystals. APD's will be described in detail in section 6.1

Table 2.3: *ECAL barrel composition.*

Unit Name	**Composition**	**Crystals/Unit**
Subunit (sU)	1 crystal + 1 capsule	1
Submodule (sm)	10 subunits	10
Module (Mod)	50/40 submodules [a]	50/40
Supermodule (SM)	4 Mod [b]	1700

[a] *Type 1 Modules contain 50 sM, whereas Types 2, 3 and 4 contain 40 sM*
[b] *One Mod per Type (1, 2, 3 and 4)*

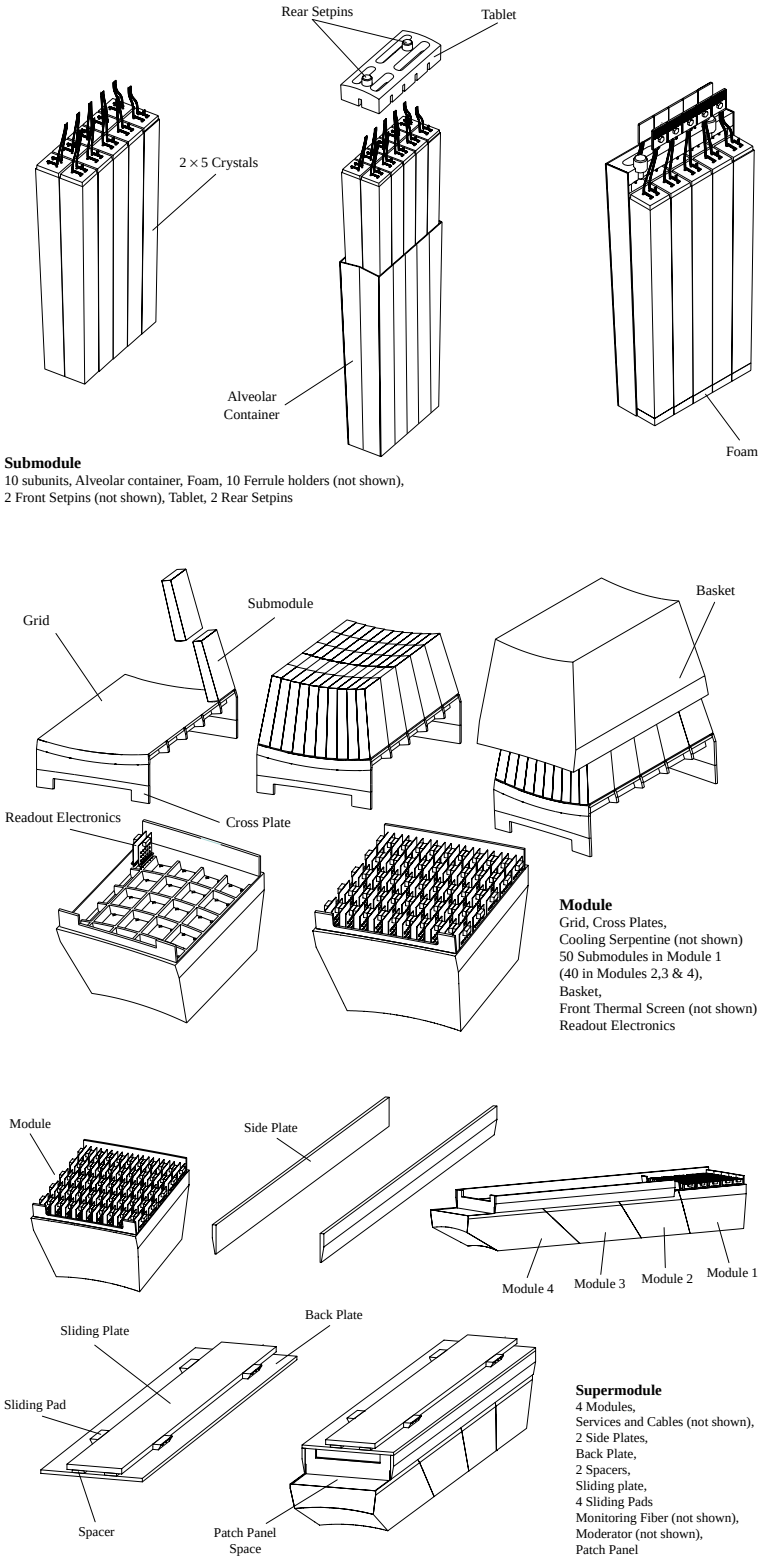

Figure 2.15: *ECAL barrel elements: Submodule, Module and Supermodule.*

ECAL endcap calorimeter

The endcap part of the calorimeter covers a pseudorapidity range from 1.48 up to 3.0. Endcaps are designed to provide precision measurements up to $|\eta|$=2.6, however, crystals will be present up to $|\eta|$=3 in order to augment the energy-flow measurement in the forward direction. The mechanical design of the endcap calorimeter is based on an off-pointing geometry using tapered crystals of the same shape and dimensions (30.0×30.0 mm at the rear face, 28.6×28.6 mm at the front face and 220 mm length) grouped together into units of 25, referred to as supercrystals. A total of 320 identical supercrystals will be used to cover each endcap. Each endcap contains 8000 crystal, corresponding to a volume of 1.51 m^3 (12.5 t), being both of them identical.

The light emitted by endcap crystals will be detected using vacuum phototriodes (VPT), as the Avalanche Photodiodes used for barrel crystals, can not be used for the endcaps, since they are insufficiently radiation-hard. The VPT's have a sensitive area of 180 mm^2, operating at gains approaching 10 in a 4 T field and with a quantum efficiency of $\approx$ 15%.

Preshower

The endcap preshower covers a pseudorapidity range from $|\eta|$ =1.65 to 2.61 and is a part of the ECAL that will be present from the start of the experiment. Its main function is to provide $\pi^0 - \gamma$ separation. In the barrel part, an optional preshower covers the pseudorapidity range up to $|\eta|$ =0.9 to enable measurement of photon angle to an accuracy of about 45 mrad/$\sqrt{E}$ in the η direction. This detector will be built and installed only if the activity of the minimum-bias events seen at LHC start-up shows that additional angular determination is necessary, although by summer 2001 it seems to be completely rejected.

The preshower detector is located in front of the crystals and contains layers of lead converters (a single one in the barrel of 2.5 X_0, and two in the endcaps with 2 X_0 and 1 X_0 respectively) followed by detector planes of silicon strips. The impact position of a particle is determined by the centre of gravity of the energy deposited with a typical accuracy of 300 μm at 50 GeV. The

energy measured in the silicon detectors is used to apply corrections to the energy deposit in the crystals, as there is an energy loss in the lead converter. The fraction of energy deposited in the preshower decreases with increasing incident energy and is $\approx 5\%$ at 20 GeV. The endcap preshower silicon detector will be operated at a temperature of -5°C, in order to keep its performances at the maximum level during its full operation time.

2.4.4 The role of CMS ECAL Regional Centers

In this section, we will explain the role of the Regional Centres to which all the PWO barrel crystals will be delivered (CERN/Geneva and INFN-ENEA/Rome) by the producers. The two regional centres (RC) mentioned above have as their principal task the construction of the whole electromagnetic calorimeter. This means that the *Assembly* of the different units of the ECAL (up to a given level defined by spatial constraints) will take place on them. In addition, the Regional Centres are in charge of developing the *Quality Control* on the $\sim$ 80000 crystals that will constitute the CMS electromagnetic calorimeter (61200 crystals in the barrel and 8000 for each of the two endcaps). There is a third RC composed by British universities that will carry out the assembling activities regarding the ECAL Endcap crystals.

In a general way, we can say that the activities developed in these centres include all the studies, measurements and manipulations performed on the crystals since they are delivered to them by the producers (see the mention to producers in section 3.2), until the assembly of the crystals to originate the modules (units that comprise 400 or 500 crystals depending on the type, as depicted in figure 2.15).

It is important to mention that the object-oriented database C.R.I.S.T.A.L. [28] is used for almost all the activities performed at the two RC. First of all, it records all the data produced by the measuring devices or the operators (like observations, or comments), allowing easy and fast analysis of data. Second, it provides continuous assistance to the operator during the assembly of the different parts. In order to provide such assistance, all the manipulations that constitute the assembly have been arranged into flow-charts or work-flows (sequences of smaller activities that must be successfully finished to complete the whole manipulation). In this manner, C.R.I.S.T.A.L. always indicates the

operator which is the next operation to perform, and hence avoids possible human mistakes. In fact, C.R.I.S.T.A.L. usage is generalized nowadays not only in the two RC mentioned above, but also in other ECAL centres where important parts are analyzed or assembled. As an example, the photo-detectors that will be glued to barrel crystals, the Avalanche Photo-diodes, are verified and assembled using a C.R.I.S.T.A.L.-controlled work-flow).

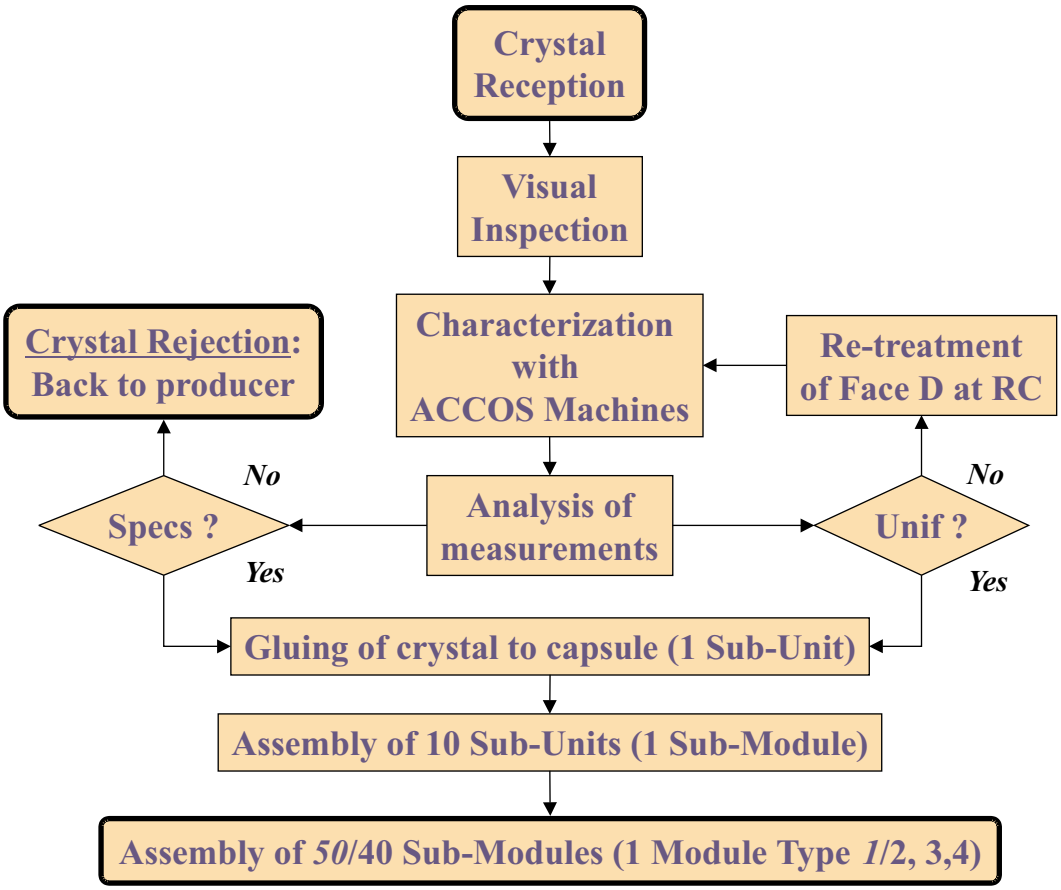

Figure 2.16: *Schema of all the activities developed at CERN Regional Centre.*

Figure 2.16 shows a detailed schema of all the activities developed in CERN RC. According to that schema we can list these activities as follows:

- *Crystal reception*: This is the first step performed with the PWO crystals at the RC. It comprises the careful unpacking of the crystals (what already allows determining if there are some damaged units due to transportation problems) and the engraving of the CERN crystal serial number on face N (big end side). Besides, the serial number corresponding

bar code is stuck on face F (see figure 3.19). Finally, the registration of the crystal into the C.R.I.S.T.A.L. database is also performed.

- *Visual inspection*: The crystal aspects studied in this step have been already explained in previous chapter. It allows a fast rejection of those crystals showing evident eye-detectable problems. All the operator observations and comments regarding this activity are recorded in the C.R.I.S.T.A.L. database.

- *Crystal characterization with ACCOS machines*: This activity can be performed with any of the existing Automatic Crystal Control System (ACCOS) machines. Nowadays, there are two versions of ACCOS machines: CERN RC and BTCP[b] are equipped with machines built at CERN as an extrapolation of the LAPP[c] prototype [26]. However, INFN-ENEA RC (Rome) and soon the SIC[d] plant are equipped with the so called ACCOR version [27] which is designed and built in Rome. At CERN RC, there are two operational ACCOS machines that will be described in detail later in this chapter. These machines are designed to measure the following crystal parameters: dimensions, longitudinal and transversal transmission, decay time, light yield and non-uniformity curve. The out-coming set of data is directly recorded into C.R.I.S.T.A.L.

- *Analysis of measurements*: When analyzing the measurements performed with ACCOS machines we must pay special attention to light yield ones. As will be discussed later, these measurements are only relative, and therefore we need to normalize them with the so-called Calibration Factors (CFs) in order to get the light yield in photoelectrons per MeV (this procedure will be explained in detail in chapter 4). After the verification of the CFs, we must check if the crystal fulfills the specifications, which are explained in section 3.6. If the crystal respects the tolerances established for dimensions, longitudinal and transversal transmission, decay time and light yield, then it is accepted. Otherwise, the crystal is sent back to producer according to the existing contractual compromises. The non-uniformity curve must be treated differently as it is not a specification on itself.

- *Uniformization of light collection*: If the treatment applied by the producers following our indications does not provide non-uniformity curves that meet our requirements (see "Light collection uniformity" chapter),

[b] Bogoroditsk Techno-Chemical Plant, Bogoroditsk, RUSSIA.
[c] Laboratoire d'Annecy-le-Vieux de Physique de Particules, Annecy, FRANCE.
[d] Shanghai Institute of Ceramics, Shanghai, CHINA.

then the crystals must be re-treated at the CERN RC. Once these crystals are re-treated, they are characterized again, and the new measurements performed are analyzed. These three activities constitute an iterative process that is repeated until a uniform light collection along the crystals is achieved. Then, the crystals can be accepted.

- *Gluing of crystals to the Avalanche Photodiodes*: After making sure that the crystals fulfill all the specifications and show uniformity curves that meet our stipulations, then the quality control can be considered as finished and therefore the assembly can start. The first step of the assembly is to glue the crystals to the Avalanche Photodiodes (APDs) to which they have been paired. Two APDs enclosed in a plastic frame called "capsule" are glued per crystal. This activity is much more complex than it may seem and requires special materials (glue, dosers) and techniques that will be explained in chapter "Extracting light from crystals". Once the gluing of the crystal and the capsule with the two APDs is performed, they become a "sub-unit".

- *Assembly of the produced sub-units*[e]: The sub-units are then inserted into the alveolar structure that will hold them inside the final detector. These structures can hold up to ten sub-units. Once the ten sub-units are safely enclosed inside this alveolar structure, we can talk about a new ECAL unit called "sub-module". Several submodules are assembled to create another unit called "module". There are four existing module types: Type 1 comprises 50 submodules, and Types 2, 3, and 4 comprise 40 submodules. The assembly of the modules to constitute the so called "super-modules" does not take place into the Regional Centres but at CERN Lab 27.

It must be mentioned that the Quality Control comprises the activities Visual Inspection, Characterization, Analysis of measurements and Uniformization, whereas the Assembly comprises the Gluing, and the Assembly of Submodules and Modules.

As has been shown, the role of the Regional Centres is of extreme importance: the final performances of the CMS ECAL will be optimized if the Quality Control of the PWO crystals and the Assembly of each part is carefully and precisely executed.

[e]Follow figure 2.15 for a better understanding of the sequence.

The first significant units of ECAL

During the last few years, several crystal matrices have been constructed with the main objective of analyzing the performances of our detector and also, in order to find the eventual problems arising during construction. These matrices, typically composed of few tenths of crystals, are usually called *Proto's*.

Some other crystal matrices have been also built in the last years. However, these ones are usually composed of much more crystals (several hundreds) and besides they correspond to real units of the electromagnetic calorimeter, since they are Modules or Supermodules (see figure 2.15). In addition, the aim of these matrices is mostly related to the discovery of potential problems during its complex construction, as most of them are not planned to be irradiated in a test-beam.

These groups of crystals can be considered as the first units of the ECAL although not all of them will be part of the final detector. They will be extensively mentioned in the following chapters, hence it is important to define them now:

- **Proto's** (e.g. Proto 97, Proto 99, Proto 2000): This term is used for the matrices of crystals (typically of 30 crystals) used for test beams in the different CERN facilities. They have been constructed at CERN Regional Centre every year since 1994 to test a wide variety of aspects like monitoring systems, electronics, glue response and differences in behavior of BTCP[f] and SIC[g] crystals (the two existing $PbWO_4$ producers) among others. They allow also to perform sum of nine crystals energy reconstructions in order to verify precisely the energy resolution achieved. These units will not be part of the final ECAL.

- **Mod #0** : This term stands for the first Module of the ECAL that was built at CERN RC. It is a type 2 module, therefore contains crystals type 6, 7, 8 and 9. It contains 40 submodules, and therefore 400 crystals. It was built between May and August 1999. This unit will not be part of the final ECAL.

[f]Bogoroditsk Techno-Chemical Plant, Bogoroditsk, RUSSIA.
[g]Shanghai Institute of Ceramics, Shanghai, CHINA.

- **Mod #0'** : This term refers to the new module that was built at CERN RC between Mars and June 2001, which is also a type 2 module. It uses as readout system new APDs closer to final ones and new alveolar structures. It is not going to be part of the final detector even if its components are in almost all cases the final ones. Thus, it can be used for the monitoring in time of the different parts, as if it were a unit of the final detector but being outside it.

- **SM #1** : It refers to the first supermodule of the CMS ECAL ever built. It will be part of the final detector and is planned to be constructed during 2002. As explained in figure 2.15 and table 2.3, it will comprise 1700 crystals, meaning 1/36 of the total CMS ECAL.

Chapter 3

THE PWO CRYSTALS

3.1 Generalities

3.1.1 Crystal Choice

In the previous chapter we have justified the choice of an homogeneous calorimeter for the ECAL of CMS in terms of the stringent energy resolution needed. Besides, it has been already mentioned (see subsection 2.4.3) that such an homogeneous calorimeter was chosen to be built of scintillating crystals. The proposal for building the calorimeter using this technique [10] instead of using the other possible choice, which at the time was a scintillating noble liquid (Xe, Ar) calorimeter, was based on the following arguments: several large scale crystals calorimeters had been built in the past (Crystal Ball with NaI(Tl), Cleo II and Crystal Barrel with CsI(Tl), L3 with BGO) and a lot of experience existed about important aspects like mechanical structures, light collection, monitoring and calibration of such detectors. Apart from that, crystal calorimeters have an excellent energy resolution with a small constant term and allow compactness of the whole detector, homogeneity and good hermeticity.

Since 1990, the Crystal Clear collaboration had been developing an exhaustive research of fast and radiation hard inorganic scintillators to be used for high resolution electromagnetic calorimetry[a]. In 1994 and after a deep study, the Crystal Clear collaboration [11] was considering three possible candidates for the construction of a crystal electromagnetic calorimeter for the CMS experiment of LHC. They were: cerium fluoride (CeF_3), lead tungstate ($PbWO_4$) and the heavy fluoride glasses (HFG:Ce). Several properties of these three scintillators plus some others typically considered as references in calorimetry are listed in table 3.1.

Table 3.1: *Properties of different scintillator crystals used in High Energy Physics*

Property	NaI(Tl)	BGO	$PbWO_4$	CeF_3	HFG:Ce
Density (g/cm^3)	3.67	7.13	8.28	6.16	6.0
Radiation Length (cm)	2.59	1.12	0.89	1.68	1.60
Moliere Radius (cm)	4.50	2.33	2.19	2.63	2.80
Decay Time (ns)	250	60 300	5 15 100	8 25	27
Emission Peak (nm)	410	480	440	300 340	329
Relative light output	100	15	1	10	0.4

Reviewing table 3.1 we notice that in spite of showing a high light output, the first two scintillators (NaI(Tl) and BGO) are too slow for the LHC requirements (the response of crystals and electronics must be within 25 and 100 ns; see subsection 2.4.2). The other three, much faster, although with a smaller light output, were the three candidates mentioned above. We are going to comment now their main advantages and drawbacks [12]:

- The first of them, the cerium fluoride (**CeF_3**) was probably the best candidate in terms of combining two of the most important requirements: a fast response and a relatively high light output. Its main drawbacks were the density, too small to allow the whole CMS calorimetry to be located inside the coil, the high cost of its production and the absence of large-scale production plants.

[a] At the present, the collaboration continues the research for new scintillating materials and besides, investigates some other application fields for such scintillators like medical imaging.

- The last scintillator appearing in the table above, the heavy fluoride glass (**HFG:Ce**) was much easier to produce and also cheaper. However, it also showed important drawbacks: its low scintillation efficiency, the fact of not being resistant enough to LHC radiation levels and its high radiation length.

- The other candidate, lead tungstate ($\mathbf{PbWO_4}$), had an important advantage which was the high density, allowing a really compact calorimeter located inside the CMS coil. Besides, the production cost per unit was much smaller than in the case of CeF_3 and even more: the production facilities to grow full size (≈23 cm) crystals were already available.

The important economic arguments playing against cerium fluoride could not be neglected and therefore, the chosen crystal in September 1994, after four years of research, was the lead tungstate ($PbWO_4$). Its main problem was the low light yield, which could be solved thanks to the technological progress made on the Avalanche Photodiodes (APD). These devices have an internal gain (in opposition to classical photodiodes) allowing weak light outputs to be used. Another important drawback of $PbWO_4$ was the strong scintillation dependence on the temperature (-2%/°C). In order to overcome that problem, a temperature stabilization system is required.

3.1.2 Lead Tungstate properties

The Lead Tungstate ($PbWO_4$ also called PWO) is a birefringent scheelite-type crystal belonging to the space group I4 1/a with a tetragonal unit cell. The dimensions of this unitary cell are: a=b=0.5465 nm and c=1.2020 nm. The interatomic distances for PWO crystals are the following:

$$\begin{aligned} W &- 4\ O : 0.1795\ nm \\ Pb &- 4\ O : 0.2580\ nm \\ &- 4\ O : 0.2637\ nm \end{aligned}$$

and the structural parameters of $PbWO_4$ are expressed in table 3.2.

The most important properties of $PbWO_4$ crystals have been already mentioned in table 3.1. However, there are other important aspects that need to be stressed. Table 3.3 lists in a more exhaustive way $PbWO_4$ properties.

Table 3.2: *Lead Tungstate structural parameters*

Atom	*Site*	*x*	*y*	*z*	*Occupation*
W	4a	0	1/4	1/8	1
Pb	4b	0	1/4	5/8	1
O	16f	0.2388	0.1141	0.0429	1

Table 3.3: *Lead Tungstate properties*

Parameter	*Unit*	*Value*
Density	[g/cm^3]	8.28
Radiation length	[cm]	0.89
Interaction length	[cm]	22.4
Moliere Radius	[cm]	2.19
Light decay time	[ns]	5 (39 %)
		15 (60 %)
		100 (1 %)
Refractive Index at emission peak		2.30
Maximum of emission	[nm]	420-440
Temperature coefficient	[%/°C]	-2
Light Yield	[pe/MeV]	≈ 10
	[ph]	≈ 100
Higroscopicity		no
Chemical Activity		inert
Melting point	[°C]	1123
Hardness	[Moh]	4

It is important to mention that the decay time has three values (5, 15 and 100 ns) in table 3.3 because the emission time is accepted to be well described by function which is a sum of three exponentials, each one having its own time constant (e.g. 5) and its own amplitude (e.g. 39%).

3.2 Growing methods and Producers

The $PbWO_4$ crystals are grown from a mixture of lead oxide (PbO) and tungsten oxide (WO_3) in proportions 50%-50%, which melt congruently at 1123°C without phase transition during the cooling (see figure 3.1).

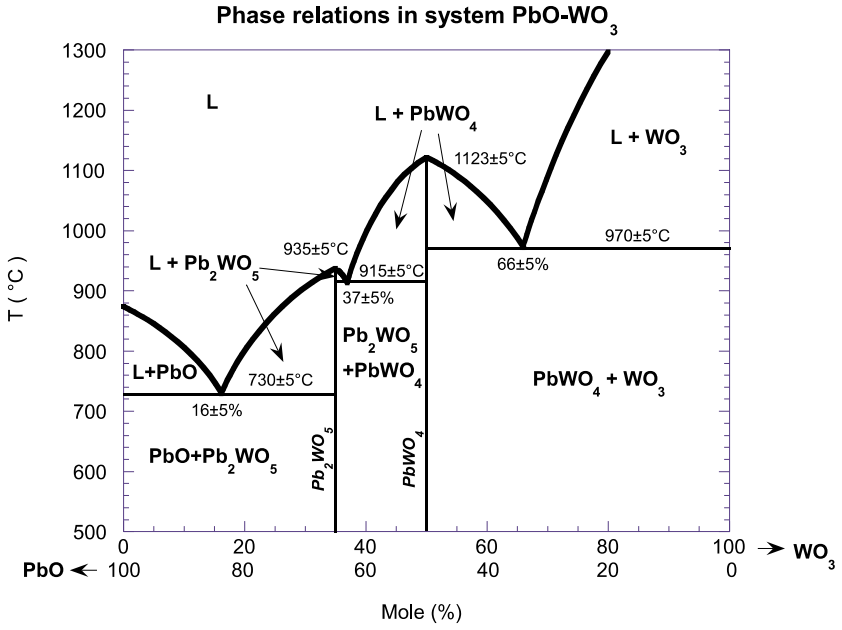

Figure 3.1: *Phase diagram of PbO-WO_3 crystals.*

Lead tungstate crystals for CMS are produced by three manufacturers at present. They are: Bogoroditsk Techno-Chemical Plant (BTCP) in Tula (Russia), the Shanghai Institute of Ceramics (SIC) in China and the Beijing Glass Research Institute (BGRI), also in China. A great effort has been performed by the producers together with CMS to optimize mass production procedures of full size, high quality $PbWO_4$ crystals. Some of these optimizations were the complete understanding of the scintillation mechanisms, the understanding of the radiation damage mechanisms and the definition of the techniques suitable to produce radiation-hard crystals, among others. There are two methods to grow lead tungstate crystals. The standard method is called the Czochralski one and is the one used in the BTCP. The other method, called the modified Bridgman-Stockbarger is the one used in China in both SIC and BGRI plants. It is important to mention that even showing some small but systematical differences, crystals of the required quality have been grown using both methods [9].

3.2.1 Czochralski growing method

This technique originates from the pioneering work by the polish scientist Jan Czochralski in 1917, who pulled single crystals of metals (that is the reason

why this method is also called *crystal pulling*). The Czochralski method is a particular method of crystals growth, used not only to grow lead tungstate but many other crystals. In this method, one has to attach a seed crystal to the bottom of a vertical arm such that the seed is barely in contact with the material at the surface of the melt contained in a crucible. The arm is raised slowly, and a crystal grows underneath at the interface between the crystals and the melt (see figure 3.2). Usually the crystal is rotated slowly, so that inhomogeneities in the liquid are not replicated in the crystal.

In the case of $PbWO_4$ crystals, the method is very similar although it presents some particularities: the raw materials are WO_3 and PbO and they are mixed in a platinum crucible in stoechiometric ratio. Then temperature is raised up to 1150-1160°C to produce the melt. Afterwards, a crystal seed is used as explained above to grow a larger diameter $PbWO_4$ crystal. In lead tungstate crystals it is commonly used the addition of special dopants that improve the optical quality of the crystals or its radiation hardness. These dopants (e.g. Nb, La) are added before the beginning of the growth and its homogeneous distribution along the growth crystals is ensured by the rotation performed when pulling the crystal. Once the crystals are growth, they are usually annealed with a low speed temperature variation to eliminate intrinsic stresses produced during the growth.

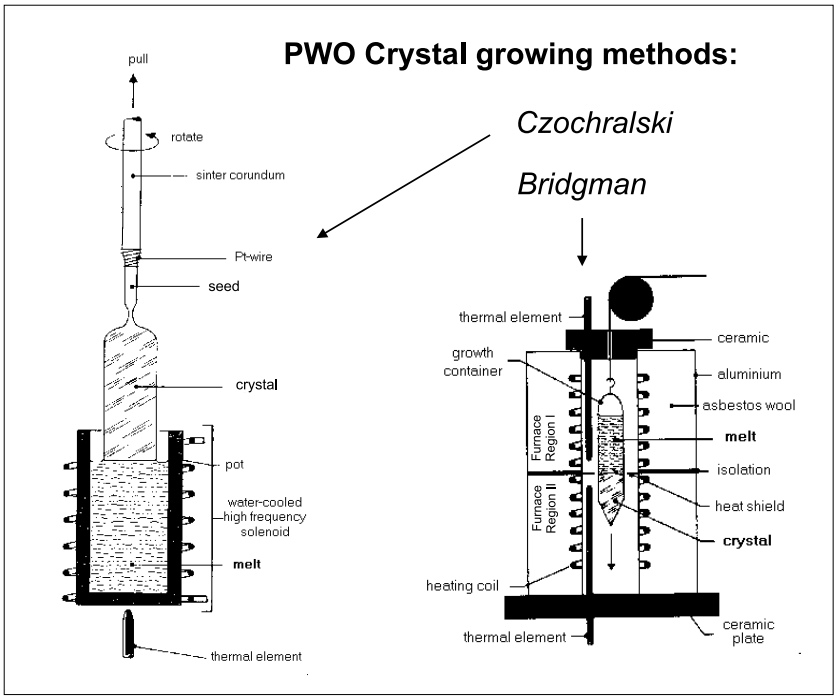

Figure 3.2: *Sketch of Czochralski and Bridgman crystal growing methods.*

3.2.2 Modified Bridgman-Stockbarger growing method

The Bridgman-Stockbarger method is also widely used for growing large crystals. This method, which was used to grow the BGO crystals used in the L3 experiment at CERN, has been successfully adapted to the growing of lead tungstate. In this case, the molten raw materials (as in previous method, WO_3 and PbO) are placed into a platinum crucible which has a cylindrical shape with a conical lower end. The materials are kept melted at 1123°C by a heating coil. At that moment, dopants can be added to the melt if needed. The crystallization is achieved due to the presence of a temperature gradient in between the two zones in which the furnace is divided (see figure 3.2): the higher part of the furnace is kept at a temperature over 1123°C and the lower part is kept at a temperature under 1123°C. In consequence, as the crucible is slowly lowered into the cooler region, a crystal starts growing in the conical tip. The lowering of the crucible to complete the crystallization of the entire melt takes several weeks (in the case of a full size ECAL crystal). The melt-solid interface is normal to the growth axis, so to assure radial uniformity there must be a control on the convective flow by careful thermal design. As in the Czochralski method, the intrinsic stresses produced in the crystals during the growing must be removed by thermal annealing.

This method is more economic than the Czochralski technique because nearly all the raw material is useful, as the crucibles are made at almost the final crystal dimensions (a slightly bigger size is always needed to allow later cutting to final dimensions). However, the production time is much longer as the lowering rate mentioned above is just some mm/h.

A view of an ingot[b] and several final shape $PbWO_4$ crystals produced with each one of both methods is shown in figure 3.3.

[b]The ingots are placed in the centre of the image. The one with larger transversal section corresponds to Czochralski method, whereas the other ingot corresponds to Bridgman-Stockbarger.

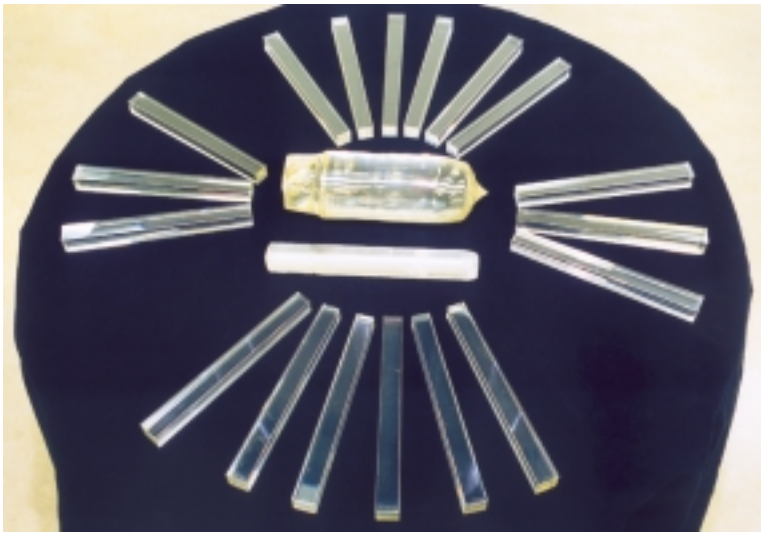

Figure 3.3: *Full size ingots and final shape $PbWO_4$ crystals produced with both methods.*

3.3 Scintillation Properties

A scintillating crystal can be described as a material that exhibits a property known as *luminescence* [13]. These luminescent materials, when exposed to certain forms of energy, for example, light, heat, radiation, etc., absorb and reemit the energy in the form of visible light. If the reemission occurs immediately after absorption or, more precisely within 10^{-8}s (being this time, roughly, the time taken for atomic transitions), the process is usually called *fluorescence*. However, if the reemission is delayed because the excited state is metastable, the process is called *phosphorescence* or *afterglow*. In such cases, the delay time between absorption and reemission may last from few microseconds to hours depending on the material.

We can distinguish between two types of luminescence according to the type of excitation: we use the term *photoluminescence* when the excitation is produced by light radiation (generally visible or UV light) and we use the term *radioluminescence* (or scintillation) when the excitation is produced by ionizing radiation (e.g. α, β, γ, X-ray).

It is clear that as we deal with crystals that will be part of a high-energy physics experiment, we are mainly interested in knowing how radiolumines-

cence works for lead tungstate. However, the mechanisms implied in radioluminescence are quite complex. On the other hand, photoluminescence is usually much easier to explain. In consequence, we will first describe the commonly accepted photoluminescence model and then we will use it to explain radioluminescence.

3.3.1 Scintillation Mechanism

The characteristic emission of light produced in luminescent materials is the result of radiative transitions between electronic levels. These energy levels responsible of the emission spectrum are the so called luminescent centres. These centres can be classified as intrinsic luminescent centres (when the electronic levels are from the crystal itself) and extrinsic luminescent centres (when the levels correspond to impurities located within the crystal).

The band theory of crystalline solids introduced by Bloch (1928) is helpful to describe how luminescence works [14]. In this model, the electronic energy states of an isolated atom or molecule consist of a series of discrete levels defined by Schrodinger's equation. In an inorganic crystal lattice the outer levels are perturbed by the mutual interactions between atoms or ions, in such a way that levels are broadened into *allowed* energy bands located between *forbidden* energy regions. In the normal state, the lower bands are completely filled whereas the higher bands are empty. The higher filled band is usually called the *valence band* and is separated from the lowest empty one, called *conduction band*, by an energy gap E_g of typically a few eV's (see figure 3.4a).

Such a simple model can be applied only to insulators having a perfect crystal lattice. In common life, lattice defects and impurities occur in the energy bands, producing local electronic levels in the normally forbidden region between the conduction and valence bands. When those levels are not occupied, electrons moving freely in the conduction band in their vicinity can enter those centres. They can be of three types:

- Luminescence centres, in which the transition to the ground state is accompanied by photon emission.

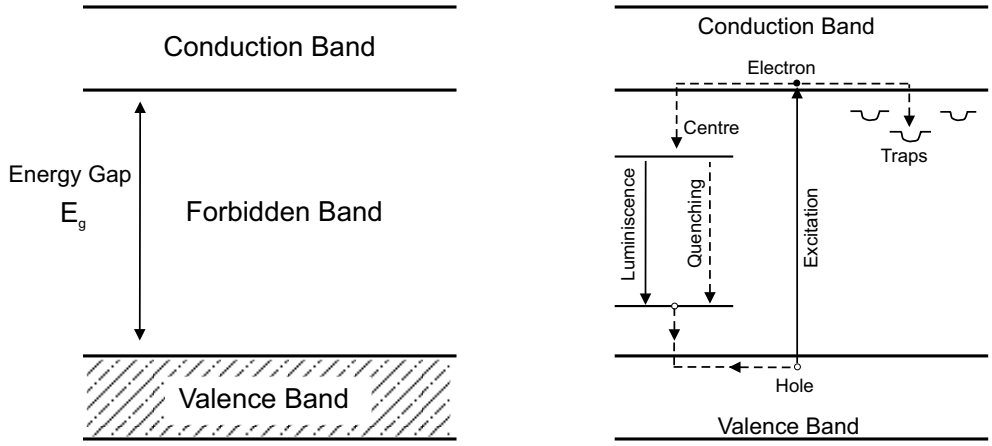

Figure 3.4: *a) Energy bands in ideal insulating crystal. b) Energy bands in impurity-activated crystal, with excitation, luminescence, quenching and trapping processes.*

- Quenching centres, in which radiationless thermal dissipation of the excitation energy can occur.

- Traps, which have metastable levels from which electrons may subsequently return to the conduction band by acquiring thermal energy from the lattice vibrations, or fall in the valence band by non-radiative transition.

The same centre may contain luminescence, quenching and/or trapping levels, each one with a relative population given by the Boltzmann statistical distribution. The luminescence and quenching centres arise from impurities, interstitial ions and/or defects, and they introduce local discrete energy levels corresponding to the ground and excited states of the centre. On the other hand, the traps arise from other lattice disturbances and provide additional levels for electrons below the conduction band (see figure 3.4b).

Conditions for the luminescence of a centre

The conditions for the luminescence and quenching of a centre can be discussed in terms of a theoretical model that is applicable to all luminescent materials. In this model, the potential energies of the ground and excited elec-

tronic states of the luminescence centre are plotted against a configurational coordinate (x) of the centre (see figure 3.5).

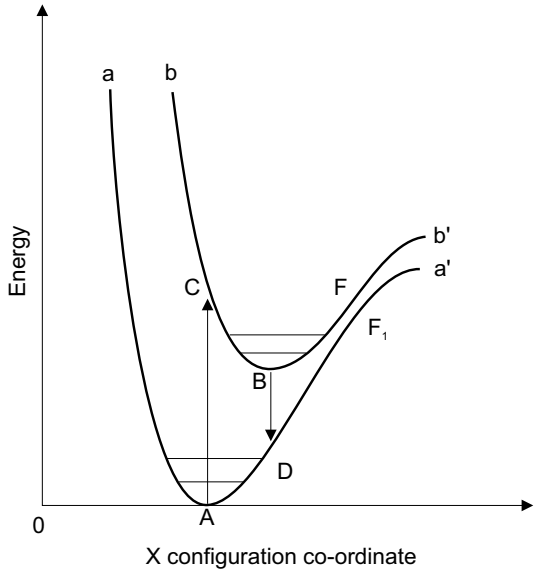

Figure 3.5: *Potential energy diagram of a luminescence centre.*

In figure 3.5 the curves aAa' and bBb' represent the vibrational amplitudes of the centre in the ground and excited electronic states respectively. Minima A and B correspond to the stable energy positions of both states. When the luminescence centre is excited by visible or UV light (i.e. *photoluminescence*) and if it has energy enough it occurs a transition between the ground state and the excited state. This transition is represented in figure 3.5 by the vertical line AC, since the transitions involved in absorption and emission occur in a time that is much shorter than the corresponding to atomic or ions movements. In this excited state the crystal is not in its minimum potential energy state, therefore, it moves from C to B. The excess of vibrational energy is dissipated thermally to its neighbors. The time spent in B depends on the probability of optical transition to D, which provides the luminescence emission. Such a transition (BD) is also vertical like the absorption performed in AC. After transition BD, the centre is again in its ground state but has to go from D to A to reach its minimum potential energy, with further thermal dissipation of excess vibrational energy (transferred in the form of phonons to the lattice). It is important to mention that emission (BD) spectrum is at lower energies (longer wavelengths) than the absorption (AC) spectrum (Stokes law), and in fact that difference is expressed by a parameter called *Stokes shift* that is given by $\lambda_{em} - \lambda_{ex}$ (where λ_{em} stands for the emission wavelength and λ_{ex} stands for the absorption wavelength).

The potential energy curves of the ground and excited states usually intersect or approach each other closely at some point F (see figure 3.5). A luminescence centre in its excited state reaching the point F can make a non-radiative transition to the corresponding point F_1 of the ground state and hence, dissipate the excess energy thermally. This process is more likely the higher the temperature is, as in this case the vibrational states closer to F can be occupied. Clearly, this implies that the probability of having a non-radiative deexcitation to the ground state increases with temperature. This phenomenon is known as internal thermal quenching, process which competes with the emission process.

Luminescence decay time

The luminescence decay time can be defined as the time interval that mediates between the crystal excitation and the detection of the emitted light. It is, of course, deeply related to the life time of the excited state. As explained above, the deexcitation from the excited to the ground state can happen in two ways: through a radiative or through a non-radiative transition (thermal quenching). In consequence, the total probability for the transition between excited and ground state is given by the sum of the two relative probabilities P_r (radiative transition) and P_{nr} (non-radiative transition). The luminescence decay time τ can be expressed in terms of both probabilities as follows:

$$\tau \propto \frac{1}{P_r + P_{nr}} \tag{3.1}$$

where, as usual, we take in account that the life time of an excited state is inversely proportional to the deexitation probability.

In a similar way, we can define the luminescence efficiency (η) as the ratio between the probability of making a radiative transition and the total (radiative + non-radiative) deexitation probability:

$$\eta \propto \frac{P_r}{P_r + P_{nr}} \tag{3.2}$$

Taking in account equations 3.1 and 3.2 we can see that luminescence decay time competes with the luminescence efficiency: as the non-radiative probability (P_{nr}) increases, the luminescence decay time (τ) decreases, whereas at the same time the luminescence efficiency (η) worsens providing therefore a weaker emission.

Radioluminescence

It has been already mentioned that radioluminescence differs from photoluminescence in the excitation mode. The former occurs due to high energy radiation whereas the second is due to visible or UV light. In the case of photoluminescence (explained in subsubsection 3.3.1) the excitation can be considered as direct, as it is directly the visible or UV light what is exciting the luminescent centre. On the other hand, the case of radioluminescence is slightly different: the excitation is produced by high energy particles that are absorbed, with the subsequent creation of secondary electron-hole pairs. These pairs have enough energy to migrate through the lattice and to relax transferring all or part of their energy to a luminescent centre where the de-excitation can happen with the subsequent light emission. We can therefore consider radioluminescence as a process comprising three stages: 1) creation of electron-hole pairs following the absorption of the incident energy, 2) migration of these pairs towards the luminescent center and transfer of energy to them and 3) radiative deexcitation of the luminescent center with emission.

The efficiency of a scintillator can be described by a widely used expression:

$$\eta = \beta S Q \tag{3.3}$$

where the parameters β, S and Q refer to the efficiencies of the three processes that characterize radioluminescence which were mentioned in paragraph above: the former, β, refers to the efficiency in the conversion of a high energy photon into electron-hole pairs; the second, S, refers to the efficiency in the transport of thermalised electron-hole pairs (or excitons) towards the emission centres; the last, Q, refers to the efficiency of radiative de-excitation of the emission centre itself. Clearly, a good scintillator will be characterized by having the three parameters the closer possible to 1.

The parameters used in expression 3.3 can be used to estimate the number of photons that a given scintillator can emit per MeV of incident energy (or light yield) in the ideal case (all efficiencies are maximum, i.e. $\beta = S = Q = 1$):

$$LY = \frac{n_{ph}}{E_\gamma} \tag{3.4}$$

where E_γ corresponds to the energy of the incident γ-particle and n_{ph} stands for the number of photons produced. This last quantity (n_{ph}) can be expressed

in terms of efficiency parameters S and Q as follows:

$$n_{ph} = n_{e-h} SQ \tag{3.5}$$

where n_{e-h} stands for the number of electron-hole pairs produced by the incident particle.

We will now try to express n_{e-h} as function of β. Firstable, we need to know that the energy needed to create an electron-hole pair (E_{e-h}) is given by $E_{e-h} = BE_g$ [16], being E_g the band gap energy of the given scintillator and B a parameter that typically is equal to 3 for semiconductors. In consequence, we can set the theoretical number of electron-hole pairs produced to be n^T_{e-h}=E_γ / BE_g. As mentioned above, parameter β gives us the electron-hole pair creation efficiency, so it must be equal to the ratio n_{e-h}/n^T_{e-h}. Therefore, in the ideal case we can say:

$$\beta = \frac{n_{e-h}}{n^T_{e-h}} = 1 \qquad \rightarrow \qquad n_{e-h} = \frac{E_\gamma}{BE_g} \tag{3.6}$$

Taking in account this last result and equation 3.5 we can re-write equation 3.4 like this:

$$LY = \frac{SQ}{BE_g} \tag{3.7}$$

By equalizing S and Q to 1 (ideal case) we get the theoretical light yield:

$$LY_{max} = \frac{1}{BE_g} \tag{3.8}$$

In our case, lead tungstate presents an energy gap E_g=4.5 eV [15] and B is known to be ≈ 7 for tungstates like $CaWO_4$ [16]. We can therefore estimate the maximum (all involved efficiencies were maximized) light yield of $PbWO_4$ by substituting these two values in equation 3.8. The light yield calculated in this manner is $LY_{max} \approx 32000$ ph/MeV.

This rough estimation is more than 300 times bigger than the real light yield measured experimentally. This happens because of the strong thermal quenching characteristic from $PbWO_4$ (light yield is reduced in 2 % per degree increased, as shown in Table 3.3). This process implies a non-radiative deexcitation towards the ground state as explained in subsection 3.3.1. Of course, the presence of non-radiative deexcitations reduces the efficiency of the luminescent centre (parameter Q), being therefore $Q \ll 1$ for $PbWO_4$. Our overestimation of Q when calculating the light yield above is the main

responsible for the big difference between the maximum light yield allowable according to internal PWO characteristics ($\approx$ 32000 ph/MeV) and the real light yield measured for lead tungstate experimentally ($\approx$ 100 ph/MeV). This calculation is however very interesting as it reveals which is the potential light production yield of a scintillating material and it is commonly made when considering new scintillating materials. In fact, for many other scintillators, like CeF_3, the calculation differs from reality only in a factor 10 [12] what means much better efficiencies and therefore a less important thermal quenching.

3.3.2 Lead Tungstate luminescent centres

A good understanding of $PbWO_4$ spectroscopical properties was already accomplished thanks to the investigations performed from the seventies onwards. However, due to the choice of lead tungstate for CMS a deeper research has been made during the last five years with lead tungstate samples that lead to a better understanding of its luminescence centers [17] [18]. Following these studies, we can state that PWO shows three luminescence bands:

- Blue band: Corresponding to a wavelength $\lambda \sim 420$ nm. This band is present in all tungstates, strongly suggesting that is due to the emission of regular WO_4^{2-} centres.
- Green band: Corresponding to a wavelength $\lambda \sim 490$ nm. This band is caused by the irregular WO_3 anionic molecular complexes appearing when anion vacancies are present in WO_4^{2-} centres.
- Red band: Corresponding to a wavelength $\lambda \sim 650$ nm. This band is also due to irregular WO_3 centres, which are in this case deformed by the presence of Frenkel defects.

When PWO is excited by ionizing radiations, the three processes explained previously take place: 1) creation of electron-hole pairs, 2) migration of the pairs and transfer of energy to the luminescent centres and 3) emissive deexcitation of the centres. In the lead tungstate, there are three types of luminescent centres, being each one responsible for each of the three bands mentioned immediately above. The whole luminescence spectra produced is due to the overlap of these three bands. These three luminescent bands with maxima

420, 490 and 650 mentioned above are depicted in figure 3.6 together with the excitation spectra of these bands.

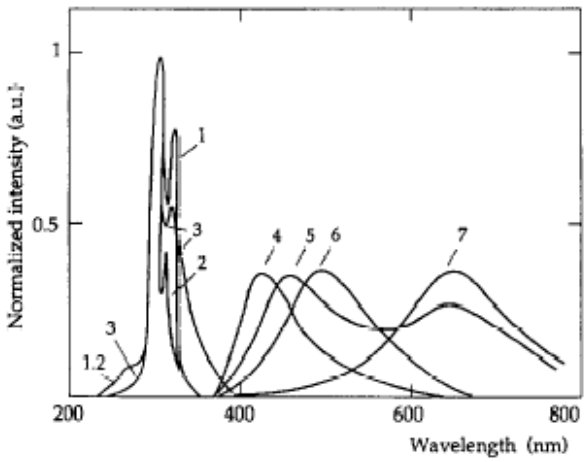

Figure 3.6: *PWO excitation and luminescence spectra at T=300 K. Excitation: (1) λ_{lum}=420, (2) 500, (3) 650 nm. Luminescence: (4) λ_{exc}=275, (5) 325, (6) 308, (7) 350 nm.*

As mentioned above, the **blue luminescence** appears to be due to intrinsic anionic molecular complexes WO_4^{2-} (this is the luminescent centre responsible for the blue emission). In the frame of the molecular orbital approximation, and using the extended version of *Hückel* method [17], WO_4^{2-} complexes have the highest occupied molecular orbital $1t_1$ which is separated from the first excited 2e state, as sketched in figure 3.7a. The final configuration resulting from the decomposition of the direct product representation $1t_1 \otimes 2e$ is found to be $^3T_1$, $^3T_2$ and $^1T_1$, $^1T_2$ respectively, being the ground state $^1A_1$ as shown in figure 3.7b. The excitation transitions $^1A_1 \rightarrow {}^1T_1$, $^1T_2$ and $^1A_1 \rightarrow {}^3T_1$, $^3T_2$ are causing at room temperature the radiative transitions from triplet levels $^3T_1$,$^3T_2 \rightarrow {}^1A_1$. The two former transitions (see in figure 3.8 their corresponding wavelengths: 325 and 275 nm) are clearly detected in the excitation spectra (see figure 3.6) whereas the deexcitation transition (see in figure 3.8 its corresponding wavelength: 420 nm) is seen in the luminescence spectra depicted in figure 3.6 .

The **green luminescence** in lead tungstate is due to the presence of an anion vacancy in a WO_4^{2-} anionic complex. In this conditions, we deal with a new WO_3 complex characterized by a lower symmetry (C_3v). Due to this lower symmetry, the crystalline field splits the triplet levels in (A + E) components, shifting the excited energy terms. It provides an increase of the Stokes shift in these irregular centres and hence also a displacement of the maximum of the

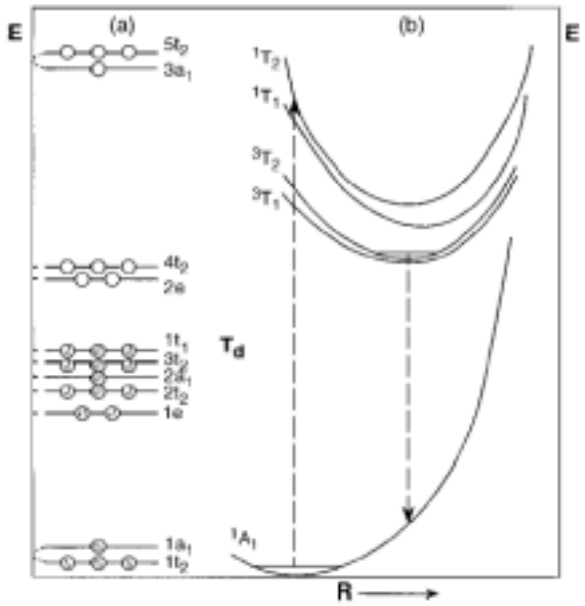

Figure 3.7: *a) Molecular orbital energy scheme for free tetrahedral (WO_4^{2-}) complexes. b) Schematic configuration coordinate model for the lowest electron transition $t_1 \rightarrow 2e$.*

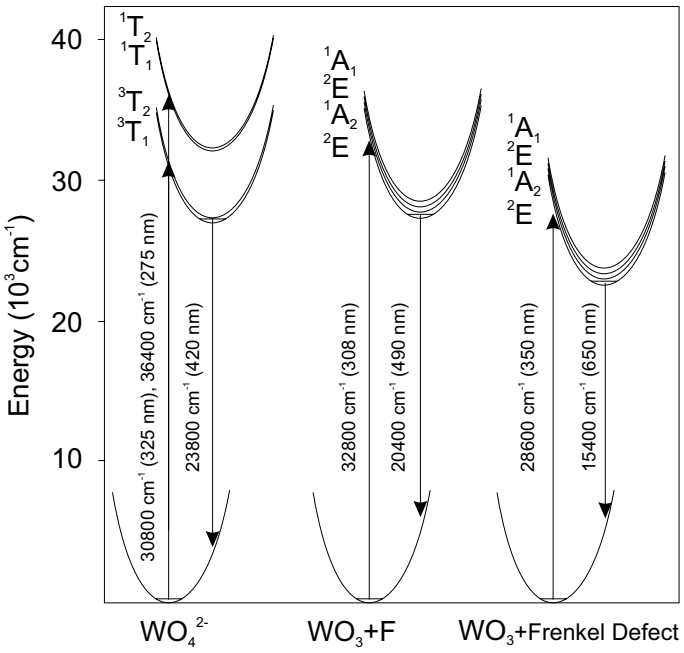

Figure 3.8: *Energy level diagram of the optical transitions in PWO crystals.*

luminescence band towards the green. The excitation transition between the ground state and the excited state (with corresponding wavelength 308 nm) can be seen in figure 3.8 with the subsequent radiative transition on the green (490 nm) for the irregular luminescent center WO_3+F.

The other luminescent center in PWO crystals is associated with the **red luminescence**. This luminescence is associated with a center that appears to be due to the incorporation of a Pb^{3+} center in PWO crystals. Such a trivalent lead ion is stabilized by a Frenkel defect in lead tungstate. This Frenkel defect is the responsible of lowering the local symmetry of such WO_3 complex towards a C_3 symmetry shifting and splitting the original excited energy levels. This distorted tungsten anionic complex, named WO_3+Frenkel defect in figure 3.8 is the luminescent centre responsible for the red luminescence. Again in figure 3.8 we can distinguish the excitation transition (350 nm) and the radiative transition giving raise to red emission (650 nm).

This complex scintillation mechanism gives raise to the emission of a light pulse which is peaking typically at $\sim$ 420 nm. Such a pulse is the result of the overlap of the three emission bands mentioned above. The classical emission spectrum of two differently doped $PbWO_4$ crystals is shown in figure 3.9.

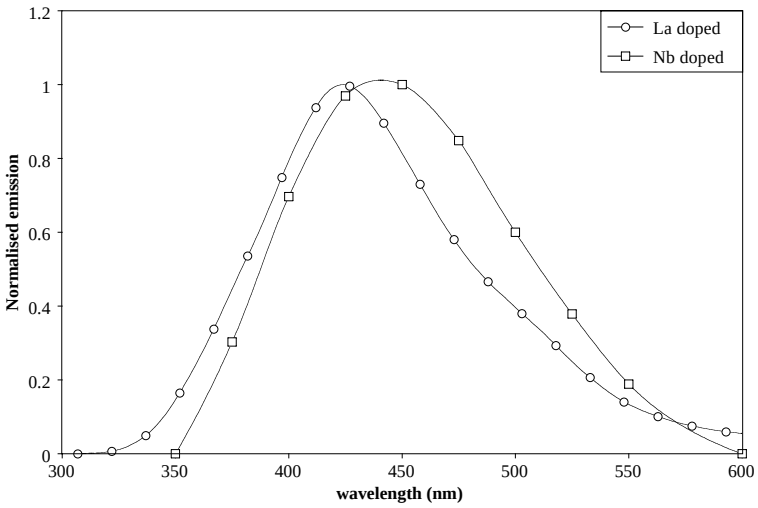

Figure 3.9: *Scintillation spectra of niobium and lanthanum doped PWO crystals.*

Recently delivered PWO crystals present an emission spectra which is mainly due to blue luminescent centres, thus peaking at 420 nm or even lower wavelengths. This happens because in the last years a big effort has been made to suppress red and green centres, as their presence is strongly related to slow

components in the emission spectra. Besides, the radiation hardness of crystals with an important presence of these centres is not as good as expected.

3.3.3 Light Yield

The light yield of a scintillating crystal is defined as the light extracted from it per unit of deposited energy. In practice, the light yield is often measured using γ-sources. The reason for it is that one of the ways in which γ-rays interact with matter (photoelectric absorption) is ideal for energy measuring, as we shall see below.

It has been already mentioned (see figure 2.11 and subsection 2.4.1) that γ-rays have three main possible ways to interact with matter. They are photoelectric absorption, Compton scattering and pair production, being the latter the dominant process for high-energy γ-rays. The atomic number (Z) of the interaction medium has a strong influence on the relative probabilities of these three interactions. As an example, photoelectric absorption cross section varies approximately as $Z^{4.5}$.

Photoelectric Absorption

The photoelectric absorption is a process in which a photon undergoes an interaction with an atom in which the photon is absorbed giving raise to an outgoing photoelectron (see figure 3.10). The interaction takes place with the atom as a whole and cannot take place with free (unbound) electrons. The photoelectron produced comes from one of the electron shells of the absorber atom and it has a kinetic energy given by the difference between the incident photon energy ($h\nu_0$) and the binding energy of the electron in its original shell (E_b). The photoelectron emission creates a vacancy in the electron shell that is filled by electron rearrangement. In the case of high-energy photons interacting via photoelectric absorption, the binding energy (E_b) can be liberated in the form of an X-ray or an Auger electron.

In consequence, we can say that photoelectric absorption of high-energy

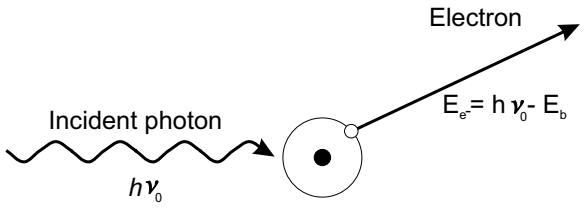

Figure 3.10: *Sketch of photoelectric absorption process.*

photons is characterized by the liberation of a photoelectron which carries most of incident γ-ray energy, together with one or more low-energy electrons and photons. If nothing escapes the detector, the sum of the kinetic energies of the created electrons and photons must be equal to the incident energy. This is the reason why photoelectric absorption is an ideal process if we are interested in measuring the energy of the original γ-ray.

The photoelectric process is a very important mode of interaction for γ-rays (or X-rays) of relatively low energy. The process is also enhanced for atomic materials of high atomic number Z. No single analytical expression is valid for the probability of photoelectric absorption per atom over all ranges of E_γ and Z, but a rough approximation can be given [19]:

$$\tau \quad \cong \quad constant \quad \times \quad \frac{Z^n}{E_\gamma{}^{3.5}} \tag{3.9}$$

where the exponent n varies between 4 and 5 over the γ-ray region of interest.

Compton Scattering

The interaction process of Compton scattering takes place between the incident γ-ray photon and an electron in the absorbing material. It is most often the predominant interaction mechanism for γ-ray energies typical of radioisotope sources.

In Compton scattering, the incident photon is deflected through an angle ϕ with respect to its original direction (see figure 3.11). The photon transfers a

portion of its energy to the atomic electron (which is assumed to be unbound and initially at rest) and then the so called Compton electron recoils at an angle θ. Because all angles of scattering are possible, the energy transferred to the electron can vary from zero to a large fraction of the incident γ-ray energy.

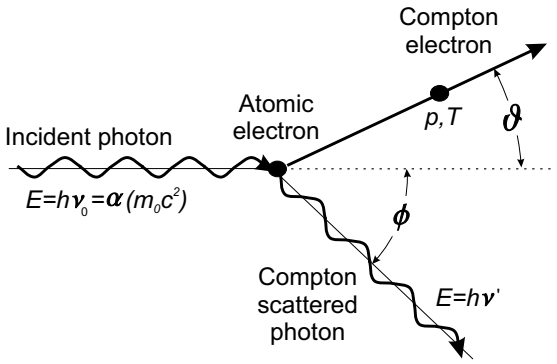

Figure 3.11: *Sketch of Compton scattering process.*

The expression that relates the energy transfer and the scattering angle for any given interaction can be derived taking in account the energy and momentum conservation laws. Taking in account symbols defined in figure 3.11 and applying the conservation of momentum we get:

$$\begin{aligned} \frac{h\nu_0}{c} &= \frac{h\nu'}{c}\cos\phi + p\cos\theta \\ 0 &= \frac{h\nu'}{c}\sin\phi - p\sin\theta \end{aligned} \tag{3.10}$$

where p stands for the Compton electron momentum. On the other hand, applying the energy conservation law we get:

$$h\nu_0 = h\nu' + T \tag{3.11}$$

where T stands for the Compton electron kinetic energy. Using the three laws expressed above and the relativistic relationship

$$(pc)^2 = T(T + 2m_0c^2) \tag{3.12}$$

and after some algebra, we can deduce two helpful relationships:

The Compton shift

$$\lambda' - \lambda_0 = \frac{h}{m_0c}(1 - \cos\phi) \tag{3.13}$$

which gives us the wavelength difference between the scattered and incident photon, for a given scattering angle ϕ.

Energy of the scattered photon

$$h\nu' = \frac{h\nu_0}{1 + \alpha(1 - \cos\phi)} \tag{3.14}$$

which gives us the energy of the Compton scattered photon as a function of its scattering angle (ϕ) and the parameter α (defined in figure 3.11 as $h\nu_0 = \alpha m_0 c^2$).

Pair production

When the energy of the incident γ-ray exceeds twice the rest mass of the electron ($2m_0c^2 = 1.02$ MeV) a third type of interaction, called pair production, can take place. The probability of interaction remains very low until the incident photon energy reaches several MeV, being therefore the pair production process exclusive of high-energy γ-rays. In this process, which occurs only in the Coulomb field of a nucleus, the γ-ray is completely absorbed and its energy is converted into the rest-mass energy ($2m_0c^2$) and kinetic energy of an electron-positron pair. If we take in account the energy conservation:

$$h\nu_0 = E_{e^-} + E_{e^+} = (T_{e^-} + m_0c^2) + (T_{e^+} + m_0c^2) \tag{3.15}$$

we can deduce the electron (e^-) and positron (e^+) kinetic energy:

$$T_{e^-} + T_{e^+} = h\nu_0 - 2m_0c^2 \tag{3.16}$$

The pair production process is complicated because of the positron, which is not a stable particle. Positrons, as electrons, are charged particles and hence dissipate energy by excitation and ionization processes and are scattered in collisions with electrons and nuclei. Besides they dissipate energy by a radiative process called *Bremsstrahlung* which is proportional to Z^2 (Z stands for atomic number) although it is only important at high energies.

Positrons differ from electrons in the following: Once its kinetic energy becomes low enough (similar to the thermal energy of the electrons in the absorber material) the positron will combine with an electron from the absorber

medium. As a consequence, both will disappear and will be replaced by two oppositely photons with energies m_0c^2 (0.511 MeV). The time required for the positron to slow down before being annihilated is small, therefore, the annihilation radiation appears in virtual coincidence with the original pair production interaction.

3.3.4 Decay Time

The decay time is usually defined as the time after which the intensity of the emitted light pulse or $I(t)$ decays to $1/e$ of its initial value, therefore we are implicitly assuming that the dependence of the intensity with the time t is as follows:

$$I(t) = A_0 e^{-t/\tau} \tag{3.17}$$

where A_0 stands for the maximum value of the intensity, and τ is the decay time of such a scintillator.

This representation is often a too simple description of the scintillator behavior and in consequence, a more detailed model is needed. This is the case of lead tungstate scintillating crystals: as mentioned in subsection 3.3.2, there are three types of luminescent centres which are responsible for PWO emission and they all contribute to it with their characteristic emitting times [20]. In consequence, PWO scintillation kinetics must be considered as the superposition of the contribution of at least three different radiating centres. Therefore, the scintillation kinetics of PWO can be described by three main stages [18][20] as follows:

$$I(t) = \sum_{i=1}^{3} A_i e^{-t/\tau_i} \tag{3.18}$$

where A_i and τ_i are respectively the amplitudes and decay time constants of the i-component. There are two other parameters commonly used to give an integral characterization, which are the contribution of each component C_i and the mean decay time τ_m. The former can be expressed in the following way

$$C_i = \frac{A_i \tau_i}{\sum_{j=1}^{3} A_j \tau_j} \tag{3.19}$$

where in fact we are giving the ratio between the emitted light due to the i-component (the numerator, which is equal to $\int I_i[t]dt$) and the total amount of emitted light (the denominator, which is equal to $\int I[t]dt$). Parameters C_i are often multiplied by 100 to give results as a percentage. The second parameter mentioned above, the mean decay time, can be expressed as follows:

$$\tau_m = \frac{\sum_{i=1}^{3} A_i {\tau_i}^2}{\sum_{j=1}^{3} A_j \tau_j} \tag{3.20}$$

where we use the classical definition of the average interval length [19]:

$$\tau_m = \frac{\int tI(t)dt}{\int I(t)dt} \tag{3.21}$$

PWO behavior can be generalized as follows: we typically find a *fast component* with a typical decay time $\tau_1 \sim$ 2-5 ns, which is usually due to the green and blue luminescence region, and which takes account for around half of the total scintillation light. Then, we find also a *medium component* characterized by a decay time $\tau_2 \sim$ 10-20 ns, mainly due to the green non-regular emission centres and that is responsible for close to another half of the total scintillation light emitted. Finally, there is a *slow component* which is characterized by a decay time much longer ($\tau_3 \sim$ 100-1000 ns) but which shows normally a quite low contribution.

Lead tungstate crystals grown in Bogoroditsk since 1995 were essentially behaving as mentioned in previous paragraph, i.e. decay constants $\sim$ 5, 15 and 100 ns, being their respective contributions $\sim$ 39%, 60% and 1%, as appears in table 3.3 or [9]. However, the exhaustive quality control undertaken during crystals growth since pre-production stage started (1998) (including previously mentioned suppression of blue and red luminescent centres in order to improve PWO scintillating properties) allows to quote much better figures: as an example, the decay time curve of a PWO crystal produced in Bogoroditsk during year 2000 as measured by ACCOS[c] machine is depicted in figure 3.12. In this plot we can see how a 3-exponential function fits very well the experimental data. The decay constants of each component (t_i in the plot) and the calculated percentual contributions C_i deduced from the fit are indicated in the plot. The mean decay time for this crystal calculated using equation 3.20 is $\tau_m = 4.7$ ns.

It must be noticed that contribution to the total kinetics of each one of the three components depends on the crystal growth conditions. As a matter

[c] Acronym for Automatic Crystal COntrol System.

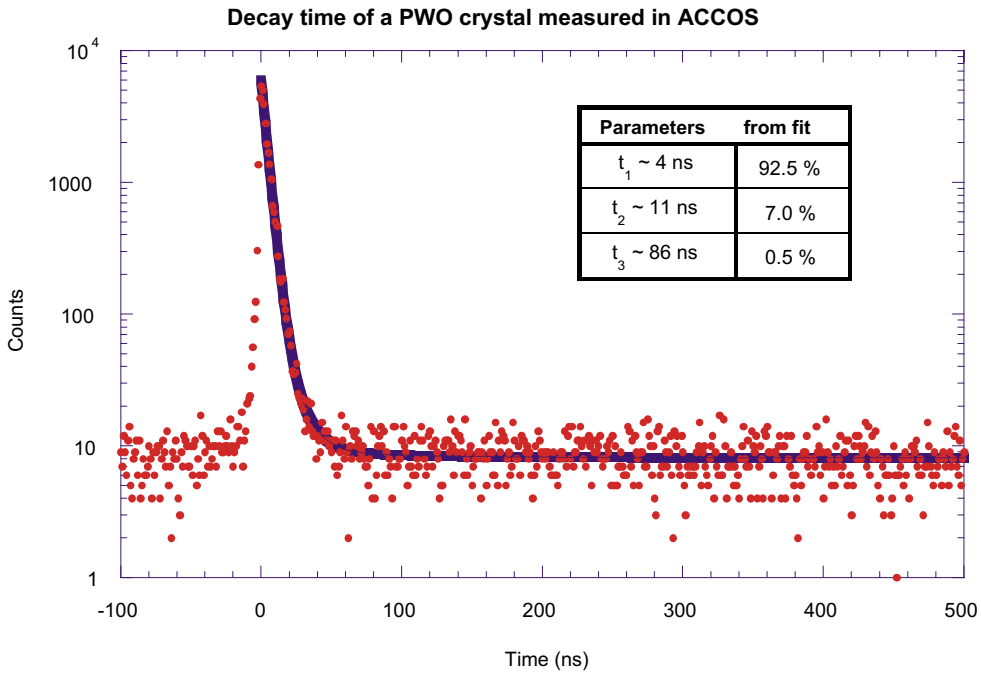

Figure 3.12: *Analysis of the decay time of a PWO crystal.*

of fact, the presence of certain defects in PWO crystals give an afterglow with decay time $\sim$ 200 μs [20]. Another mechanism that leads to a large slow component is related to the presence of some traps induced by molybdenum impurities. Optimization of growth conditions lead to much faster crystals as stated above.

3.4 Optical Properties

In order to achieve an optimum light collection for any scintillator, it is very important to maximize the fraction of photons emitted by the luminescent centres (see the emission spectrum of $PbWO_4$ crystals in figure 3.9) respect to the number of photons detected by the photodetector. This can be accomplished when the absorption of photons in the scintillator is the lowest possible. One possible source of absorption is self-absorption. It takes place when it exists an overlap between the emission and absorption spectra of the luminescent centres as shown in figure 3.13.

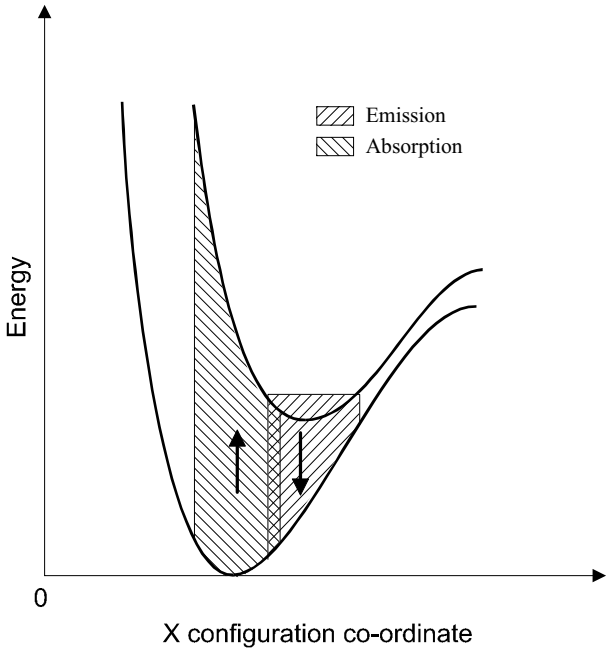

Figure 3.13: *Absorption and luminescence emission transitions showing the origin of the overlap of the absorption and emission spectra.*

Apart from self-absorption, the presence of impurities and/or internal core defects also plays an important role in the absorption of the emitted light. The study of the light transmission through a scintillator will allow us to check how important the absorption is.

3.4.1 Light Transmission

Transmission is the process by which a radiant flux incident on a surface or medium, leaves it from a different side, usually the opposite one. Transmission measurements use to compare the outgoing radiant flux with the incoming one and are generally calculated as a function of the radiant flux wavelength.

In the case of $PbWO_4$ crystal, we are dealing with an optically anisotropic medium of uniaxial type [21]. Due to this, part of light travelling inside the crystal will do it according to the usual laws of an isotropic medium (ordinary ray) and part will travel with a velocity depending on the angle between the crystal optical axis and the interface air//PWO (extraordinary ray). In

consequence, PWO crystals are characterized by the existence of two indexes of refraction, the ordinary and the extraordinary one. In order to simplify the calculations of the theoretical transmission we will consider the case of isotropic crystals.

In general, the equation describing the transmittance of an isotropic material slab of thickness d, depending on the complex refractive index N=n-ik is:

$$T(\lambda) = \frac{(1-r)^2 \exp(-\alpha d)}{1 - r^2 \exp(-2\alpha d)} \tag{3.22}$$

where $r(\lambda)$ and $\alpha(\lambda)$ are, respectively the reflectance of the single interface air//material and the absorption coefficient of the material. Their expression are as follows:

$$\begin{aligned} r(\lambda) &= \left| \frac{N(\lambda) - 1}{N(\lambda) + 1} \right|^2 \\ \alpha(\lambda) &= \frac{4\pi k(\lambda)}{\lambda} \end{aligned} \tag{3.23}$$

If we assume that a perfect crystal only suffers transmission decrease due to reflection losses, then there is no absorption (i.e. $\alpha(\lambda)$=0 and besides $k(\lambda)$=0). Hence, we can rewrite equation 3.22 like this:

$$T(\lambda) = \frac{(1-r)^2}{1 - r^2} \tag{3.24}$$

in addition, the index of refraction N will be only equal to its real part (N=n) if there is no absorption, thus $r(\lambda)$ becomes:

$$r(\lambda) = \left| \frac{n(\lambda) - 1}{n(\lambda) + 1} \right|^2 \tag{3.25}$$

The index of refraction $n(\lambda)$ can be deduced using Sellmeier law [22]. This law can be expressed as follows:

$$n^2 - 1 = \sum_i \frac{{n_{s_i}}^2}{1 - \left(\frac{\lambda_{s_i}}{\lambda}\right)^2} \tag{3.26}$$

where λ_{s_i} and n_{s_i} are the wavelengths and strengths of the optical resonances of the material. In the case of lead tungstate and in the range 320-850 nm, one resonance term in the ultraviolet and a constant term related to short wavelength resonances are enough to fit data. In consequence, Sellmeier law adequated to PWO can be written as:

$$n_{ord}{}^2 - 1 = n_{s_0}{}^2 + \frac{n_{s_1}{}^2}{1 - \left(\frac{\lambda_{s_1}}{\lambda}\right)^2} \tag{3.27}$$

The obtained value of parameters n_{s_0}, n_{s_1} and λ_{s_1} are expressed in the following table [22]:

Table 3.4: *Parameters of Sellmeier law for Lead Tungstate*

n_{s_0}	n_{s_1}	λ_{s_1}
1.5821 ± 0.0080	1.1062 ± 0.0097	270.63 ± 0.82 nm

Using these parameters we can rewrite the equation of the ordinary index of refraction 3.27 in the following way:

$$n_{ord} = \sqrt{3.516 + \frac{1.223}{1 - \frac{73239^2}{\lambda^2}}} \quad \pm \quad 0.01 \tag{3.28}$$

expression valid for $\lambda > 270$ nm. We can also write the expression for the extraordinary index [21] [22]:

$$n_{ext} = n_{ord} - 0.26 \quad \pm \quad 0.05 \tag{3.29}$$

Now we are able to construct the curve of the theoretical transmission. Firstable we calculate the index of refraction for a given λ using equations 3.28 and 3.29. Then, we substitute n in equation 3.25 to calculate the reflectance $r(\lambda)$, and later, we substitute the reflectance in the transmission equation 3.24. In this manner we can build the transmission curves depicted in figure 3.14 where the mean transmission corresponds to the average of the two transmissions deduced for the ordinary and extraordinary index of refraction.

The theoretical transmission calculated above corresponds to an isotropic crystal with no other losses than internal reflections (i.e. no internal absorption). However, lead tungstate crystals do not match this ideal model as

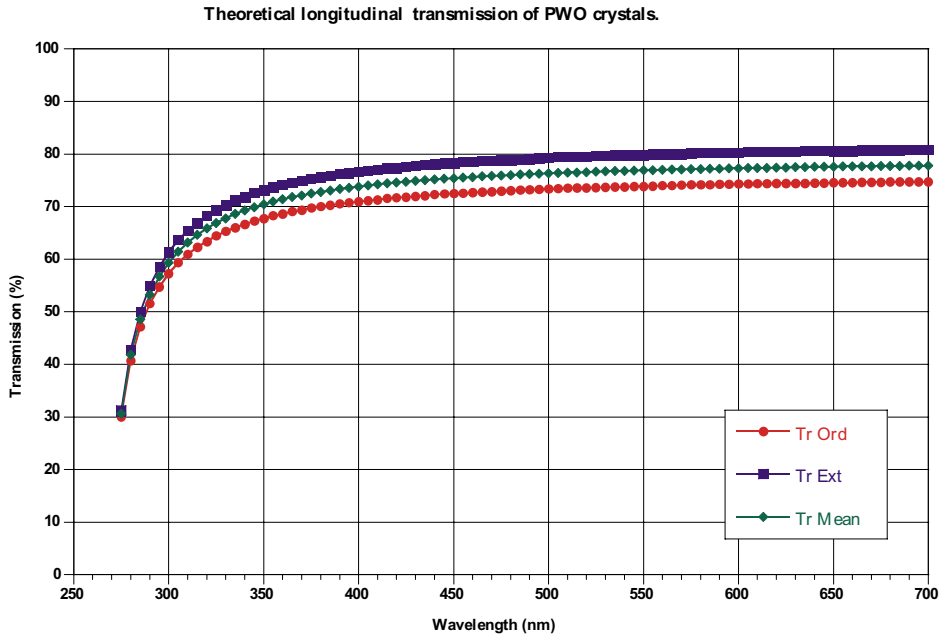

Figure 3.14: *Calculated theoretical transmissions for the ordinary and extraordinary indexes and averaged curve.*

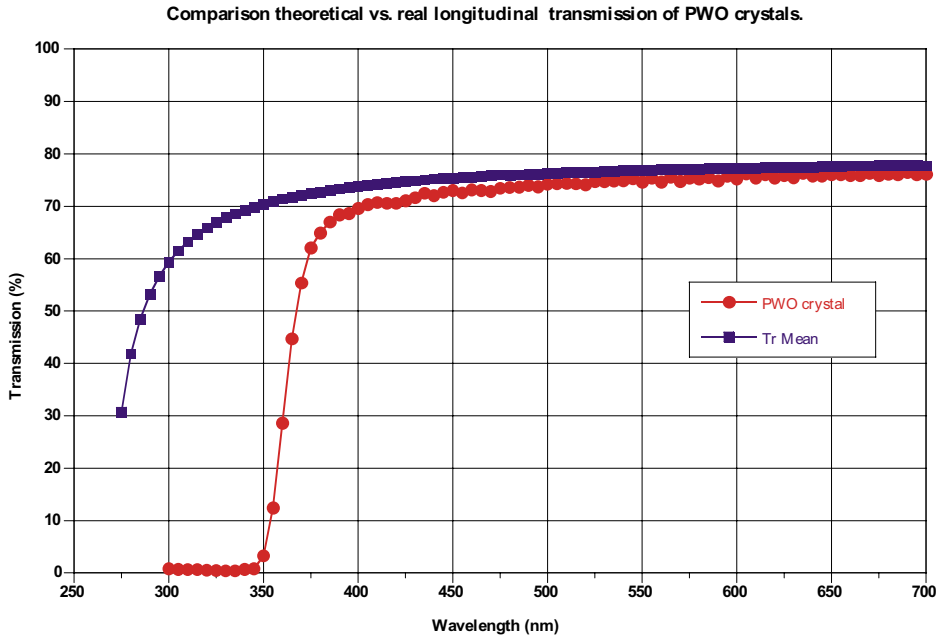

Figure 3.15: *Absorption and luminescence emission transitions showing the origin of the overlap of the absorption and emission spectra.*

mentioned previously. The real longitudinal transmission curve for a recently grown PWO crystal is represented in figure 3.15 together with the mean theoretical transmission calculated above. As we can see in figure 3.15, both curves match well for $\lambda \gtrsim 450$ nm, although an important disagreement appears mainly in the UV range (300-350 nm).

The explanation for such a difference is that the theoretical curve has been calculated assuming a simple model with no absorption and no defects in the internal structure of the crystal. However, in the model, crystals are assumed to have a conduction and valence band with an energy band gap in between as described in subsection 3.3.1 and depicted in figure 3.4a. Theoretical band gap corresponds to 4.5 eV (or, in wavelengths, 275 nm) and it gives the energy limit from which higher energies (lower wavelengths) will be absorbed and lower energies (higher wavelengths) will be transmitted. Clearly, the theoretical curves shown in figure 3.14 match these considerations. However, with real full-size PWO crystals we do not only have the absorption due to band structure but besides we do have an internal absorption which is more important the longer the distance traveled by the light through the crystal is. Such an absorption reduces transmission mainly in the UV range. This is the main reason for the shift of the band-edge in real crystals towards higher wavelengths respect to the expected theoretical value. In fact, when measuring transmission through thin layers of lead tungstate crystals (absorption is strongly reduced respect to full size crystals) we use to see band-edges much closer to the theoretical value (270 nm). There is another factor that plays a role in the band-edge shift: the presence of impurities create special sites in the lattice that modify the band structure of pure crystals. In consequence, energy states may appear within the forbidden band and hence absorption can take place with lower energies than E_{gap} (i.e. higher wavelengths than 270 nm), shifting the band-edge to higher wavelengths.

As mentioned at the beginning of present section, the transmission measurements are very important to verify that the lowest overlap possible between emitted and absorbed light exists. This is what is shown in figure 3.16 for a typical $PbWO_4$ crystal. In the plot, we can see that at the emission peak (420 nm) the transmission is almost the highest possible. Another goal of transmission measurements is to check that no absorption band exists in the region 410 - 450 nm, as it would strongly decrease the light collected. As this absorption band is typical from radiation damaged crystals, transmission measurements are also employed to monitor it.

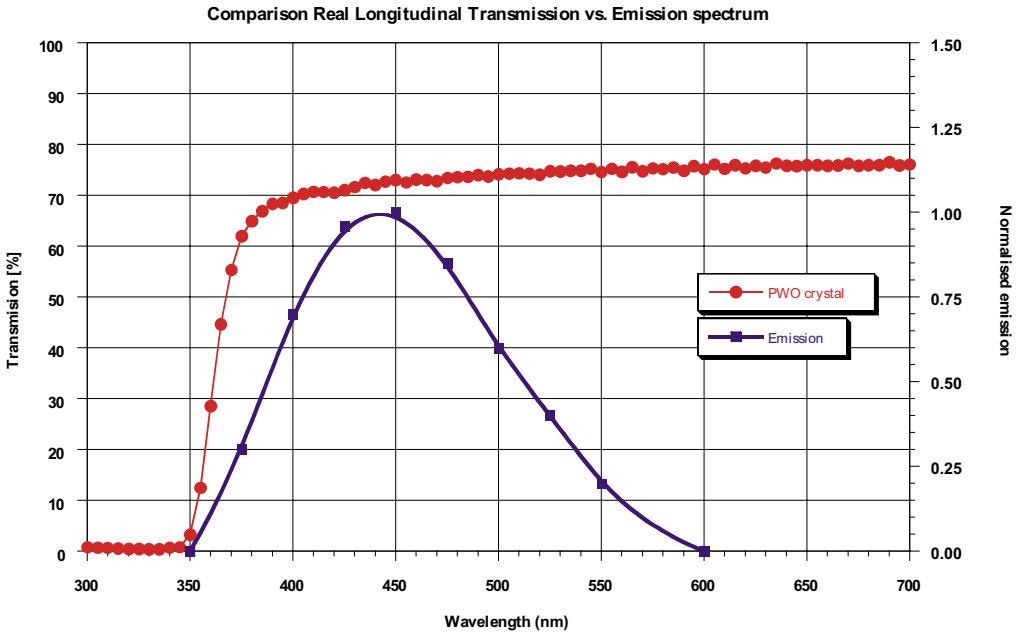

Figure 3.16: *Comparison between emission and transmission spectra for lead tungstate.*

3.5 Geometry of PWO Crystals

It has been already mentioned in subsection 2.4.3 that in the final CMS ECAL detector there will be 17 different types of crystals according to the value of η (see figure 2.14). Each one of the 17 types will have one right-hand and one left-hand version. A set of one right-hand and one left-hand crystals from the same type configures the so called flat-pack (see figure 3.17) because they can be placed together to form a more simple geometrical shape. Every different crystal shape is characterized by a given length (230 mm) and six lateral dimensions (AF, BF, CF, AR, BR, and CR) which are defined in figure 3.17.

The different values of these six lateral dimensions for each one of the 17 types are reported in table 3.5. Another representation of this is given in figure 3.18, where the six dimensions are plotted for the 17 groups of 5 crystals (i.e. 85 in total) in which a half of the CMS ECAL barrel has been divided according to its pseudorapidity. In this way, crystals 0 to 25 correspond to types 1-5, 25 to 45 corresponds to 6-9, and so on. Figure 3.18 allows us to see clearly that when increasing the type, rear dimensions AR and CR decrease, whereas front

Table 3.5: *Dimensions for the 17 types of crystals*

Crystal ID TYPE	CRYSTAL SIZES (mm)					
	FRONT			REAR		
	AF	BF	CF	AR	BR	CR
1	21.83	23.59	21.85	25.84	25.48	25.86
2	21.83	22.22	21.87	25.81	26.22	25.86
3	21.83	22.34	21.91	25.75	26.28	25.84
4	21.83	22.47	21.94	25.67	26.32	25.80
5	21.83	22.61	21.97	25.56	26.34	25.72
6	21.83	22.60	22.00	25.43	26.18	25.63
7	21.83	22.55	22.03	25.29	25.96	25.52
8	21.83	22.67	22.05	25.14	25.92	25.39
9	21.83	22.82	22.08	24.98	25.90	25.26
10	21.83	23.08	22.10	24.82	26.00	25.12
11	21.83	23.14	22.12	24.65	25.89	24.97
12	21.83	23.29	22.14	24.49	25.86	24.83
13	21.83	23.47	22.15	24.33	25.87	24.68
14	21.83	23.71	22.17	24.17	25.95	24.54
15	21.83	23.88	22.18	24.02	25.96	24.40
16	21.83	24.02	22.20	23.88	25.99	24.27
17	21.83	24.29	22.21	23.74	26.07	24.15

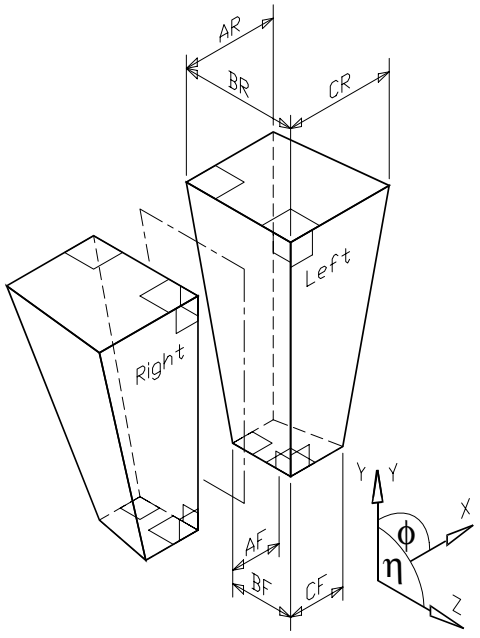

Figure 3.17: *The flat pack configuration.*

dimension BF increases. The other dimensions (AF, CF, and BR) change very little or remain completely unchanged (AF). Looking at figure 3.17 it is easy to see that these changes in lateral dimensions are going to reduce the general tapering (angle between longitudinal faces) of the crystals. In consequence, we have to conclude that crystals corresponding to lower types have a more important tapering than higher types, consideration that will be reconsidered later as tapering plays a major role in the focusing of the light inside crystals.

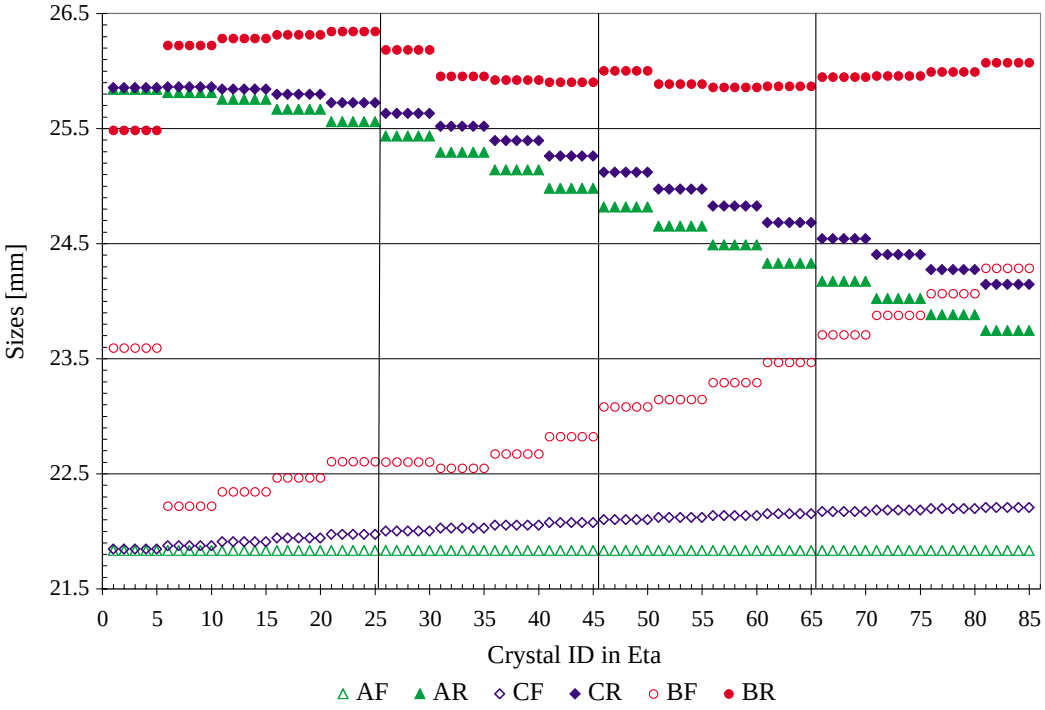

Figure 3.18: *Shapes of the 17 different crystal types.*

3.6 Specifications for PWO Crystals

The ambitious performance goal of the ECAL and the high radiation levels present at LHC impose strict requirements in the design of the detector as was mentioned in subsection 2.4.2. This is going to play an important role on several parameters of lead tungstate crystals, like for example: light yield (which must be high in order to avoid domination of statistical fluctuations in the reconstructed energy resolution), decay time (scintillation light must be collected in a short time to allow integration and electronic readout between bunch crossings, i.e. each 25 ns) or radiation hardness (light yield losses under

irradiation must be low to allow precise corrections from monitoring systems), among others.

All the parameters that must be controlled for PWO crystals are usually grouped in three main fields:

- Geometry
- Optical Properties
- Radiation Tolerance

The specifications define the acceptance values for those parameters and the procedures to be performed at the production centre before shipment, and in the regional centres at the reception of the crystals. Often complex measurements are needed to control these parameters. However, a visual inspection of the crystals already allows us to determine the presence of chips or cracks as well as defects inside crystals. In consequence it is performed on every crystal.

3.6.1 Visual inspection

Some parameters of the crystals quality such as possible colouring, cracks, chips or scratches of any sort can be easily detected by performing a visual inspection. With this purpose, it exists a check list that allows quick rejection of crystals showing the defects mentioned above. Besides, some other possible problems are also detectable: bad positioning of the barcode label that every crystal must have in face F (see face naming schema in figure 3.19), mistakes in the depolishing of one lateral crystal face (face depolished must be always face D, for Left and Right crystals) or presence of core defects inside the crystals, which clearly decrease light transmission and hence also light collection.

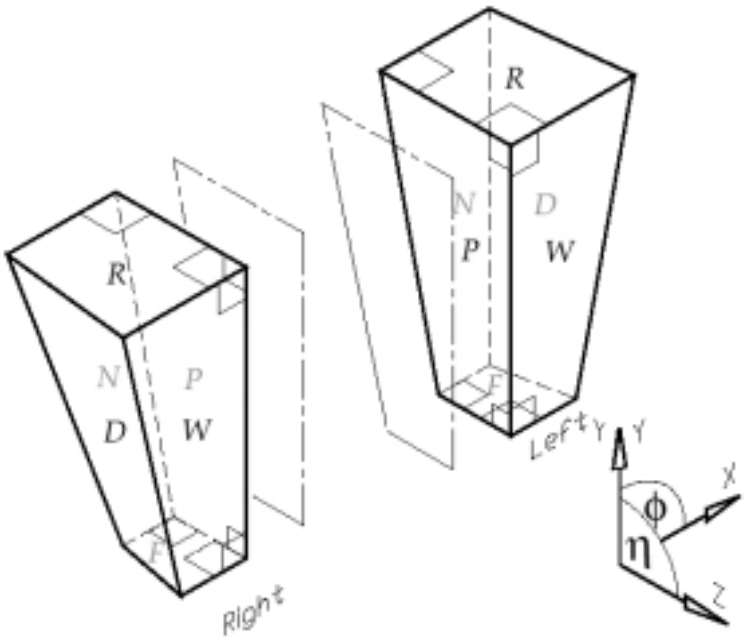

Figure 3.19: *Face naming schema for Left and Right barrel crystals.*

3.6.2 Geometry

We must impose stringent specifications on dimensions due to two main reasons: first, in order to be completely sure that crystals are small enough to fit inside the alveolar structure that will hold them in the final configuration and second, to be sure that they are big enough so that the interspace between crystals is minimized.

As we already mentioned in section 3.5, there are 17 different crystals shapes, each one in right-hand and left-hand versions. Each shape is characterized by six lateral dimensions (AF, BF, CF, AR, BR and CR) also mentioned in section 3.5 and a length (L) of 23 cm which is identical for all types. Obviously, small tolerance ranges must be imposed on them due to reasons explained in paragraph above. The planarity of each face, the angles between faces and the chamfer widths are also important parameters to ensure an optimum mounting of crystals within alveolar structures. Besides, the surface finish of the six faces must be also carefully specified. The tolerances of all these parameters are listed below:

- A play of $\sim$ 50 μm around the crystals must be guaranteed in order to avoid transmission of constraints from crystal to crystal. Therefore, all crystal dimensions must be between Nominal and Nominal - 100 μm for the 17 types. This affects to **length** (nominal value is 230 mm) and to the six **lateral dimensions** (nominal values expressed in table 3.5). In consequence, L, AF, BF, CF, AR, BR and CR must be within +0 mm and -0.1 mm from nominal value.

- **Planarities** of all faces should be smaller than 20 μm to ease the mounting.

- **Chamfers** are made on all 12 edges. Each chamfer should be cut to the following limits: $0.3 \leq$ chamfer $\leq$ (in mm). The surface finish of chamfers can be left at a roughness of 0.5 μm.

- The **angular tolerances** for faces normal to references are specified in perpendicularity, being the relevant tolerance 0.050 mm across a maximum length of 25 mm.

- The **surface finish** of the six crystals faces is given in terms of roughness (Ra). In this way, faces F, R, N, W, and P (see figure 3.19) must show an optical polishing characterized by Ra $\leq$ 0.02 μm. Face D is the face that must show a semi-polishing surface finish, characterized by Ra $\approx$ 0.40 $\pm$ 0.05 μm.

3.6.3 Optical properties

It is easy to understand that a complete optical characterization of each crystal would require both too much time and too complex equipment. Clearly, this is hardly compatible with a facility based in an apparatus that attempts to measure several tens of crystals per day, as is the case of CMS ECAL Regional Centres with the so-called ACCOS[d] devices (explained in following chapter). In consequence, only simple fastly measurable properties are systematically studied. They are: light transmission, decay time and light yield. However, extensive studies were performed in order to find correlations between these simple properties and some other more complex ones. This is particularly true for the radiation hardness, as will be explained later. In this way, only the simple correlated property is measured whereas the complex one is just studied on a sampling basis.

[d] Automatic Crystal COntrol System.

Optical Transmission

Transversal and longitudinal transmission spectra through PWO crystals are rather easy and fast measurements. They give useful indications on the crystals optical quality and have a clear correlation with radiation hardness [23]. Several years of R&D lead to the following tolerances:

- *Longitudinal light transmission*: In order not to affect the light collection uniformity in the crystal a minimum threshold of 55% for the longitudinal transmission at 420 nm is established for accepting a crystal. It guarantees a minimum absorption length of ~ 80 cm. A low transmission at higher wavelengths indicates the presence of a core defect that may affect light collection. In consequence a minimum threshold of 65% for the longitudinal transmission at 620 nm is established for the crystals acceptability. Besides, crystals showing an absorption band at the band edge use to present a weak radiation hardness. Therefore it also exists a specification for this topic: Longitudinal transmission must be not less than 25% at 360 nm.

- *Transversal light transmission*: It is usually measured in six positions, starting at 1.5 cm from the front face (face F in 3.19) and then going on in steps of 4 cm each one (starting from face F, positions are 1.5, 5.5, 9.5, 13.5, 17.5 and 21.5). The only specification is related to the dispersion of the band edge position when comparing the six available measurements: transversal transmission curves, as longitudinal ones, are fitted by a complicated multi-parameter exponential function [24]. Thanks to this fitted function we can find the wavelength that corresponds to a 50% transmission. By comparing the wavelength got in this manner for each one of the six transversal measurements, we can establish the maximum difference between them. This parameter called $\Delta\lambda$ must not exceed 3 nm in order to guarantee crystal homogeneity.

- *Band edge slope*: Also taking into account the fitting curve described above, we can calculate the slope of the band edge in the region 340-370 nm. As mentioned before, such a slope allows us to predict the radiation hardness behavior [23]. In this way, it has been agreed that those crystals with a slope value $\geq 3\%/\text{nm}$ [e] must fulfill our radiation hardness requirements.

[e]The slope specification value mentioned in [23] is not 3%/nm but 1.5%/nm. This is due to the method used to estimate the slope: initially we were using a simple straight line to fit the transmission in the band edge region (340-370 nm) and in this way, the limit

Light Yield

The light yield of PWO crystals is critical for the photostatistics contribution to the energy resolution (stochastic term) and for the signal over electronic noise ratio (noise term). The measured light yield with a crystal will depend on the light emission spectrum and on the quantum efficiency and matching factor of the photodetector employed. As was mentioned in section 3.6.3, the PWO emission spectra peaks at 420 nm. For such crystals, in several test beams campaigns, a value of ≈2 photoelectrons per MeV was measured at a temperature of 18°C with one EG&G avalanche photodiode (APD) in a gate of 100 ns.

In the final configuration of the calorimeter, the crystal section will be larger than the one referred above. Hence, two APDs will be glued at the rear face of the crystals, resulting in an increased light signal of ≈ 3 photoelectrons per MeV, which will guarantee acceptable contributions to the energy resolution. This light level corresponds to ≈ 8 photoelectrons per MeV measured in the following conditions: Temperature of 18°C, pulse integration within a gate of 100 ns and crystal excitation by a ^{60}Co source at $8X_0$ from PWO Front face. Besides, measurements in these conditions must be performed with a Phillips Photo-Multiplier Tube (PMT) XP2262B covering completely the crystal rear face, which is coupled to the PMT with a silicon coupling grease (index of refraction n = 1.5). It is important to mention that in these measurements, crystals are wrapped with 1 Tyvek[f] layer. Clearly, measurements in these conditions are easily performed in the laboratory, being therefore the lower light yield acceptable for them fixed to a limit of 8 pe/MeV.

The uniformity of light collection is not a specification on itself. Only the roughness range of one side face will be indicated (as mentioned in the subsection related to geometry specifications).

value was found to be 1.5 %/nm. Later we changed to the fitting function mentioned above. Calculating slopes with this function is shifting slope values to 3%/nm for the same crystals.

[f]High density Polyethylen fibres, Du Pont Engineering Products S.A., 2894 Luxembourg.

Decay Time

It is generally accepted that PWO is intrinsically fast (15 ns), as was already mentioned in previous sections. However, impurities or defects are often at the origin of slow components (in the 100 ns to 1 μs range) or even afterglow (1 ms range). In spite of that, it is often assumed that if 90% of light is emitted within the first 100 ns, the effect induced by the slow components should be negligible.

Besides, and in order to limit the afterglow, a limit 0.5% of the peak amplitude for the afterglow component is fixed (with a ^{60}Co source and a counting rate of 1 MHz).

3.6.4 Radiation hardness

Radiation hardness is one of those parameters for which systematic and direct measurements are not possible. Hence, a big effort has been made aiming to find other properties correlated with radiation hardness.

There are two important aspects that must be carefully checked when determining if a crystal is radiation hard or not. The first is related to the total damage induced in the crystals when, after irradiation, they are fully saturated in all its volume. This damage should not exceed a certain level, which is defined by a density above which more complex phenomena (collective processes and molecular defect stabilization) can take place. Such a level corresponds to a defect density which in the case of lead tungstate is $3{\cdot}10^{17}$ colour centers per cm^3. For such a defect density, the corresponding induced absorption coefficient should not exceed 1.5m^{-1} at 420 nm when the crystal irradiation occurs from the side at a dose of at least 50Krad, with a dose rate of 10 Krad/h. These conditions are easily reproduced at the Geneva Cantonal Hospital, with a ^{60}Co therapy unit.

The other aspect is related to the light yield losses of the crystals when operating in the LHC as part of the electromagnetic calorimeter. Calculations about expected LHC radiation levels reveal that the barrel will be exposed

to a dose rate of 15 rad/h at high luminosity at maximum energy deposition region (in this case, 3 cm from Front face) decreasing by a factor 10 at the back of the crystal. Such a dose profile is complicated to reproduce, although seems that a frontal ^{60}Co irradiation at the same dose rate (15 rad/h) allows a reasonably good estimation of the damage. Due to this, a special setup has been developed [25] which for the moment is used on a sampling basis. It is accepted that a light yield loss of less than 6% in the front irradiation setup at the dose rate explained above should guarantee a loss at LHC conditions of less than 10%, which is an acceptable value for the monitoring system. This limit is easily predictable with the band edge slope [23].

Last but not least, fast recovery times must be excluded to avoid rapid light yield variations during collider filling times which would be difficult to monitor out without large errors. Therefore, no recovery time constant shorter than 1 hour should be accepted.

All the specification for the CMS ECAL lead tungstate crystal production mentioned in this section are resumed in table 3.6.

Table 3.6: *Specifications for PWO crystal production*

GEOMETRY
• *L, AF, BF, CF, AR, BR, CR*: 0 $\leftrightarrow$ -0.1 mm
• *Planarity*: $<$ 0.02 mm for all faces
• *Angles*: $\leq$ 0.05/d
• *Chamfers*: 0.3 mm $\leftrightarrow$ 0.7 mm in diagonal projection
• *5 faces optically polished*: Ra $\leq$ 0.02 μm
• *Face D polished only to*: Ra $\approx$ 0.45 $\pm$ 0.05 μm
OPTICAL TRANSMISSION
• *Longitudinal*: $\geq$ 25% at 360 nm. $\geq$ 55% at 420 nm. $\geq$ 65% at 620 nm.
• *Transversal*: $\Delta\lambda \leq$ 3 nm at transmission of 50% for 6 measurements every 4 cm, starting at 1.5 from F face
• *Band edge slope* of longitudinal transmission when fitted between 340 and 370 nm: $S \geq$ 3 %/nm
SCINTILLATION LIGHT
• *Light Yield*: $\geq$ 8 photoelectrons/MeV in the following conditions: measured at 18°C, in a 100 ns gate, with ^{60}Co source at 8X_0 from PWO F face, with a Phillips XP2262B PMT, covering all PWO R face, with a n=1.5 silicon coupling grease, wrapped on 4 sides and end face in 1 Tyvek layer.
• *Decay Time*: - LY(100 ns)/LY(1 μs) $\geq$ 90% - Afterglow $\leq$ 0.5 % of peak amplitude, with a 1 MHz counting rate ^{60}Co source
• *Radiation Hardness*: - Induced Absorption for full crystal saturation: $\mu \leq$ 1.5 m^{-1} at 420 nm, for lateral ^{60}Co irradiation, $\geq$ 50 Krad, $\geq$ 10 Krad/h. - Light Yield loss $\leq$ 6% for front ^{60}Co irradiation, 200 rad, 15 rad/h. - No recovery time constant shorter than 1 hour.

Chapter 4

CHARACTERISATION OF PWO CRYSTALS

In this chapter we are going to explain how the complete characterization of the crystals is performed at the CMS Regional Centres. The characterization of the crystals is a complex task in which many different crystal aspects must be carefully studied. For each one of these crystal aspects or properties, there are several related measurable parameters. The comparison of these measurements with existing specifications, which were described in previous section 3.6 is mandatory, since it guarantees the quality of the crystals selected for the CMS ECAL. In order to perform these measurements we have used for a long time the so-called classical benches (light yield benches and spectrophotometers). However, the duration of the measurements and of their analysis as well as all the crystal manipulations needed would make the control of several ten thousands of crystals fastidious, costly in man power and risky for the crystals. This is why systems of benches named Automatic Crystal COntrol System (ACCOS) were designed. They allow fully automatic characterization of crystals and automatic transfer to a database. ACCOS machines are going to be extensively described in this chapter, emphasizing the stability studies performed on them and the correlations to classical benches established.

4.1 Instrumentation

In this section we will perform a detailed description of the ACCOS machines used at the CERN Regional Centre and of the classical benches used to calibrate them. We will start by describing the classical spectrophotometer and the classical light yield benches called B3 and B5. It is important to mention that at an early stage of the pre-production of PWO crystals (before 1998) these classical benches were the only ones used to perform the characterization of the crystals. It is, of course, since that time that the need of an automatic crystal control system (ACCOS) to reduce crystal manipulations and working time was understood. Later on, we will describe the first ACCOS machine installed at CERN, called ACCoCE 1. This machine was built in LAPP/Annecy in collaboration with INP/Minsk, and was installed at CERN in summer 1998. Since then, it has helped to characterize more than 5000 lead tungstate crystals. Then, we will explain the small differences between ACCoCE 1 and the second ACCOS device installed at CERN RC, called ACCoCE 2. This machine was installed at CERN in summer 2000, and since then it has measured few thousands of barrel and endcap crystals. It basically keeps the same working principles than ACCoCE 1 but with some improvements that will be explained.

The stability of most of these devices will be illustrated, as well as the correlations between the Light Yield data and Non-Uniformity curves obtained with ACCoCE 1 or ACCoCE 2 compared to classical Light Yield benches. Light transmission data measured with both ACCOS devices will be also correlated to the classical spectrophotometer data.

4.1.1 Classical Light Transmission bench: The Spectrophotometer

Description of the spectrophotometer

The main goal of the classical spectrophotometer used at CERN Regional Center is to compare the light entering into the crystal and the light leaving it. The aim of this is to know the crystal light transmission as a function of

the wavelength. In order to measure the optical transmission of PWO crystals at CERN, we use a double-beam (see figure 4.1) spectrophotometer built at CERN for which the commercial PERKIN ELMER LAMBDA15 spectrophotometer was taken as a model. Its principal components are a monochromator, a 150W Xenon lamp and a photomultiplier tube acting as a radiant power detector. The light emitted for the lamp is focalized to the entrance of a monochromator and a set of filters placed at the end of the monochromator will eliminate the higher order diffractions and the parasite light.

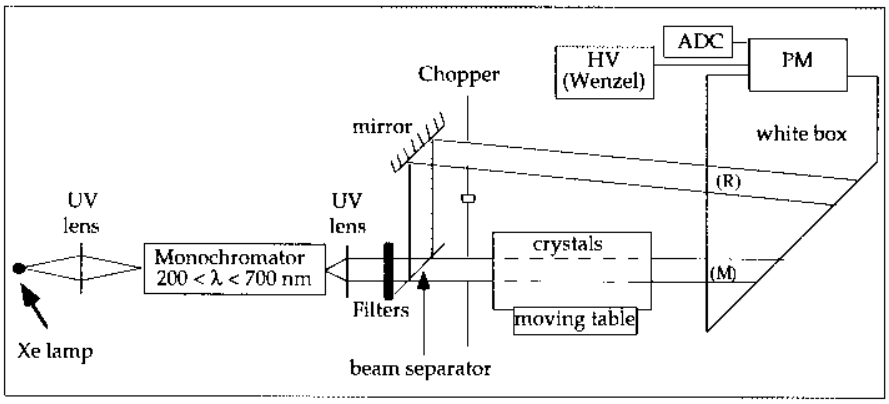

Figure 4.1: *Schema of the CERN Regional Centre spectrophotometer.*

The main elements that compose this spectrophotometer are:

- a 150 Watt discharge xenon lamp which cover the wavelength region from 200 to 700 nm,
- several UV lenses to focalize the light into the monochromator and collimate it as much as possible after it,
- a Jobin Yvon H20 UV monochromator (see figure 4.2) to select the wavelength. A stepping motor coupled to it allows the automatic scanning of the wavelength in a given region,
- several filters are used in order to eliminate upper order diffractions (the higher order harmonics) of the beam coming from the monochromator. Depending on the monochromator wavelength (see table 4.1) a stepping motor changes the filters. Figure 4.3 shows the filters spectra emission,
- a chopper which splits the beam in two beams: a direct and an indirect one, which alternate 50 times per second. One of the beams traverses the crystal and the other one is used as a reference. This chopper is a

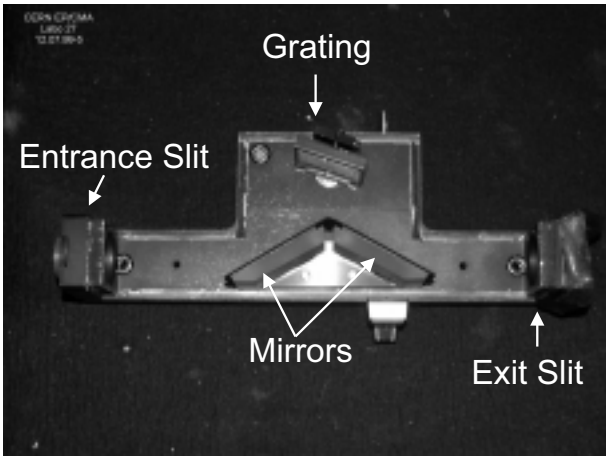

Figure 4.2: *Photograph of the monochromator employed.*

Table 4.1: *Wavelength interval of the filters used in the CERN RC Spectrophotometer.*

FILTER	**WAVELENGTH INTERVAL**
UV	200 to 249 nm
No filter	250 to 340 nm
Blue	341 to 469 nm
Yellow	470 to 605 nm
Red	606 to 700 nm

small wheel that turns with a constant speed and which has two holes and two special UV mirrors,

- a white box that diffuses the light in order to collect it all and to make it arrive as uniformly as possible to the photomultiplier (PM), as the measured signal is dependent on the impact position of the light on the PM photocathode. This white box has two entrances, one for the light that comes through the crystal and the other one for the light diverted to be the reference measurement,

- a XP2254B PHILIPS photomultiplier which measures the light from the white box, that is the light coming either from the crystal or from the reference window,

- a moving table driven by a stepping motor where crystals are placed to be measured,

- a VME data acquisition system where the intensities of the two beams are compared and the transmission coefficient of the crystal is calculated.

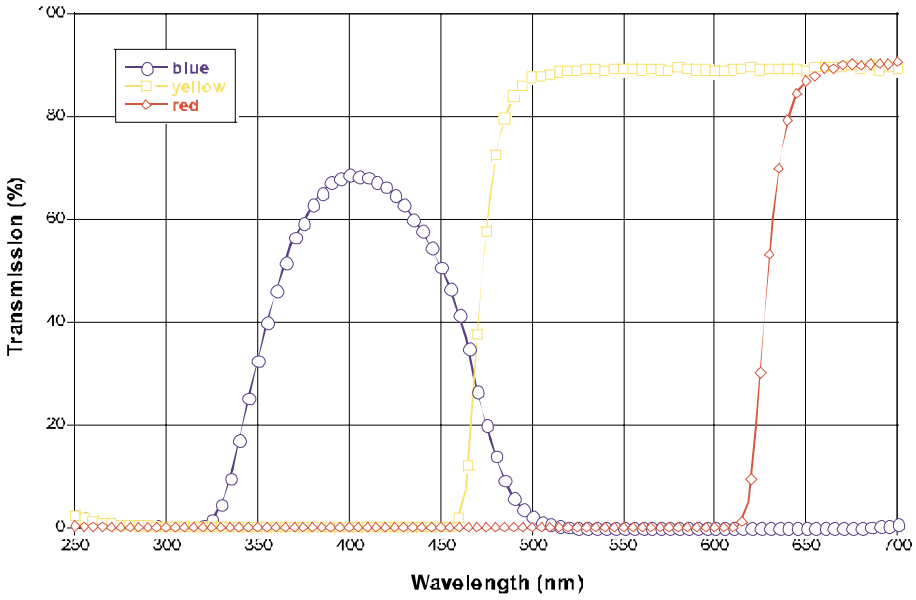

Figure 4.3: *Transmission curves for some of the used filters.*

When measuring with the spectrophotometer we use to measure 25 times for every wavelength, and then a program calculates the value for K, which is defined as:

$$K(\lambda) = \frac{\langle M \rangle}{\langle R \rangle} \tag{4.1}$$

where $\langle M \rangle$ is the mean value for the measurement beam (through the crystal), and $\langle R \rangle$ for the reference beam (not through the crystal). This value is independent of lamp and photomultiplier variations, but depends on the wavelength λ not only through the crystal characteristics but also because the mirror reflectivity and the beam splitter separation are function of λ. This induces some differences between the light going through the upper light path and the lower light path (R and M respectively, in figure 4.1). Every morning, before starting the daily measurements, a reference measurement without crystal is performed, in order to separate these dependencies from the crystal spectrum. This reference measurement is used to compare both beams in the same conditions (no crystal placed in any of both light paths). When dealing with a reference measurement, equation 4.1 becomes:

$$K_{ref}(\lambda) = \frac{\langle M_{ref} \rangle}{\langle R_{ref} \rangle} \tag{4.2}$$

and therefore, if we take into account the differences between both optical paths expressed in equation immediately above, we can rewrite the final transmission

equation obtained as follows:

$$T(\lambda) = \frac{K(\lambda)}{K_{ref}(\lambda)} = \frac{\langle M \rangle}{\langle M_{ref} \rangle} \tag{4.3}$$

With the double-beam method, these transmission measurements are very stable, due to the fact that fluctuations in voltage supply, source intensity, variations in detector response and other irregularities are automatically compensated.

A graphic interface program called Fiat Lux working on a Macintosh, allows the user to define several parameters: the filter positions, the table position, the chopper, the high voltage, the number of measurements per selected wavelength and the wavelength step in a fixed range for the reference. In the case of PWO crystals, it has been observed that 25 measurements every 5 nm in the 300 to 700 nm range is enough.

This spectrophotometer has been used during the last years to measure the transmission spectrum of all the $PbWO_4$ crystals received at CERN RC, although nowadays it use is restricted to the crystals employed in certain irradiation tests and also to the crystals used for periodic comparison checks. This is a consequence of the much shorter time needed to perform transmission measurements with any of ACCOS devices.

Two types of measurements can be performed with our crystals in the spectrophotometer: the *longitudinal transmission* and the *transversal transmission*. The crystal is positioned differently depending on the measurement to be done:

Longitudinal transmission: The beam enters the crystal parallel to the crystal longitudinal axis and traverses the total length of the crystal. In this measurement, the crystal stays in the same position during all the measurement. This longitudinal measurement through the 23-cm-long crystal allows the detection of even weak absorption bands that give a good indication about the light yield and radiation hardness of the crystal. The beam passes through the crystal parallel to its longitudinal axis. This measurement lasts around 8 minutes.

Transversal transmission: The crystal is placed perpendicular to the beam and the light only goes through the width of the crystal. In the PWO case, it has been chosen to measure transversal transmission at 6 different positions only. For the barrel crystal, this measurement goes from 1.5 cm to 21.5 cm (origin in the small end of the crystal) every 4 cm. In the case of endcap crystals, the same measurements are done but from 1 cm until 21 cm (also respect to small end), in 4 cm steps. This measurement takes a little less than 50 min to be done, i.e. 6 times the 8 minutes needed to do a single longitudinal transmission measurement.

Stability of spectrophotometer measurements

The specifications related to transmission in PWO crystals were initially established taking in account spectrophotometer measurements obtained for crystals behaving as desired. Thus, it is important to study not only the stability of this device but also its correlation to ACCOS devices. In this section we will illustrate the first aspect, whereas the latter will be explained in section 4.1.6.

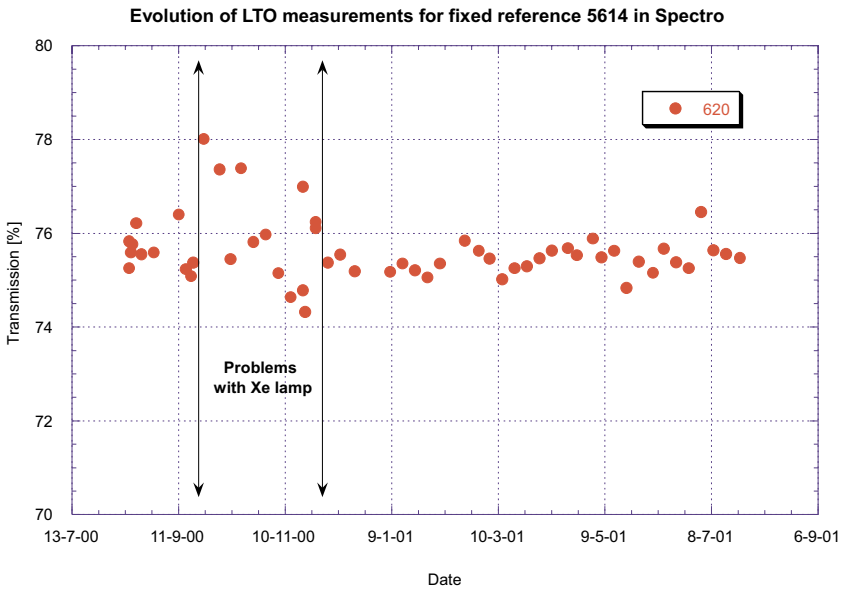

Figure 4.4: *Long-term stability of Spectrophotometer when measuring longitudinal transmission at 620 nm for fixed reference crystal 5614.*

Fixed spectrophotometer reference 5614 (see "References Protocol" in Appendix A) is the crystal most commonly measured in this bench. As a

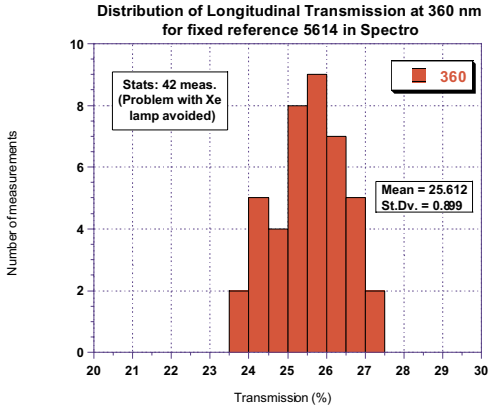

(a) Transmission at 360 nm

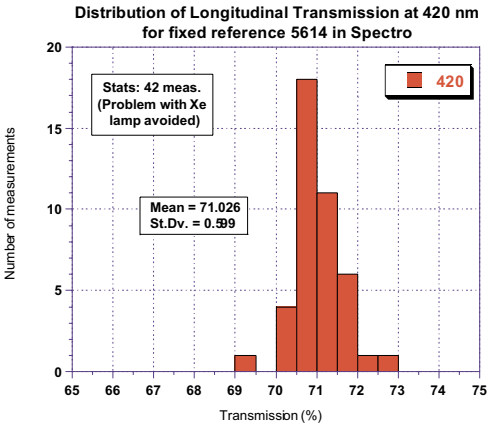

(b) Transmission at 420 nm

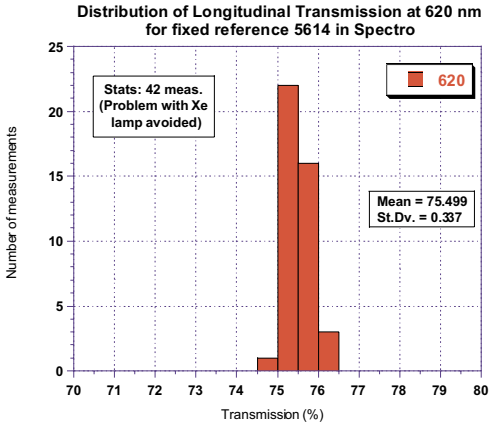

(c) Transmission at 620 nm

Figure 4.5: *Long-term stability of Spectrophotometer when measuring longitudinal transmission of fixed reference crystal 5614*

matter of fact, it is measured once per week in longitudinal transmission. This has been made since $\sim$ 1 year now, thus, we can show the statistics for about 50 measurements of this crystal. However, it is important to remark that during this time there has been an instability period due to problems with the Xenon (Xe) lamp. This is shown in figure 4.4. As we can see in this figure, there is a period of $\sim$ 2 months (from 25^{th} September to 27^{th} November) during which one of the "specified" wavelengths (620 nm) shows much more important fluctuations than in any other period of the year. In fact, these fluctuations were found to be also affecting to other wavelengths (among them, the other two related to specifications: 360 and 420 nm). The reason for this problem was found to be the ageing of the Xe lamp used, and in fact, since it was replaced, the device became again very stable. Therefore, in order to illustrate

the stability of the classical spectrophotometer we are going to construct the histograms of all available longitudinal transmission (LT) measurements at 360, 420 and 620 nm, although we are not going to consider the instability period mentioned above.

Figure 4.5 shows these histograms for 42 LT measurements of crystal 5614. As can be observed, dispersion found for LT at 360 nm (∼0.9%) is higher than the one found for LT at higher wavelengths (∼0.6% for 420 nm and ∼0.3% at 620 nm). The reason for this is simple: the intrinsic accuracy of this device when fixing a wavelength strongly affects to the transmission measured at 360 nm, since this transmission is very sensitive to small wavelength changes due to its location at the middle of the transmission band edge (see PWO transmission example in figure 3.16). On the contrary, the influence on transmission measured at 420 nm or 620 nm is much reduced, since the sensitivity of these transmissions to small wavelength changes is much lower. Another important factor that play against spectrophotometer dispersions is the positioning of the crystals in the classical spectrophotometer which is not as accurate as in ACCOS devices. In any case, we will explain later that ACCOS devices are able to perform absolute transmission measurements, thus, the accuracy achieved with the classical spectrophotometer is not as important as in the case of light yield (we will also see that ACCOS devices measure relative values that must be corrected according to classical bench).

4.1.2 Classical Light Yield bench B3

Description of B3

The light yield measurements attempt to quantify the amount of light collected on the photocathode of a photomultiplier when the scintillator (the PWO crystal) is excited by a radioactive source.

The bench called B3 was built at the end of 1997 and still today is frequently used. This bench 3 can be operated in two modes: light yield or tagging. These two modes are differentiated by the way the linear gate before the ADC is opened. In light yield mode the anode signal is discriminated against the background noise and that makes the pedestal disappear. For that

reason a random generated pedestal is injected to the signal, which goes then to the timing unit and the linear gate. Typically, we use a ^{60}Co source when operating in LY mode (see disintegration schema in figure 4.6-a). However, in the tagging mode, we use a ^{22}Na source which is emitting two collinear 511 KeV gamma rays due to the annihilation of the emitted positron (β^+ decay) with an electron from the absorbing material where the source is encapsulated (see ^{22}Na disintegration schema in figure 4.6-b). One of the gammas goes into the PWO crystal and the other into a BaF_2 crystal attached to a small PM. The signal coming from both PMs is discriminated and sent to the timing unit in order to produce the linear gate. In this way, pedestal does not need to be externally injected. This tagging-mode allows more accurate determination of the non-uniformity curves, but as a drawback, it needs much larger statistics than the light yield one. Therefore, we typically use only the Bench 3 in Light Yield mode.

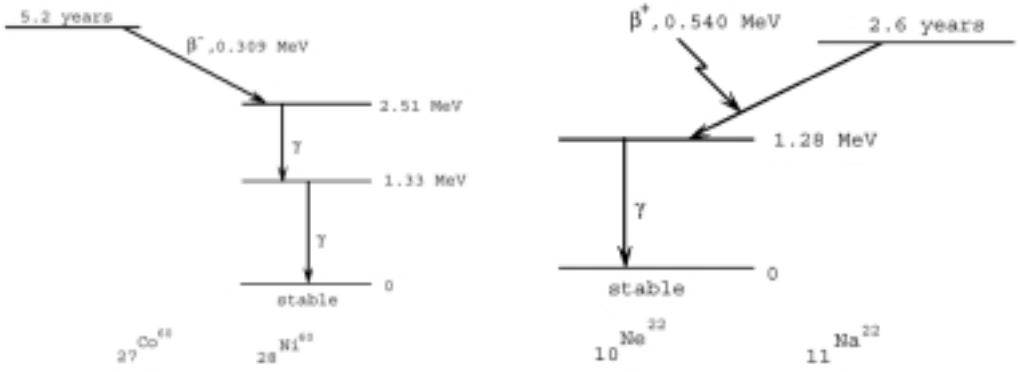

(a) Disintegration of ^{60}Co

(b) Disintegration of ^{22}Na

Figure 4.6: *Disintegration schema of ^{60}Co and ^{22}Na sources used in B3*

The basic B3 set-up is composed of:

- a PHILIPS 2262B photomultiplier (PM) coupled to the largest crystal section with optical grease; it is protected with a μ-metal and attached to a PM base or voltage divider,
- a cooling unit with water circulation to maintain the crystal, the PM and the voltage divider at 18°C,
- a radioactive source attached to the BaF_2 crystal, which is coupled to a small PM plugged into its base. In tagging mode this PM is operational

as it is used to detect one of the two gamma rays emitted by the ^{22}Na source, whereas in light yield mode it is switched off and just acts as a source holder. The ensemble is connected to a stepping motor that allows it moving vertically all along the crystal,

- all the electronics needed to process the signal coming from the PM (including a QVT Multichannel Analyzer[a]) and to produce the High Voltage needed for the two PMs (typically $\sim$ 2000 Volts),

- a PC to control and analyze the signal.

In order to maximize the light collection, is important to minimize the reflection at the coupling face. It is why a special grease is used for the optical coupling. This transparent grease has a similar index of refraction than the PM window ($n_{photocathode}$=1.5). It is important to mention that the ideal would be to have an optical coupling with index n satisfying: $n_{photocathode} < n < n_{PWO}$ but finding a grease with n >1.5 is very complicated, therefore we accept a grease with $n \approx 1.5$. We have been using until now the Rhodorsil Silicones "*Pâte* 7", with a refraction index of 1.5 at 300nm (this product is a CERN standard).

Crystals are usually wrapped into a tyvek[b] envelope for the measurements performed in B3. The reason for this can be found in existing related specification: as mentioned in section 3.6, the lowest acceptable light yield for a crystal is given by 8 pe/MeV [c], measured, among other things, at a temperature of 18°C and with a tyvek envelope.

The first step to be performed by the PM tube is the conversion of incident light photons into electrons. This process of photoemission can be thought of as occurring in three sequential stages:

- The absorption of the incident photon and transfer of the energy to an electron within the photoemissive material.

[a] Le Croy Research Systems Corporation. NIM Model 3001.

[b] High density Polyethylen fibres, Du Pont Engineering Products S.A., 2894 Luxembourg.

[c] This light level is generally agreed to correspond to ≈3 photoelectrons per MeV with twin APD readout in beam conditions, value that guarantees an acceptable contribution to the energy resolution.

- The migration of that electron to the surface.
- The escape of the electron from the surface of the photocathode.

The energy that can be transferred from the photon to an electron in the first step is given by the quantum energy of the photon $h\nu$. For blue light (typical in the light emission of many scintillators), the quantum energy is about 3 eV. In step 2, some of that energy will be lost through electron-electron collisions in the migration process. Finally in step 3, there must be sufficient energy left for the electron to overcome the inherent potential barrier that always exists at any interface between material and vacuum. This potential barrier (called also work function) is normally greater than 3 or 4 eV for most metals but can be as low as 1.5 - 2 eV for suitable prepared semiconductors.

The photocathode converts the light photons into electrons with a given efficiency known as the quantum efficiency (QE), defined as:

$$QE = \frac{Number\ \ of\ \ photoelectrons\ \ emitted}{Number\ \ of\ \ incident\ \ photons} \tag{4.4}$$

The photoelectrons are collected on the first dynode and then multiplied on the 13 successive dynodes. The analog signal of the anode and of the last dynode can be used for analysis. The anode signal discriminated against noise can be used to trigger the linear gate. The width of the gate is adjustable in a timing unit. A 100ns gate is usually employed in our measurements to approach the CMS calorimeter conditions. The signal is converted in a multi-channel analyzer (ADC) operating in Q mode. The electronics scheme used in B3 is depicted in figure 4.7.

The light spectrum is composed of three well resolved peaks (see figure 4.8): pedestal, single photoelectron and photoelectric peak, the position of which is proportional to the energy of the incident particles. Besides, the Compton continuum appears above the also present background in a wide range of the spectrum (from pedestal up to photopeak).

The light yield in Bench 3 at Lab. 27 at CERN is measured with a ^{60}Co source, but the crystal light yield is not high enough to allow the separation of the 1.17 MeV and 1.33 MeV ^{60}Co lines (its disintegration schema is depicted in figure 4.6). That is why we only see a single photopeak instead of distinguishing clearly the two peaks. The single electron is a signal produced by the normal

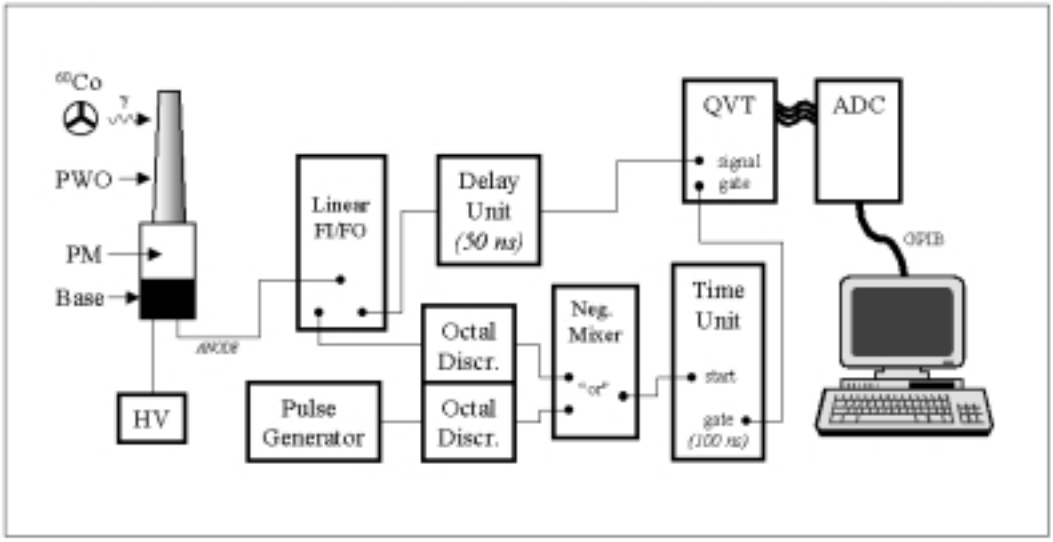

Figure 4.7: *Electronics used in Light Yield bench B3.*

conduction electrons within the photocathode, which can occasionally have enough energy to escape from the photocathode if they are close enough to the surface (at room temperature and normal HV conditions). The pedestal corresponds to gates with no corresponding linear signal. It represents the zero value of the amplitude (or energy) scale. It can be adjusted by adding a DC level to the analog pulse. The width of the pedestal is due to the electronic noise. The difference between the position of the single electron peak and the pedestal allows us to calibrate the ADC channels in terms of photoelectrons.

In order to know the Light Yield we have to determine the position of the peaks and perform some calculations. In consequence, the produced spectrum is fitted in the following way: First, pedestal and single electron are estimated. Then a gaussian fit is performed to the single electron peak, to determine precisely its position. Pedestal is then subtracted and we use the value of the single electron ($s.e.$) to express the ADC channels (c_{ADC}) in number of photoelectrons (m): $c_{ADC}/s.e.{=}m$. After that, we try to fit the photoelectric peak, in order to know the number of photoelectrons that corresponds to it. This fit is performed using two functions [31]: a Poissonian distribution plus a function that takes in account the Compton continuum and its edge. The use of a Poissonian distribution is based on the limited number of photoelectrons produced (mean value is typically ~ 10 photoelectrons) in spite of the large number of events analyzed (several thousands), what clearly indicates that the probability of each single event is quite low. On the other hand, Compton scattering must be also taken into account: photons with energy E entering

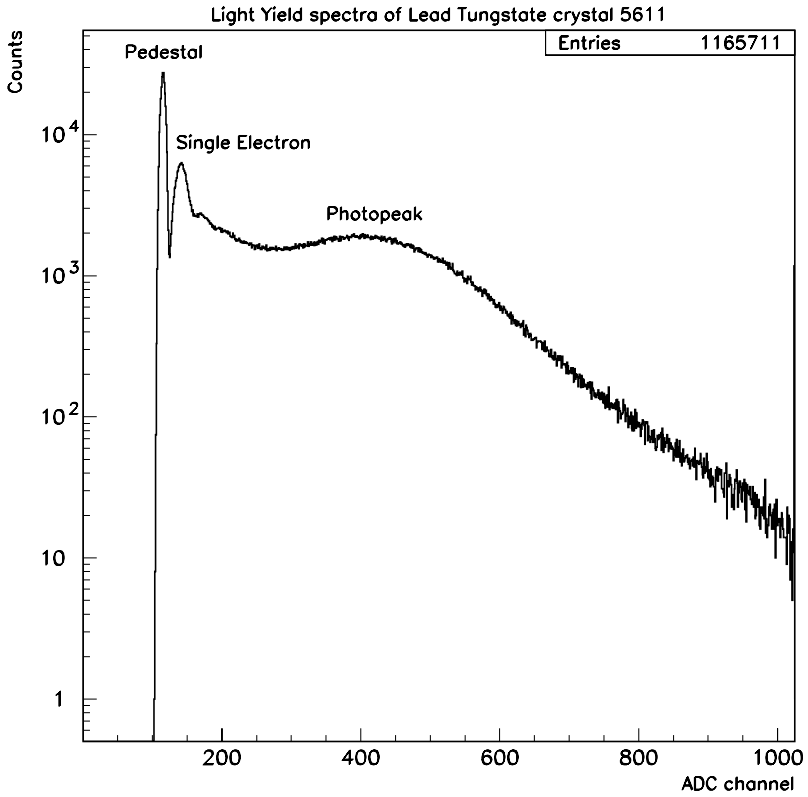

Figure 4.8: *Light yield spectrum of a PWO crystal measured in B3.*

the crystal can suffer Compton scattering (as explained in previous chapter) and the produced photon have a chance of leaving the crystal without deposing its energy (E'). If this happens, the maximum allowed deposed energy is given by the maximum energy that the scattered electron can carry after a single interaction. This limit is known as the Compton edge (E_c) and it can be shown to be:

$$E_c = E\left(\frac{1}{1+\frac{m_e c^2}{2E}}\right) \tag{4.5}$$

This edge is smeared by the resolution effect and by secondary photon interactions although it remains located around E_c. In order to fit this Compton contribution we use a Fermi-Dirac function [31]. Hence we can write down the function used to fit the photoelectric peak as follows:

$$Function = N \cdot P(m, N_{pe}) + \left[\frac{B}{1+e^{\left(\frac{m-E_c \cdot Npe/E}{T_c}\right)}}\right] \tag{4.6}$$

where N is a normalization factor, m is the corresponding number of photoelectrons to a given ADC channel (we used single electron calibration to

switch from channels to photoelectrons), N_{pe} is the average number of photoelectrons produced and $P(m, N_{pe})$ is the Poissonian probability of producing m photoelectrons when the expected value is N_{pe} according to:

$$P(m, N_{pe}) = \frac{{N_{pe}}^m \cdot e^{-N_{pe}}}{m!} \tag{4.7}$$

Besides, in equation 4.6, B establishes the value of the Compton continuum, at lower energies than the Compton edge E_c defined above, E stands for the energy of the incoming gamma ray and T_c is a parameter that controls the slope of the Fermi-Dirac distribution in the inflexion point and that is called temperature only to keep the original Fermi-Dirac distribution nomenclature.

Several MINUIT [d] minimization routines attempt to minimize the differences between the function described above (equation 4.6) and the real number of counts registered for a given number of photoelectrons (corresponding to an ADC channel) in a region that is usually defined around the photopeak value. An example of how the fit works is depicted in figure 4.9. In this picture we can see in the upper position a real photopeak acquired with B3, fitted to the double function described above, with the estimated Compton edge overimposed. In central position we can see what does the photopeak looks like after subtracting the Compton background (remaining data looks like a Poissonian distribution). In the lower position we see the χ^2 calculated for all the points. The X-axis corresponds to ADC channels and the Y-axis to number of counts per channel. Two thin vertical lines represent fitting limits.

After the minimization, the parameter N_{pe} is giving us the number of photoelectrons that correspond to the fitted photopeak. It is, the number of photoelectrons produced in the photocathode when the photons emitted by the crystal due to the complete absorption of the incident gamma ray strike on it. If we want to know the real number of photons (N_{ph}) reaching the PM photocathode we need to know its quantum efficiency (QE). This efficiency strongly depends on the wavelength of the incident light. Typical quantum efficiency curves of Philips 2262B PM are peaking at $\sim$ 350 nm providing at that point an efficiency of $\sim$ 30%. However, we generally give the Light Yield in photoelectrons per MeV of incident energy instead of using photons. In spite of not being photocathode-independent this value is much more precise than the absolute number of photons per MeV. The reason is that in order to pass from photoelectrons to photons, we would need to measure precisely the quantum efficiency of the used PM and to convolute it with the emission spectra of each crystal used (see figure 3.9). A very rough approximation of

[d] MINUIT-Function Minimization and Error Analysis. CERN Program Library.

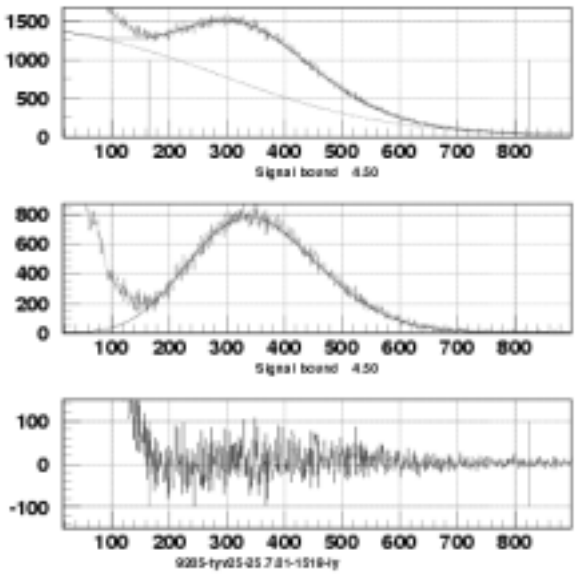

Figure 4.9: *Example of a fit performed in B3 on the light yield spectrum of a PWO crystal.*

this convolution is to assume that the efficiency is $\sim 13\%$. This figure can be only taken into account when we want to roughly know the number of photons impinging in the PM photocathode:

$$N_{ph} = \frac{N_{pe}}{QE} \approx \frac{N_{pe}}{0.13} \tag{4.8}$$

As mentioned previously, we use to express LY in photoelectrons per MeV although no distinction can be made between the 1.17 MeV and 1.33 MeV gamma rays emitted by ^{60}Co source. Therefore, a mean value of 1.25 MeV is taken (the contribution of both gamma is similar) and we can write:

$$LY\left[\frac{N_{pe}}{MeV}\right] = \frac{N_{pe}}{1.25} \tag{4.9}$$

These calculations are done for all measured points along the crystal, resulting in a curve like the one seen in figure 4.10.

The non-uniformity of the light collection is usually measured at fixed steps of 1 cm along the crystal. Typically 21 measurement points are done from 3.5 cm until 22.5 cm. Points between 11.5 cm and 19.5 cm from the big base (called Front part) are fitted by a straight line. The light yield of the crystal is taken as the value of that fitted line at 15.5 cm, corresponding to the region of the shower maximum development ($8X_0$) for 100GeV electrons or γ rays.

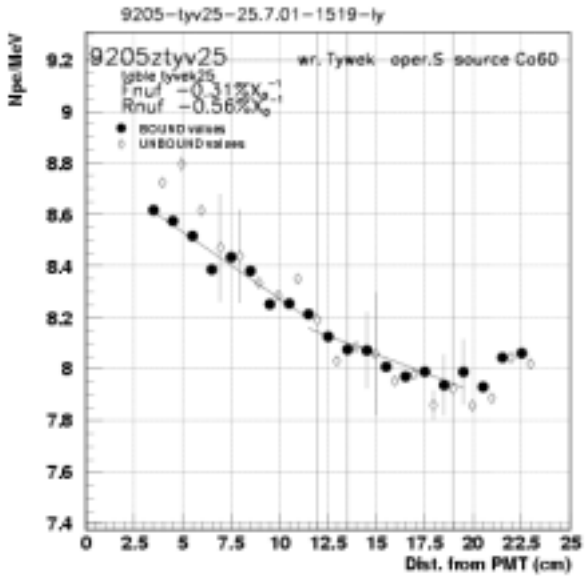

Figure 4.10: *Example of a uniformity curve measured in B3 for a PWO crystal.*

Points between 3.5 and 11.5 from big end constitute the so-called Rear part of the crystal. Each part is characterized by a parameter that defines how non-uniform the crystal is on it. They are the so called Front and Rear Non-Uniformity (Fnuf and Rnuf from now onwards). For their definition we use the two fitted straight lines. They will be called $y_F(x)$ and $y_R(x)$:

$$\begin{aligned} y_F(x) &= a_F \cdot x + b_F \quad , \quad x \in [11.5, 19.5] \\ y_R(x) &= a_R \cdot x + b_R \quad , \quad x \in [3.5, 11.5] \end{aligned} \tag{4.10}$$

we will also define a reference light yield (y_{ref}) which is given by the average value of both fitted lines at x=11.5 cm:

$$y_{ref} = \frac{y_F(11.5) + y_R(11.5)}{2} \tag{4.11}$$

So, now we can define the Fnuf and Rnuf parameters. They are giving us the slope in each one of the two parts of the crystal that they represent but instead of having as units $\frac{N_{pe}}{MeV}/cm$ we switch to $\%/X_0$ as follows:

$$\begin{aligned} Fnuf[\%/X_0] &= a_F \cdot \frac{100}{y_{ref}} \cdot X_0 \\ Rnuf[\%/X_0] &= a_R \cdot \frac{100}{y_{ref}} \cdot X_0 \end{aligned} \tag{4.12}$$

where X_0 must be used in cm ($X_0 = 0.89$ cm). Figure 4.10 shows an example of an uniformity curve where Front and Rear fitted lines are plotted and its

values are indicated. As mentioned above, the light yield of the crystal is given by the Front fitted line at 15.5, so, LY at $8X_0 = y_F(15.5)$. In this plot we can see that the Light Yield of this crystal is $\sim$ 8 photoelectrons per MeV. If we want to have a rough estimation of the number of photons per MeV produced we can take in account equation 4.8. Thus, the emitted light by this PWO crystal is $\sim$ 60 photons per MeV of incident energy.

Stability of B3 measurements

It has already been mentioned that from Bench 3 measurements we can extract three parameters important for us: Light Yield, Front NUF and Rear NUF. In order to show how stable B3 is, we are going to show the evolution in time of these three parameters for the reference crystals 5611, 5624 and 5654 (see "References Protocol" in Appendix A).

It is important to mention that the tyvek used to measure the fixed reference 5611 during the nights and the non-reference crystals during the day (see discussion in appendix A) is destroyed after being used for $\sim$ 3-4 weeks, for the reasons explained later. Then, a new tyvek is made attempting to make it the most similar possible to the previous ones.

The evolution of LY, Fnuf and Rnuf measurements for reference 5611 since April 00 to May 01 is depicted in figure 4.11. The data are grouped according to the different tyveks used (from tyvek number 9 up to number 22). If we observe these three plots, we can understand several important facts: Looking at plot (a) and (c) we notice that the ageing of these wrappings is very evident. The LY data measured with a given tyvek is typically more than 5 % lower after being used for 1 month (see tyveks 12 and 15, for example). In the case of Rnuf, immediately after making a tyvek we use to measure Rnuf $\approx$ -0.5 $\frac{\%}{X_0}$, whereas one month later this value can decrease to Rnuf $\approx$ -0.1 $\frac{\%}{X_0}$ (again see tyveks 12 and 15). Such an ageing is not affecting so strongly to Fnuf (see evolution plot (b) in the same figure 4.11).

The explanation for this phenomenon is simple: due to the insertion and removal of several crystals per day the inner side of the wrapping gets small scratches that reduce its reflectivity. This affects the LY produced at

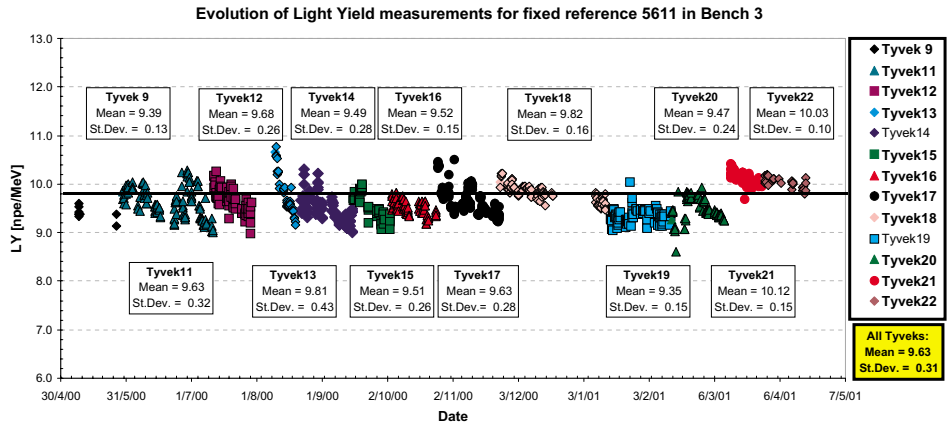

(a) Light Yield

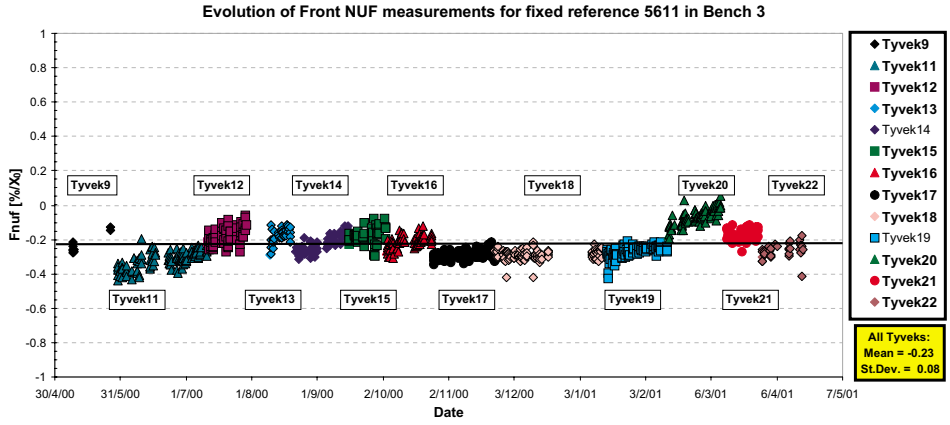

(b) Front NUF

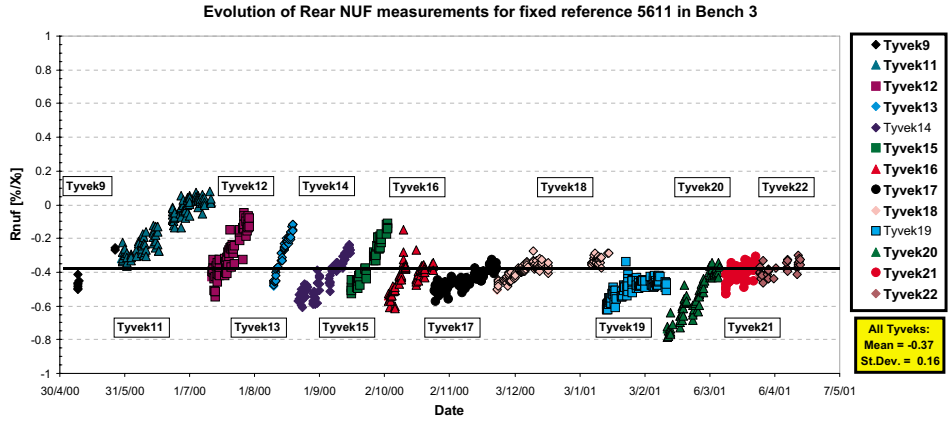

(c) Rear NUF

Figure 4.11: *Long-term stability of Bench 3 when measuring Light Yield, Front NUF, and Rear NUF for fixed reference 5611*

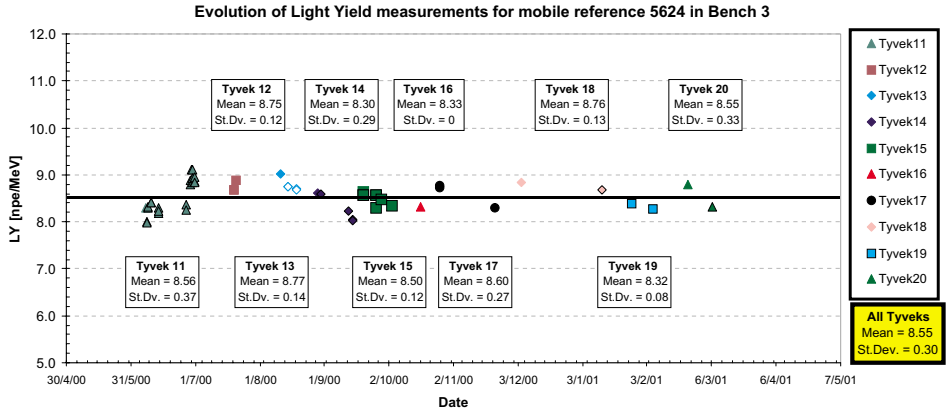

(a) Light Yield - Ref: 5624

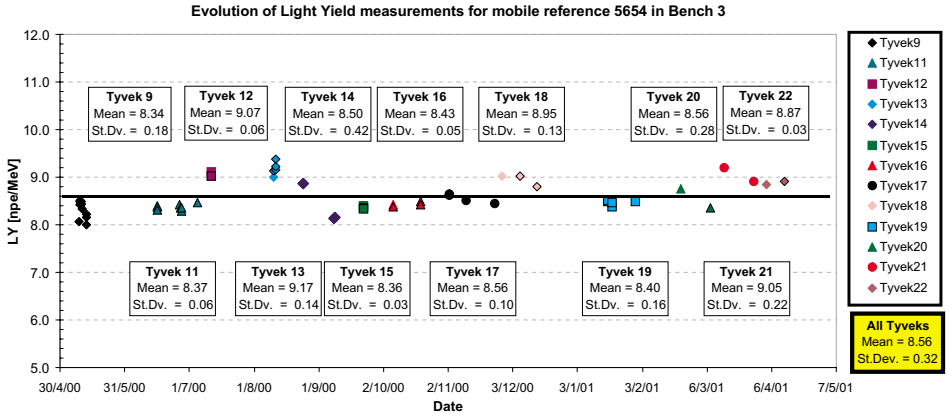

(b) Light Yield - Ref: 5654

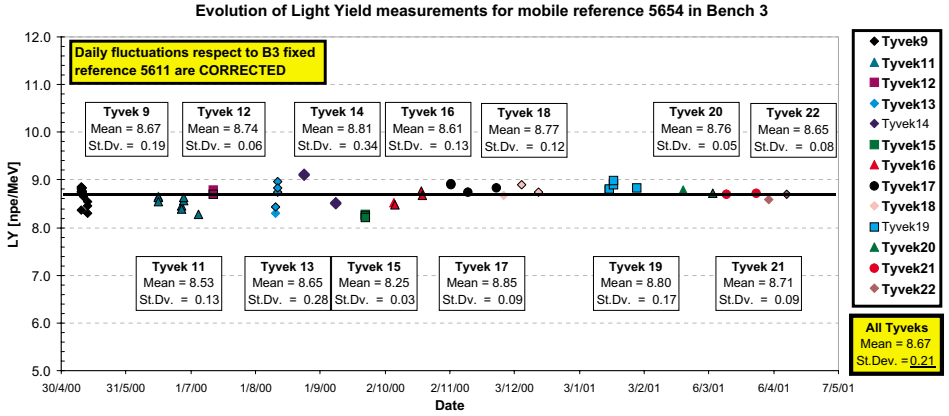

(c) Light Yield Corrected for Daily variations - Ref: 5654

Figure 4.12: *Long-term stability of Bench 3 when measuring Light Yield of mobile references 5624 and 5654*

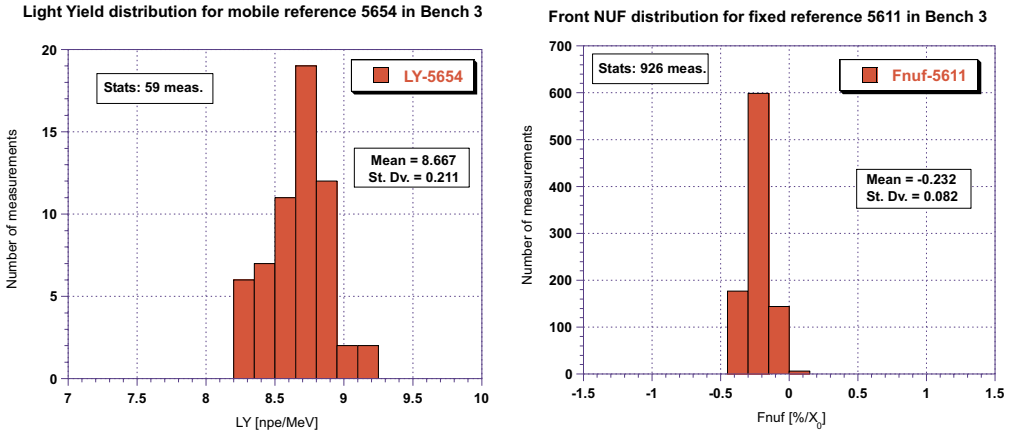

(a) LY Distr. - Ref: 5654 (b) FNUF Distr. - Ref: 5611

Figure 4.13: *Long-term stability of Bench 3 when measuring Light Yield of mobile reference 5654 (corrected) and Front NUF of fixed reference 5611*

all crystal positions, since all the PWO barrel crystals have a depolished face, which destroys internal reflection and increases sensitivity to tyvek reflectivity. This lowers more or less equally the LY produced at any point of the crystal, thus not affecting Fnuf or Rnuf, but only LY. On the other hand, as a tyvek is more and more used, it becomes loose especially in the "entrance" of the tyvek (crystal has $\sim 1/2$ mm play inside), in spite of being made quite tight initially. This is producing the so called "channeling effect": the light that normally, with a tight tyvek, is always internally reflected and later collected in the PM now is sometimes escaping the crystal and travels in between crystal and tyvek suffering many reflections that produce an important loss of light. As this looser part of the tyvek is placed at its entrance (big end of crystal), the shift to lower LY values due to the homogeneous loss of reflection of tyvek is enhanced in the rear part, where more losses are produced due to channeling. This reduces the general LY of the crystal, keeping Fnuf as before, but decreasing the absolute value of Rnuf (it becomes less negative). This is the reason why we use to assume that the lifetime of our tyveks is only $\sim$ 3-4 weeks, since in this period of time the measurements are still not too disperse: standard deviation of Rnuf including all tyveks used is $\approx 0.16\ \frac{\%}{X_0}$, only a factor 2 higher than the one got for Fnuf: $\approx 0.08\ \frac{\%}{X_0}$ (which is very similar to precisions got for ACCOS devices, as we shall see). The Light Yield standard deviation for all tyveks used is $\approx 0.3\ \frac{N_{pe}}{MeV}$.

It is evident that the LY and Rnuf dispersions stated above are strongly dominated by the tyvek ageing. Such a domination is much weaker in the case

of Fnuf, although it is also present. This tyvek ageing affects all the crystals measured using it, i.e. not only the references but all the others measured in order to calibrate ACCOS devices. Thus, it is important to find a way to normalize all measurements performed with a given tyvek in order to avoid ageing. Such a procedure, outlined in appendix A, is used for LY values: the mean value of all LY data for crystal 5611 is 9.63 $\frac{N_{pe}}{MeV}$ (see plot (a) in figure 4.12), however, this value is dominated by tyvek ageing, and what we want to do is to establish an absolute LY value tyvek-ageing independent to which we can normalize all data. We can deduce that value with the measurements performed using recently made tyveks. Such an "absolute" LY for fixed reference 5611 has been estimated in that way to be ≈ 9.8 $\frac{N_{pe}}{MeV}$ (less than a 2% higher than the averaged value of all measurements). In this way, every non-reference crystal measured during a given day in B3 with a given tyvek is LY corrected according to the ratio between the official absolute LY of 5611 (9.8 $\frac{N_{pe}}{MeV}$) and the average of the five measurements performed for 5611 during the previous night with the same tyvek.

Such a procedure improves reliability on LY measurements. This is illustrated in figure 4.12, where in plots (a) and (b) they are depicted the LY evolution from April 00 to May 01 for mobile references 5624 and 5654. The LY dispersions in plots (a) and (b) are very similar (≈ 0.3 $\frac{N_{pe}}{MeV}$) to the one got for 5611 in figure 4.11-(a) and it is easy to understand as the tyveks used are the same ones used for 5611 and dispersions are dominated by tyvek ageing. However, we have made the exercise of correcting every measurement of reference crystal 5654 as we do for non-reference ones (explained in paragraph above). The result is plotted in evolution plot (c) of figure 4.12. As we can see, the dispersion is reduced in a 30% (≈ 0.21 $\frac{N_{pe}}{MeV}$). This is a good estimator of the uncertainty of the LY measurements performed in B3 for the non-reference crystals used to calibrate ACCOS devices.

Such a corrected LY for crystal 5654 (tyvek independent) and the Fnuf for fixed reference 5611 (which was the less sensitive parameter to tyvek ageing) are histogrammed in figure 4.13 in order to see clearly the dispersion of both relevant parameters.

4.1.3 Classical Light Yield bench B5

Description of B5

The classical light yield bench B5 is installed at CERN RC since summer 1998. The aim of this device is, as in the case of Bench 3, to quantify the amount of light emitted by a PWO crystal and collected by the photocathode of a photomultiplier when the scintillating crystal is excited with a radioactive source.

This bench B5 is the only classical LY bench capable of measuring endcap crystals, as the inner receptacle foreseen for crystals in B3 is too narrow for bigger size crystals as the endcaps. Due to this, since the installation at CERN RC of the automatic device ACCoCE 2 (the first one allowing fully automatic characterization of endcap crystals) many endcaps have been measured in classical bench B5 in order to establish the calibration factors for Light Yield measurements (as we shall see ACCOS devices measure relative LY values that must be corrected according to classical bench). That is why it is important to explain how this bench works, although we will be mainly focused on the differences respect to the other classical LY bench that was already described in detail (Bench 3). Deeper explanations on B5 working principles can be found elsewhere [32]. Also due to the few measurements performed in this bench we will not show stability plots of it.

The bench 5 can be used, as bench B3, in tagging or light yield mode although since this bench was installed at CERN RC it has been always used in light yield mode. Figure 4.14-a illustrates the basic set-up used in B5. As we can see it is very similar to the one used in B3: B5 also uses a water-cooled envelope which allows stable temperature during measurements (performed at 18°). A moving source-holder also scans the crystal vertically, including as well a small PMT and a tagging crystal collinear to the source (although they are only used for tagging mode, when the source is not ^{60}Co but ^{22}Na). However, B5 is not using a classical photomultiplier tube (PMT), but a hybrid photomultiplier tube (HPMT) also called hybrid photodiode (HPD). Besides, the whole setup is operated under computer control and automated to optimize performance and minimize operator time.

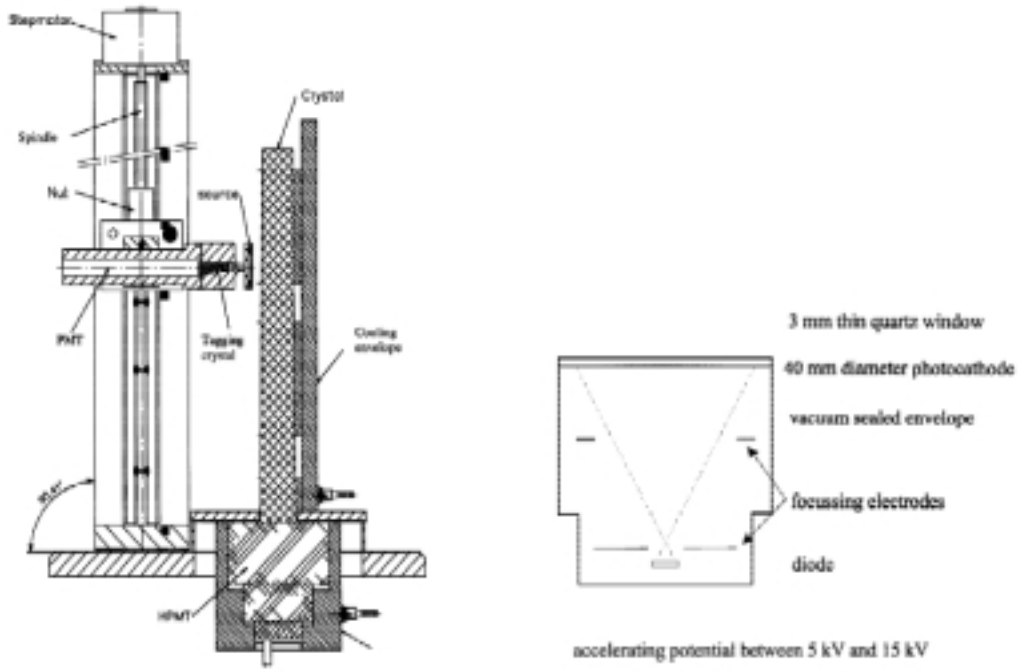

(a) B5 set-up

(b) Profile of B5 HPMT

Figure 4.14: *The set-up used in B5 and detail of its HPMT*

As stated above, the photodetector used in B5 for the detection of the light emitted by the PWO crystal is an HPMT. It has been manufactured by DEP [e] in collaboration with the authors of the paper [33] where the detailed working principles of an HPMT can be found, thus, only a brief description will be made here. In this HPMT, a high-resistivity silicon diode faces a photocathode in a vacuum tube (see figure 4.14-b). An appropriate electric field (15 kV) accelerates and focuses electrons produced at the photocathode onto the silicon diode, generating electron-hole pairs in a sufficient amount to be detected by proper electronics. The active surface of the HPMT is a 40 mm diameter area. The photocathode type is an UV-extended S-20 one, evaporated in a 3 mm thick quartz window. Such a photocathode allows for optimum quantum efficiencies in the UV-blue spectral region[f] and for optimum light collection efficiency, as the window is flat, thin and wide. The silicon diode is a 2 mm diameter one, and produces little electronic noise, shows an excellent single photoelectron resolution and resolves peaks with sequentially increasing numbers of photoelectrons up to ~ 20 photoelectrons.

[e] Delft Electronische Produkten, Roden, The Netherlands.

[f] According to producers, quantum efficiency is ~ 28 % at 300 nm and ~ 24% at 400 nm.

In B5, the crystals are placed in the same way as in B3: Vertically, with the big end of the crystal on the HPMT quartz window, whereas the small end remains on top. The optical contact between the crystals and the quartz window of the HPMT is made with the same optical coupling grease used for B3. All the crystals (barrel or endcaps) are scanned at 21 positions in B5, starting at 22 cm from the big end and finishing at 2 cm from it, moving in 1 cm steps.

The signals coming from the HPMT are first pre-amplified, then shaped and stored in a Multi Channel Buffer (MCB) which is directly computer controlled. A LabView program controls the source-holder stepping motor, the temperature of the cooling envelope and the High Voltage power supply needed to provide 15 kV to the HPMT. This program also calls an analysis routine after each step of the motor. This routine is in charge of starting acquisition, plotting the spectra acquired, and analyzing it in order to establish the light yield per position. This computer routine is named Maestro[g]. The LabView program stores the light yield value calculated by Maestro for each position and when the crystal has been scanned by the source for all the 21 positions, it creates a file with the relevant data and plots the uniformity curve of the crystal.

4.1.4 ACCoCE 1

Description of ACCoCE 1

The ACCoCE 1 machine is composed of a circular server presenting the crystals alternatively to a dimension-measuring machine and two optical benches either fixed or mounted on a linear movement bolted to a rectangular table (see ACCoCE 1 photograph and design in figure 4.15). The 110 cm diameter server for 20 crystals arranged radially is bolted on a turntable driven by a step by step motor yielding a crystal positioning precision of a few tenths of mm.

The position of the crystals is such that it allows all measurements with

[g]Maestro, EG&G Ortec.

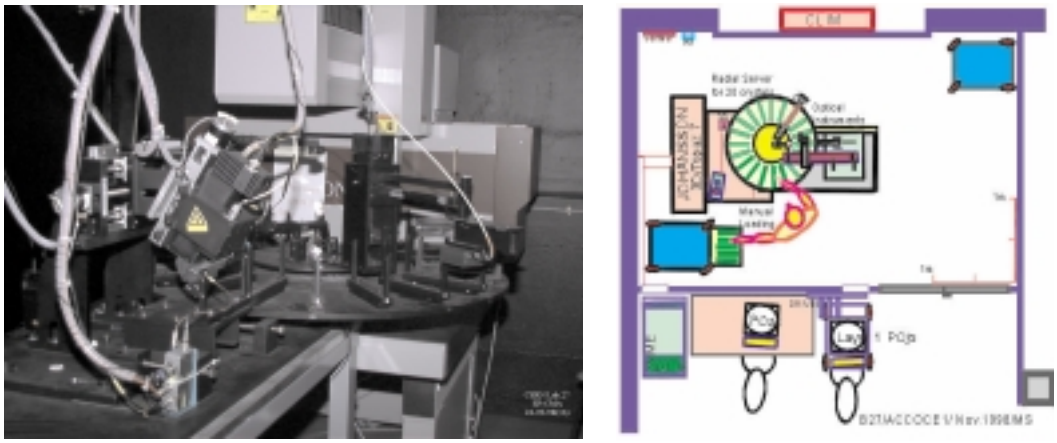

(a) Photograph of ACCoCE 1 (b) Design of ACCoCE 1

Figure 4.15: *Different aspects of the ACCoCE 1 machine*

minimum limitations. The crystals have their section tilted by 60° and are supported horizontally near their extremities by two thin vertical pillars. The small section of the crystals is always placed facing the center of the circular server and carries a label with a barcode. A fixed barcode reader identifies each crystal as it stops facing it during an initial turn of the server. Each crystal number is then associated to a position on the server in a look-up table.

The normal sequence of measurement is the following: first the crystals Dimensions are measured (measurement called 3D), then the Longitudinal Transmission (called LTO) followed by the Decay Time (or kinetics) and finally the Transversal Transmission (called TTO) are measured on each crystal. This sequence is fully automatic with continuous indication of the measurement being currently performed and online presentation of the measured spectra. For each crystal number, ACCoCE 1 communicates with the C.RI.S.T.A.L. system and its "Objectivity" database, in order to know what has to be measured next. The raw data acquired is transferred to the database together with some calculations on them that take place after each type of measurement. The present total time is about 7 hours for 20 crystals. As was mentioned in appendix A, one of these 20 crystals is a reference crystal which is never moved and allows studying ACCoCE 1 stability. This reference is the so-called "fixed" reference (see "References Protocol" in Appendix A). Another crystal of the 20 ones placed in a normal ACCoCE 1 run plays the role of "mobile" reference (in 19^{th} pillar). We will proceed to explain now the different measurements performed by ACCoCE 1:

- *Dimension measurement*:

A classical three-dimensional (3D) machine[h] is used to measure the dimensions of the crystals (see figure 4.16). This machine is capable to measure with a precision of ~ 5 μm per point and has an open geometry for easy crystal presentation by the circular server. Each crystal in turn is presented to the dimension measurement with end-faces vertical or nearly and side faces at 30 or 60 degrees from vertical. 15 points are measured on each lateral face of the crystal and 9 points on the 2 end faces, allowing precise reconstruction of the 6 planes. In order not to loose precision by probing slanting faces, the 2 mm diameter balls, ending the 5 stylets of the star-shaped probe (see figure 4.16), approach the crystal surface slowly and perpendicularly on the last millimeters. There is always a calibration on a reference ball ($\sim$ 30 mm diameter) allowing to redefine the origin of the coordinate system and to recalibrate the diameter of the probe balls for corrections. A set of 7 variables for Left and Right parity (mirror symmetry) determines the geometry of the crystal for each of the 17 different types of crystals (see section 3.5). The crystals are all and always placed in the same way: Face P is on the support pillars with the same orientation (at 60° from vertical, whether Left or Right).

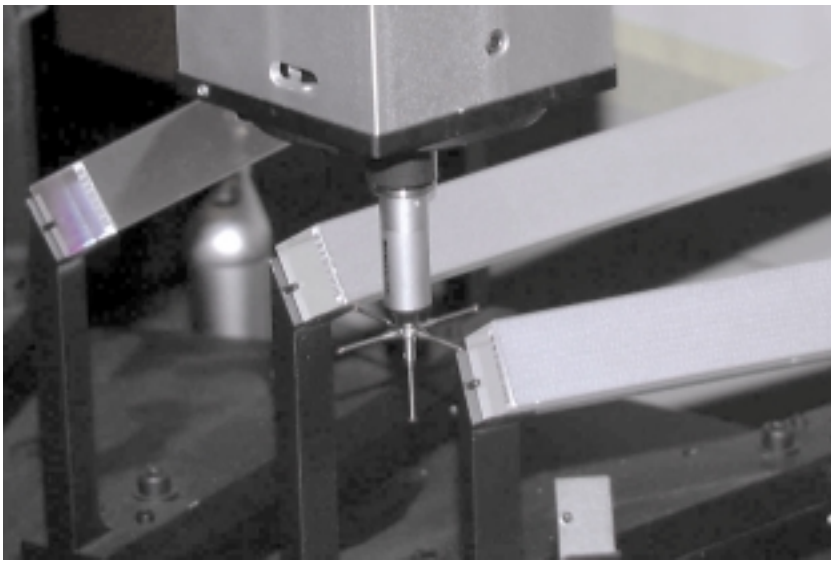

Figure 4.16: *Detail of the 3D machine installed in ACCoCE 1.*

The 3D machine only contacts the crystal faces at several points keeping track of their coordinates. Afterwards and after having applied some calculations, these points become angles, planarities, distances... etc. For each face

[h] Johansson Topaz 7, Eskilstuna, Sweden.

of a measured crystal, a plane is fitted to the measured points. The planarity of the face is defined as the distance between the 2 planes parallel to the fitted plane and passing by the points most distant from it, outside and inside. With these measured planes, 3 volumes can be defined: the average volume corresponding to the fitted planes, the outside volume (relevant for the insertion into alveolar structures) and the inside volume. The crystal corners are defined as an intersection of the three planes corresponding to the three related faces. The dimensions AF, BF, CF, AR, BR and CR are derived according to their definition (see figure 3.17).

For the length measurement, we have four values, defined as follows: first one is along the sideline perpendicular to the end faces (PW intersect). The 3 others are defined as the length between the 3 other small section corners and their projections on the large section, parallel to the PW intersect line. Four length values can also be defined for the outer and inner crystal volume. For fast comparisons or for physics, the average of the 4 length values can be taken.

- *Transmission measurements*:

The optical transmission part is composed by two compact spectrophotometers (7 x 8 x 22 cm^3) which measure the transmittance through the crystal length or width of a light beam produced by a 20 W halogen lamp. ACCoCE 1 performs transmission measurements only at eleven discrete wavelengths. These eleven wavelengths are defined by interference filters chosen for best determination of the band edge slope and of possible absorption bands. A large UV-extended pin photodiode (PD) [26] detects the transmitted light.

For Transversal Transmission Optics (TTO), the light beam always passes through the optically polished faces N and W (see face naming schema in figure 3.19) and the PD is located at $\sim$ 5 cm from the light emitting optics. The spectrophotometer makes eleven measurements every 2 cm, starting at 1.5 cm from the small end. It is fixed on a chariot mounted on a linear motorized support that moves along the crystal. The diameter of the light beam is adjusted to $\sim$ 10 mm. A calibration measurement with no crystal (100 % transmittance) is taken at an external position respect to it for each wavelength. It is used to be compared to the transmittance through the crystal: by calculating the ratio of both, we get the transmission of the crystal in percentual values for a given wavelength.

For Longitudinal Transmission Optics (LTO), the PD is located at $\sim$ 27 cm from the light emitting optics which was optimized for such a distance: quasi-parallel beam of $\sim$ 7 mm diameter entering the crystal and $\sim$ 9 mm exiting. This diameter provides adequate sensitivity to clouds of scatter points, sometimes present near the central axis of the crystal. The light beam is centered on the crystal when the system is stopped in its measuring place, and of course, the LTO optics and its PD are in fixed position while this measurement is being done. There is also a calibration measurement that is performed having the light beam at an intermediate position between two crystals (the circular crystal server turns half the distance needed to change from one crystal to the following), i.e. transmittance is 100 %. This calibration is made between the two crystal measurements. The aim of this calibration is the same than for TTO, explained above.

- *Decay Time, Light Yield and Non-Uniformity measurements*:

To measure Light Yield (LY), LY Non-Uniformity (NU) and LY decay time, a method which allows deriving the three parameters from a single time spectrum was chosen. One of the principal reasons for preferring to measure a scintillation decay time spectrum instead of a direct measurement of light yield, was the relatively low light yield of PWO crystals. It makes direct light yield measurement with a source and a photomultiplier quite difficult unless good optical contact is provided, which is rather unpractical for a fully automatic measuring device like ACCOS.

The measurements are made by a classical start-stop method and its scheme is depicted in figure 4.17. The start channel is made of a small BaF_2 crystal (20x20x20 mm^3) associated to a R5900U Hamamatsu photomultiplier (PM) and with a punctual ^{22}Na source with activity lower than 200 KBq. The stop channel is made with the same type of PM used for start channel. It measures the light output from the PWO crystal to which it is distant by $\sim$ 10 mm. Both channels are connected to an amplifier with gain 10. Signals are then sent to a constant fraction discriminator (CFD). After passing by the CFD, the signals are received on a Fast logic unit that provides a fixed delay (typically 250 ns) between start and stop signals. This allows an accurate determination of the mean background level. Time spectra are collected with a multi-hit TDC[i].

[i]Time to Digital Converter.

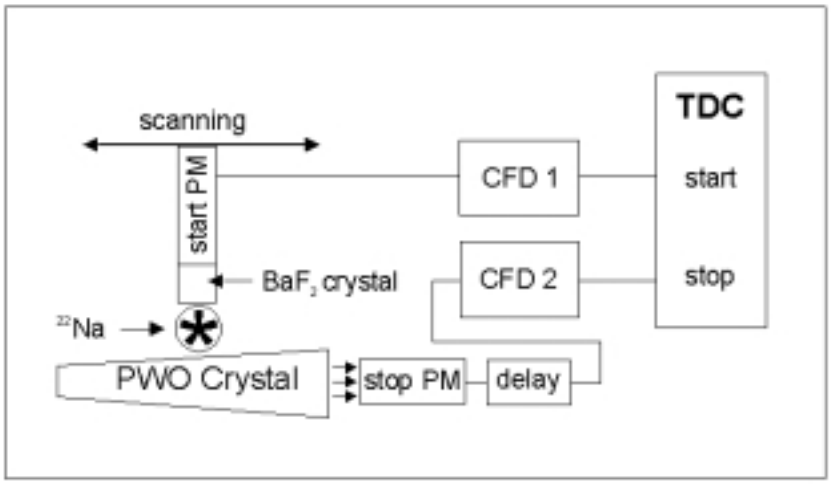

Figure 4.17: *Scheme of ACCoCE 1 kinetics setup.*

The time differences between the start and the stop signal produced by the two collinear gamma rays (from now onwards γ_1 and γ_2, both with energy 511 KeV) emitted by the ^{22}Na source are analyzed in the TDC. For the time spectrum shape and the LY measurement to be correct, the detected light of PWO must not be larger than a few tenths of photoelectrons per ^{22}Na event [29]. The BaF_2/Na/PWO geometry is very compact in order to maximize the γ solid angles and, thus, the rates. The start telescope, comprising PM with divider, small crystal and source, is moved along the PWO crystal on the same chariot as the TTO spectrophotometer from 1.5 cm up to 21.5 cm from small end, in 1 cm steps (i.e. 21 positions)

The light yield collected is derived from the Poissonian probabilities of detecting 0 photons in the stop channel during a time interval equal to full TDC scale [30]. Assuming that the average number of hits detected in the stop channel in those conditions is ε_T, then the probability of detecting 0 photons would be:

$$P(0, \varepsilon_T) = e^{-\varepsilon_T} \tag{4.13}$$

which is deduced from the general equation of the Poissonian probability of detecting m photons when the expected value is ε:

$$P(m, \varepsilon) = \frac{\varepsilon^m \cdot e^{-\varepsilon}}{m!} \tag{4.14}$$

This probability $P(0, \varepsilon_T)$ must equal the ratio between Empty events (start without stop events) and Total events (total number of start events). Therefore ε_T can be rewritten in terms of both parameters taking in account that the

value of suppressed background hits at the beginning of the TDC scale (δ) must be subtracted from the number of empty events:

$$\varepsilon_T = \ln\left(\frac{Total\ \ Events}{Empty\ \ Events - \delta}\right) \tag{4.15}$$

However, the total number of hits detected in the stop channel (ε_T) is composed of signal hits plus background. Therefore we can decompose ε_T like this: $\varepsilon_T = \varepsilon_S + \varepsilon_B$, where ε_S is the average number of signal hits, which is proportional to light yield and is the parameter we want to quantify and ε_B is the average number of background hits. Therefore the Light Yield measured by ACCoCE 1 using this method for a given position i (i= 1,...,21) can be expressed as [j]:

$$LY(npe/MeV)_i = K_i \cdot \left[\ln\left(\frac{Total\ \ Events}{Empty\ \ Events - \delta}\right) - \varepsilon_B\right] \tag{4.16}$$

where K_i is a factor that converts this average number of signal hits detected in the stop PM (ε_S) into Light Yield in number of photoelectrons per MeV of incident energy for a given position i. This set of factors is established by comparison to the classical LY bench B3 which has already been described. As this bench allows good optical coupling, the absolute number of photoelectrons per MeV for a given position can be precisely measured on it. In consequence, normalization of ACCoCE 1 raw Light Yield data to B3 data allows precise determination of K_i, also called Calibration Factors (CF_i). Comparisons to classical LY bench B3 will be illustrated in subsection 4.1.6.

Once the Light Yield per position is known, we can deduce the uniformity parameters Front and Rear NUF. The former is giving us the percentual variation of the Light Yield per radiation length (X_0) in the Front part of the crystal (the one corresponding to the small end of barrel crystals). Rear NUF has the same definition but corresponds to the rear part of the crystal (big end of barrel crystals). Further discussions about Front and Rear NUF can be found in subsection named "Description of B3", as well as their detailed definitions (series of equations 4.10 to 4.12).

Stability of ACCoCE 1 measurements

As mentioned above, ACCoCE 1 can measure several parameters related to dimensions, scintillation kinetics and light transmission. In consequence, and

[j] Detailed calculation methods for parameters δ and ε_B can be found elsewhere [30].

in order to illustrate the stability of this machine, we are going to show the reproducibility of the results when measuring the fixed and mobile references in ACCoCE 1 (see appendix A and table 9.1 for explanation of "references protocol").

• **Crystal Dimensions:** In order to show ACCoCE 1 dimensions measuring part (3D) stability we are going to focus on seven parameters that precisely determine the crystal geometry: L, AF, BF, CF, AR, BR and CR. It was already stated that from ACCoCE 1 3D measurements we can deduce much more information than these seven parameters, as for example, planarity of all faces, volumes, chamfers, etc. However, plotting all parameters distribution would make this section extremely long. Hence, only histograms of the seven mentioned parameters will be shown, together with the statistics used, mean values and standard deviation.

A steel standard (SSD) was manufactured to the dimensions of a Type 6 left crystal to a precision of ~ 10 μm. The SSD was measured three times on each one of the 19 pillars, i.e. 57 times being the SSD replaced and repositioned each time. The distributions of several Front and Rear dimensions (AF, AR, CF and CR) are shown in figure 4.18. As can be observed, the reproducibility of the results is very good, since the standard deviations indicated in the plots are within the range σ=1.0-1.3 μm. Besides, the comparison of these dimensions to Type 6 nominal values (3.5) show a good agreement within a 20μm margin [34].

In addition, we are going to illustrate as well the long term stability of ACCoCE 1 when measuring fixed reference 5649. So, figure 4.19 shows the histogram of 261 measurements on crystal 5649 of L parameter by ACCoCE 1. It is important to mention that four different measurements of L are performed with ACCoCE 1 3D machine (see "Dimension measurement" in ACCoCE 1 description) although it is the average of them what is typically taken for physics analysis. In figure 4.19, each event corresponds to the average of the four different L-estimations performed on each measurement. The results are quite interesting as we can see that using this L-average procedure, the reproducibility of the results when measuring crystal length is excellent (St.Dev. $\sim$ 1.5 μm).

Figure 4.20 depicts the distribution of parameters AF, BF, CF, AR, BR and CR (see definitions on figure 3.19) for 5649 on the same 261 measurements

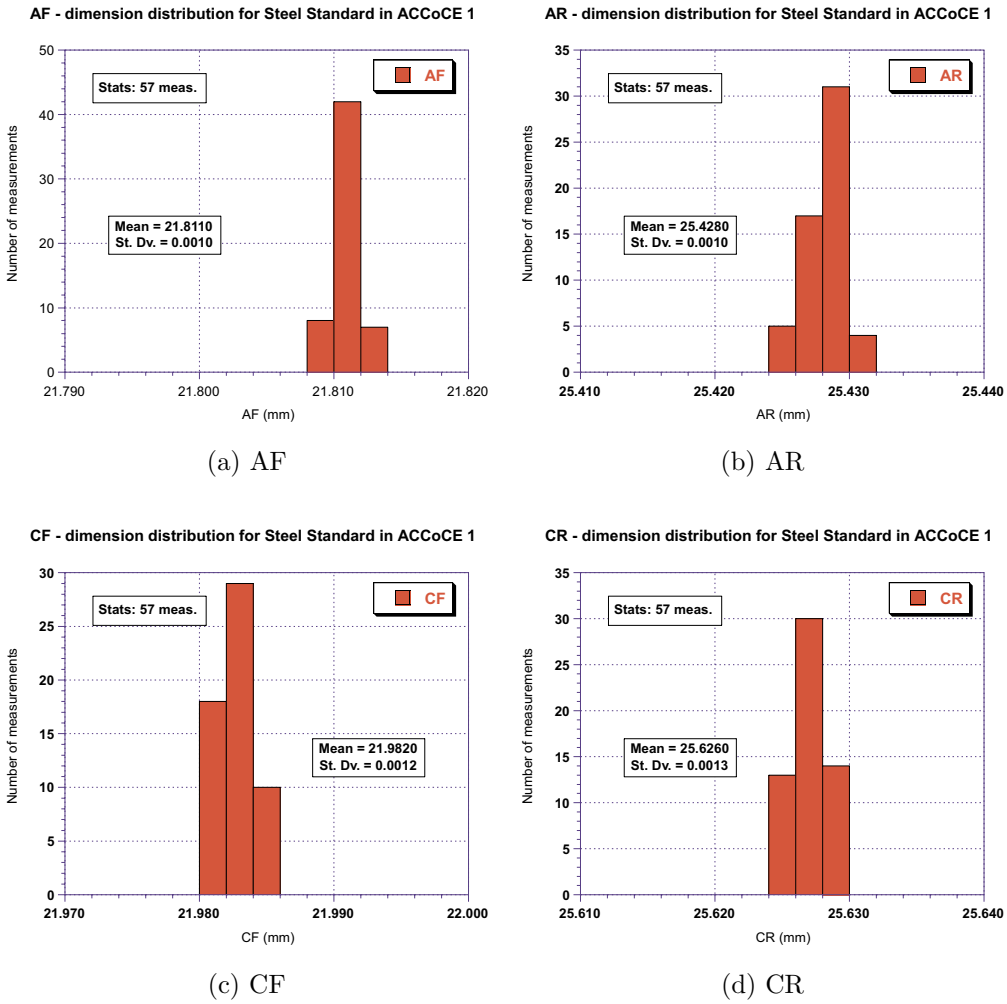

(a) AF (b) AR

(c) CF (d) CR

Figure 4.18: *Distribution of the 57 steel standard measurements for some Front and Rear dimensions.*

analyzed in previous plot for parameter L. It must be stated that ACCoCE 1 measures parameters BF and BR on faces P and D. In consequence, BF value on P (BFP) and BF value on D (BFD) are averaged for having one single BF value, which is the one plotted in the histogram. Similarly, BR value plotted is averaged from BRP and BRD. The results confirm the precision achieved for parameter L (St.Dev. is $\sim 1.5\ \mu m$) for the other six parameters. We can conclude that ACCoCE 1 3D measurements show an excellent reproducibility.

• **Transmission:** It has been already mentioned that ACCoCE 1 can perform two types of transmission measurements, which are longitudinal and transversal. In the former case, the measurement is performed only for one sin-

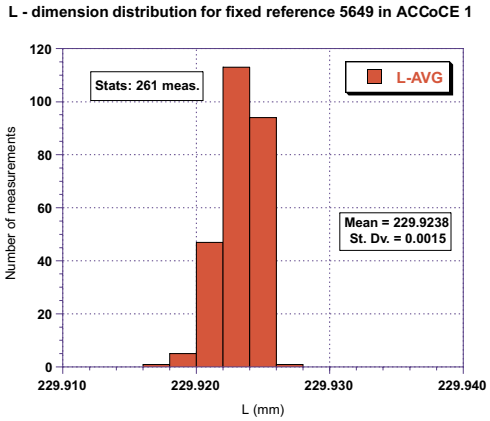

Figure 4.19: *Long-term stability of ACCoCE 1 when measuring L dimensional parameter for fixed reference 5649.*

gle position, whereas in the latter case, eleven positions are measured. For any of those measurements, eleven discrete wavelengths are analyzed. It would make this section too long if we show plots of stability of each one of the transversal positions, and for each one of the wavelengths used. Besides, when measuring through the whole length of the crystal (23 cm), a very slight change in the position of the crystal can produce much more changes in the measured transmittance than when we measure through just $2 \sim 3$ centimeters (transversal mode). This means that a good stability in longitudinal transmission ensures a better stability when measuring transversal transmittance, provided that both measuring systems are equal. In consequence, we will only show results on a crystal (fixed reference 5649) when it is measured in longitudinal transmission, and we will focus on the three wavelengths that must satisfy a minimum level (i.e. those wavelengths for which it exists an specification): 360, 420 and 620 nm.

Figure 4.21 shows the long-term stability of longitudinal light transmission at 360 nm (the behaviors found at 420 and 620 nm were very similar to this one) for crystal 5649. As we can see, results are very stable, since variations in transmission are within 2% for a period of a year.

We will also show the distributions of the measurements at 360, 420 and 620 nm in that stable period of time. They can be found in figure 4.22. In this plot we include statistics (234 measurements) and, as usual, mean value and standard deviation. Observing plots (b) and (c) in that figure, we see that the standard deviation of the ACCoCE 1 transmission system is ~ 0.12 % when dealing with high wavelengths (420 and 620 nm.). Such a precision is very

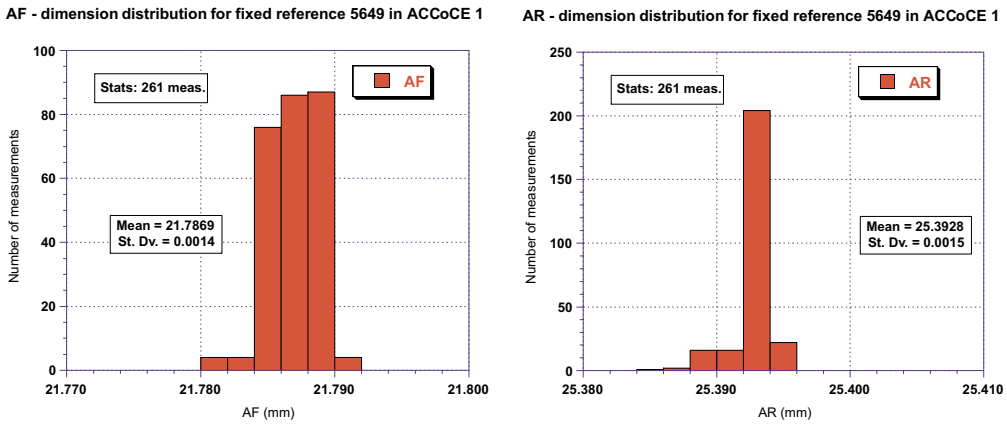

(a) AF (b) AR

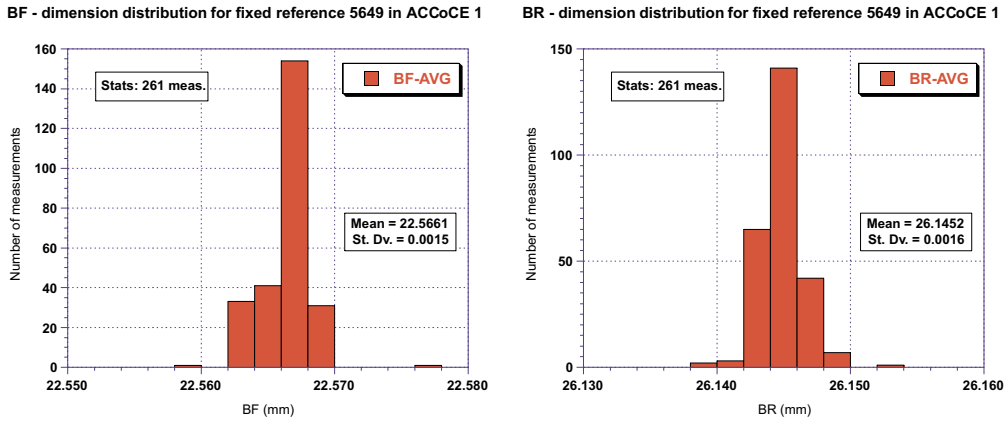

(c) BF (d) BR

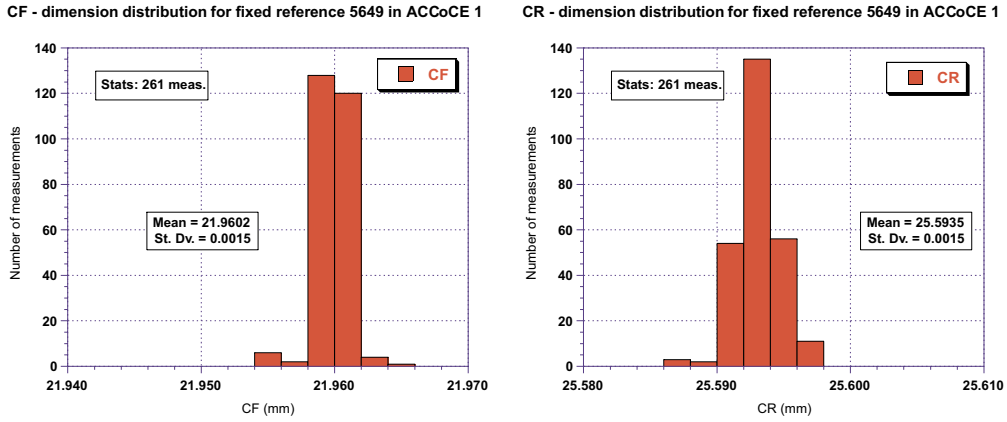

(e) CF (f) CR

Figure 4.20: *Long-term stability of ACCoCE 1 when measuring dimensional parameters other than L for fixed reference 5649*

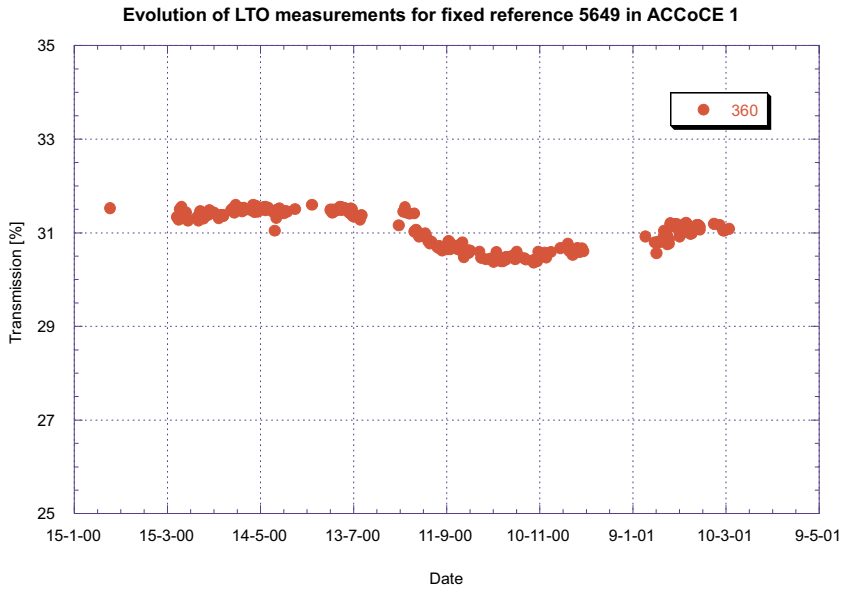

Figure 4.21: *Evolution with time of Longitudinal Transmission measurements at 360 nm for crystal 5649 in ACCoCE 1.*

good and reveals a good reproducibility of the system. However, if we observe histogram (a) in the same figure, we realize that the standard deviation of the 234 measurements at 360 nm. is more than a factor 3 higher: St. Dev. $\sim$ 0.40 %. The reason for this is the same given for the Spectrophotometer (where such a higher standard deviation at 360 nm was also observed): since a wavelength of 360 nm corresponds to the middle of the transmission band edge, the determination of the transmission at that point is much more sensitive to possible error sources.

• **Light Yield:** The crystals measured most often in ACCoCE 1 are the fixed reference 5649 and the two mobile ones: 5624 and 5654. Therefore, and in order to illustrate the stability of this device, we will show the statistical distributions of the parameters Light Yield, Front NUF and Rear NUF measured for those three crystals. These distributions correspond to a period of $\sim$ 1 working year (April 00 - April 01). Obviously, the three crystals have not been measured the same number of times during that period. Hence, statistics (number of events used in the histogram) are indicated together with the distribution mean value and standard deviation. The other important parameter that is deduced from kinetics measurements in ACCoCE 1 is the decay time. However, the decay time results of these crystals will not be shown, as they are very simple to summarize: the three are emitting 99% of light in 100 ns, as happens with all the other PWO crystals characterized in ACCoCE 1. In fact, no crystal rejection has been made up to now due to an emission of less

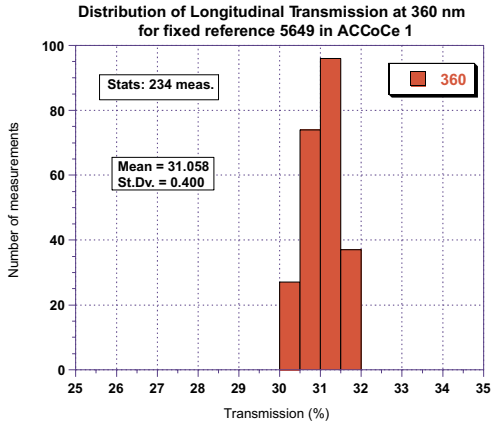

(a) Transmission at 360 nm

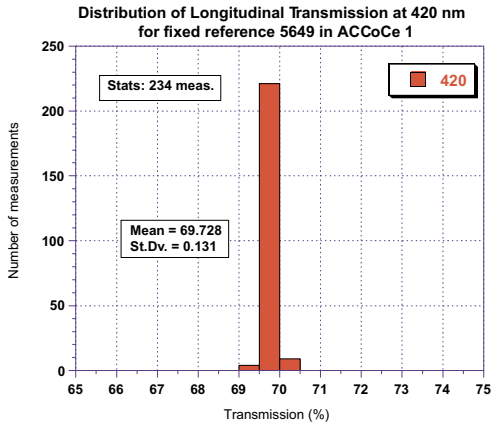

(b) Transmission at 420 nm

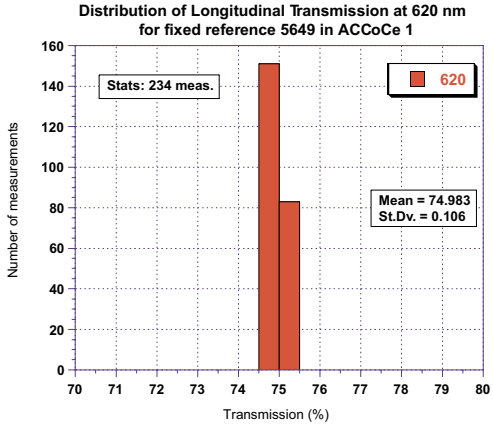

(c) Transmission at 620 nm

Figure 4.22: *Long-term stability of ACCoCE 1 when measuring longitudinal transmission of fixed reference crystal 5649*

than 90% of light in 100 ns (which is the existing specification, as shown in table 3.6).

Figure 4.23 shows all the light yield measurements performed for reference crystal 5649 in ACCoCE 1 from May 00 to March 01 (297 in total). As we can see there is a period of instabilities that lasts around two months (end of September 00 to beginning of December 00). It corresponds to a problem with ACCoCE 1 PMT that was solved after its replacement. Since that time, results were as stable as initially, as can be observed in that figure. The resulting stability histograms obtained for this crystal after removing data corresponding to unstable period from statistics are shown in figure 4.24.

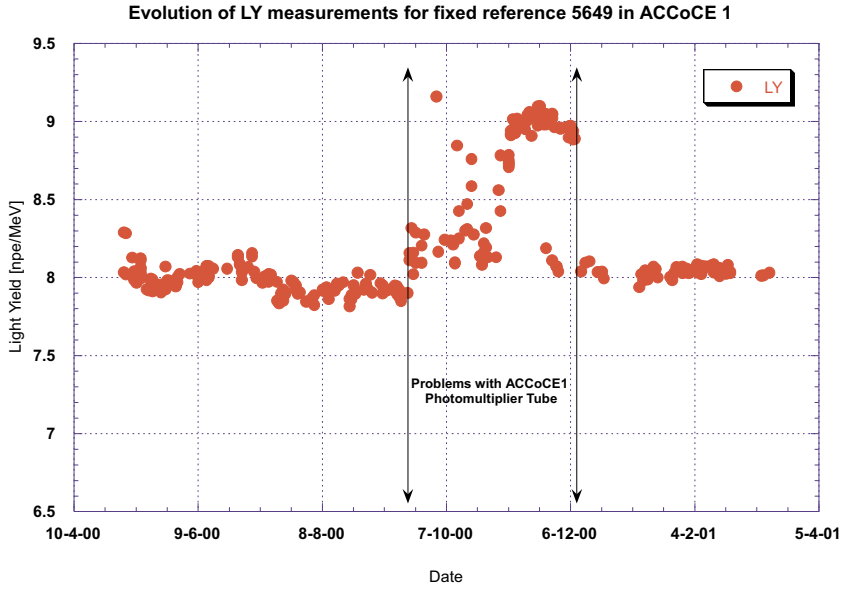

Figure 4.23: *Evolution with time of Light Yield measurements for crystal 5649 in ACCoCE 1.*

Figure 4.25 depicts obtained results (corresponding only to stable period) for mobile references 5624 and 5654. Observing histograms (b) and (c) from figure 4.24 and histograms (c), (d), (e), and (f) from figure 4.25 we can deduce that the average standard deviation of Fnuf and Rnuf is $\sim 0.11\ \frac{\%}{X_0}$. This is a good estimation of ACCoCE 1 precision when measuring uniformity parameters. Besides, it must be noticed that there is no difference between those deviations related to fixed reference (never moved from 1^{st} pillar) and the ones related to mobile references (replaced every week from 19^{th} pillar).

If we analyze Light Yield standard deviations in histograms (a) from figure 4.24 and (a) and (b) from figure 4.25, we will notice that fixed reference results have a better reproducibility (St.Dev. $\sim 0.08\ \frac{n_{pe}}{MeV}$) than mobile ones (St.Dev. $\sim 0.11\ \frac{n_{pe}}{MeV}$ for 5624 and St.Dev. $\sim 0.15\ \frac{n_{pe}}{MeV}$ for 5654). This is due to the logical human incapability of achieve an accurate repositioning of the crystals when placing them several times on the same pillar. A tenth of a millimeter difference in the position of the crystal respect to the PM can affect the Light Yield measured, and hence, a crystal that is never moved from its pillar will show more stable results with a narrower LY distribution. Indeed, the standard deviation calculated for LY measurements of mobile references is still quite good ($\sim 0.13\ \frac{n_{pe}}{MeV}$ in average) what is a very good precision for a Light Yield measuring device as ACCoCE 1. We can therefore conclude that when performing kinetics measurements, ACCoCE 1 behaves as a very stable device showing a very good reproducibility of results.

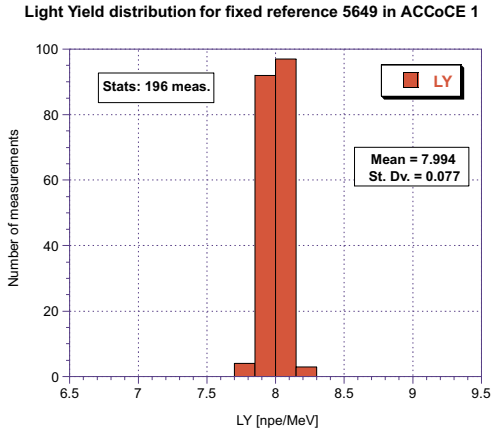

(a) Light Yield

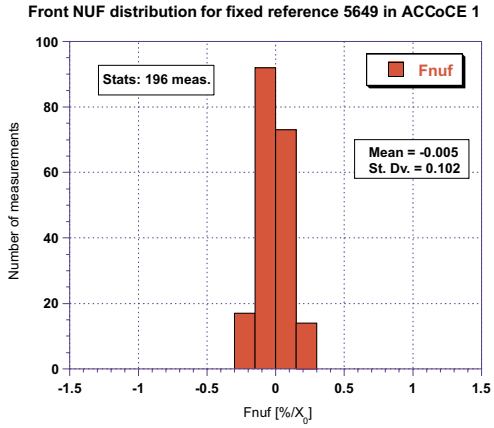

(b) Front Nuf

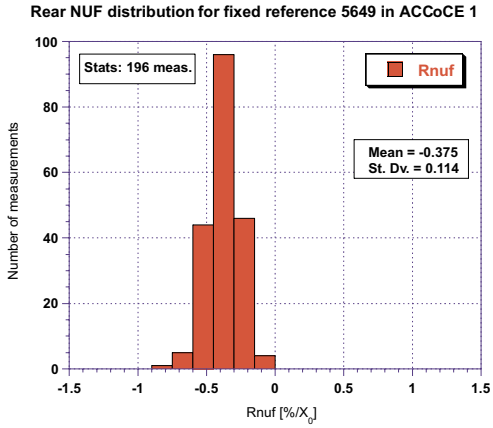

(c) Rear Nuf

Figure 4.24: *Long-term stability of ACCoCE 1 when measuring LY, Fnuf and Rnuf of fixed reference crystal 5649*

4.1.5 ACCoCE 2

Description of ACCoCE 2

The description of ACCoCE 2 will be very brief, as it is basically a duplicate of ACCoCE 1 device. All the measuring devices are similar: it exists an equivalent 3D machine to perform the same measurements than ACCoCE 1; then we also have the kinetics measurements performed exactly in the same way; finally we also measure longitudinal and transversal transmission with the

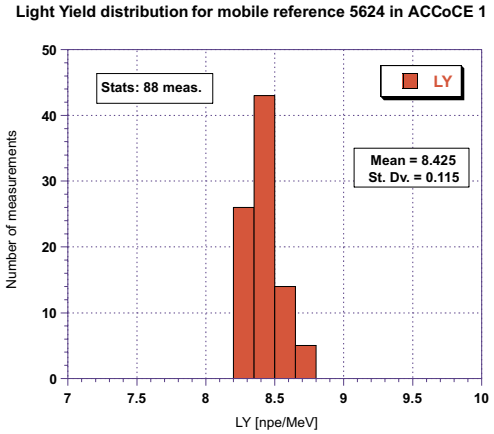

(a) 5624 - Light Yield

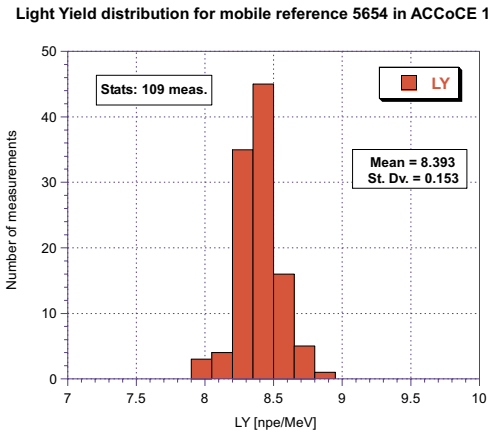

(b) 5654 - Light Yield

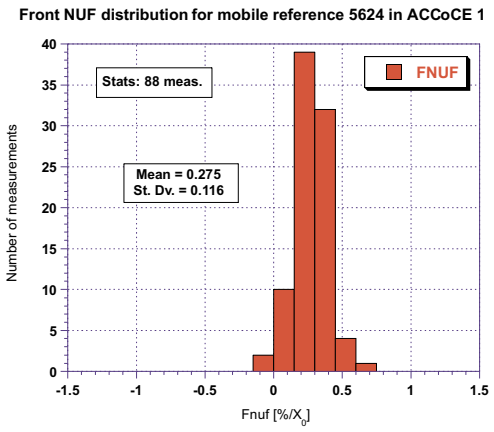

(c) 5624 - Front Nuf

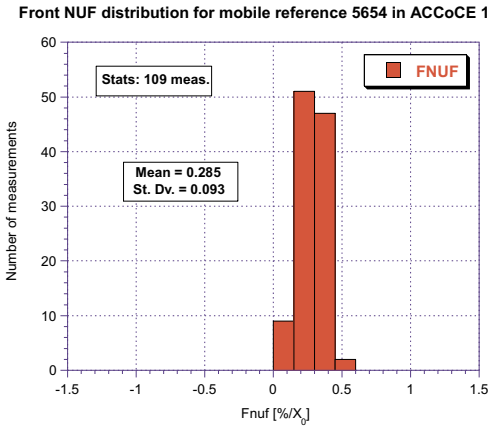

(d) 5654 - Front Nuf

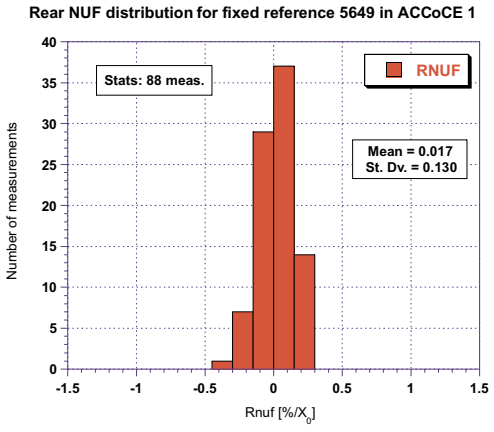

(e) 5624 - Rear Nuf

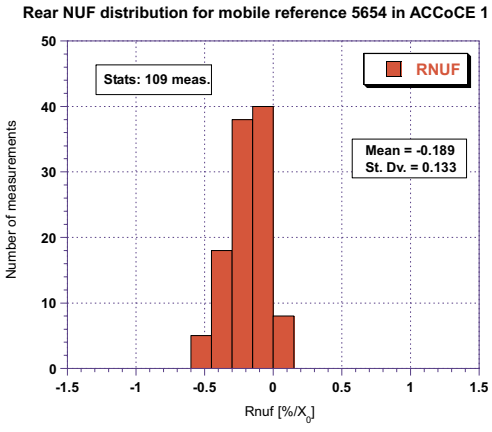

(f) 5654 - Rear Nuf

Figure 4.25: *Long-term stability of ACCoCE 1 when measuring LY, Fnuf and Rnuf of mobile references 5624 and 5654*

same equipment and techniques as ACCoCE 1. There are only two differences among them regarding the crystal server geometry and the measuring sequence used in each machine.

As described in previous subsection, the crystal server used in ACCoCE 1 was circular and was able to hold up to 20 crystals. However, in ACCoCE 2 we use a 6 petals flower-shaped server where the crystals are placed without touching them (see photograph in figure 4.26). This is achieved using specially conceived multifunctional boxes (called multiboxes) that are placed at the loading system (at the left, in the lower part of the photograph) after removing its cover. A pneumatic system allows putting up a set of pillars in order to hold the five crystals that were inside the multibox and also allows raising them up several centimeters to the measuring position. In this manner, up to 30 crystals can be loaded in ACCoCE 2 without placing them manually on the pillars, which was the case in ACCoCE 1. Besides, this petal-shaped server allows dedicating some petals to endcap crystal measurements, just by using special pillars. As mentioned before, ACCoCE 1 does not allow to measure these bigger size crystals. This different server geometry implies several mechanical differences respect to ACCoCE 1 that will not be described in detail, as the working principle of both machines remains unchanged.

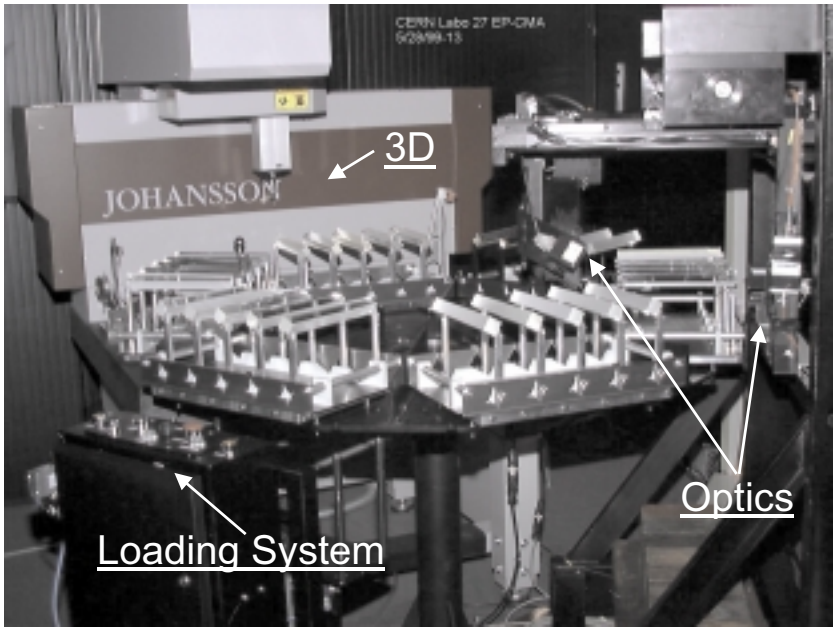

Figure 4.26: *Photograph of ACCoCE 2 machine.*

As was stated when describing ACCoCE 1, the normal sequence of measurements performed with that device was the following: first 3D measurement,

then the Longitudinal Transmission followed by the Decay Time (or kinetics) and finally the Transversal Transmission was measured on each crystal. However, ACCoCE 2 does not use the same sequence as it allows simultaneous measurements of 3D and kinetics: while a crystal is being characterized with the 3D Johansson machine, the decay time spectra of another crystal is being acquired in another petal of the server. The aim of this is to reduce the time needed for a single run, as if the ACCoCE 1 sequence were used for ACCoCE 2, each run would last around 10 hours (as we measure 30 crystals instead of 20), what would forbid the foreseen two runs per day schedule. Thanks to this simultaneity a single ACCoCE 2 run lasts not more than 7 hours, as is the case in ACCoCE 1.

All data acquired by ACCoCE 2 are registered into C.R.I.S.T.A.L. database exactly in the same way as it was done for ACCoCE 1. Measurements are labeled according to the machines used for performing it. This allows to easily recognize which crystal measurements were performed into ACCoCE 1 and which ones into ACCoCE 2.

As occurs with ACCoCE 1, special attention must be paid to Light Yield measurements. These measurements are performed using the same principles described for ACCoCE 1, therefore all LY measurements must be compared to a classical bench to precisely determine the calibration factors present in equation 4.16. Comparison between ACCoCE 2 and the classical LY benches will be illustrated in subsection 4.1.6.

Stability of ACCoCE 2 measurements

It has already been mentioned at the beginning of this section that ACCoCE 2 use at CERN RC was started in summer 2000. At the beginning of this period, many adjusts and tunings were performed on it, and hence, we did not start reliable characterizations of PWO barrel or endcap crystals with ACCoCE 2 until some months later. That is why the histograms that will be shown in order to illustrate ACCoCE 2 stability will show poorer statistics than in the case of ACCoCE 1 (in use since 1998).

Indeed, since ACCoCE 2 situation was acceptable, some reference crystals

were placed on the petals in order to have long term statistics of its stability. These reference crystals are endcap crystals with engraved number 359 (barcode 30399000000359) and 367 (barcode 30399000000367). We will show here statistics corresponding to measurements performed for those two crystals in ACCoCE 2.

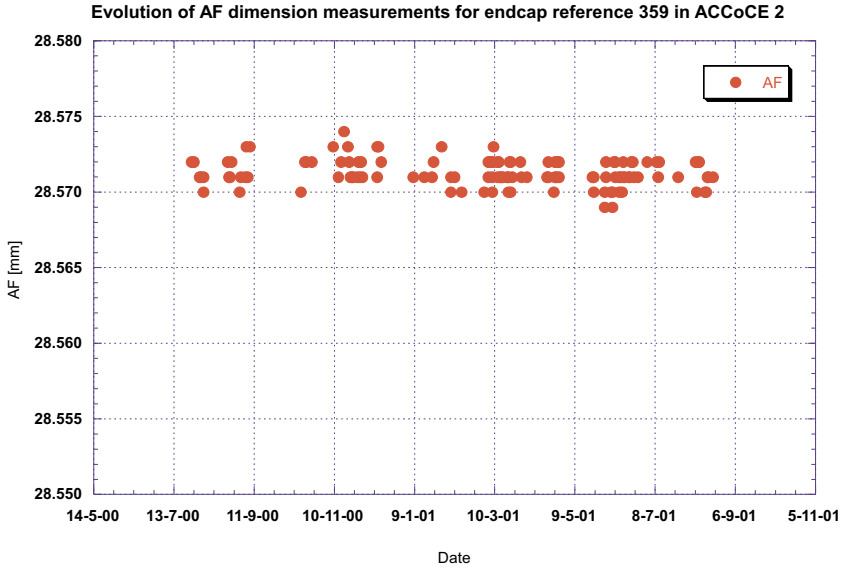

Figure 4.27: *Evolution with time of dimensional parameter AF for crystal 359 in ACCoCE 2.*

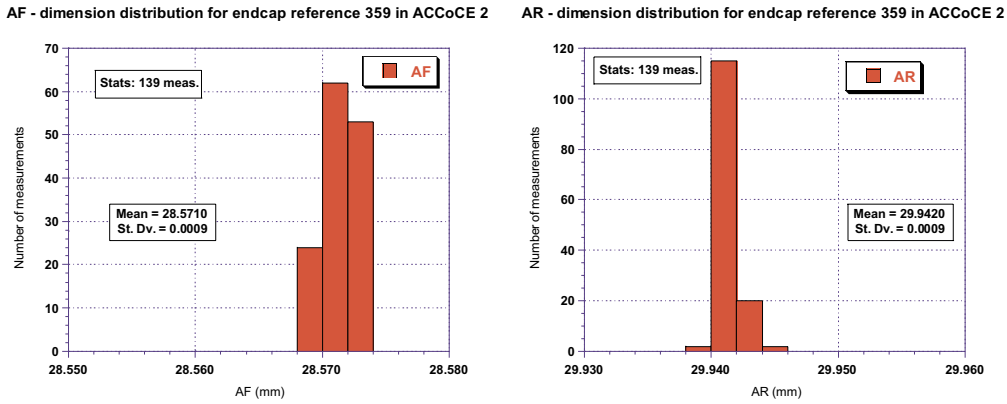

(a) AF (b) AR

Figure 4.28: *Long-term stability of ACCoCE 2 when measuring dimensional parameters AF and AR of endcap references 359*

• **Crystal Dimensions:** Stability of dimensional parameter AF as measured in ACCoCE 2 is illustrated in figure 4.27. As we can see, along a period

of $\sim$ 1 year the fluctuations in the measurement of parameter AF for reference 359 are within the 5μm range. Similar behaviors are obtained for the other dimensional parameters (L, BF, CF, AR, BR and CR). Since ACCoCE 2 was very stable within the analyzed period of time, we can construct the corresponding dimensional parameters distributions. However, as the 3D machine in charge of performing 3D measurements in ACCoCE 2 is exactly equal to the one used in ACCoCE 1[k], and its long-term stability has been already illustrated (see figures 4.19 and 4.20 and corresponding discussion) we will not present here histograms of the seven parameters, but only two: AF and AR (see figure 4.28). As we can notice in these histograms, the standard deviations calculated for ACCoCE 2 are of the same order than the ones shown for ACCoCE 1 (typically $\sim$ 1μm).

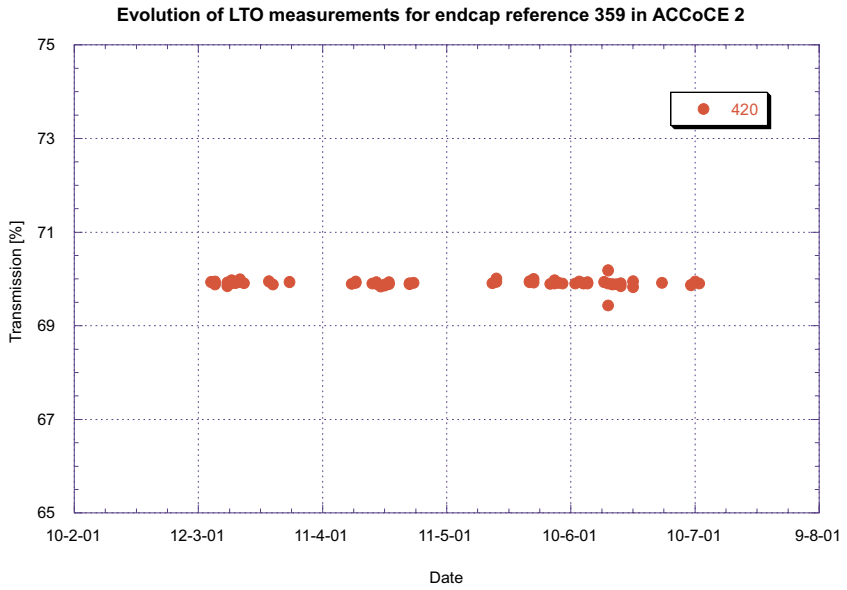

Figure 4.29: *Evolution with time of Longitudinal Light Transmission measurements at 420 nm for crystal 359 in ACCoCE 2.*

• **Transmission:** Figure 4.29 shows the results obtained with ACCoCE 2 for crystal 359 when measuring longitudinal transmission at 420 nm along a period of five months. Such a shorter period of time respect to the one considered for plot shown above for parameter AF (figure 4.27) is due to instabilities present in ACCoCE 2 spectrophotometer during its first operational months. In the stable period of time to which figure 4.29 corresponds, the measurements show small deviations, and as this also happens with the other specified wavelengths, we can construct their corresponding histograms. They are shown in figure 4.30. This figure depicts longitudinal transmission at the wavelengths which have an specification (360, 420 and 620 nm) for endcap

[k]Johansson Topaz 7, Eskilstuna, Sweden.

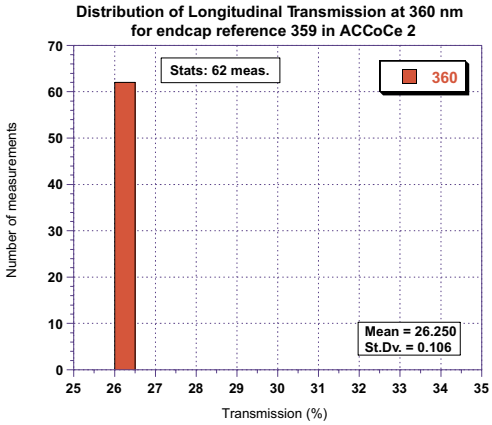

(a) 359 - LT at 360 nm

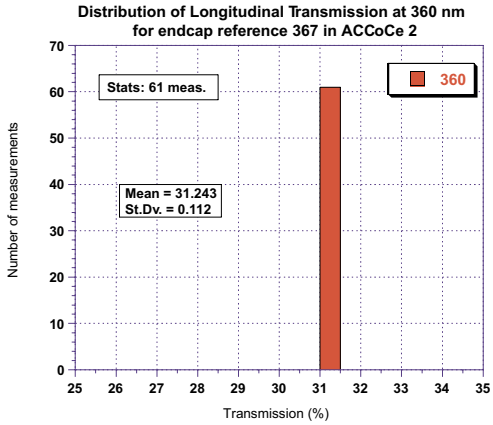

(b) 367 - LT at 360 nm

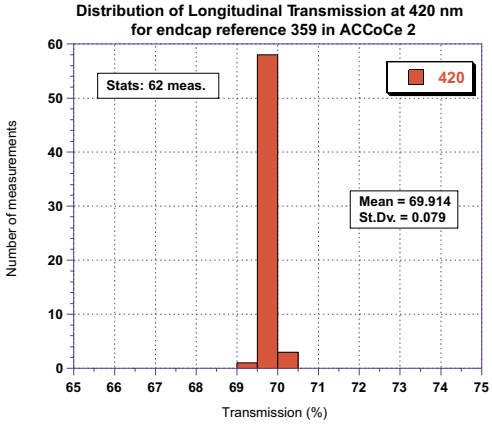

(c) 359 - LT at 420 nm

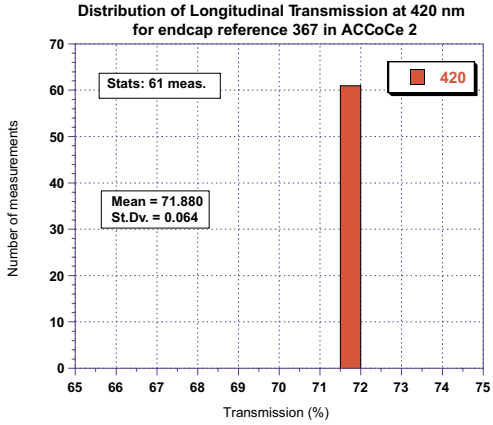

(d) 367 - LT at 420 nm

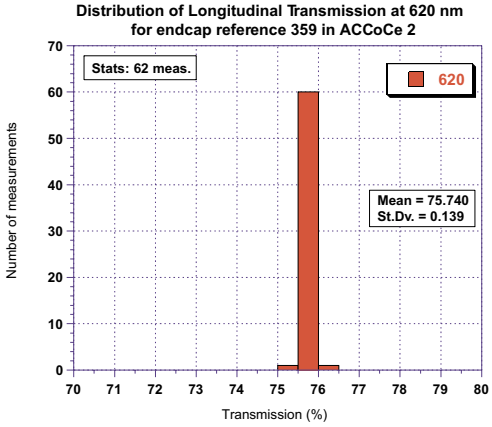

(e) 359 - LT at 620 nm

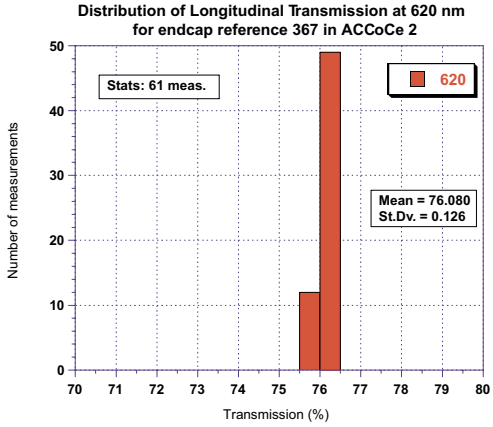

(f) 367 - LT at 620 nm

Figure 4.30: *Long-term stability of ACCoCE 2 when measuring longitudinal transmission of endcap references 359 and 367*

reference 359 (histograms a, c and e respectively in the figure) and for endcap reference 367 (b, d and f). Analyzing the dispersions found in the six depicted histograms we see that its average value is ~ 0.10 %. The most remarkable thing is that in ACCoCE 1 histogram of Longitudinal Transmission at 360 nm for reference 5649 we had a dispersion much higher (0.4 %, see histogram (a) in figure 4.22) which was justified according to the higher sensitivity of transmission to tiny wavelength changes in the band edge range compared to higher wavelengths ranges. However, in this case transmission of both crystals behaves normally at 360 nm. This is probably due to the better repositioning of crystals achieved with ACCoCE 2 automatic loading system.

• **Light Yield:** Figure 4.31 depicts Light Yield, Fnuf and Rnuf for endcaps 359 (histograms a, c and e respectively in the figure) and 367 (b, d and f). Observing them we can see that the average standard deviation for both crystals when measuring uniformities (Fnuf and Rnuf) is very similar to the one obtained in ACCoCE 1: St.Dev. $\sim 0.10\ \frac{\%}{X_0}$ ($\sim 0.11\ \frac{\%}{X_0}$ for ACCoCE 1). Regarding the Light Yield we can see that the average deviation is $\sim 0.11\ \frac{n_{pe}}{MeV}$ whereas for ACCoCE 1 we were finding ~ 0.08 (fixed reference) and ~ 0.13 (mobile ones). These low dispersions allow to conclude that ACCoCE 2 performs stable LY, Fnuf and Rnuf measurements in a long term scale. Consistency between ACCoCE 1 and ACCoCE 2 dispersions means that the kinetic characterization of PWO crystals in both devices is equally trustable.

4.1.6 Calibration of ACCOS devices with classical benches data

The calibration of ACCOS devices with classical benches data is only performed for those parameters needing it, namely: LY, Fnuf and Rnuf. However, as specifications related to transmission in PWO crystals were initially established on the basis of spectrophotometer measurements, it is quite interesting to show the correlations between the light transmission data obtained in ACCOS devices and the measurements of the same parameters performed on classical spectrophotometer. In consequence, we will divide this section in two parts. In the former we will describe the calibrations of ACCOS LY measurements, which are performed using classical LY benches data and in the second we will show data correlations between transmission measurements performed in ACCOS devices and the classical spectrophotometer.

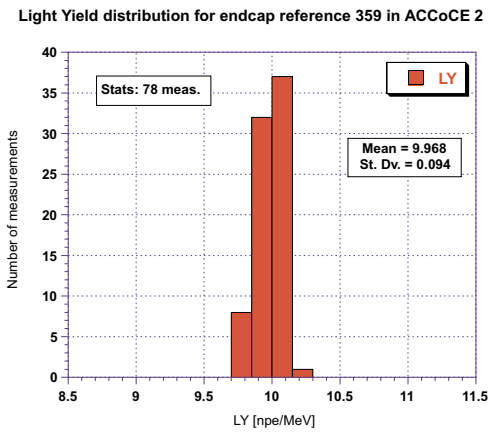

(a) 359 - Light Yield

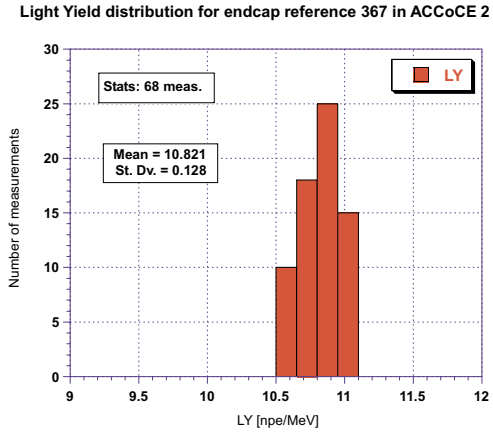

(b) 367 - Light Yield

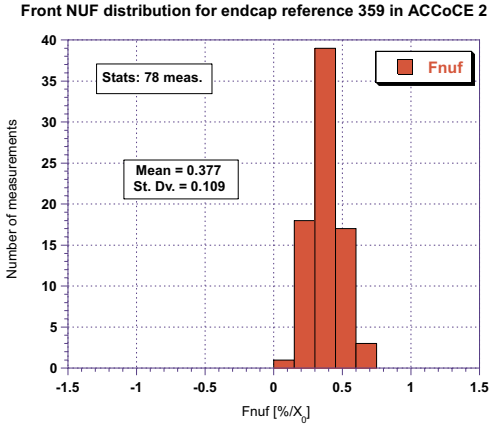

(c) 359 - Front Nuf

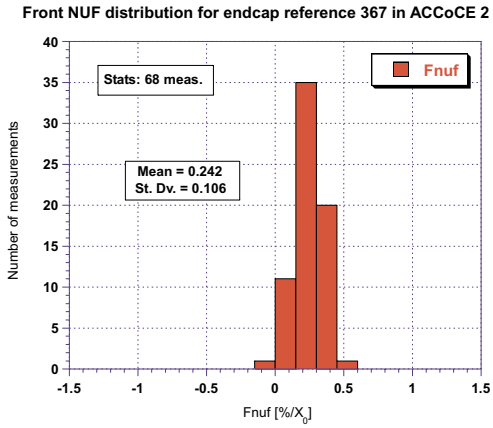

(d) 367 - Front Nuf

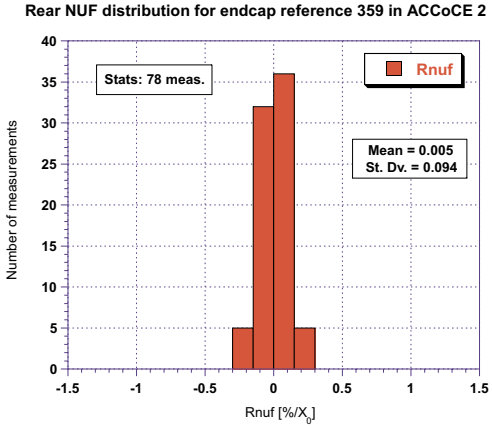

(e) 359 - Rear Nuf

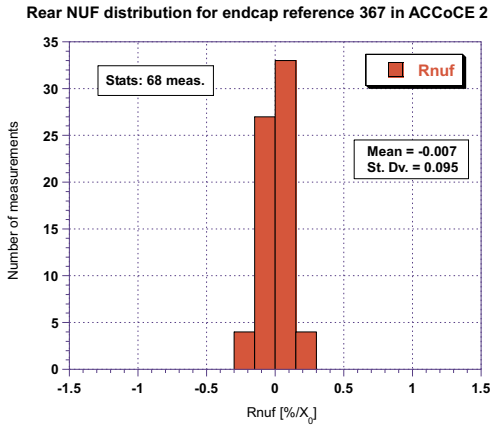

(f) 367 - Rear Nuf

Figure 4.31: *Long-term stability of ACCoCE 2 when measuring LY, Fnuf and Rnuf of endcap references 359 and 367*

Calibration of LY measurements in ACCOS devices:

As mentioned above, ACCOS devices (1 and 2) are measuring relative Light Yield values at 21 different positions. These values must be corrected according to classical benches in order to have a properly calibrated device. The set of values that correct ACCOS devices raw data are called Calibration Factors (CF), as stated previously.

We have already discussed about the special configuration of ACCOS devices regarding the kinetics measurements: the naked PWO crystal is placed at $\approx$ 1 cm from the PM. And we have also discussed about B3 method for measuring Light Yield: the crystal is wrapped in a tyvek envelope, and the optical contact between crystal and PM is made with an special optical grease. The Calibration Factors must allow to get rid of all the differences between both devices:

a) An important aspect to be taken into account is *crystal geometry*: it is obvious that the existing different crystal barrel geometries will play a role, as for example the face through which light is extracted and detected in ACCOS devices has a different size for each crystal type. Therefore, the set of CF needed for a set of Type 1 crystals will not be necessarily the same needed in case the set would correspond to Type 17. Hence, we would theoretically need a special set of CF for each crystal type (17).

b) Of course, as each ACCOS device has its own PM to detect light, their quantum efficiency are not the same and also, the distances between crystal and PM are not exactly equal, therefore we would also need two different set of CF for measuring the same crystal in each one of *ACCOS devices*: ACCoCE 1 or 2.

c) Another aspect that plays an important role is that, as barrel crystals have a depolished face, the light lost through that face behaves very differently in B3 (light is reflected by the tyvek wrapping) and ACCOS devices (light is lost since crystal is naked), therefore, depending on how depolished that face is, the CF will have to be different in order to correct for those situations. In this manner, two crystals that have received different *treatments* will need different sets of CF. Thus, when crystals are uniformized at CERN RC, a special set of CF different to the initial ones (CF corresponding to the roughness provided

by producer) must be established.

As we have seen, we would need different CF for each one of the different 17 crystal types, and for each given type we would also need different CF according to the machine used (ACCoCE 1 or 2) and also according to the different treatment applied to the depolished face. This makes ACCOS calibration a quite complicated task. However we have tried to simplify a little bit this task:

- Crystals are delivered and received in batches of several hundreds of crystals, which use to be grouped in similar crystal types. Therefore we have re-grouped the 17 different geometries in six groups. Natural delivery distinction between Batch 9 (Types 1-4), Batch 10 (Types 5-7), Batch 11 (Types 7-9), Batch 12 (Types 10-12), Batch 13 (Types 13-15) and Batch 14 (Types 16-17) has been used for this purpose. A set of CF per each one of these batches has been established following the procedure explained below.
- As we want to know the calibration of all these crystal batches in both machines, we have calculated a set of Intercalibration Factors (IF^i, for i=1 to 21) between ACCoCE 1 and ACCoCE 2, that for example, allows us to have an initial estimation of which will be the CF for a Type 6 crystal (Batch 10 CF) in ACCoCE 2 once ACCoCE 1 set of CF for this batch are known ($CF^i{}_{ACCoCE2}$=$IF^i \times CF^i{}_{ACCoCE1}$).
- For all those crystals needing to be treated at CERN RC in order to achieve an uniform light collection a special set of CF must be calculated. Usually the new set of CF for CERN RC treated crystals does not differ too much from the initial set of CF established for crystals with Face D depolished by the producer. In fact commonly it only changes slightly the final LY measured and not shape of the applied correction (e.g. CF-Treated-Type6^i = $K \times$ CF-Type6^i, being K a constant). This K use to be $\gtrsim 1$ % for crystals which are depolished[1] (roughness increased respect to initial value) and $\lesssim 1$ % for crystals polished (roughness decreased).

The procedure to establish the CF for a given batch will be illustrated with an example: the calibration of Batch 14, which was measured in ACCoCE 2. It must be stated that the same method is applied when we want to establish a set of CF for a batch of crystals measured in ACCoCE 1.

[1]See Uniformization Method in chapter 5.

The first thing to do is just to take a set of crystals (typically ~ 15) of the uncalibrated batch 14 (in this case). Then, we have to measure them in the classical bench B3 (unless they are endcaps, as in that case they must be measured in B5). Later we compare the results to ACCOS data. In order to illustrate how different the results between the benches are initially we have included figure 4.32, which corresponds to Batch 14. It must be stated that in this figure, ACCoCE 2 raw LY data were corrected with the standard set of CF (the one set as default in C.R.I.S.T.A.L. database).

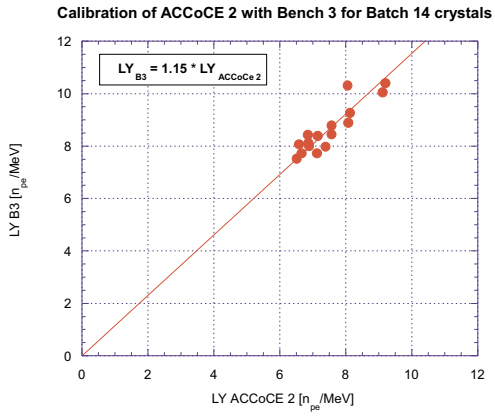

(a) Light Yield

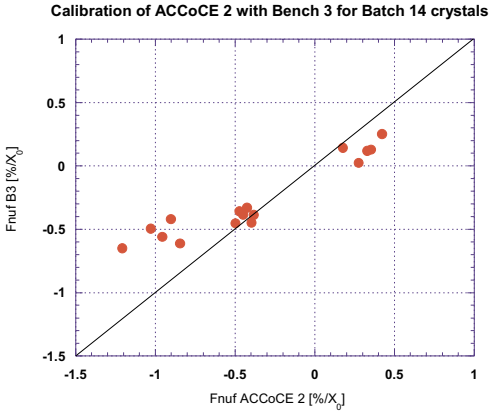

(b) Front NUF

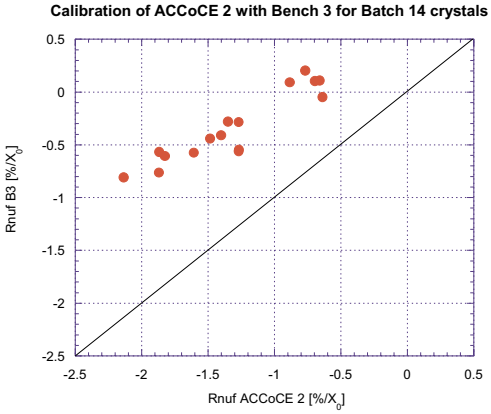

(c) Rear NUF

Figure 4.32: *Comparison of initial ACCoCE 2 data (using standard set of Calibration Factors) and B3 data for Batch 14 crystals*

As we can see in figure 4.32, the LY data measured in ACCoCE 2 is 15 % lower than B3 data for the same set of crystals, therefore it must be corrected. Front NUF is behaving acceptably well for the two clouds of data corresponding to very positive and intermediate Fnuf values. However, too

negative Fnuf are not well correlated (ACCoCE 2 exaggerates Fnuf values measured by B3). Another important disagreement is also seen for Rear NUF, where all ACCoCE 2 data are shifted by $\sim$ -0.8 $\frac{\%}{X_0}$.

Then, what we must do is to compare the Light Yield measured in B3 and ACCoCE 2 (in this case) position by position, trying to establish the ratio among both machines for each one of the 21 different positions where the Light Yield is measured. Then, this ratio is applied to the standard set of CF used for ACCoCE 2 data, so that it accounts now for the differences observed between the measurements performed in both machines. The product of this ratio per position and the standard set of CF yields the resulting new set of CF for this batch. An example of how Batch 14 measurements in ACCoCE 2 are correlated to B3 after correcting them with the new CF established in this manner is showed in plots (a), (b) and (c) of figure 4.33.

Looking at figure 4.33 we can see that LY and Rear NUF (plots (a) and (c)) are in a good agreement when using the new set of CF. However, in the case of too negative Front NUF values (b) we still observe a deviation from the diagonal which is not present for too positive and close to zero values. In order to correct that we modify the CF so that values are projected on the diagonal. The resulting values are depicted in plot (d) and as we can see, the agreement between B3 and ACCoCE 2 data is now excellent.

We usually apply these set of CF to the measurements performed for all the crystals of that given batch and later we randomly pick a small set of crystals to verify the calculated set of CF. Of course, an agreement between B3 and ACCoCE 2 data is expected but it will be probably not as good as the one shown in figure 4.33 as these data are the ones used to perform the calibration. In spite of that, the results are excellent as depicted in figure 4.34. This figure plots the results of all the verifications performed since batch 8, including the verification for batch 14 discussed above. The correlations B3 - ACCoCE 1 or 2 for Light Yield, Front NUF and Rear NUF are shown in plots (a), (c) and (e) respectively, whereas the ratio between Light Yield values, and the differences between Front and Rear NUF measured with both devices are depicted in figures (b), (d) and (f). Data corresponding to Batches 8, 9, 11, 12 and P1 refers to verifications between ACCoCE 1 and B3 whereas batches 14 and P2 data refers to ACCoCE 2 - B3 verifications.

Another aspect that can illustrate how good the calibrations of ACCOS

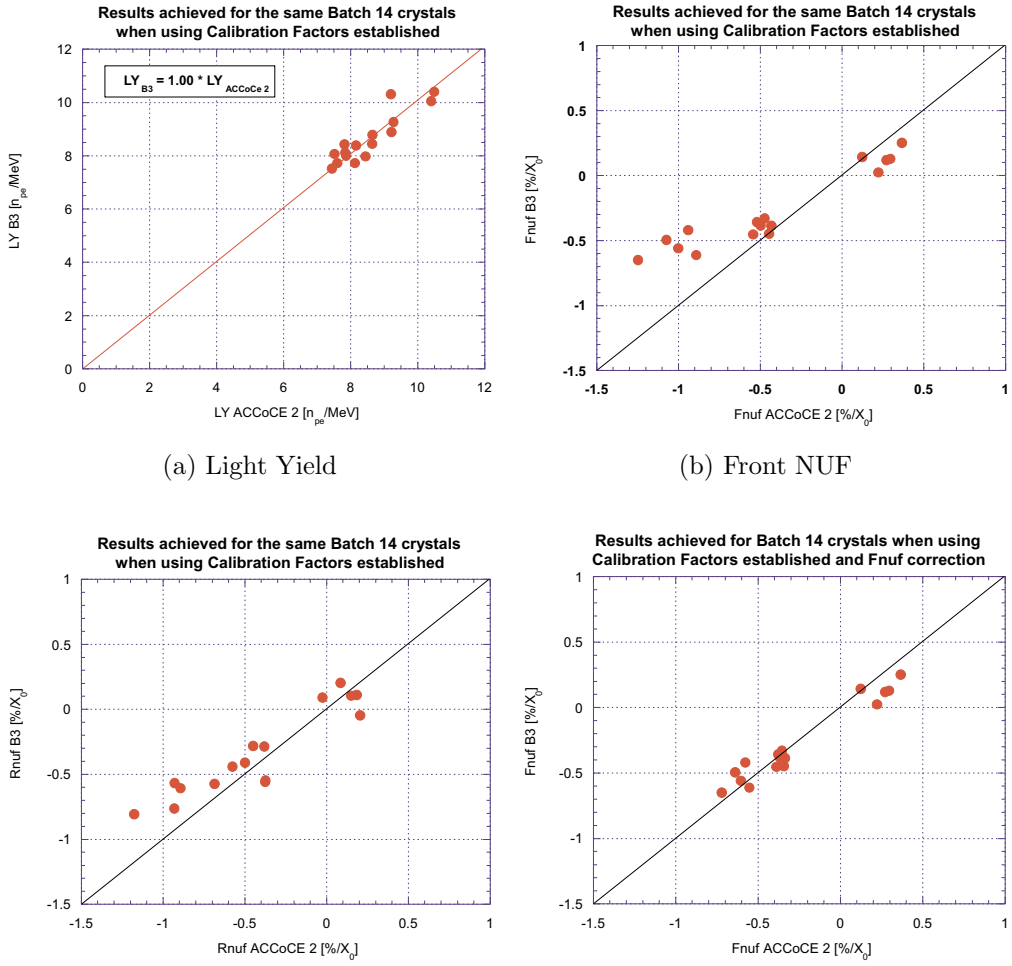

(a) Light Yield

(b) Front NUF

(c) Rear NUF

(d) Front NUF Corrected

Figure 4.33: *Comparison of ACCoCE 2 data after calculation of new set of Calibration Factors and B3 data for Batch 14 crystals*

devices are is to compare the measurements performed for mobile references crystals (5624 and 5654) to classical bench data. All these reference crystals belong to the same batch, therefore, the same set of CF is used for them all. Hence, by comparing the Light Yield values for both crystals we can have an idea of how good this CF calculation procedure is. Let us recall figures 4.25 and 4.12 with this purpose. With the LY data extracted from them we can build table 4.2.

Taking in account the precision of each measuring device (which can be deduced from standard deviations quoted in table 4.2) we can see that

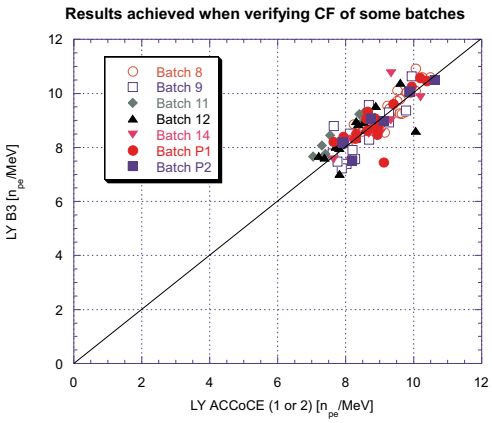

(a) Light Yield

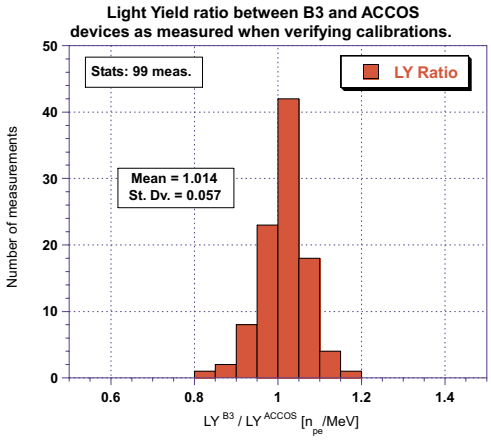

(b) Light Yield Ratio

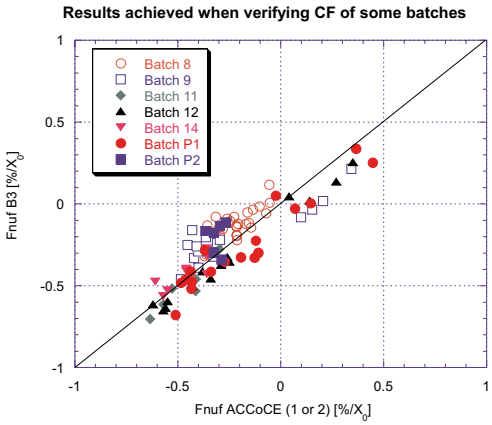

(c) Front NUF

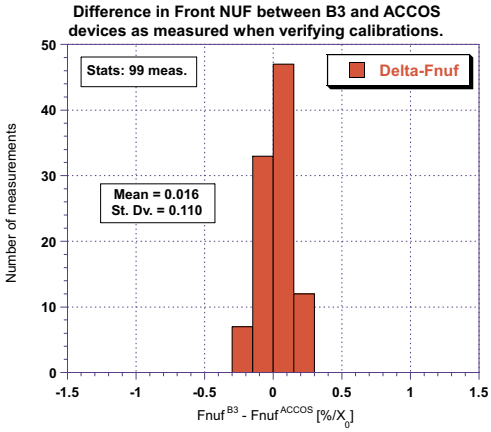

(d) Δ Front NUF

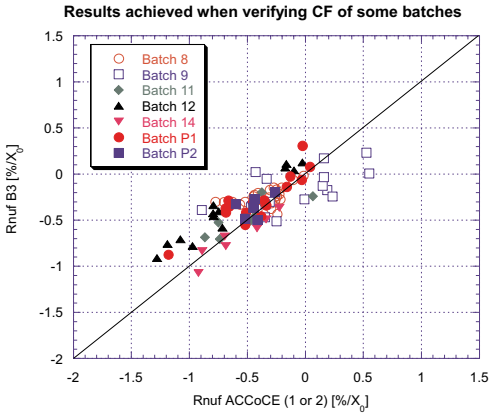

(e) Rear NUF

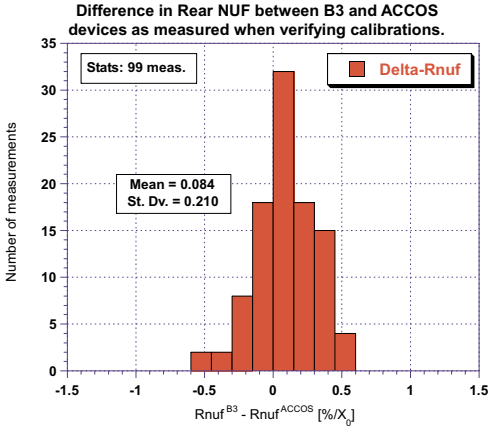

(f) Δ Rear NUF

Figure 4.34: *Correlations between LY, Fnuf and Rnuf measured in B3 and ACCOS devices as deduced from verifications of Calibration Factors in several crystal batches*

Table 4.2: *Comparison of Light Yield values for mobile references in ACCoCE 1 and Bench 3.*

	5624		5654	
	LY	St.Dv.	LY	St.Dv.
Bench 3	8.55	0.30	8.56	0.32
ACCoCE 1	8.43	0.12	8.40	0.15

the resulting LY values for each crystal measured on both devices are entirely compatible.

Correlations of Transmission measurements between Spectrophotometer and ACCOS devices:

As ACCOS devices can also measure light transmission, it is a good crosscheck for us to compare the results got on them with the ones got on our classical spectrophotometer. This is something we do from time to time in order to be sure of the stability of ACCOS transmission measurements.

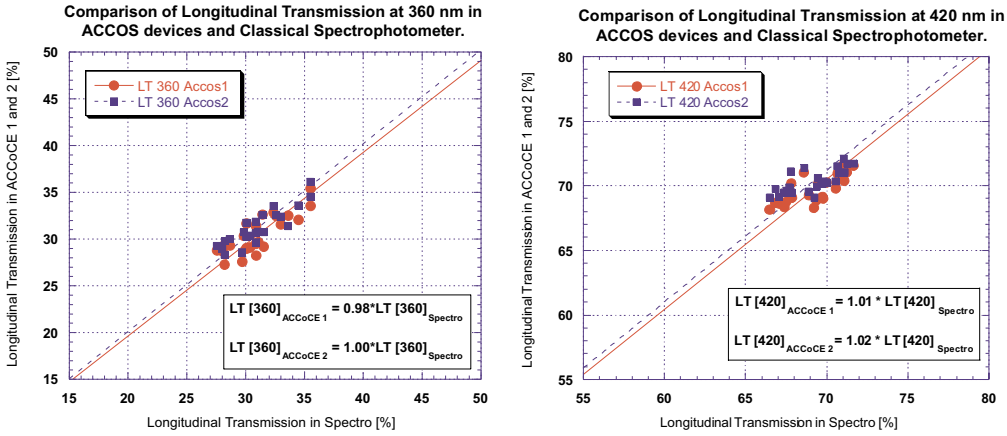

(a) Comparison for 360 nm (b) Comparison for 420 nm

Figure 4.35: *Comparisons between Longitudinal transmission measured in classical spectrophotometer and ACCOS devices*

The longitudinal transmission at 360 and 420 nm of 24 Batch 13 crystals measured in ACCoCE 1, ACCoCE 2 and in the classical spectrophotometer are compared in figure 4.35. As we can see, the agreement is excellent (within a 2% difference) for two of the wavelengths included in the specifications (360 and 420 nm).

Chapter 5

LIGHT COLLECTION UNIFORMITY

In this chapter we are going to focus on our ambitious goal of achieving an uniform light collection uniformity for all the Lead Tungstate crystals used for the CMS ECAL barrel. Therefore, we will first discuss the importance of this objective. Then we are going to illustrate and explain the natural non-uniformity of the crystals, and later we will describe the methods chosen for uniformizing them. It must be clarified from the beginning that the method established at CERN Regional Centre to provide uniform crystals has already been transferred to BTCP[a] producer. Thus, nowadays this producer delivers the crystals only after having applied to them the pre-defined treatment. Hence, most of crystals are received at CERN RC showing already the correct light collection profile, although there are always some of them that need to be re-treated at CERN RC. The results obtained for 5500 pre-production crystals will be presented, focusing on the Light Yield and the uniformity parameters Front NUF and Rear NUF and in the differences between these parameters after and before being retreated at CERN RC.

During the working period that corresponds to this Ph.D., an important parameter that strongly affects longitudinal uniformity of light collection was found: the Transversal Transmission Gradient. Hence, we will report on the different studies that lead to its discovery, and will also explain the reasons

[a]Bogoroditsk Techno-Chemical Plant, Bogoroditsk, RUSSIA.

for its influence on uniformity. It is also extremely important to clarify that the uniformities achieved with the methods described in this chapter are not varying when measuring with different crystal wrappings. As mentioned in previous chapter we use to measure in our laboratories with a tyvek wrapping, and when we use ACCOS devices (where crystals are naked) we normalize to tyvek measurements. On the other hand, as we also said in first chapter, the crystals will be hold in an aluminized alveolar structure. Therefore, it could be possible that the uniformities measured with both wrappings are not the same, thus changing the limits we should impose to uniformity parameters. Due to this, the non-existing influence of the wrapping envelope on the measured uniformity will be illustrated in this chapter. Besides, the low Light Yield losses induced with this method will be also discussed.

5.1 Introduction

The Uniformization of the Light Collection attempting to improve the calorimeter performances has some distinguished precedents. In the late 80's, the famous CERN L3 homogeneous electromagnetic calorimeter composed of $\sim$ 12000 BGO crystals already faced this problem [35]: as the influence on the energy resolution of heterogeneities in the structural composition of the detector was already known at that time, the need of an uniform light collection was quickly assumed. Several different ways to achieve it were proposed, and, at the end, the painting of the four lateral faces of the crystals with a reflective white paint was the method chosen. However, other technique considered was the depolishing of two of the longitudinal faces of the crystals to a given state of roughness. In fact, this was the method initially chosen and it was applied to an important amount of BGO crystals. However, the Light Yield loss induced by the depolishing method appeared to be higher than in the case of the painting, thus leading to the rejection of the former. This procedure was reconsidered for CMS PWO crystals, resulting to be the best method for uniformizing the light collection of these scintillators, the painting giving non-reproducible results.

Clearly, the experience gained through the L3-BGO crystals uniformisation task (also performed at CERN Lab 27) has been extremely valuable for us when facing the CMS ECAL adapted version of the problem. Indeed, some of the CMS ECAL requirements add new complex aspects that make

this task even more challenging as it was in the BGO case if not more. Some of these requirements are, among others: the huge amount of PWO crystals to uniformise ($\sim$ 60000 for the barrel and also possibly 16000 for the endcaps), the fact of working with 17 different crystal geometries that potentially could demand special treatments per each crystal type, or the excellent energy resolution required for the light Higgs decay detection we aim for (see section 2.4.2) that make the acceptable "slope" range of the light collection curve specially narrow.

5.2 Importance of the Light Collection Uniformity

In the shower development that takes place when high-energy particles are absorbed in the block of matter which is the sensitive part of the calorimeter, the energy of particles is degraded to the level of atomic ionizations or excitations that may be detected. The precision with which the energy of the showering particles can be measured is limited by [37]:

- fluctuations in the processes through which the energy is degraded,
- the technique chosen to measure the final products of the cascade processes.

The fluctuations in the shower development process are unavoidable. In electromagnetic showers, they determine the ultimate limit on the achievable energy resolution. However, because of the measurement techniques, the energy resolutions obtained in practice with calorimeters are usually worse than that. Some of the fluctuations contributing to energy resolution obey the rules of Poisson statistics, as for example, fluctuations in the number of quanta (scintillation photons in our case) that constitute the calorimeter signals. However, other fluctuations like shower leakage are not Poissonian. In general, for linear calorimeters measuring signal quanta that follow the rules of Poisson statistics, the energy resolution can be expressed as follows:

$$\frac{\sigma}{E} = \frac{a}{\sqrt{E}} \tag{5.1}$$

where it is clear that the relative precision of the energy measurement improves with increasing energy. However, not all types of fluctuations contribute to energy resolution as $E^{-1/2}$. Some of them are energy independent, e.g. fluctuations resulting from non-uniformities in the calorimeter structure. Others depend in a different way, as the fluctuations resulting from electronic noise (E^{-1}). If we take into account all possible fluctuations, we will return to the already known equation (review section 2.4.1):

$$\frac{\sigma}{E} = \frac{a}{\sqrt{E}} \oplus \frac{b}{E} \oplus c \tag{5.2}$$

As stated above and in section 2.4.1, the non-uniformities present in the calorimeter structure play a major role in the so called constant term c of equation 5.2. In our case, some non-uniformities inducing large fluctuations are related to the longitudinal Light Collection along the PWO crystals. Therefore, our aim is to reduce this non-uniformity in order to minimize contributions to c term, and thus to energy resolution.

The effect of longitudinal non-uniformity of light collection in $PbWO_4$ crystals on electron shower reconstruction has been simulated elsewhere [36]. There we can see that when dealing with a crystal showing severe non-uniformity, the width of the observed energy distribution increases. In particular, the region around the shower maximum region is required to be relatively flat. We can give a qualitative argument to understand this phenomenon:

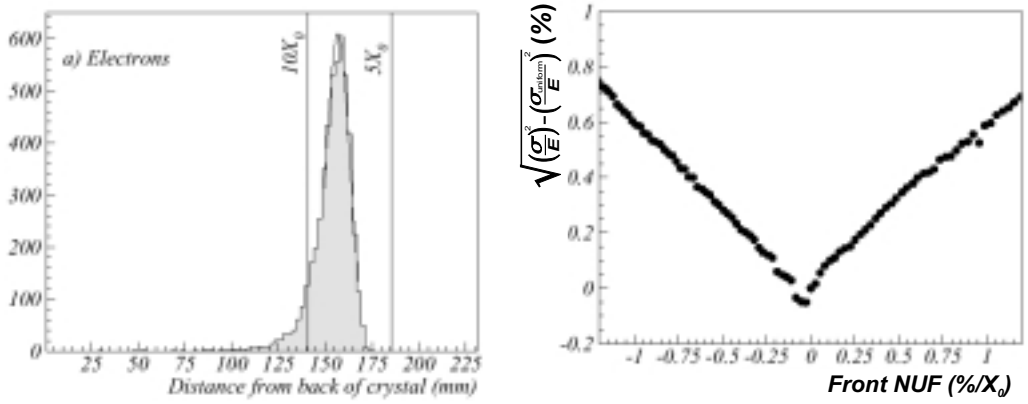

(a) Shower maximum position in PWO for 50 GeV electrons

(b) Contribution to Energy Resolution as a function of Fnuf

Figure 5.1: *Distribution of the shower maximum position for 50 GeV electrons in $PbWO_4$ and Contribution to energy resolution for 120 GeV electrons as a function of the Front NUF*

The simulated distribution of the shower maximum profile for 50 GeV electrons impinging into the front face of a $PbWO_4$ crystal is depicted in figure 5.1-(a). Two vertical lines are positioned at $5X_0$ and $10X_0$ from the front face of the crystal. A Gaussian fit to this distribution yields a sigma: $\sigma = \sim 0.7X_0$. If in the shower maximum region (5-10 X_0) the slope of the light yield curve (i.e. the change in Light Yield per radiation length X_0) is $+1\frac{\%}{X_0}$, then it is clear that the energy deposited at $10X_0$ will yield 5% less light than the energy deposited at $5X_0$. When reconstructing the energy distribution for a crystal, we need to use the light collected and measured by a photodetector. Clearly, the resolution on this measurement will be related to the dispersion of the shower maximum position (σ) and to the slope of the light collection in the shower maximum region for this crystal. Thus, in this way:

$$\textit{Contribution to energy resolution} \approx 0.7X_0 \times 1\frac{\%}{X_0} = 0.7\%.$$

The simulated contribution to the energy resolution for different slopes in the shower maximum region (i.e. for different Front NUF values) is depicted in figure 5.1-(b) [36]. Looking at this plot we can see that the example appearing above (contribution to the energy resolution when Fnuf = $1\frac{\%}{X_0}$) agrees with this simulation results.

Already in section 2.4.2, it was mentioned that we aim for an excellent energy resolution with constant term $c \lesssim 0.5\%$. In consequence, since there are several other contributions, we must limit the contribution of the light collection non-uniformity to this term as much as possible. A maximum contribution of the heterogeneities in the light collection of 0.3% has been agreed to be acceptable. In order to keep Front Non-uniformities contribution below 0.2 %, we must limit Fnuf values within a range, which can be deduced from figure 5.1-(b):

$$\boxed{-0.35\ \%/X_0 \ \leq \ Fnuf \ \leq \ +0.35\ \%/X_0} \tag{5.3}$$

The limits on Fnuf expressed above impose to PWO crystals non-uniformity the strongest constraints that we are going to take into account for our Uniformisation task. However, not only the shower maximum region (Front part) contribution must be limited. Also the rear part of the crystals will have an influence on the energy resolution and hence its contribution must be limited, although the range of acceptable values will not be that narrow, as we shall see.

The contribution of different values of the Rear part slope has been also studied [36]. The contribution to the energy resolution when assuming different possible slopes in the Rear part of the crystal are depicted in figure 5.2 in the case of 120 GeV electrons.

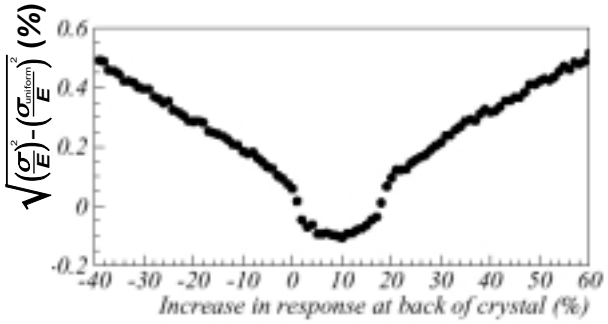

Figure 5.2: *Contribution to energy resolution for 120 GeV electrons as a function of the increase in response at the back of the crystal.*

The first thing we can notice when observing this plot is that the X-axis is not what we could guess (the Rear NUF or Rnuf parameter). However, the parameter used is very similar to it. Simple considerations reveal that the magnitude *Increase in response in the back of the crystal* (or I_{back}, corresponding to X-axis in plot 5.2) divided by $11.2X_0$ is giving us Rnuf values, although with the sign changed, as an increase of the light response towards the back of the crystal ($I_{back} > 0$) yields a negative slope ($Rnuf < 0$), according to Rnuf parameter definition (equations 4.10 to 4.12).

Observing figure 5.2 we can notice that the contribution to the energy resolution is less than 0.1% when $I_{back} \in$ [-3%,20%] (i.e. Rnuf $\in$ [+0.27%/X_0,-1.8%/X_0]). In fact, for certain values of I_{back}, the contribution is even reduced with respect to that one corresponding to the uniform case (completely flat light collection profile). This happens because such an increase in response in the rear part of the crystal helps to compensate for the rear leakage of late developing showers and to eliminate the resulting tail on the low energy side seen with a longitudinally uniform response. In consequence, keeping Rear NUF between the following limits also helps to limit or even reduce the contribution to the energy resolution of light collection non-uniformities:

$$\boxed{-1.8\ \%/X_0 \ \leq \ Rnuf \ \leq \ 0.25\ \%/X_0} \tag{5.4}$$

If we compare figures 5.1-(b) and 5.2, we can see that the contribution to energy resolution depends much more on the slope in the Front part of the crystal (Fnuf) than on the Rear part (Rnuf). In consequence, the acceptable limits for the former parameter (equation 5.3) are much narrower than in the case of Rnuf (equation 5.4).

These acceptability limits in Front and Rear Non-Uniformity parameters define the acceptable longitudinal light collection curve for PWO barrel crystals. The limits on this curve are sketched in figure 5.3

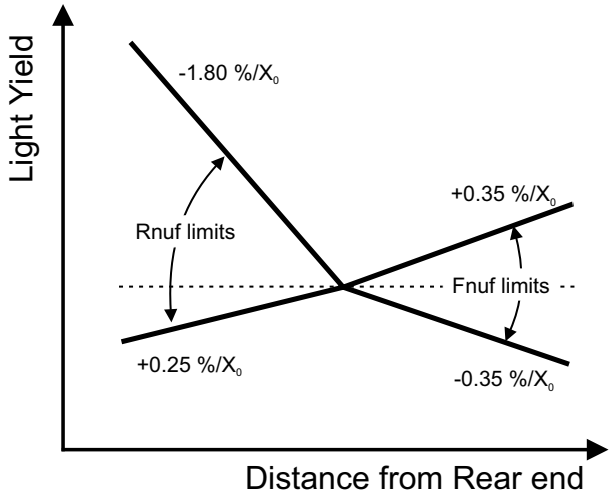

Figure 5.3: *Limits on the acceptable light collection curve.*

As stated above, the total contribution of heterogeneities in light collection must not exceed 0.3% to guarantee an optimum energy resolution, therefore, by keeping Fnuf values within limits from equation 5.3 (contribution lower than 0.2%) and Rnuf values within limits from equation 5.4 (contribution lower than 0.1%), we satisfy the requirement on the total contribution.

5.2.1 Natural Non-uniformity in CMS-ECAL barrel crystals

It has already been discussed that CMS ECAL barrel crystals will be organized in 17 different geometries, according to figure 3.17 and table 3.5. Looking at that figure we can deduce that the 17 different geometries present an important tapering from the front end to the rear end. This is going to produce a focusing effect on the light emitted due to scintillation as depicted in figure 5.4.

This picture compares the trajectories of a photon emitted at the front small end of a PWO crystal with a given angle β in the case of a non-tapered crystal (left) and a normally tapered one (right). As we can see, in the tapered

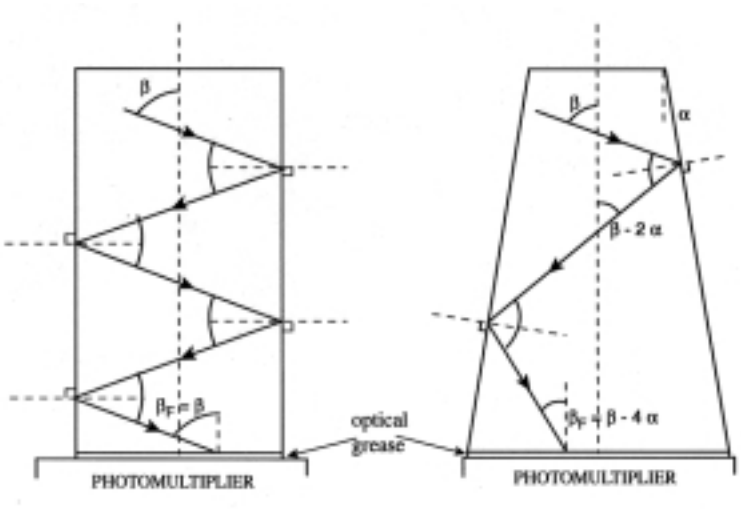

Figure 5.4: *Illustration of the naturally produced focusing effect in tapered crystals.*

configuration the light emitted far from the photodetector has an incidence on the rear face which is more perpendicular than in the non-tapered one, thus having a bigger chance of traversing the rear face and being detected in the photodetector. Hence, tapering favors the light emitted at the small (front) end of crystal whereas the light emitted at the big (rear) end of it remains almost unaffected by tapering since it suffers considerably less number of reflections.

The focusing due to the tapering of PWO crystals is going to play an important role in the light collection uniformity although it is not the only effect that participates. Also absorption of light through crystal length is very important. Obviously, the light emitted at the front end of crystals, which travels 23 cm through the PWO crystal will have a lower chance of reaching the rear face than the light emitted close to rear end (as it travels much shorter distances). This is due to the natural self-absorption of light inside the crystal. This effect will have the opposite effect to focusing, as depicted in figure 5.5.

Focusing and absorption are the two main parameters affecting light collection uniformity. The compromise of these competing effects will define the uniformity of the light collection of a crystal. In consequence, any change in them can completely modify a light collection profile.

The important quality improvement achieved for production PWO crys-

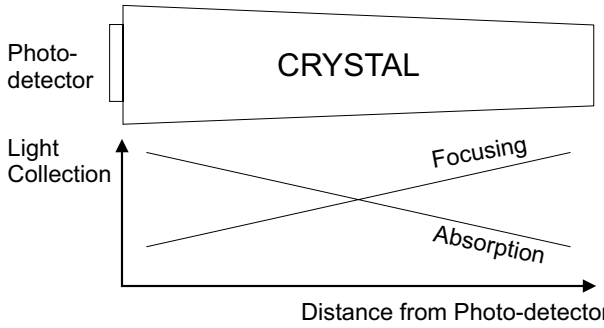

Figure 5.5: *Sketch of the competing effects that define the Non-uniformity of Light Collection.*

tals with respect to R&D ones results, among other things, in a much better transparency. So, when analyzing these recent crystals, we find an attenuation length of typically several meters, whereas for R&D ones, this length was $\sim$ 80 cm. This means that scintillated light can travel through these recent crystals with a smaller probability of being self-absorbed. Of course, this improvement in the transparency of crystals is good for our objectives, but it has an important consequence on the light collection profile, as it makes the absorption effect less important and hence, the focusing dominates (provided that all faces they are optically polished). This is the reason why nowadays, completely polished crystals show uniformity curves that clearly favor the light emitted at the front end, as seen in figure 5.6-(a).

If we want to reduce this focusing in order to provide a flat light collection profile, there are several possible methods that will be discussed in following section. One possibility is to adapt to our case the method initially used for L3-BGO crystals mentioned above: to depolish one[b] of the longitudinal crystal faces. By doing this, we destroy all the internal reflections that would take place on that face, and therefore, the light emitted far from the rear face, will only be focused if the reflections it suffers are produced on the other 3 longitudinal faces. This produces the desired effect as it strongly reduces the focusing as can be seen in figure 5.6-(b). The degree of depolishing of the two crystals from this picture is obviously excessive as uniformity parameter Fnuf is too negative and far from our acceptable limits. However, by comparing figures 5.6-(a) and 5.6-(b) we can already guess which is going to be our uniformisation method: to depolish a longitudinal crystal face to a given roughness,

[b]BGO crystals were depolished in two longitudinal faces only at the beginning of its production. Later, the painting of the four lateral faces was adopted as the final method.

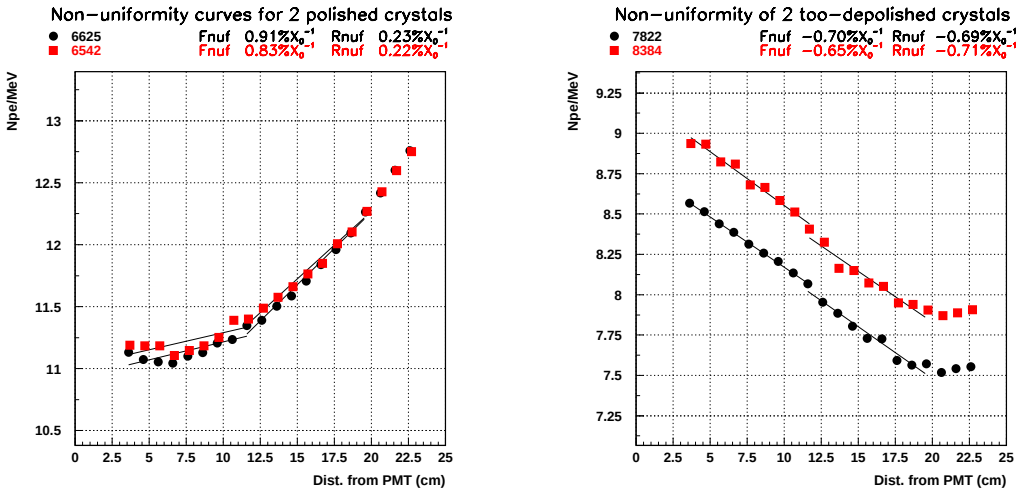

(a) Completely Polished (b) One face too depolished

Figure 5.6: *Non-uniformity curves for several Lead Tungstate crystals*

intermediate between 0 μm (completely polished) and 0.5 μm (typical roughness achieved after lapping that face) in such a way that the focusing effect is reduced until its contribution to the light collection is balanced respect to the absorption. An example of uniform light collection for two PWO crystals is shown in figure 5.7, where are shown the uniformity curves for two crystals for which we depolished to the adequate roughness one lateral face. These

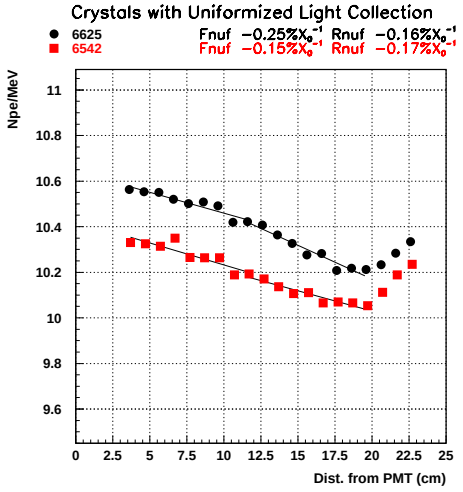

Figure 5.7: *Crystals showing an uniform profile of light collection after being treated.*

two crystals are the same which were initially completely polished and were appearing in figure 5.6-(a).

In this figure are included the uniformity parameters Fnuf and Rnuf of both crystals. As we can see, they are verifying our acceptability limits (equations 5.3 and 5.4), hence, these crystals could be considered as acceptable for the CMS Electromagnetic Calorimeter.

5.3 Uniformization Method

5.3.1 Historical Approach

Initially several methods were tried in order to uniformise the crystals. The three more promising methods considered were: 1) Differential Wrapping, 2) Deposits on the crystal, and 3) Depolishing of a crystal face. Two important aspects to be satisfied by these methods were: a) The reduction of light produced due to its application should be the lowest possible and b) The method should be suitable for mass application to all barrel crystals (~ 60000), yielding reproducible results.

1) Differential Wrapping:

In this method, to modify the non-uniformity curve, we were using different wrappings on different parts of the crystal. Among the alternatives used we can mention: black tape on the crystal, or on the inner side of the tyvek, and also ink stripes on the tyvek. As a matter of fact, some units of the 25 crystal matrix used for the 1996 beam tests were uniformised following the ink stripes method giving adequate results, although the light losses were quite important (10-20%). However, this technique seemed not suitable for mass application since each crystal had to be studied individually, and therefore, was discarded. Further information on this method can be found elsewhere [39].

2) Deposits on the crystal:

A direct deposit on a crystal which prevents the formation of an air gap around the crystal reduces drastically the total internal reflection and thus should reduce the focusing effect. Very thin deposits of silver were applied under vacuum on five faces of the crystals, with the secondary aim of obtaining a high light yield. The results were good as a change in the slope of the non-uniformity profile was observed but some technical difficulties arose. Another variation of this technique was the use of reflective mineral white paint applied to crystal faces. This technique, already applied for BGO crystals in L3 was studied in PWO crystals. In order to tune the uniformity with this technique we need to paint on one or two faces, but this increases dramatically light yield losses. On the other hand, this method was providing not too severe light yield losses when five faces were painted although the light collection use to be still non-uniform [38]. In any case, the thickness of the paint layer was extremely hard to control, and this was a major problem for us, since the play of our crystals inside the alveolar structures is only 100 μm. Due to that, this technique was discarded.

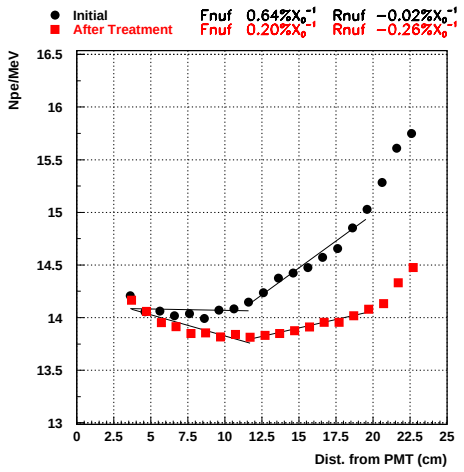

Figure 5.8: *Uniformity before and after depolishing a lateral face for PWO crystal.*

3) Depolishing of a crystal face:

The effect of depolishing one or several end or lateral faces have been also investigated, and the best results, as a combination of low light yield losses and good uniformity, were achieved when depolishing a single longitudinal face. The results of the depolishing of a lateral face for two completely polished crystals were already shown in figures 5.6-(a) and 5.7. However, the uniformity profile after and before depolishing one lateral face to a given extent can be again observed in figure 5.8, where both curves are overlapped to better illus-

trate the change. This technique, is the method finally chosen, as it effectively satisfies the two aspects stated above: it induces little light yield loss and can easily be adapted to huge amounts of crystals.

5.3.2 Method chosen

As stated above, the depolishing of a lateral face reduces the internal reflection and re-scatters the light, thus reducing the focusing effect. The degree of depolishing of the surface controls the magnitude of the induced change. A natural parameter to quantify the degree of roughening of a surface is the roughness (Ra) in microns, parameter that corresponds to the mean height of the inhomogeneities on the surface.

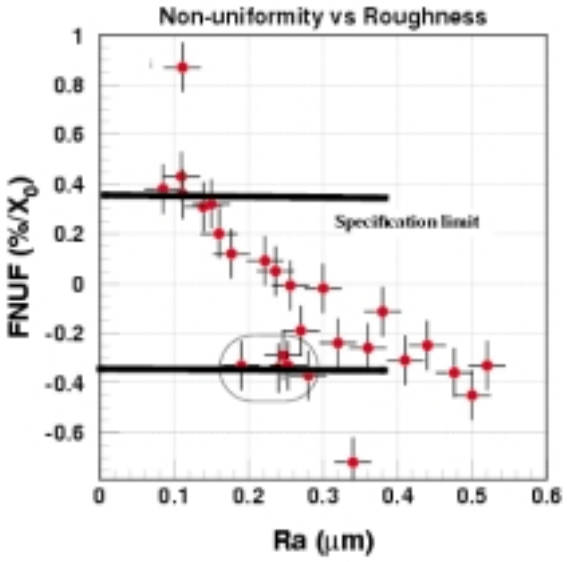

Figure 5.9: *Variation of the Fnuf with the Roughness of the depolished longitudinal face. Surrounded points are due to an additional effect described in section 5.6.*

The technique used at CERN Regional Centre, based on the depolishing of a longitudinal crystal face was proved to be suitable once we could establish a simple correlation between the roughness of the treated surface and the resulting non-uniformity curve induced in the treated crystals. Such a correlation is illustrated in figure 5.9. This allowed us to fix a roughness range (Ra $\sim$ 0.25-0.30 μm) that when applied with the right method to the crystal face

should provide the expected uniformity curve. However, the problem was not only that, as another aspect to verify was that the final method chosen should allow to easily reproduce the desired roughness, yielding very small differences between crystals of the same quality.

Since 1996, different versions of the same depolishing method were considered [41], however, the definitive uniformisation procedure was established during 1998 at CERN Regional Centre with BTCP R&D crystals [38]. These crystals were delivered completely polished, therefore, the first step of the treatment was to perform a **lapping** on the desired face. This treatment roughens the face to a greater extent than required, but allows to start from a common state and removes any surface effects. During the lapping, the crystals (three at a time) are held rigid within plastic supports on a resin wheel. In addition, the crystals are under an uniformly distributed 30 Kg load. A 15 μm diamond powder solution is spread on the wheel as it turns, thus lapping the crystal face in contact with the wheel. This treatment is typically applied during 5 minutes and use to provide a uniform surface state characterized by a final roughness of 0.50 μm $\pm$ 0.03 μm. Then, crystals were cleaned and prepared for the **polishing**. This operation is performed on a second wheel protected with a soft tissue. The effect of this tissue is that there is far less roughening of the crystal face and hence, the surface is polished to an state in between that of the lapped and the optically polished crystals. For this step of

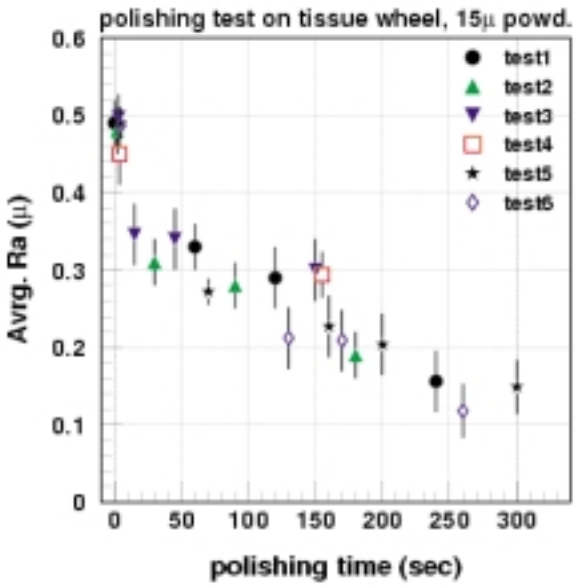

Figure 5.10: *Evolution of the obtained roughness with the applied polishing time.*

the treatment, the crystals are also held rigidly, and are under a 15 Kg load. The wheel also turns spreading the same 15 μm diamond powder solution, that thanks to the soft tissue placed on the wheel polishes the crystal face in contact with it. The Ra versus time dependence obtained with this method is depicted in figure 5.10. As can be deduced from this figure, in order to achieve the desired Ra values derived from figure 5.9 (0.25-0.30μm) we must polish during $\sim$ 100 seconds.

Once the technique was completely defined, it was transferred to producers, in such a way that since that moment, they are the ones applying it. This implies certain variations in the method described above which are coming from a simple fact: the crystals used for the definition of the method at CERN RC were presenting an optical polishing in their six faces. However, producers do not polish optically all faces to then apply our method. What they do is to start from the crystal surface state obtained after their cutting. Such a state is characterized by a Ra $\sim$ 2 μm, thus being much rougher than the surface state provided by the lapping. Therefore, producers first perform a lapping of the six crystal faces in order to get rid of undesired surface defects, and then they proceed to polish optically five faces (F, R, P, N and W). For face D, they apply a similar polishing process but it is stopped at a certain time that yields the requested roughness (0.25-0.30 μm, according to figure 5.9).

CERN RC intervention in order to uniformise crystals is only required when the treatment applied by producers does not provide an uniform light collection, fact that, as we will see in the following section, does not happen frequently unless any of the factors that define the uniformity is substantially modified. The transfer of the method to producers was made with the requested Ra range to be 0.25-0.30 μm. However, since that time, some tuning in the crystal transparency properties reduced their absorption and hence made the focusing effect to dominate. This produced a shift to positive Fnuf values that will be explained and illustrated in following sections. Such a problem forced us to modify the value of the requested Ra to producers, 0.35-0.40μm being the actually requested Ra range.

5.4 Results obtained for pre-production crystals

From September 1998 to December 2000 we have received, inspected and characterized in the CERN Regional Centre, 5500 pre-production crystals produced and delivered in 13 different batches by the BTCP[c]. All these crystals were treated at the BTCP according to the method explained in previous section. Table 5.1 summarizes several informations about these batches.

Table 5.1: *Summary on the first 5500 crystals received from BTCP.*

Batch	Reception Date	Crystals	Types	Non-Uniform
1	04/09/98	100	6	100[†]
2	03/11/98	100	7	8
3	08/12/98	200	8-9	6
4	22/03/99	200	6-9	57
5	22/06/99	400	6-9	177
6	30/08/99	500	1-5	348
7	18/11/99	550	13-17	199
8	21/01/00	650	1-13	56
9	11/04/00	800	1-4	57
10	26/06/00	500	5-7	52
11	08/08/00	500	7-9	50
12	08/09/00	500	10-12	102
13	20/12/00	500	13-15	18

[†] *All crystals were delivered completely polished in all faces, thus all were treated at CERN RC.*

From table 5.1 we can know for each batch: its reception date, the total amount of crystals delivered on it, the types included on the batch and the amount of non-uniform crystals (i.e. the amount of crystals treated at the BTCP according to our method, which, once characterized at CERN RC, appear not to be satisfying the Front NUF condition expressed in equation 5.3).

It is important to clarify why when we use the term "non-uniform" we

[c]Bogoroditsk Techno Chemical Plant.

just refer to a crystal with Fnuf not verifying equation 5.3, and we do not refer to Rnuf. In fact, it appears that Fnuf and Rnuf values are quite related to each other. As depicted in figure 5.6-(a and b), a quite positive Rnuf characterizes a crystal with Fnuf too positive (a), and the opposite is also true: a crystal with a too negative Fnuf (b) has usually a too negative Rnuf as well. This phenomenon is illustrated for the 550 crystals from Batch 7 in figure 5.11-(a).

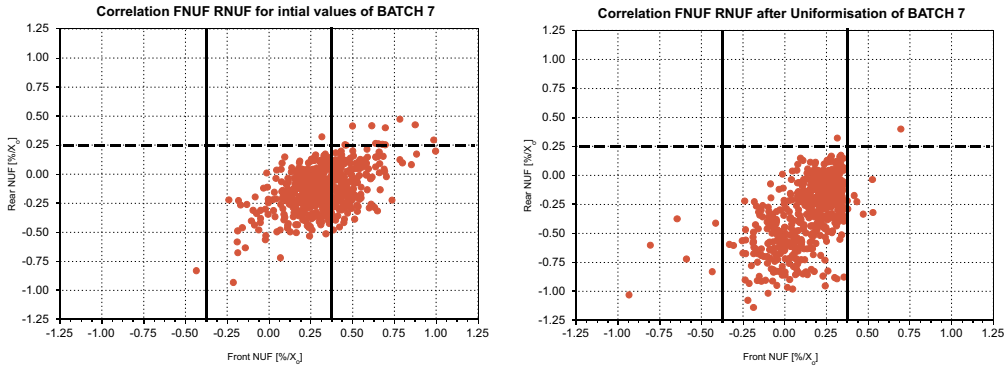

(a) Batch 7 - Initial

(b) Batch 7 - After Unif.

Figure 5.11: *Correlation between Front and Rear NUF for Batch 7 in the initial situation and after uniformisation task*

As we can see in this plot (a), it exists a clear correlation between Fnuf and Rnuf. In general, when a crystal has a flat light collection in the front part, the rear part will be also flat or slightly negative. From this, we can deduce that if we manage to control the Fnuf following our requirements, we will make also the Rnuf to be within our limits. This is depicted in figure 5.11-(b), where the values shown were measured after uniformisation. As we can see, the shift of the data cloud due to uniformisation from plot (a) to (b) is not lateral but diagonal, thus meaning that the change in Fnuf induced with our method affected also Rnuf. As a matter of fact, the crystals with a "pathological" Fnuf behavior after uniformisation (crystals which were not uniform after being treated at BTCP, and which are still bad after being re-treated at CERN RC) use to present together with this Fnuf out of limits, also a Rnuf out of the imposed limits. In consequence, we have focused during this uniformisation task on the Fnuf parameter, and hence, we consider a crystal as "uniform" when Fnuf verifies equation 5.3, fact that in most cases also implies verifying Rnuf limits (equation 5.4).

The non-uniform crystals for each batch appearing in last column from table 5.1 must be uniformised at the CERN Regional Centre. Now we are going to analyze the situation of the batches, grouping them according to the

behavior of their Fnuf distribution:

Batches 1-4:

If we analyze the amount of initially non-uniform crystals we can see that for Batches 1 to 4, the amount of crystals needing treatment was reasonable ($\sim$ 10 %), with the exception of Batch 1, for which all crystals were treated at CERN RC since they were delivered with all faces completely polished. As depicted in figure 5.12, Front Nuf distributions were well centered around zero for these batches. It is important to remind that, as explained in last paragraph of previous section, the roughness requested to the BTCP producers immediately after the definition of the method (1998) was 0.25-0.30 μm.

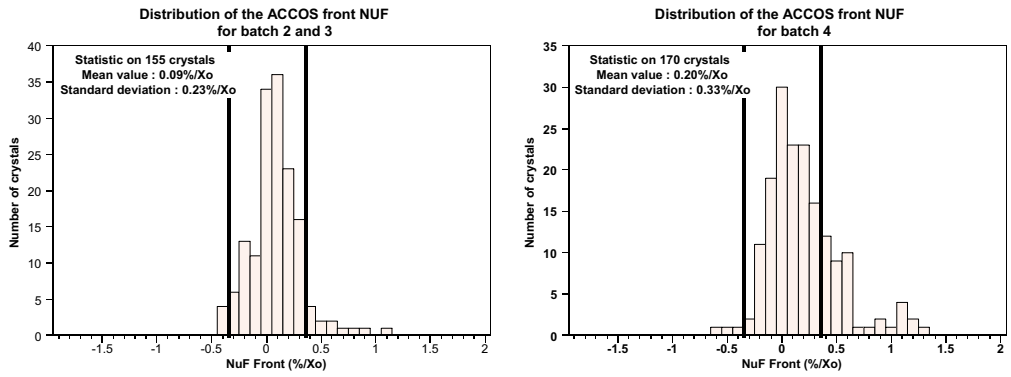

(a) Batch 2 and 3 (b) Batch 4

Figure 5.12: *Front Non-uniformity distributions for Batches 2, 3 and 4*

Batches 5-7:

If we look at the amount of non-uniform crystals quoted in table 5.1 for Batches 5, 6 and 7, we will notice that it is much more important than for other batches. The explanation for this is simple: during batch 5 production, the producers tuned their methods at the crystal growing stage. In fact, the tuning was related to the doping used for these crystals. The change from single (La) doping to double (Y,Nb) doping (change that was promoted due to the better radiation hardness of double doped crystals) affected the light collection as will be illustrated in the following section, resulting in light collection curves dominated by the focusing effect. In this way, the light collection was enhanced at the crystals small end, yielding higher Fnuf values. The initial Light Yield, Front Non-uniformity and Rear Non-uniformity distributions corresponding to two of these three batches (6 and 7) are depicted in figures 5.13-(a, c and e) and 5.14-(a, c and e) respectively. In them, the Fnuf distribution centered at

too positive values can be clearly observed.

In these figures we can also observe the resulting distributions after the uniformisation task (plots 5.13-(b, d and f) for Batch 6 and 5.14-(b, d and f) for Batch 7). In this case, as the crystals were trending to too high Fnuf values, a stronger depolishing was needed. Therefore, we proceed to perform a lapping on the treated face of these crystals. This increases roughness, and therefore reduces the focusing, thus the light collection curve is flatter on the front part. By comparing these plots (b, d and f) to the ones before uniformisation (a, c and e) we can appreciate the success of the method, as only few, pathological crystals remain out of Fnuf limits after uniformisation and besides, Rnuf distributions trend to more negative values than before uniformisation.

Batches 8-13:

In order to solve this problem in the light collection uniformity induced by the change in the doping, we decided to ask for higher roughness directly to BTCP producers, i.e. the requested roughness would be, as stated in previous section, 0.35-0.40μm from that moment on. In these conditions we received Batches 8, 9, 10, 11, 12 and 13. The initial results of some of these batches are depicted in plots (a, c and e) of figures 5.15 (Batch 8) and 5.16 (Batch 10). On these plots we can appreciate than the initial situation for these batches provided with the new requested Ra is much better than the initial situation of batches 6 and 7. In fact, more than 95% of crystals are behaving properly in Front and Rear NUF as supplied by producers, thus requiring a small CERN RC intervention. The results of this intervention appear in plots (b), (d) and (f) from figures 5.15 and 5.16. As can be observed, the change produced in the distributions is very small, as the amount of crystals needing to be re-treated at CERN RC was very low.

These results show that our ambitious goal of achieving a uniform light collection for all the CMS ECAL PWO crystals in order to optimize the energy resolution of our final detector is realistic and that, nowadays, more than 95% of the first 5500 crystals delivered by BTCP are satisfying this constraint. This also means that the uniformisation technique defined at CERN RC and transferred to producers is successful, and allows trusting it for future delivery of crystals.

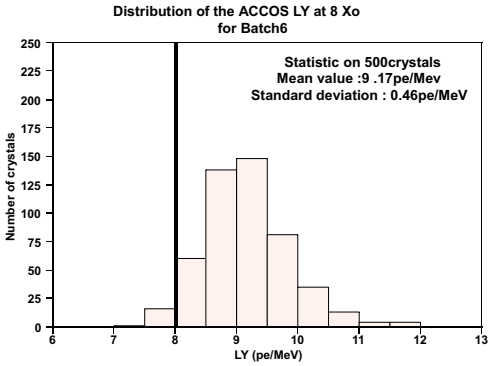

(a) Initial LY distribution

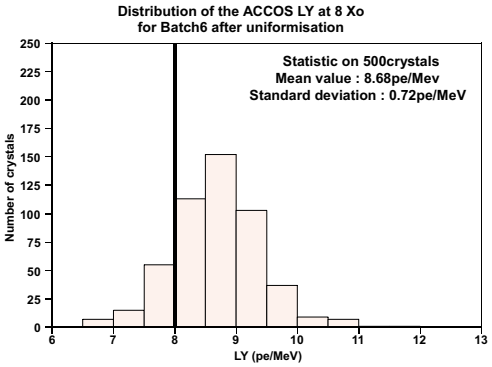

(b) LY distribution after Uniformisation

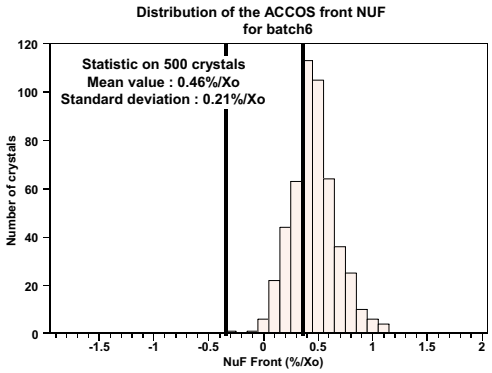

(c) Initial Fnuf distribution

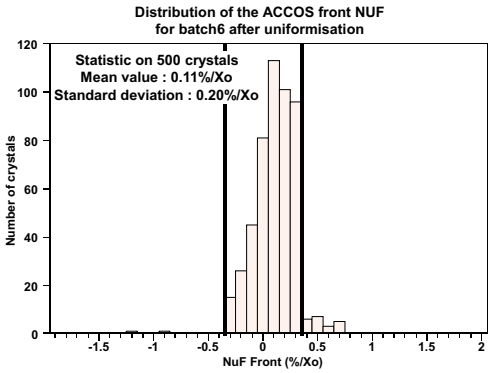

(d) Fnuf distribution after Uniformisation

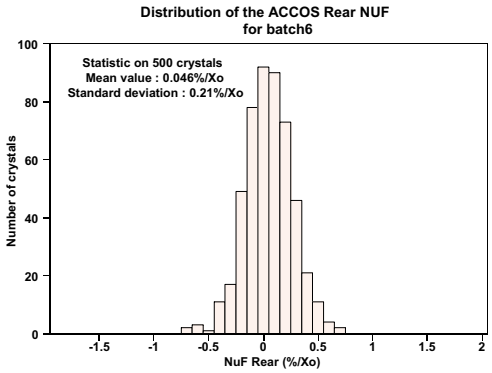

(e) Initial Rnuf distribution

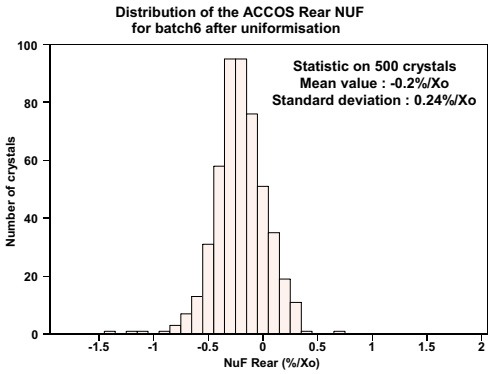

(f) Rnuf distribution after Uniformisation

Figure 5.13: *Results before and after Unformisation for Batch 6*

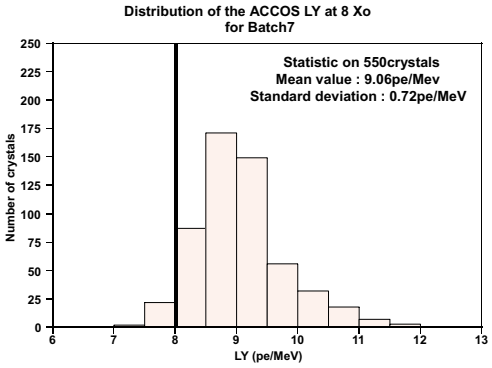

(a) Initial LY distribution

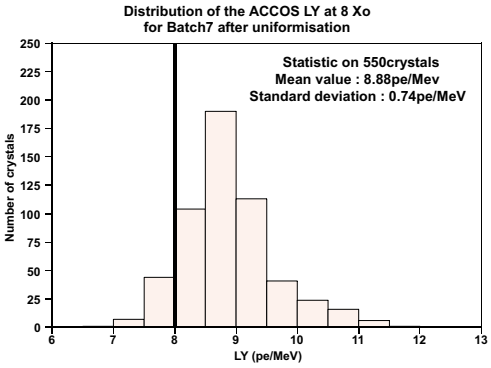

(b) LY distribution after Uniformisation

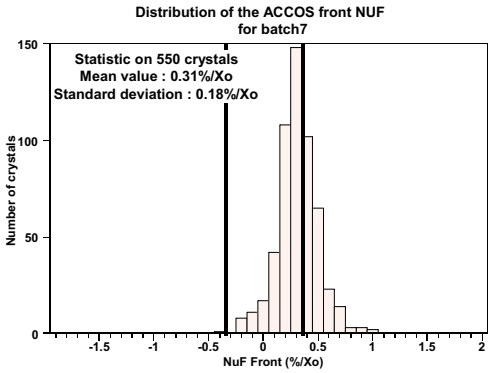

(c) Initial Fnuf distribution

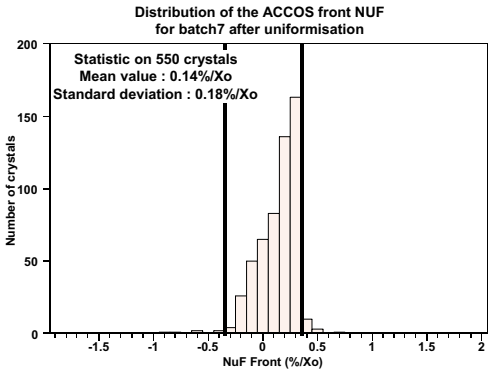

(d) Fnuf distribution after Uniformisation

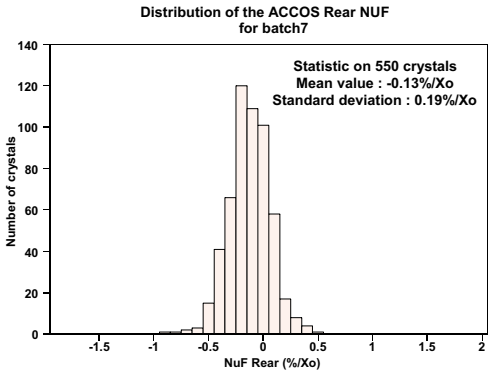

(e) Initial Rnuf distribution

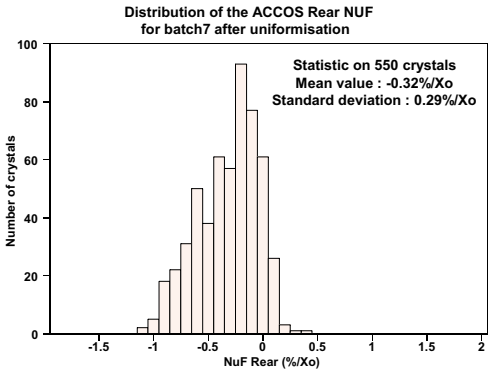

(f) Rnuf distribution after Uniformisation

Figure 5.14: *Results before and after Unformisation for Batch 7*

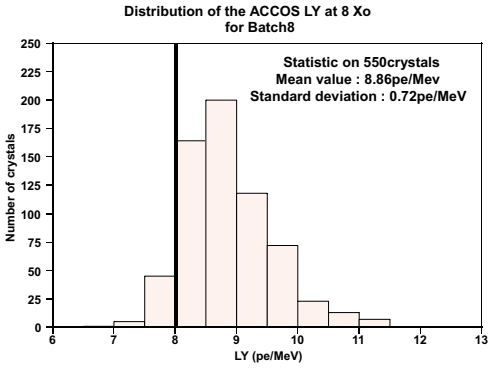

(a) Initial LY distribution

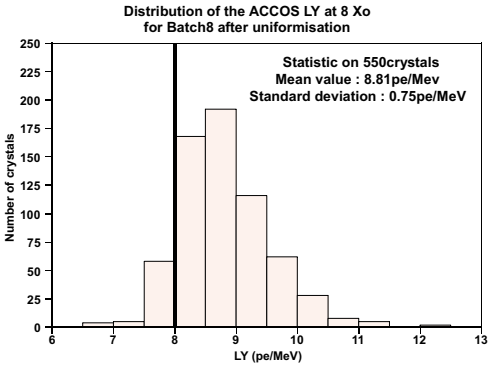

(b) LY distribution after Uniformisation

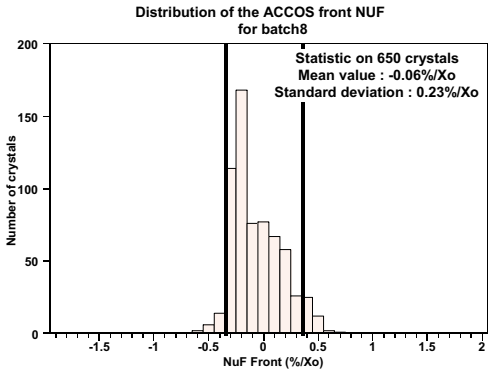

(c) Initial Fnuf distribution

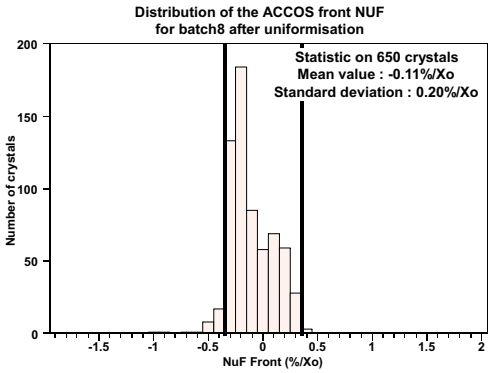

(d) Fnuf distribution after Uniformisation

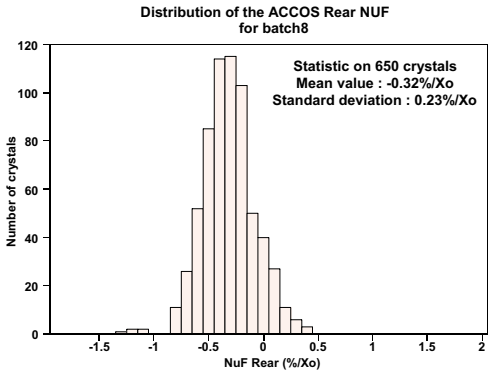

(e) Initial Rnuf distribution

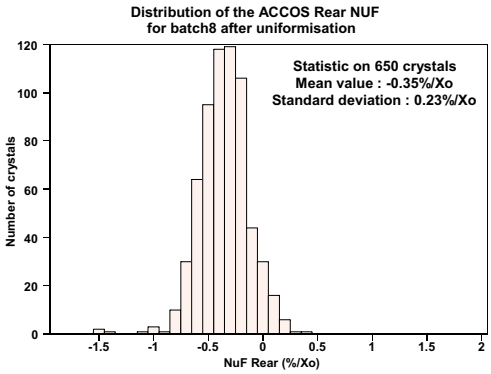

(f) Rnuf distribution after Uniformisation

Figure 5.15: *Results before and after Unformisation for Batch 8*

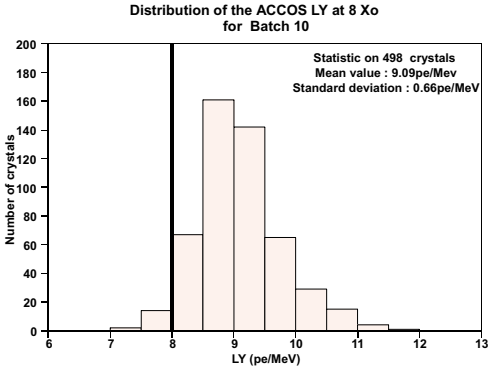

(a) Initial LY distribution

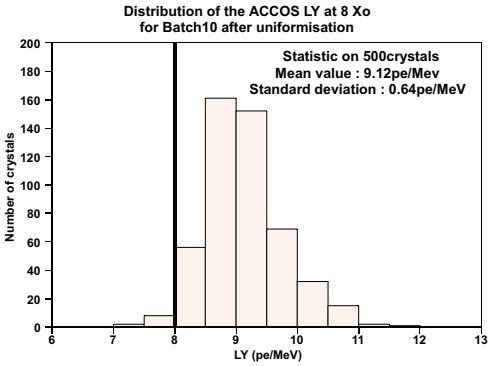

(b) LY distribution after Uniformisation

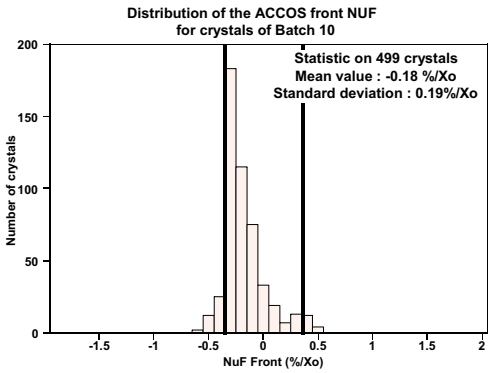

(c) Initial Fnuf distribution

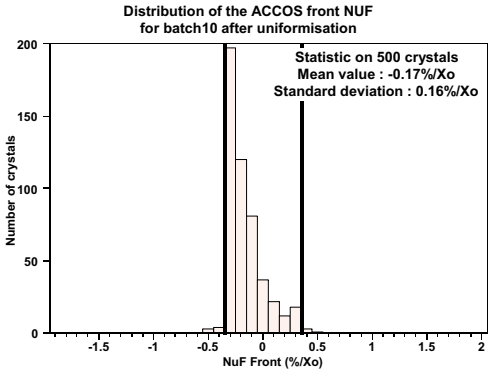

(d) Fnuf distribution after Uniformisation

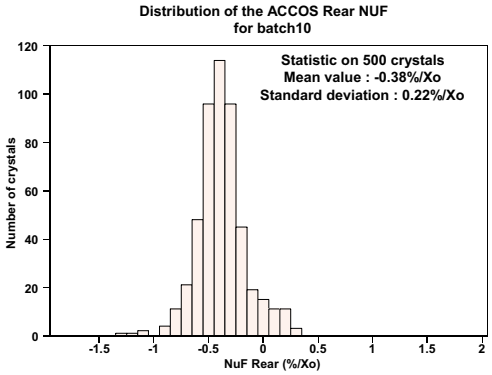

(e) Initial Rnuf distribution

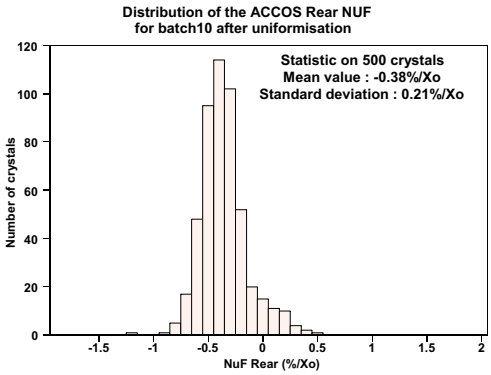

(f) Rnuf distribution after Uniformisation

Figure 5.16: *Results before and after Unformisation for Batch 10*

5.5 Induced changes in Light Yield and Front NUF

In this section we are going to analyze the changes induced in the Light Yield and Front NUF of the crystals when applying our uniformisation method defined above. However, we are not going to be focused only in the standard uniformisation method defined at CERN RC and applied nowadays by the producers, but we will also illustrate the changes induced by the *correcting* treatments that must be applied at CERN RC when crystals treated and delivered by producers does not satisfy uniformity limits. These correcting treatments are two: Standard Lapping and Soft Polishing.

The changes induced in light collection curves by standard uniformisation method, described in section 5.3, were studied in a group of 20 type 3 crystals from Batch 9. These crystals were initially presenting all faces optically polished. Thus, the light yield curves for all of them were typically like the ones depicted in figure 5.6-a (in fact the two crystals depicted in this figure belong to this group of 20). In this manner, the mean value of the initial Fnuf distribution was $\approx 1.2\frac{\%}{X_0}$. These 20 crystals were treated according to our standard method at CERN RC. The resulting Fnuf distribution achieved for these crystals is depicted in figure 5.17-(a). As we can see, the uniformisation method worked well for all except two crystals (which are indeed very close to

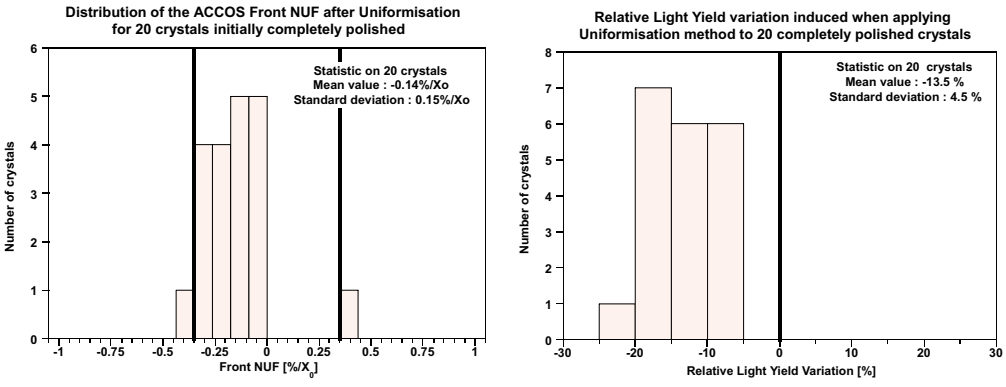

(a) Final Fnuf distribution (b) Relative Light Yield variation

Figure 5.17: *Final Front NUF distribution measured for a group of 20 crystals initially completely polished (a) and Relative Light Yield variation induced with Uniformisation method for same crystals (b)*

Fnuf limits), yielding a final Fnuf distribution with mean value -0.14$\frac{\%}{X_0}$. On the other hand, it is obvious that this method is going to produce a decrease in the measured LY at $8X_0$, since we are killing the focusing effect due to the depolishing of a face and this worsens the collection of the light emitted at front end. In plot (b) from figure 5.17, we present a histogram of the Relative Light Yield variation induced for each crystal by this method.

The Relative Light Yield variations ($\Delta_R LY$) from figure 5.17 are calculated as follows:

$$\Delta_R LY \ [\%] \ = \ \left(\frac{LY_{final} - LY_{initial}}{LY_{initial}} \right) \times 100 \qquad (5.5)$$

where $LY_{initial}$ stands for the Light Yield before CERN RC intervention, this is, the one measured when the crystal remains as delivered by producers, and LY_{final} is the one measured after being corrected at CERN. As we can see the $\Delta_R LY$ is $\approx$ -13.5%. This loss is not very important as the initial LY of completely polished crystals uses to be quite high ($\gtrsim$ 10 pe/MeV), thus even with this loss the final LY is still higher than 8 pe/MeV. In the case of the 20 crystals, the final LY distribution was centered in $\sim$ 8.9 pe/MeV, hence the induced losses are acceptable.

The treatments applied at CERN RC to correct crystals showing bad uniformity of light collection are two: *a*) A **standard lapping**, when the Front NUF of the crystals is too positive. This treatment is the same defined in section 5.3, and is applied also during typically 5 minutes. This was the treatment applied at CERN for Batches 6 and 7 which were showing initial Fnuf distributions too positive (see (c) plots from figures 5.13 and 5.14); and *b*) A **soft polishing**, when the initial Front NUF is too negative (see tail on the left of the distributions of plots (c) in figures 5.15 and 5.16. This polishing is made in the same way as the one described in the standard method (section 5.3) although it lasts less (typically only 30-40 seconds).

Of course, with the lapping we increase the roughness of the face, hence, we expect a decrease in the Fnuf values and also a decrease in Light yield (for the same reasons explained above for the standard method). However, for the polishing we are decreasing Ra, thus we favor the total reflections in that face and also the focusing. In consequence, we must get more positive Fnuf values and also higher LY at $8X_0$.

These arguments are confirmed in figure 5.18: In plot (a) we depict

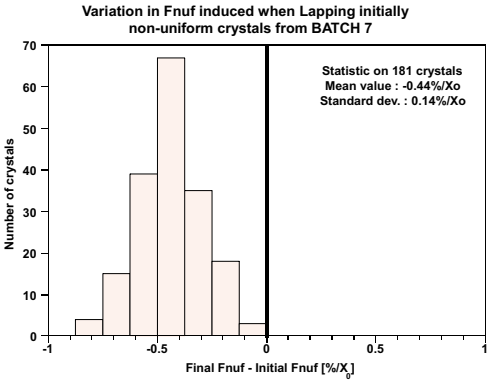

(a) Fnuf variation induced by Lapping

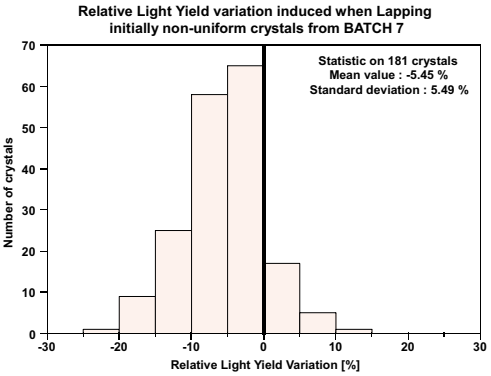

(b) Relative Light Yield variation induced by Lapping

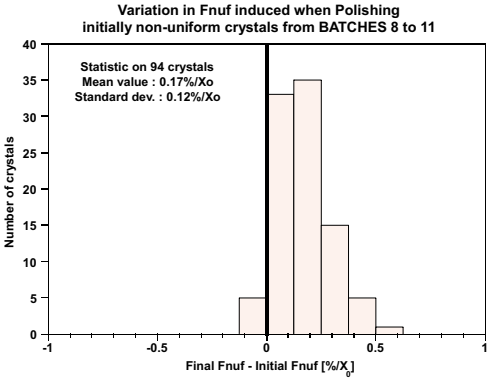

(c) Fnuf variation induced by Polishing

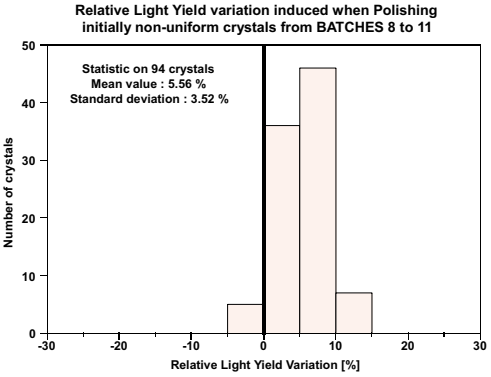

(d) Relative Light Yield variation induced by Polishing

Figure 5.18: *Variations in Front NUF and Light Yield induced by Lapping and Polishing*

the Fnuf variation (Fnuf$_{final}$-Fnuf$_{initial}$) induced in 181 Batch 7 crystals by lapping, as they were initially too positive in Fnuf. In plot (b) we represent the $\Delta_R LY$ distribution for the same crystals (calculated according to equation 5.5). As we can see, lapping treatment produces a final Fnuf which is, on average, $0.44\frac{\%}{X_0}$ lower than initial Fnuf together with a relative light yield loss of 5.45%.

Plots (c) and (d) from figure 5.18 correspond to 94 crystals from Batches 8, 9, 10 and 11 (the small tails on the left of the initial Fnuf distributions showed already in this chapter). These crystals were initially too negative in Fnuf, thus requiring a soft polishing in order to favor the focusing and

hence tilt up the light collection at the front end. In (c) we depict the Fnuf variation induced with the polishing. As we can deduce, the Fnuf after this short polishing is, on average, $0.14\frac{\%}{X_0}$ higher than initial Fnuf values. We can observe as well that the light yield is increased by 5.56%.

So, we can conclude that the standard method and the two correcting treatments applied at CERN RC provide experimentally the expected results, thus revealing a good understanding of such a delicate task as the uniformisation of light collection in PWO crystals together with the success of the chosen uniformisation techniques.

5.6 The transversal transmission gradient

In this section we are going to present the studies performed on the transversal transmission gradient, which is a parameter that influences the non-uniformity of light collection. It was first observed when analyzing a set of endcap crystals, hence, we will start by explaining this first observation. Then we will show how this parameter looks like for barrel crystals from previously mentioned batches, and later we will show the influence of the doping on the dispersion of the transversal transmission gradient values for a given batch.

5.6.1 Study on 10 endcap crystals

During 1999 we received a batch of 10 endcap crystals, all produced at the same time, with all faces completely polished and with very similar longitudinal light transmission curves. In these conditions, the focusing and the absorption effects were supposed to be very similar from one crystal to another. Hence, we were expecting an homogeneous behavior of light collection in this batch.

The resulting Fnuf and Rnuf values for these 10 crystals are shown in table 5.2, where we can also find the values of the longitudinal transmission (LT) at 420 nm (the closest wavelength to PWO emission peak). Clearly, the light collection profiles for these crystals were grouped in two families: 4

Table 5.2: *Results of the batch of 10 endcaps studied.*

Crystal	Front NUF [%/X_0]	Rear NUF [%/X_0]	LT at 420 nm [%]
2204	-0.04	-0.28	69.20
2205	1.12	1.24	69.87
2206	1.06	0.88	69.39
2207	1.28	0.84	69.70
2208	-0.02	-0.43	69.60
2209	1.21	0.76	66.04
2210	-0.02	-0.57	67.48
2211	1.14	1.05	66.45
2212	1.28	1.04	67.08
2213	-0.13	-0.31	64.63

of those crystals were behaving as expected[d] in the endcap crystals (Fnuf $\sim$ 0 %/X_0) and 6 were behaving very differently, with a Fnuf $\gtrsim$ 1 %/X_0. As can be noticed, no correlation between the LT and the Fnuf and Rnuf can be established. Besides, and in order to illustrate how different the light collection is for these two groups, we have included figure 5.19-(a and b), where the LY curve for endcaps 2204 (behaving as expected) and 2205 (strange behavior) are shown.

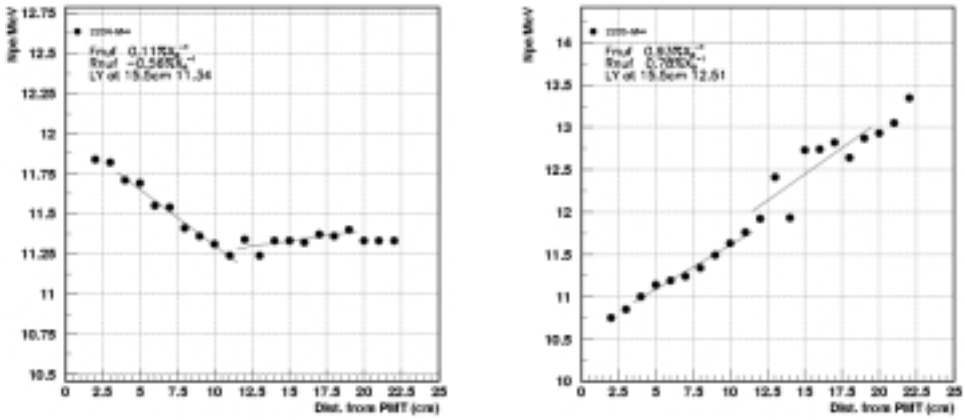

(a) 2204 (b) 2205

Figure 5.19: *Uniformity of Light Collection for endcaps 2204 and 2205*

We performed different studies after which we only could establish a

[d]Since their tapering is much reduced respect to barrel crystals, we expect a flat uniformity in the front part even if endcaps are completely polished in all faces.

difference between these two groups of crystals. This difference was coming from a gradient in the transversal transmission of light along the crystals: we could observe that for the crystals behaving as expected, the transmission at the band edge ($\lambda \sim 345$ nm) was increasing when moving from the front to the rear end of the crystals, whereas for the crystals with an unexpected behavior, the response was the opposite: the transmission at the band edge was decreasing when moving from front to rear end. This is illustrated in figure 5.20, where a detail of the transversal transmission curves obtained for endcaps 2204 and 2205 are shown. As can be observed in this figure, the band edge is oppositely shifted for these two crystals when measuring from front to rear end.

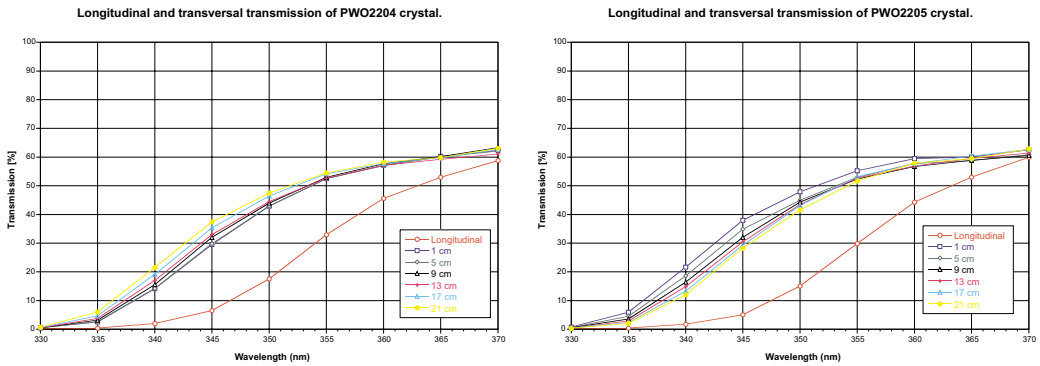

(a) 2204 (b) 2205

Figure 5.20: *Detail of Transversal Transmission curve for endcaps 2204 and 2205*

We tried to generalize the situation for the whole batch of 10 endcaps by depicting the evolution of the transversal transmission at 345 nm from the front to the rear end for the two groups of crystals. The results are plots (a) and (b) from figure 5.21. As can be observed, the two groups are clearly distinguishable by constructing these plots.

We defined then a parameter called the *Transversal Transmission Gradient* (TTG) that can be understood as the percentual variation in the transversal transmission at the band edge (345 nm for transversal measurements on the endcaps) per centimeter of crystal, starting from the front end. In fact, it is the slope of a linear fit on the plots from figure 5.21. As can be observed, this plot corresponds to 6 transversal measurements, as is usual in Spectrophotometer measurements (the only bench that could be used for the endcaps before AC-CoCE 2 was functional). Of course, if we calculate this parameter for the 10 endcaps studied, we are going to observe two groups that correspond to the

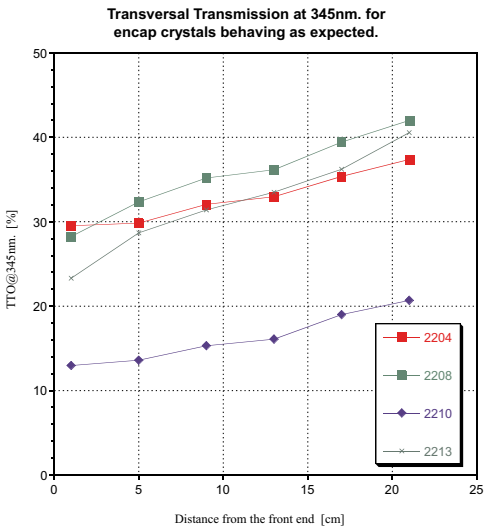

(a) Endcaps with uniformity as expected

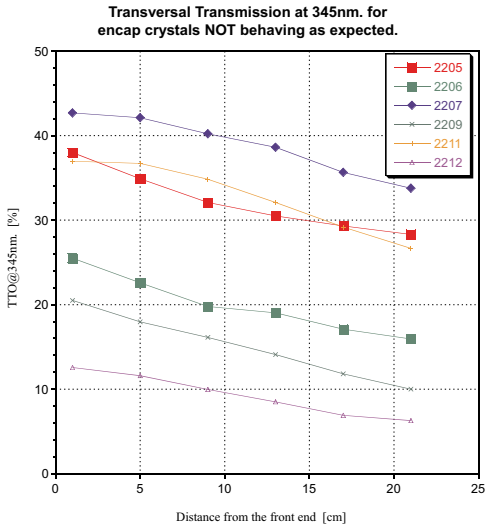

(b) Endcaps with uniformity not as expected

Figure 5.21: *Transversal Transmission at the band edge region for the set of 10 endcap crystals*

two types of behavior (positive TTG values correspond to good behavior and negative ones to bad behavior), as can be deduced from figure 5.21. However, and in order to crosscheck the validity of this parameter to predict uniformity behaviors we extended the study to a previous batch of 12 endcaps received some months before. The resulting TTG values for these 22 endcaps correlated to their Front NUF can be observed in figure 5.22. As can be observed, the TTG allows to foresee if the light collection will be as expected or not.

The TTG is giving us an idea of how heterogeneous the crystals are intrinsically, thus the fact of having two kinds of crystals similar in TTG absolute value but different in its signs reveals that the crystals are equal but in some cases the heterogeneities are going from the small to the front end and in the other cases, the other way round. This led us to think about the cutting sense as the reason for the existence of two families in the light collection behavior. Since the beginning of PWO production, a fixed cutting sense was established that should always be respected: the seed of the ingot must match the small Front end of crystals. However, at a given moment, the application of this precept was relaxed and in consequence, we were receiving crystals randomly cut. If a crystal is cut properly, then the heterogeneities described by the TTG will be as expected and hence, the combination of focusing, absorption plus intrinsic heterogeneities will slightly favor the rear

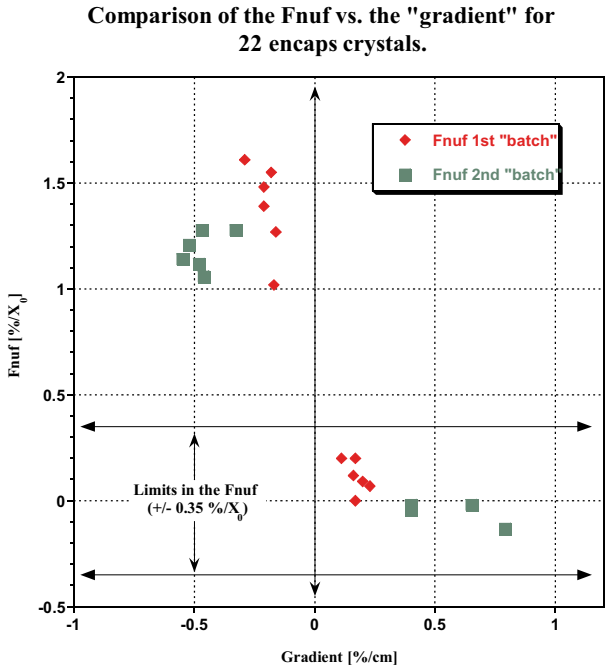

Figure 5.22: *Correlation Fnuf vs. Transversal Transmission Gradient for 22 endcap crystals.*

end, yielding an uniformity curve as expected (see figure 5.19-(a)). However, if the cutting sense is not respected, the intrinsic heterogeneities of the crystal will play an opposite role in the light collection, favoring in this case the front end, as depicted in figure 5.19-(b). Of course, since this problem was detected, the information was transferred to producers. In any case, as we shall see, for the batches already delivered (1^{st} to 7^{th}), the distinction between well and bad cut crystals can always be made by using the Transversal Transmission Gradient.

5.6.2 Application to barrel crystals

As stated above, the cutting sense of PWO crystals became random since a given moment we can not establish precisely. So, this problem affected for sure barrel crystals from Batches 1 up to at least Batch 7, since we could not react until we discovered the origin of the problem and when we did, the production of 7th batch was already finished.

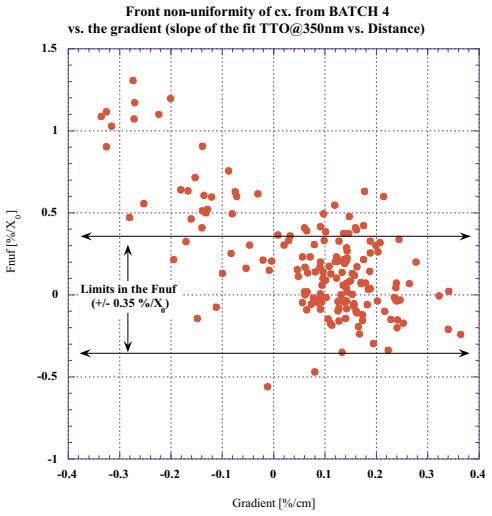

(a) Batch 4

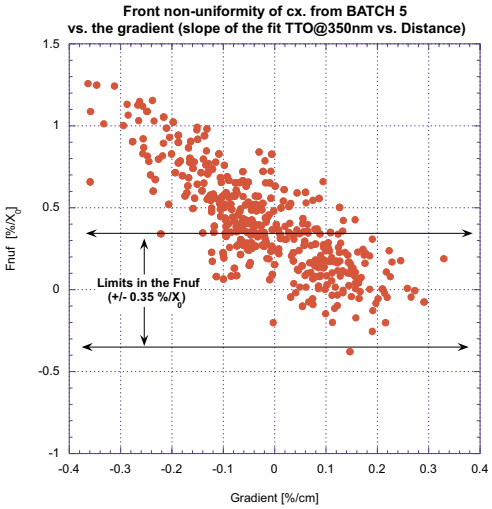

(b) Batch 5

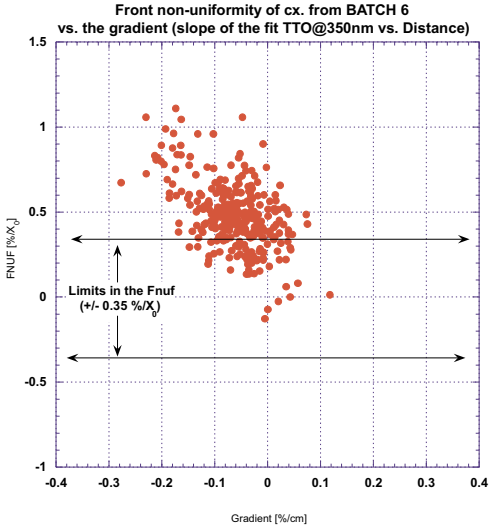

(c) Batch 6

Figure 5.23: *Front Non-uniformity vs. Transversal Transmission Gradient for Batches 4, 5 and 6*

It is important to clarify that in the case of barrel crystals the data used to calculate the TTG is from ACCoCE 1, hence, we are acquiring 11 transversal positions instead of 6, which was the case for the endcaps described above, and besides, we are not any more acquiring data at 345 nm. Therefore, for barrel crystals, the calculation of the TTG will be made by calculating the slope on the plot of the transversal transmission at 350 nm (the closest wavelength available) vs. the position from front end in cm (thus we fit 11 points).

In plots (a) and (b) of figure 5.23, we can observe the correlation Fnuf vs. TTG for Batches 4 and 5. Similarly to what was presented for the two batches of endcap crystals depicted previously, the TTG helps to determine the crystals cut in the good way (the majority in the case of Batch 4). The crystals showing a too high Fnuf can be identified by its too negative TTG in plot (a), which in fact correspond to the tail at the right of the distribution showed in figure 5.12-(b). Respect to Batch 5 (plot (b) in figure 5.23), we can see that it looks different than Batch 4. Instead of having a cloud of points centered within Fnuf limits and some wrongly cut crystals with too positive Fnuf, we have a continuum of points from too positive to too negative TTG values. However, Batch 6 (plot (c) in figure 5.23) is even more strange: in spite of presenting random cutting senses (we communicated the problem to BTCP producers just before batch 8 production), the total dispersion of the TTG values is much more reduced. The explanation of this is related to the change of doping already mentioned that took place during Batch 5 production. This is explained in following subsection.

5.6.3 Change in doping and its influence on TTG dispersion

As was already mentioned in previous section, during Batch 5 production, BTCP producers switched from single La doped crystals to double Nb+Y crystals. The reason for this change is motivated by the important improvements achieved in radiation tolerance with double doped crystals [40]. In fact, Batch 5 was a transition batch between fully single doped crystal batches (Batch 4 and precedents) and fully double doped crystal batches (Batch 6 and followings). In consequence, batch 5 was presenting two types of crystals showing slightly different behaviors, as is depicted in figure 5.24.

In this plot we correlate Light Yield and Longitudinal Transmission at the band edge (360 nm) with the producers numeration, seeing clearly two types of behavior for each half of the batch. A higher LY and LT at 360 nm characterized the first half (BTCP numeration from crystal 850 up to 1050), whereas the second half (BTCP numeration starting at 1050) was characterized by lower LY and LT at 360 nm. The fact of knowing that there were two types of families inside Batch 5 and knowing as well that LY and LT at the band edge were changing in the middle of the batch (the moment when producers switched from single to double doping), made us think that we could maybe distinguish

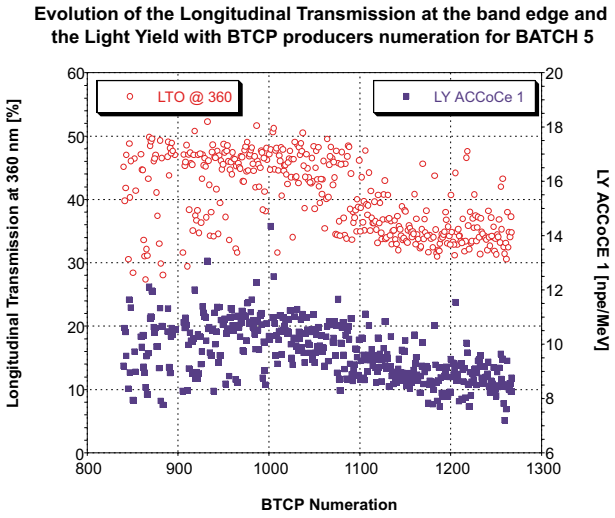

Figure 5.24: *Variations in Light Yield and Longitudinal Transmission at 360 nm for Batch 5 according to BTCP numeration.*

between single and double doped crystals using any of these parameters (LY or LT). Thus, we constructed plots comparing the Light Yield and the Front NUF with Longitudinal Transmission at the band edge for the three batches. These plots together with LT at 360 nm distributions for the three batches are included in figure 5.25.

In this plot we can clearly observe the differences between the batches: Firstable, Batch 4 shows a LT at 360 nm distribution centered in $\sim$ 46.5 %, with LY values around 10 pe/MeV and a Fnuf distribution being mostly well centered. However, Batch 5 shows a double-peaked LT distribution, with maxima at $\sim$ 34.5% and $\sim$ 46.5%. For the lower LT peak, LY was smaller than for the higher LT peak ($\sim$ 9 pe/MeV compared to $\sim$ 10 pe/MeV) and Fnuf was shifted to too positive values. On the other hand, Batch 6 was fully corresponding to a LT distribution centered in $\sim$ 34.5%, presenting LY and Fnuf values as the ones seen for Batch 5 crystals corresponding to left LT peak.

In consequence, we can state that the change in doping can be recognized by a shift in the band edge. Such a shift affects to the Longitudinal Transmission measured at wavelengths located near the band edge region (e.g. 360 nm) being this parameter typically $\sim$ 46.5 % for single La doped crystals and $\sim$ 34.5 % for double doped Nb+Y crystals. Besides, we can say that this change in dopant is providing a slight Light Yield loss (from $\sim$ 10 to $\sim$ 9 pe/MeV) and shift in Fnuf towards too positive values (from $\sim 0\ \frac{\%}{X_0}$ to $\sim$ 0.5

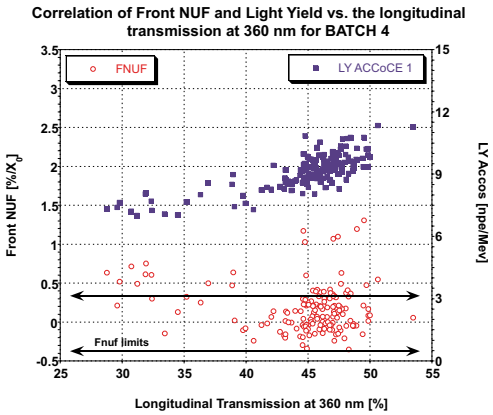

(a) Batch 4

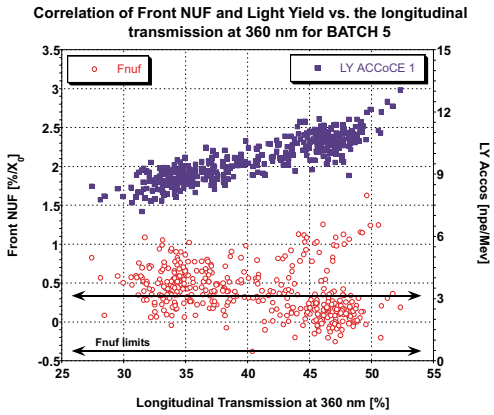

(b) Batch 5

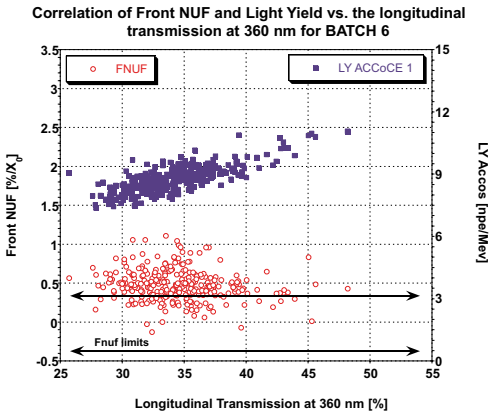

(c) Batch 6

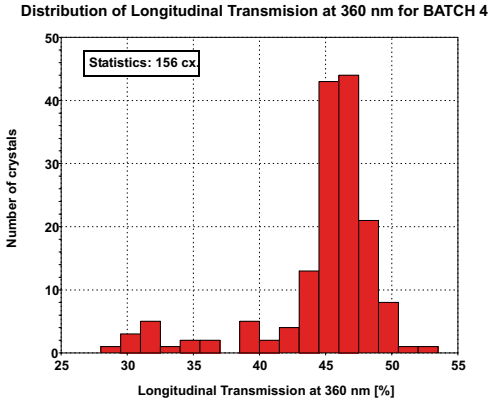

(d) Batch 4

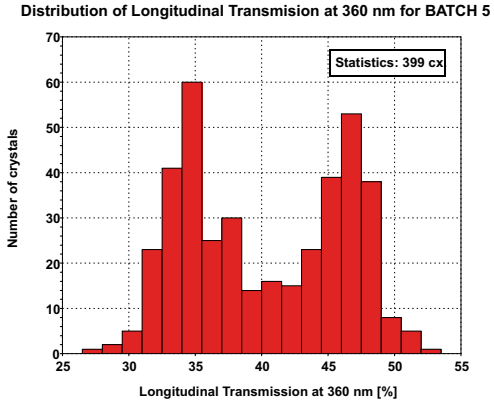

(e) Batch 5

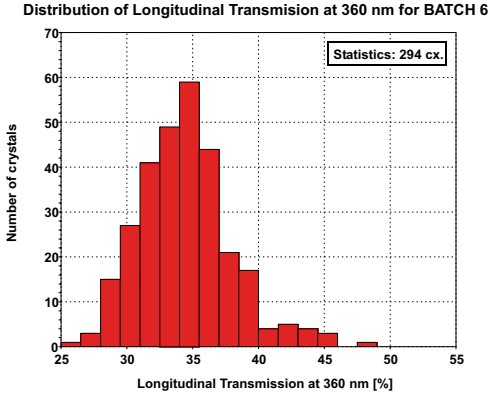

(f) Batch 6

Figure 5.25: *Behavior of Fnuf and LY depending on the Longitudinal Transmission at 360 nm for Batches 4, 5 and 6.*

$\frac{\%}{X_0}$). These two apparent drawbacks are not dramatic: even with this LY loss, we still have at least 95% of crystals for these batches over the 8 pe/MeV limit imposed in specifications and the Fnuf shift to positive values can be easily corrected with a stronger depolishing of face D, as can be seen in the figure depicting the results after uniformisation for batch 6 (figure 5.13-(d)). In any case, the suppression of radiation damage provided by the double doping is so important than it is an argument strong enough on itself to justify the change.

Once we establish a procedure to distinguish between single and double doped crystals we tried to analyze the influence of this crystal change on the Transversal Transmission Gradient of crystals (TTG). In this manner we reconstructed the plot (b) from figure 5.23 (which depicts Fnuf vs. TTG for Batch 5) but making in this case a difference between single and double doped crystals. The results are depicted in figure 5.26.

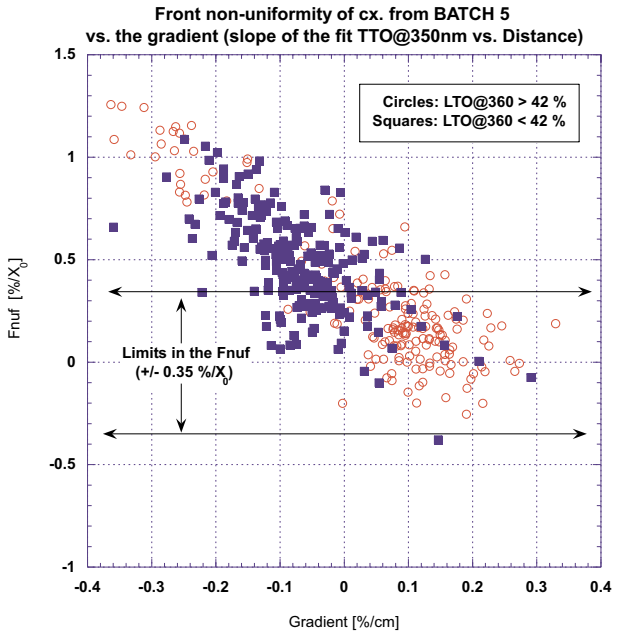

Figure 5.26: *Correlation Fnuf vs. Transversal Transmission Gradient for Batch 5, distinguishing between single and double doping.*

As we can see, single doped crystals (LT at 360 nm higher than $\sim 42\%$) show a typical Fnuf vs. TTG behavior as was seen for batch 4 (figure 5.23-(a)), characterized by a cloud of well centered data (crystals well cut) and some wrongly cut crystals showing too negative TTG values and too positive Fnuf values. However, double doped crystals (LT at 360 nm lower than $\sim$ 42%) present a Fnuf vs. TTG behavior much closer to Batch 6 (figure 5.23-(c)), being characterized by a simple cloud of data (even if cutting sense was

still random, like for Batch 4 and 5) with TTG values closer to zero and Fnuf values around 0.5 $\frac{\%}{X_0}$. Hence, we can conclude that single doped crystals are less homogeneous longitudinally, and thus, the uncontrolled cutting sense produces a big dispersion in TTG values measured for them, whereas for double doped crystals, the longitudinal homogeneity is further improved, thus yielding TTG dispersion much narrower even with an uncontrolled cutting sense.

The reason for this can be found on the segregation coefficient of the different dopings used. The *segregation coefficient* is a parameter to qualify impurity introduction in the melt during crystal growth. A crystal doped with an element with segregation coefficient different from one will show a gradient along the crystal in optical properties, whereas a doping with coefficient close to 1 will present an homogeneous longitudinal distribution of the dopant. Coming back to our case, single doped crystals were doped with Lantanum (La), element that has a segregation coefficient ≈ 2.5, on the other hand, double doped crystals were doped with Niobium (Nb) plus Yttrium (Y), both having segregation coefficient ≈ 1. Hence, La doped crystals shows a concentration of the doping in the tail part of the crystals which is quite reduced respect to the seed part, thus providing important heterogeneities in the optical properties which depending on the cutting sense will yield very positive (for well cut crystals, i.e. front end of crystal matching with seed) or very negative TTG values (in the opposite case). However, double doped (Nb+Y) crystals present an homogeneous distribution of the dopant along the crystal longitudinal thus, being far less sensitive to wrong cutting senses and therefore giving TTG values closer to zero.

To conclude we can state that the Transversal Transmission Gradient is a very helpful parameter to identify inhomogeneity problems in the crystals due to wrong cutting senses being these wrongly cut crystals clearly correlated to strange Fnuf behaviors. However, this is less evident for double doped crystals as the change from single to double doping yields not only better crystals from the point of view of radiation hardness but also crystals more homogeneous. In consequence, the wrong cuttings became less important for double doped crystals, presenting narrower Fnuf distributions although shifted to higher values due to doping change. In any case from Batch 7 onwards the cutting sense is strictly controlled matching always crystal seed with front end.

In addition, we have to mention that the influence on the light collection of crystal heterogeneities lead to a redefinition of the initial transversal transmission specification. In this manner, the new specification establishes a

maximum allowable shift of 3 nm of the wavelength corresponding to a 50% transmission as was explained in section 3.6.3, whereas old specification limit was 6 nm [23]. In order to better match the TTG parameter to this specification, the former was redefined as is explained below.

5.6.4 Redefinition of the TTG

By the end of 1999 a considerable effort was made in order to be able to find a function suitable to PWO light transmission curves in the range 300 to 700 nm [24]. The final function used is the following:

$$T(\lambda) = P_3 \exp\left(\frac{P_4}{\lambda} - \exp\left[P_2(P_1 - \lambda)\right]\right) \tag{5.6}$$

where λ stands for the wavelength and $T(\lambda)$ stands for the transmission at a given wavelength λ. A set of typical parameters for this function is the following:

$$P_1 = 346nm \quad ; \quad P_2 = 0.143nm^{-1} \quad ; \quad P_3 = 70\% \quad ; \quad P_4 = 61nm.$$

The aim if this study was to be able to calculate the transmission at a given wavelength directly on the fitted function, thus avoiding the fluctuations induced by using directly the ACCOS devices raw data, as explained in section 3.6.3. This is specially important for the wavelengths that must present a minimum transmittance (i.e. the ones appearing in specifications). This allowed to redefine the parameter mentioned in sections above, the Transversal Transmission Gradient as follows:

The TTG definition used for barrel crystals in previous sections was analyzing the variation in the Transversal Transmission at 350 nm (roughly, the band edge) all along the crystal. However, and in order to agree with the existing specifications related to transversal transmission (see section 3.6.3), we decided to study the variation along the crystal of the wavelength corresponding to a 50% transmittance. Of course, this wavelength is calculated on the fitted function. In this manner we can construct new plots similar to the ones depicted in figure 5.21 but in the Y-axis we represent now the wavelength for a 50% transmission ($\lambda_{50\%}$), keeping position at X-axis (although in millimeters now). Then we fit the resulting data to a line and its slope (with units nm/mm) is our redefined Transversal Transmission Gradient.

Of course, and by definition, this new TTG parameter is almost equivalent to old one. This is illustrated for 259 crystals from Batch 6 in figure 5.27.

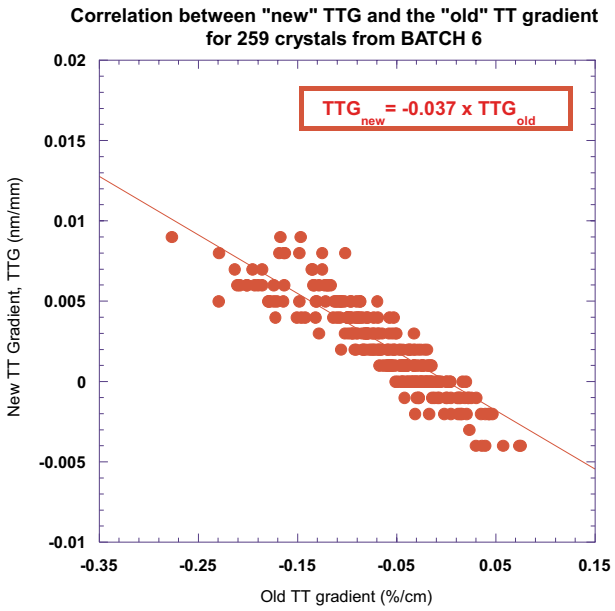

Figure 5.27: *Correlation between "old" and "new" Transversal Transmission Gradient for Batch 6.*

As we can see in plot above, both parameters are clearly correlated. If we re-plot the dependence of the Fnuf with the TTG using the new definition for any of the batches discussed above we can see that the new plot looks very similar to the one got using the old definition. This can be observed by comparing plot (c) in figure 5.23 (corresponding to Fnuf dependence with old TTG for Batch 6) with figure 5.28, which is the same[e] but using TTG values calculated using redefinition explained above. The only visible differences are coming from the change in sign introduced with the new TTG definition, thus implying that crystals wrongly cut will not show anymore too negative TTG values, but too positive ones.

In future publications and reports, this important parameter (Transversal Transmission Gradient) will be always calculated according to the redefinition explained in this subsection.

[e]Figure 5.23-(b) shows the results on 294 crystals, whereas statistics for figure 5.28 is 487 crystals.

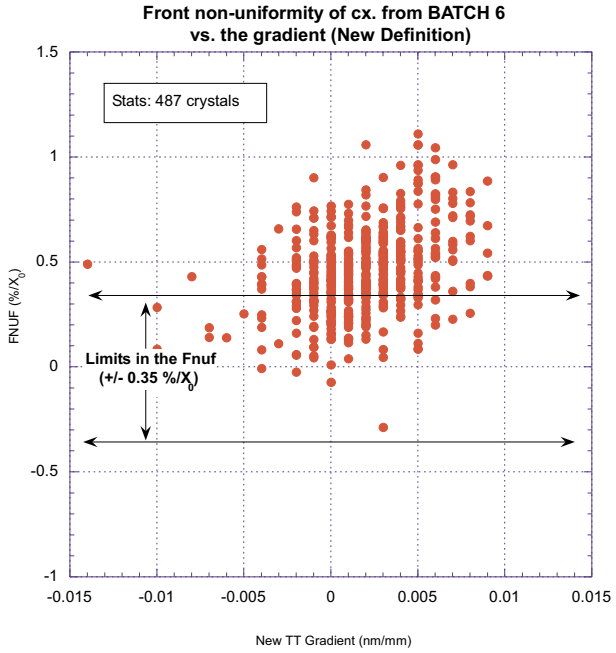

Figure 5.28: *Front Non-uniformity vs. redefined Transversal Transmission Gradient for Batch 6.*

5.7 Influence of the wrapping on the uniformity

It has been already mentioned that crystals must be depolished in one longitudinal face in order to provide a uniform light collection. This depolishing destroys the total reflection in that face, thus increasing the amount of light that leaves the crystal. In order to recover that light we use tyvek envelopes for measuring the Light Yield of the crystals, as explained in previous chapter. However, tyvek is not the final reflector that will be used to wrap the crystals in the final detector. The final reflector is a 25 μm aluminium foil with quartz deposited. This foil will be attached to the alveolar structures that will hold crystals. Therefore, it is important to verify that the uniformities measured with tyvek wrappings are equal to the ones measured with the final alveolar structures presenting the final reflector on their inner sides.

In order to verify this we measured two crystals with three different wrappings: tyvek, aluminized mylar and final alveolar structure with the final reflector. The two crystals were presenting very different uniformity curves as one of them was completely polished and the other was lapped in one face.

The results are given in figure 5.29.

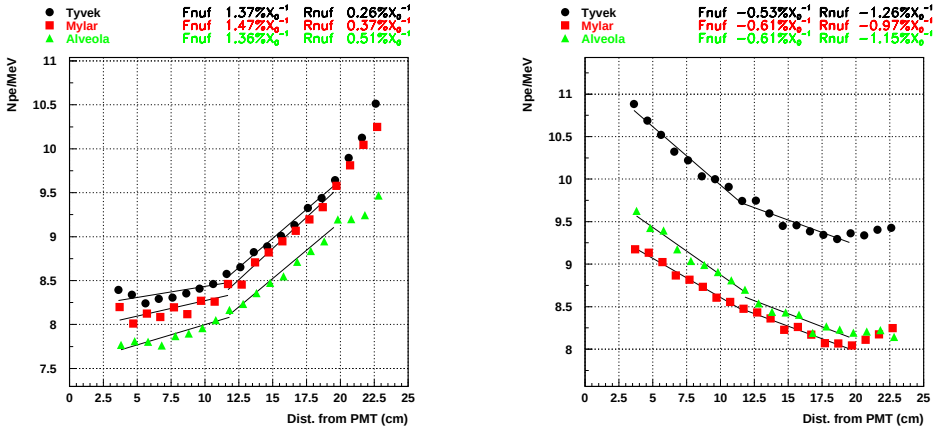

(a) All faces polished

(b) One face lapped

Figure 5.29: *Light Yield curves for a crystal with all faces optically polished (a) and for a crystal with one face depolished (b) using different wrappings.*

As we can see in this figure, the uniformity is, for both crystals, independent on the wrapping used. Besides, we can notice that the LY is more sensitive to the quality of the employed wrappings in the case of the lapped crystal. This is an expected result, as when a crystal is completely polished, the total reflection dominates, thus being not too sensitive to external wrappings, whereas for a crystal with one face lapped, the light has a bigger chance of leaving the crystal, thus the recovery of this light depends on the quality of the reflector. Observing figure 5.29 we can notice that aluminized mylar and final alveolar structures are providing a LY which is $\sim 90\%$ of the one got with tyvek, which is a percentage that agrees with existing literature [41].

Chapter 6

EXTRACTING LIGHT FROM CRYSTALS

As was explained in previous chapters, the optimization of the light collection in crystal calorimeters is a specially important and complex matter. An aspect that must be considered during this optimization is the reduction of Fresnel reflections at the interface between the crystal and the photodetector. This is achieved by avoiding the presence of any air gap between them, which can be readily obtained using silicon gels, oils or optical glues to perform the contact. The use of optical glues allows, in addition, to ensure the mechanical adhesion, which in our case is mandatory, as we shall see. These considerations, among others, lead CMS ECAL community to start a quest for the most suitable glue to perform the optical contact and also to start thinking about the techniques needed to accomplish the high rate of gluings per day requested.

In this chapter we will report on many aspects regarding the gluing of the photodetectors to the crystals. As we already dedicated a whole chapter to describe the PWO crystals, we will now dedicate a section to the Avalanche Photodiodes, the photodetector chosen for the CMS ECAL barrel and which will be glued to barrel crystals. Then, we will describe in detail all what concerns the optical glue chosen for the CMS ECAL barrel. Later we will report on the gluing techniques and procedures which have been specially developed for the PWO crystals. To finish, we will illustrate the results achieved during this complex gluing task.

6.1 The Avalanche Photodiodes

The relative low Light Yield of $PbWO_4$ scintillating crystals together with the high magnetic field and the adverse radiation environment in CMS strongly limits the choice of suitable photodetectors.

From these inconvenients, the first, related to low Light yield, implies that unity gain devices, such as silicon or vacuum photodiodes, are not capable of delivering the noise performance needed for electric signals. The second is related to the high magnetic field and it means that we have to rule out vacuum devices in the central region (barrel), besides it limits the number of gain stages usable in the forward region (endcaps). The third inconvenient (hostile radiation levels, mainly in high η regions) excludes solid-state and hybrid devices in the forward direction. In addition, the high bunch-crossing frequency at the LHC (25 ns) demands fast response photodetectors.

The final photodetectors chosen are silicon Avalanche Photodiodes (APD) for the barrel region and Vacuum Phototriodes (VPT) for the endcaps. In this section, we will be focused on the former ones (APDs). Of course, APDs have been chosen as they meet the requirements mentioned above. Therefore, the APDs

1. provide an internal amplification to allow dealing with the low light signal from crystals,

2. have a response fast enough for LHC requirements,

3. resists to radiations fluxes[a] up to 2×10^{13} neutrons/cm^2,

4. allow working in the 4 T CMS magnetic field.

[a]In the barrel region the maximum neutron fluence is estimated to be 2×10^{13} neutrons/cm^2 with an energy spectrum peaking around 1 MeV. The dose is estimated to be $\approx$ 300 Gy [9].

6.1.1 APDs working principle

The large-area silicon avalanche photodiodes are relatively new devices in high energy physics experiments. In the last years, they have undergone a considerable development. The APDs are similar to silicon photodiodes, with the exception of a buried p-n junction reverse-biased at a very high electric field. A sketch of APDs internal structure is depicted in figure 6.1.

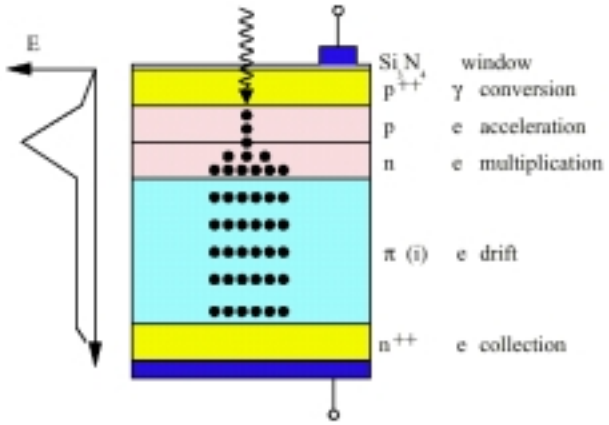

Figure 6.1: *Sketch of Avalanche Photodiodes working principle.*

The APDs working sequence can be described as follows[b]: the light emitted by the crystal enters the device via the p^{++} layer and is converted into electron-hole pairs in the p^{+} (or p) layer. Then, the electrons are accelerated by a high field towards the p-n junction. There they are amplified by impact ionization with the development of an avalanche in the n^{+} (or n) layer and finally drift to the n^{++} electrode (where the charge is collected) via a π-material. A rough estimation of the electric profile in function of the layers depth is also depicted in figure 6.1.

[b]With + or ++ we denote the amount of doping resulting in very high or even higher conductivity.

6.1.2 Characteristics of APDs

The APDs for the ECAL of CMS were initially developed under contract with two manufacturers: EG&G Optoelectronics[c] in Canada and Hamamatsu Photonics in Japan. Since 1995 around 30 different APD prototypes delivered by these two producers were investigated. In July 1998 the choice between the two vendors was made in favour of Hamamatsu Photonics. Then, and during a year, some more (10) prototypes were studied. Finally, in July 1999, the decision on the final structure was made. The APDs are characterized by Hamamatsu prior to its delivery. Once they are received at CERN APD Laboratory, they are irradiated and are again characterized on a sample basis.

The quantum efficiency of recent APDs is $\sim 72\%$ at 420 nm, thus being quite high at the $PbWO_4$ scintillation peak. Latest generation avalanche photodiodes allow to measure with a gain of 50 for a bias voltage ~ 380 Volts, as can be deduced from figure 6.2. In this figure, we plot the gain as a function of the applied bias voltage for a recently delivered Hamamatsu APD.

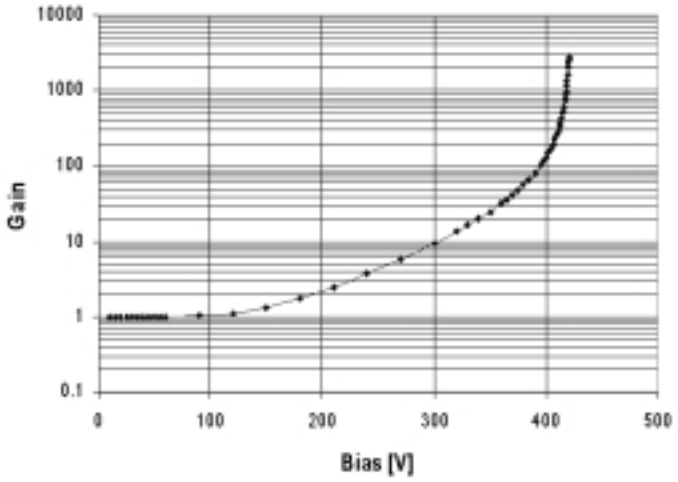

Figure 6.2: *Gain curve for a recent Hamamatsu APD.*

The stability of APDs depends strongly on the stability of the gain. On the other hand, the gain depends on the mean free path length of the electrons and therefore on the temperature. Besides, as APDs gain is a rather steep function of the bias voltage (see figure 6.2), a stable voltage source is required. The relative dependence of gain (M) on these two parameters is depicted in figure 6.3, where V stands for Voltage and T for Temperature. Currently found

[c]Actually Perkin Elmer Corporate.

coefficients for the dependence of M on V and T are, at gain 50, 3.3%/V and -2.3%/°C.

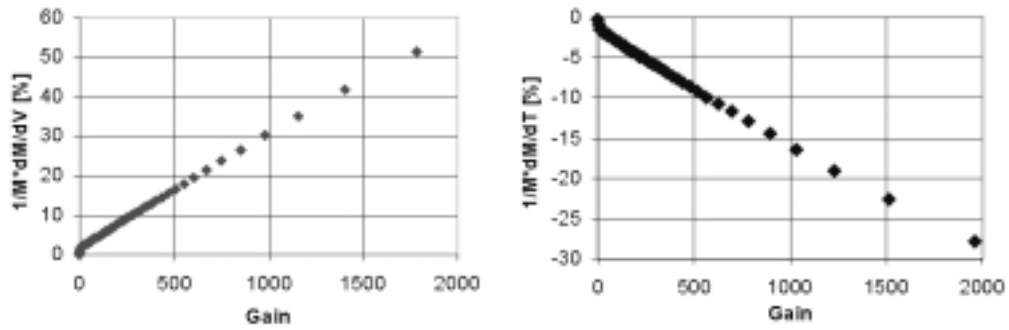

(a) $\frac{1}{M}\frac{dM}{dV}$ (b) $\frac{1}{M}\frac{dM}{dT}$

Figure 6.3: *Relative gain dependence on the bias voltage (a) and on the temperature (b) as a function of the gain.*

The APDs do have an impact on the resolution of the calorimeter. As explained in previous chapter and in section 2.4.1, the resolution of an electromagnetic calorimeter can be expressed as:

$$\frac{\sigma}{E} = \frac{a}{\sqrt{E}} \oplus \frac{b}{E} \oplus c \tag{6.1}$$

where a, b and c correspond to stochastic, noise and constant term, respectively. The APDs contribute to the three terms:

- the stochastic process of avalanche multiplication contributes to stochastic term a as an excess of the fluctuations of photoelectrons, expressed as $\sqrt{F/N_{pe}}$. The excess noise factor F, which is given by $\sqrt{1+(\sigma_M/M)^2)}$, is related to the ratio of the ionization coefficients for holes and electrons.

- the capacitance contributes to b with a series noise term, while the dark current contributes with a parallel noise term, given by the leakage current flowing in surface of the device (I_s, which does not undergo multiplication) or through it (called bulk current, I_b, which undergoes multiplication).

- the gain variation with bias voltage and temperature (explained above) contributes to the constant term c.

As stated at the beginning of this section, LHC imposes severe radiation conditions, thus, it is very important to understand the effect of radiation on the performances of the APD. Radiation damage on APDs may occur through two main mechanisms:

1. surface damage, or the creation of defects in the front layer may lead to an increase in the surface current and a decrease in the quantum efficiency,

2. bulk damage, due to the displacement of atoms from their lattice sites, causes an increase in the dark current. It depends on the non-ionizing energy loss of the radiation in the medium, which varies with particle type and energy. Normally 1 MeV neutrons are taken as reference.

The main consequence of neutron damage is the creation of defects in the silicon lattice, like vacancies and displacements of atoms, which can be either isolated point defects or more complex defects, like clusters. Because of these defects, new allowed energy levels appear in the forbidden gap of the semiconductor. These levels cause an additional dark current, which increases linearly with the concentration of defects, and thus with the neutron administered dose.

During last years many studies have been performed on the APDs. From them, we can conclude [9] that the dark current induced by the irradiation shows a linear behavior with the administered fluence. Besides, concerning the recovery, we can affirm that the time dependence of recovery for APDs shows a similar behavior to the one observed for PIN diodes, at least regarding fast components. Measurements also indicate the presence of a long recovery time constant. In addition, no difference is observed in the recovery of APDs when kept under bias or zero bias voltage. Similarly, no difference is observed in the recovery time constants of APDs irradiated at different fluences. It is very important to mention that there is a clear evidence for strong reduction of the APDs recovery time at low temperature.

Long term exposure to neutron irradiation will lead to a domination of the bulk current on the electronics noise. It is therefore mandatory to foresee its evolution during the CMS operation, taking into account damage and recovery produced according to LHC running schedule. Thus, a simple

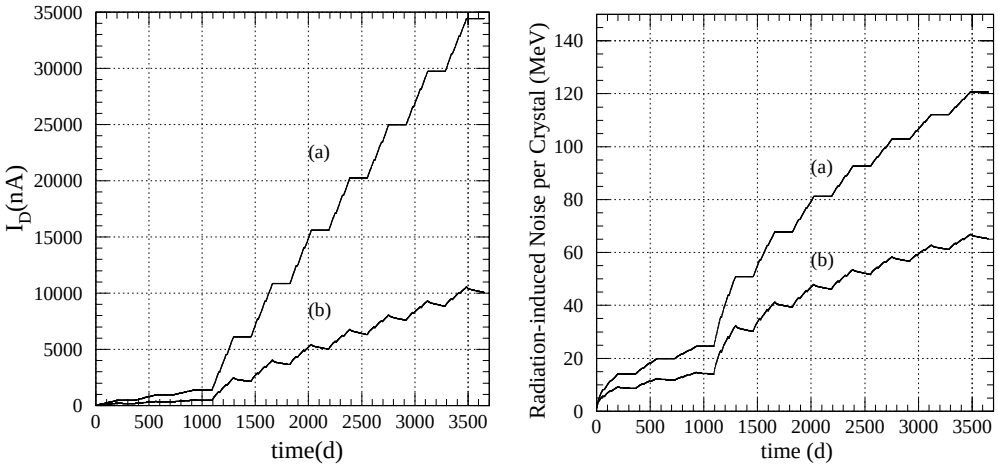

(a) Radiation induced dark current (b) Radiation induced noise

Figure 6.4: *Dark current into APDs (left) and noise per crystal (right) induced by radiation according to foreseen LHC running scenario in realistic conditions (b-labeled curves) and with the hypothesis of no recovery (a-labeled curves).*

model has been conceived to predict dark current behavior in these conditions [9]. According to this model, and taking into account foreseen LHC schedule and the measured weight and lifetime of radiation induced traps in the silicon, we can estimate the increase of dark current and the resulting contribution to the noise, as is illustrated in figure 6.4 (left and right plot, respectively). In the two plots appearing in this figure, the curves labeled as (b) correspond to realistic conditions (measured parameters have been used for the damage and recovery at 18°C), whereas curve labeled as (a) does not take into account recovery.

6.1.3 The capsules

The area of each APD is 5×5 mm^2, which is quite reduced respect to barrel crystals rear face (roughly $\sim$ 25×25 mm^2), thus, in order to increase photo-statistics, it was decided to glue two of these APDs per barrel crystal. Therefore, the acceptable APDs are sent to the IPNL[d] where they are assembled into what we call **capsules**, which comprise two APDs per unit enclosed on a plastic frame and connected to a kapton cable (see the aspect of final

[d]Institute de Physique Nucleaire de Lyon, France.

APDs in figure 6.5-a and the final capsules in figure 6.5-b).

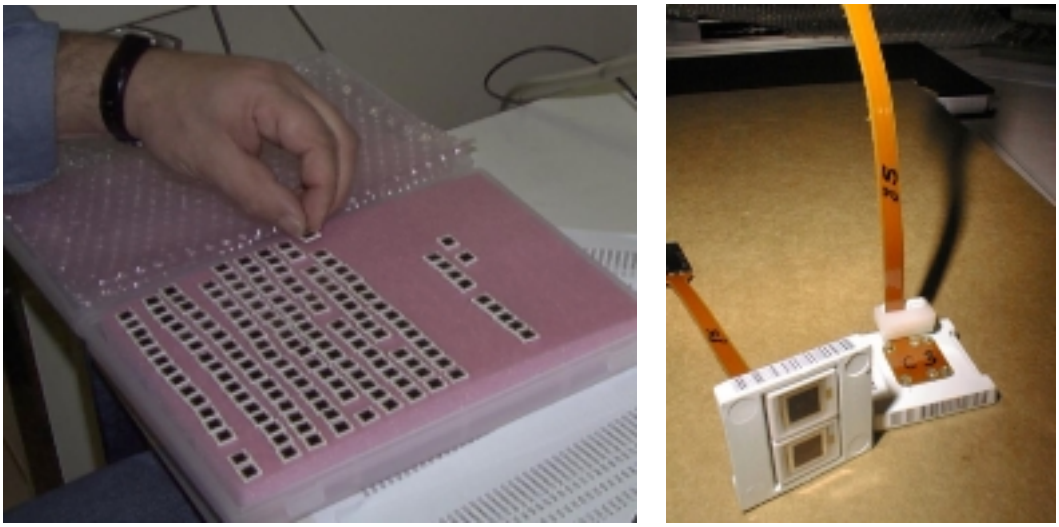

(a) APDs (b) Capsules

Figure 6.5: *Photograph of several APDs (left) and aspect of them once they are mounted in a capsule (right).*

The capsules are as well characterized at IPNL to verify parameters measured previously at the producers and at CERN APD Lab. Once the capsules are completely acceptable, they are delivered to the CMS ECAL Regional Centres, where they are glued to PWO crystals rear face (i.e. two APDs are glued to each crystal).

6.2 The glue

In this section we are going to focus on the importance of having a suitable glue in between crystal and photodetectors. This glue must satisfy several requirements which will be explained in following subsections. We will also report on the different candidates considered, describing their advantages and drawbacks. Finally, the properties of the chosen glue will be commented.

6.2.1 Importance of the glue

There are several reasons why the characteristics of the optical glue used to couple PWO crystals and its photodetectors are extremely important. Among others, we can find optical, chemical and mechanical reasons that lead to impose strict requirements on the glue [42]. The list of requirements is the following:

1. Refractive index:

Lead tungstate crystals present a low Light Yield, thus it is important to maximize the amount of photons emitted by them reaching the photodetector. As we shall see, its high index of refraction ($n_{PWO} = 2.3$) yields important losses by total reflection if the optical matching is not performed with a suitable glue.

An incident ray of light approaching a boundary between two media (1 and 2) with different indices of refraction can experience reflection or refraction (transmission) as depicted in figure 6.6. The reflected ray presents

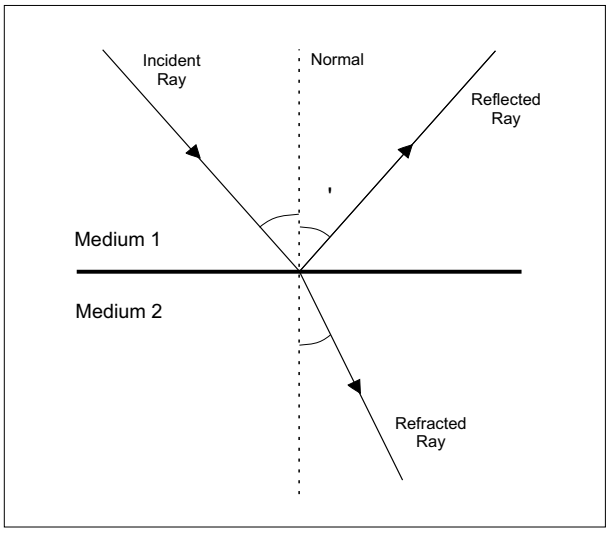

Figure 6.6: *Reflection and refraction of light at the boundary between two materials with different indices of refraction.*

the same angle respect to the normal than the incident ray, thus $\theta_1 = \theta_1{}'$ in figure 6.6, whereas the refracted ray, if present, will show a different angle θ_2. Snell's refraction law gives us the expression to calculate the refracted angle

θ_2 according to θ_1 and the indices of refraction of medium 1 and 2, as follows:

$$n_1 \sin\theta_1 = n_2 \sin\theta_2 \tag{6.2}$$

As we can deduce from this expression, the value given by $\theta_1 = \arcsin(n_2/n_1)$ is yielding the maximum possible incidence angle providing a refracted ray. This is the so-called critical angle (θ_c). For an incidence angle $\theta_1 > \theta_c$, the refraction (transmission) is not possible, and thus total reflection will occur. If we consider that light travels through a number of media m, of which l is the one with lower index of refraction, then Snell's law becomes:

$$n_1 \sin\theta_1 = n_2 \sin\theta_2 = \ldots = n_l \sin\theta_l = \ldots = n_m \sin\theta_m \tag{6.3}$$

and thus, the critical angle θ_c for the incident ray on first medium will be given by the ratio of the lowest index of refraction n_l and the one from first medium, i.e. $\theta_c = \arcsin(n_l/n_1)$.

The APDs show several layers which must be considered as different media: there is a silicon wafer (with $n \sim 5$ at 430 nm), coated by a film of Si_3N_4 (with $n \sim 2$ at 430 nm) and there is also a protective epoxy window with $n = 1.57$ at 430 nm. In the case of lead tungsate the index of refraction is 2.3, thus, in these conditions: n_l=1.57, and n_1=2.3, and so $\theta_c \approx 43°$. Therefore, if do not want to reduce this critical angle given by the epoxy window (what increases probability of suffering total reflection), the index of refraction of the optical glue must be at least as high as the epoxy one in the wavelength range defined by PWO scintillation spectra (350-600 nm), i.e. $n_{glue} \geq 1.57$.

2. Absorption Length:

The thickness of the glue layer is going to affect the light collection on the photodetector only if it has the same order of magnitude than the absorption length. The absorption length of a given medium can be defined as the distance that a photon of a given wavelength must travel through it to reduce its transmittance in $1/e$ of the original value. Lets assume that we have a glue layer of thickness d, through which theoretical transmission is T_t. Then, the real transmission measured through it (T_m) can be calculated as follows:

$$T_m(\lambda) = T_t(\lambda) \cdot e^{-d/\Lambda(\lambda)} \tag{6.4}$$

where $\Lambda(\lambda)$ is the absorption length.

In our case, recent APDs have a convex epoxy layer that makes the glue layer thickness to range from 0μm (center of APD) to 200 μm (sides),

therefore, we can assume an averaged thickness value of 100 μm. In these conditions, an absorption length for that glue of $\sim$ 10 cm at 430 nm would yield a relative loss in transmission $\sim 0.1\%$, whereas an absorption length of $\sim$ 0.1 cm at 430 nm would yield a loss in transmission $\sim 10\%$ (see $\Lambda(\lambda)$ curve for several glues in figure 6.7). This confirms that a glue with absorption length much greater than the glue layer will induce negligible losses in light collection. In consequence, we aim for a glue with $\Lambda \gg 100$ μm in the whole wavelength range given by PWO emission (350-600 nm).

3. Mechanical Adhesion:

As was mentioned in previous section, APDs will be mounted in pairs into the so called capsules (see figure 6.5-b). Once the capsules are glued to barrel crystals rear face, they must be inserted into the alveolar structures that conform a submodule. After the insertion, the kapton connectors must be grouped into a larger new connector. During this manipulation, the kapton cable of each capsule is strongly stressed as it must be plied to a S-shape. This constitutes a potential source of problems for those glues presenting a weak mechanical adhesion even after a complete curing (e.g. silicones), as we could easily unglue the capsule during the manipulation.

In addition, the mechanical adhesion of the capsules to the crystals is also very important as it ensures that the foreseen glue gap in between crystal and APD will continue having the same thickness for the whole CMS running period and also that the positioning of the capsule respect to crystal rear face will stay the same after the manipulations the capsule suffers during the assembly sequence.

4. Curing Time:

It has been agreed that we must be able to glue a maximum rate of crystals of 50 units per day in order to comfortably comply with the CMS construction schedule. In addition, we have to take into account that the gluing operation will be performed on specially dedicated gluing benches that allow performing fast gluings and that integrate some quality control tools. We also have to bare in mind, that most of valid glues are very sensitive to manipulations on the capsule frame which are performed immediately after the gluing. Therefore, the gluing benches must include a storage position, and it will be the the glue curing time what determines the volume of crystals that this position must contain. The requirements imposed by CMS construction schedule and the

gluing bench desing lead us to focus on those glues with curing time equal to 2-3 days at maximum.

5. Chemical Activity:

In the gluing of a capsule to a crystal we can consider two kind of contacts: a) PWO crystal with capsule plastic frame and b) PWO crystal with APD epoxy window. Besides, the glue can eventually enter in the region in between capsule plastic frame and APDs (see figure 6.5-b), thus getting in touch with APDs contacts and kapton. Of course, the glue must be chemically inert with all the parts participating in the gluing, since the opposite would have unpredictable consequences.

6. Ageing:

The optical, mechanical and chemical properties of the glue must remain unchanged during the whole CMS lifetime (5 years of construction and 10 years running). The difficulties predicting possible changes induced by glue ageing at normal temperature can be overcome with a technique based on the heating of the glue specimens. In order to use this technique, we must also assume a relation between temperature and ageing (time) which is given by Arrhenius law [42]:

$$t = C \cdot \exp \frac{E_a}{KT} \tag{6.5}$$

where t is the time to reach a specified endpoint or lifetime at the temperature T (in Kelvin), E_a is the activation energy (in eV), K is the Boltzmann constant (eV/K) and C is a constant depending on the material.

7. Radiation Hardness:

The properties of the glue must also remain unchanged during the 10 years of CMS running, even if in this time, it is expected to receive 2×10^{13} neutrons per square centimeter with an energy spectrum peaking around 1 MeV, among other particles. In this hostile environment, using a radiation-hard glue is mandatory for our purposes.

6.2.2 Choice of the glue

The study of some optical glues suitable for CMS requirements started a long time ago. Already in 1995, a study was made [43] from which the most promising glue was the so called Cargille thermoplastic Meltmount 1.704, a glue which must be heated up to $\sim$70°C to become liquid and thus to ease handling. This glue cures when the temperature slows down, allowing reversible mounting just by heating it up.

Later on, the matrices used for CMS ECAL Testbeams in 1997 and 1998 demanded already the use of a radiation hard optical glue. The one most commonly used during this period was the so called General Electrics RTV 615, a two components glue which, as all two parts glues, starts to cure since the two components get in contact. Besides, at CERN RC several tests were performed during these years with the first glue mentioned (Meltmount 1.704) noticing the difficulties arising when trying to perform bubble-free gluings with this thermoplastic glue. These difficulties were coming from the variable viscosity of this glue in function of the temperature, thus demanding very quick gluing operations. During the gluing of ECAL matrix called Proto 99 (used for 1999 ECAL Testbeams) we used a new glue very promising optically called Histomount, from National Diagnostics. This one is a solvent-based glue, i.e. cures by evaporation of the solvent. The results were not as expected, since adhesion was not at all ensured, and besides, some APDs appeared not to be working after the gluing, thus indicating maybe some chemical incompatibility among the parts participating in the gluing.

The study went on during following years, being mainly performed by Marco Montecchi, from INFN-ENEA/Rome Regional Centre. He has studied all the requirements listed above for many optical glues. Among them we can find the ones mentioned in previous paragraphs (Meltmount 1.704, RTV 615 and Histomount) although many other possible candidates were also considered. Table 6.1 lists all the considered candidates, giving some important characteristics of the glues together with some basic optical parameters [42].

This table gives for each considered glue, 1) the manufacturer, 2) the type of glue (one or two components), 3) the time it needs to cure together with the factor inducing the curing, 4) the index of refraction at 430 nm (PWO peak emission), 5) the absorption length in centimeters averaged over the whole

Table 6.1: *Summary of investigated glues.*

Glue	**Producer**	**Parts**	**Curing**	n@**430nm**	Λ**(cm)**	**D/E(%)**
Histomount	National Diagnostics	1	12h@RT (solvant evaporation)	1.63	>10	11.2
RTV 3145	Dow Corning	1	3d@RT (reaction with air)	1.49	1.44±0.06	9.4
NOA 61	Norland Products	1	∼10min (UV irradiation)	1.59	0.55±0.01	10.9
UVO114	Epotek	1	∼2min (UV irradiation)	1.60	0.37±0.01	10.7
Meltmount 1.582	Cargille	1	(thermoplastic)	1.60	6.8±1.5	11.1
Meltmount 1.704	Cargille	1	(thermoplastic)	1.73	0.10±0.01	10.3
Naphrax	North. Biological Supp.	1	(thermoplastic)	1.80	0.086±0.003	9.7
TSE 3250	GE Bayer silicones	1	4h@100°C	1.47	>30	9.4
RTV 615	GE Bayer silicones	2	∼7d@RT	1.47	>15	9.4
RTV301	Epotek	2	1d@RT	1.57	2.8±0.03	10.9
RTV301-2	Epotek	2	2d@RT	1.60	>10	11.1
RTV 302	Epotek	2	1h@RT	1.62	0.47±0.01	10.8
X-38-406	Shin Etsu	2	4h@100°C	1.53	>25	10.3
Epoxy	Shin Etsu	2	150°C in nitrogen	1.57	12±6	10.9

PWO scintillation spectrum and 6) the ratio detected (D) to emitted (E) photons averaged over the whole PWO scintillation spectrum and the incident angles considering the realistic system given by:

$$PWO//Glue(0.3mm)//Epoxy(0.3mm)//Si_3N_4(65nm)//Si$$

Details on the calculation of n, Λ and D/E can be found elsewhere [42]. There are several things that must be clarified on this table. When we state that a glue is thermoplastic (as Meltmount 1.704, for example), we mean that its curing process is as follows: it must be heated before manipulation and it cures as it cools down, which normally is very quickly (that is why we did not quote any figure for its curing time). On the other hand, some other glues like TSE 3250 or Epoxy must be heated up to polymerize, thus we quote no figure for curing time again. Besides, two component glues polymerize since the two parts get in contact (so, we did not specify the reason why they cure), generally not immediately, that is why we did include now some curing times for these glues.

All these considered candidates were analyzed respect to the list of requirements appearing in previous section. When considering optical requirements, we were forced to reject the two glues with absorption length verifying $\Lambda \approx 0.03$ cm. Therefore, thermoplastic glues Meltmount 1.704 and Naphrax (see Λ in table 6.1) were considered as not suitable. Besides, when considering similar types of glues as for example UV curing ones (NOA61 and UVO114), we rejected the one with worst optical behavior, remaining with the other. In this manner, UVO114 was rejected among the UV curing ones, and RTV 302 was rejected among the two parts Epotek ones. Then, radiation hardness tests revealed RTV 301 and RTV 301-2 to be not enough radiation hard, as their Λ was decreasing considerable after irradiation. Two of the glues that needed to be heated up in order to cure them (namely TSE 3250 and X-38-406) showed a bad mechanical adhesion after cooling down, thus being rejected. Two more glues (Meltmount 1.582 and Epoxy) were rejected due to its complicated curing conditions. Realistic tests were performed at CERN RC with thermoplastic Meltmount 1.582 to check if this glue could be adapted to our needs. Problems like possible crystal or APD damage when getting in contact with the glue at 70°C, or the achievement of a bubble-free gluing in such a short time (it was cooling down very quickly) lead to its rejection. Epoxy glue was demanding to be heated up to 150°C, in presence of nitrogen, to completely cure, thus imposing too severe curing conditions for us. Finally, another of the candidates considered from the very beginning (RTV 615) was also rejected as it was presenting a too low (1.47) index of refraction, too far from our conditions ($n \gtrsim 1.57$ at 430 nm) and besides, as it was a two-parts glue its was providing many bubbles in the glue when mixing the two parts, thus requiring an extra

system to remove them.

In these conditions, only three glues were still on the list: Histomount, RTV 3145 and NOA 61. The three glues were showing their own advantages and drawbacks, as will be explained in following subsection and besides they were satisfying all the requirements exposed above, with only one exception: the index of refraction of RTV 3145 is lower than 1.57, thus reducing the critical angle and therefore, the amount of detected photons (that is why D/E ratio for this glue is the lower among the remaining three). However, there were many reasons to keep it on the list of the definitive candidates: first of all, it is the chosen glue for bonding the endcap crystals to VPTs. This means that this glue stands very well radiation, as CMS endcaps (pseudorapidity interval from 1.48 to 3.0) are exposed to a much more severe radiactive environment than barrel region. Besides, this glue is, as we shall see in following subsection, the easiest to use, and the one implying less danger for operators.

6.2.3 The final candidates

In this section we will review the characteristics of the three definitive candidates for the bonding of the APDs to CMS ECAL barrel crystals: Histomount, NOA 61 and RTV 3145. We will be focused on the advantages and drawbacks of each one.

The optical properties of these three glues are depicted in figure 6.7, as extracted from [42].

1. Histomount:

This glue consists of vinyl-toluene suspended in a mixture of xylenes. The latter inhibits the polymerization of the vinyl-toluene, thus acting as its solvent. Curing happens when the solvent (xylenes) is evaporated. Histomount is a transparent and quite liquid glue that becomes very rigid after curing. This glue has been used for most of the gluings performed for the Module 0 (see section 6.4.1) and also for the so called Proto 99 (ECAL Testbeam matrix composed of 30 crystals).

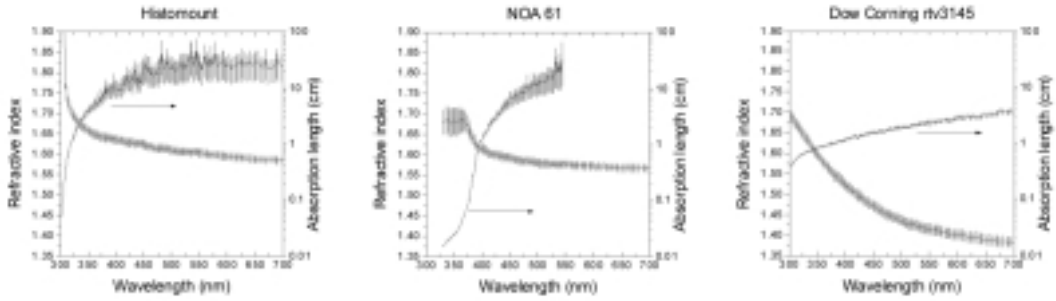

(a) (b) (c)

Figure 6.7: *Refractive index and absorption length of the three definitive candidates.*

• *Advantages:* As can be seen in table 6.1 Histomount is the best glue optically (as it presents the higher index of refraction n at 430 nm and also the best absorption length Λ) of the three final candidates. This glue also passed all ageing and radiation tests performed. Mechanical adhesion is not a problem for this glue, provided it is completely cured. No evidences of incompatibility between Histomount and any of the neighbouring parts (APDs, capsule, etc.) have not been found until now [42], in spite of initial results achieved with Proto 99 (some APDs were not working after the dismounting of the matrix and the glue was considered the responsible of this at that time).

• *Drawbacks:* The xylenes mixture (Histomount solvent), is a quite hazardous chemical product. According to EPA[e], short term inhalation exposure to mixed xylenes in humans results in irritation of nose and throat, gastrointestinal effects, mild transient eye irritation and neurological effects, among others. Also according to EPA, long term inhalation results in central nervous system effects, such as headache, fatigue, tremors and incoordination. Therefore, a complex and expensive air ventilation system would be absolutely mandatory to allow gluing operator to work safely with Histomount.

Besides, according to tests performed with CMS ECAL barrel crystals in realistic conditions, this glue takes a long time to cure, not passing the adhesion tests even after curing for one month. This constitutes an extremely severe argument against the choice of Histomount as final CMS ECAL barrel glue. They have been studied at CERN RC several possible methods to accelerate Histomount curing time. Finally, it was observed that only by heating

[e]United States Environmental Protection Agency. Web Page: http://www.epa.gov

up to ∼65°C for not more than 10h, the mechanical adhesion was further improved respect to several weeks at room temperature. However, heating up Histomount is also a dangerous task, since xylenes flash point[f] is 25°C.

In addition, the final situation is not reversible: once Histomount is completely cured, it does not allow to easily unglue (e.g. if there is presence of bubbles).

Another important problem affected the gluing of the 400 crystals of Module 0 performed during summer 1999 with Histomount: due to the concave profile of the APDs used at that time, the formation of bubbles was very easy. This constitutes a serious problem, since we have an important region of APD effective area without the right index of refraction, thus dramatically decreasing the critical angle and also the ratio detected over emitted (D/E) photons. This problem is explained in detail in section 6.4.1.

2. NOA 61:

The NOA 61 is a monocomponent resin which reticulates in 100% under UV irradiation. The maximum absorption takes place in the range 350-380 nm. The energy needed to achieve complete reticulation is 3 Joule/cm^2. It is transparent and quite liquid before UV irradiation is started. This glue has only been considered since few months (February 2000), thus we have tried it only for 50 crystals out of the 400 of Module 0' (see results in section 6.4.2).

• *Advantages:* Using a UV lamp of irradiance 1600 mW/cm^2 we found that few minutes ($\sim$ 3) was enough to provide good mechanical adhesion. This is an extremely good characteristic of this glue since it allows to glue a set of crystals (a multibox[g] of 5 crystals, for example) and cure them immediately just by irradiation with a suitable UV lamp. In this manner, the multibox would be ready to be used for the subsequent mounting step only few minutes after its gluing. This would have an important impact on the design of the gluing bench, as we would not need to foresee a gluing bench including vertical

[f]The flash point is the lowest temperature corrected to a barometric pressure of 101.3 kPa, at which application of an ignition source causes vapors of the specimen of the sample to ignite under specified conditions of the test. In general, substances with a flash-point less than 60°C are considered hazardous and must be treated with extreme care during handling.

[g]Review ACCoCE 2 description in Instrumentation section of Chapter 4 to find more explanations about multiboxes.

storage positions (it would just need a gluing post with a UV lamp pointing to crystals).

Optically it presents a good index of refraction (see table 6.1) although absorption length is the worst among the three final candidates. However, ratio D/E for NOA 61 is only less than a 3% worse than the one for Histomount. Ageing and radiation tests were satisfactorily passed by this UV curing glue. Another advantage of this glue is that it does not imply any risk for operator, provided he uses special glasses to avoid eye exposure to UV light during glue irradiation.

• *Drawbacks:* Even if gluing procedure was very simple for NOA 61 according to producers we found that, in the short time we dedicated to adapt this glue to our needs, it was very complicated to find a technique to perform good quality gluings. The problems we detected were related to strange cracks or scratches appearing in the glue few minutes after UV irradiation (see section 6.4.2).

Another drawback of this glue is that UV irradiation with our lamp (1600 mW/cm^2) must be performed through the crystal length, in order to arrive properly to crystal rear face. Thus, this damages crystal transmission, although according to our studies, several minutes of irradiation is typically lowering light transmission by only 2-3% from 380 to 700 nm. Besides, this damage is completely recovered in few days with no action on them.

UV curing glue NOA 61 is completely cured after some minutes irradiation (typically 3 min). This glue becomes very rigid after reticulation, and hence, the eventual ungluing of capsules showing problems is very complicated. This caused many problems during the gluing of Module #0', as will be discusssed in section 6.4.2.

3. RTV 3145:

This glue is a siliconic adhesive which polymerizes by reaction with air humidity. Curing times are typically 2-3 days at room temperature and at a relative humidity of 50%. The curing time can be reduced by increasing relative humidity of the room. Its siliconic nature gives this glue a very viscous consistency before curing and a quite plastic consistency after it. This glue

has been used for 350 crystals of Module 0' (see the results in section 6.4.2) and also for Russian and Chinese Proto 2000 (ECAL Testbeam matrices, composed of 30 Russian and Chinese crystals respectively, which were tested during summer 2000).

• *Advantages:* Curing times needed for this glue (2 or 3 days in vertical position) are reasonable and allows to keep CMS expected gluing rates. Thanks to its viscosity it has always given bubble-free gluings, even if it is true that all gluings performed were made on recent convex APDs (as we shall see in section 6.4.2).

This glue is almost inoffensive for the gluing operator, only being recommended the use of gloves for its manipulation. No problems derived from inhalation of RTV 3145 are known. Due to its siliconic consistency, once completely cured, gives a good mechanical adhesion but being not completely rigid. In this manner, adhesion tests are successfully passed and also ungluings can be easily achieved: mechanical torsion of the APDs on the crystal rear face allows to easily unglue the two parts. This glue passed with no problems all the ageing and radiation hardness tests. Besides, it has been used for several Proto matrices with no negative feedback respect to its transparency after irradiation.

• *Drawbacks:* Optically it presents the lower index of refraction n of the three candidates (1.49), which is in fact lower than the index of the Epoxy layer. Thus, this reduces the critical angle and hence also the ratio detected to emitted D/E photons. In fact D/E for RTV 3145 is only 9.4%, what compared to Histomount value (11.2%) gives a difference in detected photons of $\sim$2 for each 100 photons emitted in favour of Histomount (roughly a 20% ratio).

Conclusions:

After explaining the advantages and drawbacks of the three last candidates, we can state the following:

a) Drawbacks mentioned above for Histomount appear to be too severe to accept its use. We must absolutely reject a glue presenting a curing time of more than a month in realistic conditions. Besides, its dangerous handling constitutes another strong argument to reject it. We can only think about

using Histomount if we accelerate curing process (i.e. if we heat it up to ∼60°C) but this requires specially conceived ovens to be adapted to existing gluing benches, and also to adapt expensive safety systems (air ventilation) on these ovens. The high cost of these modifications together with the danger to which operators would be exposed lead us to affirm that Histomount is not the best choice.

b) NOA 61 is a very interesting glue, which offers the interesting possibility of completely curing the gluings immediately after performing them. However, techniques to successfully handle this glue are not well known and in consequence, very few successful gluings could be performed with it. Hence, we suggest to reject this glue for the CMS ECAL.

c) RTV 3145 also presents severe drawbacks related to its optical properties, which reduce detected to emitted photons in a 19% respect to Histomount and a 16% respect to NOA 61[h]. However, all the other characteristics of this glue make it very friendly to the operator and suitable to fit requested gluings/day rate. We consider that the loss of detected light can be accepted considering the critical drawbacks of the other candidates and thus we recommend its choice.

6.3 The gluing bench

In this section we are going to describe the gluing bench built at CERN RC in order to accomplish the gluing task of half of the total amount of barrel crystals (the other half will be glued at INFN-ENEA/Rome RC). In addition, we will describe one of the tools used to visually establish the quality of the gluings performed, the so called "bubble viewer".

The mission of this bench is to provide an space to perform the gluings, using a multibox-based concept of it, also to store the glued multiboxes vertically during curing time, allowing them to be removed from gluing position

[h]Experimental results provided by INFN-ENEA RC seem to yield an improvement of the D/E ratio of NOA 61 respecto to RTV 3145 much smaller than expected: 6.4% instead of 16%.

immediately after gluing with no damage on glue layer (which is usually still liquid). It must also include a quality control tool, in order to verify that APDs sensitive region is uniformly covered with glue and not with air (bubbles).

We can distinguish several parts in the gluing bench, which is depicted in figure 6.8-(a):

- *Gluing position:*

There are two gluing positions, placed at both sides of the PC (see figure 6.8-a), where we vertically fix multiboxes[i] and perform the gluing of five capsules to the five crystals inside it. The glue is dropped onto the capsules using an special micro-doser depicted in figure 6.8-(b). This foot-controlled microdoser[j] allows to provide drops of glue of the desired size on the APDs and it does not pose any problem to work with a very liquid substance (like Histomount) or a very viscous one (RTV 3145).

In each gluing position, there is a set of 5 pillars, which are used to push up capsules once the glue drops have been placed on them. These pillars can be screwed up along a path of several centimeters, thus getting in contact with crystals, and therefore spreading the glue in between crystal and capsule. When pillars are completely screwed, they permit to insert the so called "forks" which hold the recently glued sub-unit (capsule + crystal) over the multibox, thus allowing to screw down the corresponding pillar. Once the five pillars have been lowered, we can release the chariot on which multibox lays from its fixed position and move it gently on the rails, towards storage position, where it will be kept vertical during the required curing time.

- *Storage rails:*

As stated above, the multiboxes attached to its respective chariots can slide on the rails with no dramatic action on the still liquid glue. The aim of this storage system is to keep capsules with crystal weight on them (so, vertically) for the whole curing time needed. Thanks to rails length, we are able to store up to ∼30 multiboxes (150 crystals) in total. Multiboxes can be removed from the bench by behind (close to wall end of rails) or by the gluing position,

[i] In the gluing bench, the multiboxes are placed on special chariots which can smoothly slide on two rails and which can be fixed at the gluing positions.

[j] Eleco Produits; Model EB 100 V.

(a) The CERN RC gluing bench

(b) Operator placing glue drops on a capsule

Figure 6.8: *Pictures showing two different aspects of gluing procedure.*

which is strongly recommended as in this manner we can perform a last visual inspection of the quality of the gluing using the bubble viewer.

- *Bubble Viewer:*

The bubble viewer (BV) is a simple tool that allows to verify the quality of the gluings performed. As was explained above, the presence of a region with no glue in between the sensitive region of the APD and the crystal (i.e. the presence of an air gap) reduces strongly the critical angle and induces unacceptable losses in the number of photons detected. These air gaps can be produced by the presence of bubbles (see figure 6.13) or by a bad spread of the glue when pushing the capsule against the crystal.

The BV we used initially at CERN RC is illustrated in figure 6.9. It was based on the setup proposed by INFN-ENEA/Rome RC people [45].

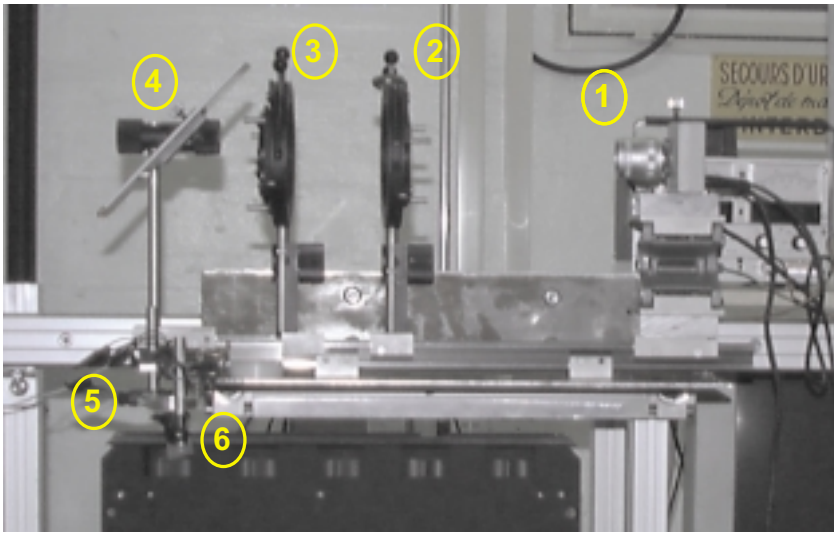

Figure 6.9: *Bubble viewer used at CERN Regional Centre gluing bench.*

We can distinguish several parts in this tool: there are two lenses with specially chosen focal lengths so that its combination acts as a magnifier of the image (corresponding to components 2 and 5 in figure 6.9). In addition, we use a light to illuminate the PWO//APD interface through the crystal length (component 6 in figure 6.9). We also include a video camera (1), a polarizer (3) and a mirror (4). The camera is used in order to be able to perform the inspection using a TV screen. Besides, by connecting this camera to a computer equipped with a special software we can record sequences of images, and export pictures. The polarizer is employed in order to avoid the image

twinning induced by PWO birefringence.

With this system we were able to distinguish bubbles of $\sim 100\mu$m diameter, which means 1/50 of the side of the black square determining the APD sensitive region (5mm $\times$ 5mm). However, when dealing with bubbles with a diameter lower than 100μm it is extremely complicated to distinguish if it is really a bubble or a tiny defect on the APD. That is why we started to think about a new device allowing us to see capsules integrally (very important to verify the good spread of the glue over the APDs) but also details of APDs with great resolution. In order to do this we installed an objective including a video zoom system[k] that can be attached to our video camera, and which includes a polarizer. Besides, we installed a new light source, and therefore, the ensemble substitutes the whole system illustrated in figure 6.9. This new system constitutes our new bubble viewer and is illustrated in figure 6.10.

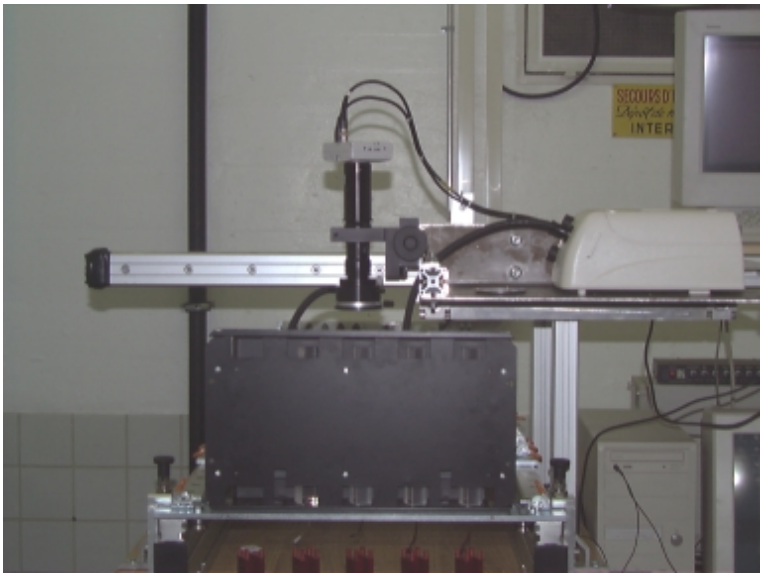

Figure 6.10: *New objective attached to video camera used as bubble viewer at CERN Regional Centre gluing bench.*

An example of two views that can be achieved with this objective are depicted in figure 6.11. As we can see, we are able to supervise the glue spreading by having a vision of the entire capsule (a) in the whole TV screen, and besides by using the zoom we can see details of APDs with great resolution (b), also in the whole TV screen. In this manner, bubbles with diameter size $\sim 50\mu$m can be resolved, which yields a further resolution improvement.

[k]Optic Video Zoom MA 705-Z-1-272 from Optical Measuring Systems Marcel Aubert SA; CH-2501 Bienne (Switzerland).

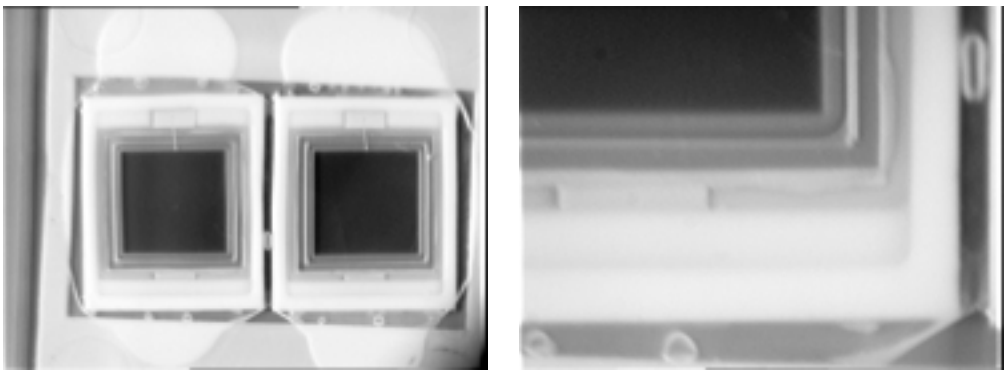

(a) View of whole capsule (b) View of a detail of an APD

Figure 6.11: *Two different views of an APD got with new bubble viewer.*

- *PC equipped with C.R.I.S.T.A.L. software and a barcode reader:*

As mentioned in chapter 4, most of the activities performed at the regional centres are controlled by a special object-oriented database designed and conceived for CMS purposes called C.R.I.S.T.A.L. [28]. We have set up a precise work-flow to ease gluing operator manipulations and minimize the risk of mistakes. The PC is equipped with a barcode reader, as the gluing operator will have to verify that the barcode of the crystal and the barcode of the capsule have been previously matched into a new sub-unit into the frame of C.R.I.S.T.A.L. database.

6.4 Gluing results for Mod #0 and Mod #0'

In this section we are going to explain the results achieved during the gluing of the 800 crystals that form Mod #0 and Mod #0'. We will describe the techniques used for the different glues used in them, the problems found for each glue, and also we will mention the amount of successful gluings and ungluings performed.

6.4.1 Module #0

The gluing of Mod #0 was performed during summer 1999, more precisely from beginning of May to end of August (nearly four months). For the gluing of Mod #0 we used two different glues: Two components glue RTV 615, and solvent based Histomount (both described in previous sections of this chapter). The former was used for only 19 subunits out of the total amount of 400. All the rest were glued with Histomount.

RTV 615

Since RTV 615 is a two-parts glue, we must mix the two parts in order to begin its polymerisation. This manipulation used to provide many bubbles which could affect the APD sensitive region. In consequence, before using this glue with capsules and crystals, we needed to introduce the mixture of the two parts in a vacuum pump aiming to remove air bubbles. The results achieved revealed that apart of this requirement related to the degasification the glue, the handling was not complicated. The gluings performed were in most of cases bubble-free, although we could notice that mechanical adhesion was not always provided after 2-3 days.

Histomount

Regarding Histomount, since the beginning of its use for the Mod #0, we noticed that it was providing bubbles very easily due to the concave surface profile of APDs (see figure 6.12). The reason for this creation of bubbles is simple: bubbles used to be created at the moment of the contact between the PWO crystal and the glue drops placed on APD. If APD profile were convex, then bubbles created at the moment of the contact would flow away, thus not remaining in the APD effective area (which is our objective). However, as the APD profile was concave, bubbles were remaining in the APDs sensitive region and as the glue takes a long time to cure, it remained very liquid during time enough to allow the flow of bubbles towards the point where the gap crystal-APD is bigger, i.e. the centre of the APD. During this flow, bubbles were

finding more space to increase their size. These bubbles flow towards APD centre together with the increase of their size can be observed in figure 6.13, corresponding to a concave APD, glued to a PWO crystal in May 1999.

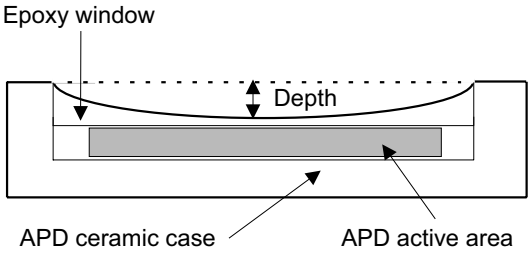

Figure 6.12: *Concave epoxy window profiles for old Hamamatsu APDs.*

In order to simulate a convex APD profile, the idea of pre-treating the APDs before the gluing was proposed. This pre-treatment consisted of dispensing a drop of Histomount on each APD, covering it all, and let it cure for one day. In this manner, when we were gluing those pre-treated capsules the day after, we were placing new drops of glue on the cured Histomount layer dropped the day before. The consistent surface generated (flat or convex) was acting in the same way as new APDs delivered with a convex Epoxy layer: bubbles created at the moment of the contact were flowing away towards the sides, therefore not remaining in APD sensitive region. This allowed to improve the rate of successful gluings since, when not using this pre-treatment, the amount of bubble-free gluings performed was considerably lower than 50% (i.e. more than one of each two gluings performed without pre-treatment, had to be unglued and reglued once capsule and crystal were clean).

However, the importance of this improvement was minimized since we found that curing times were excessively long. For the gluing of the first half of Mod #0 with Histomount, we found curing times of $\sim$ 1 week which were already not very good according to our requirements. However, for the second half of the gluings we discovered that sometimes 1 month was not time enough to ensure mechanical adhesion. Thus, many gluings which were bubble-free and after 1 week were stored in horizontal position (since we thought the glue was cured) had to be unglued and repeated due to glue displacements at the PWO-APD interface.

We can conclude that the gluings performed with Histomount (with or without pre-treatment) had to be repeated at least in 1/3 of cases, thus revealing that in order to supply 381 subunits properly glued with Histomount,

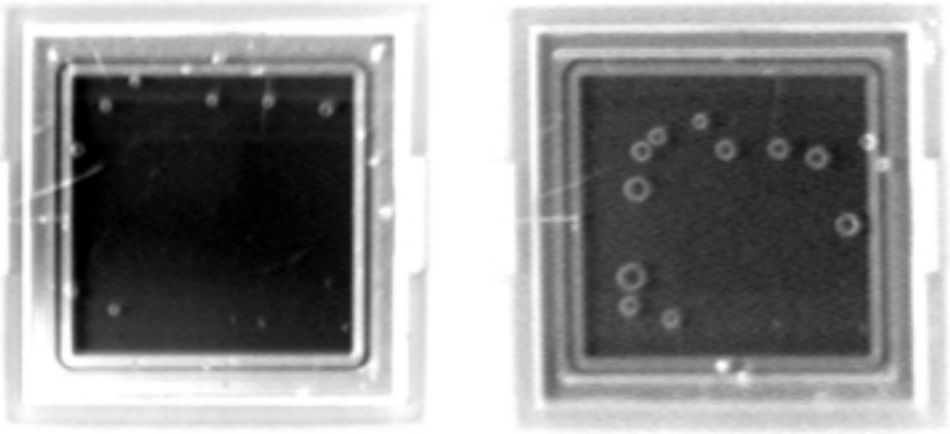

(a) 4h after gluing (b) 47h after gluing

Figure 6.13: *Pictures showing the evolution of the bubbles present in a gluing of an APD to a PWO crystal with Histomount.*

we had to perform a total amount of more than 550 gluings. The random curing times, together with the complicated handling of this glue led us to think, already at that time, that this glue could be only used for mass production if a method to accelerate curing times was found and proper safety systems were installed (the only method found, several months later, was related to the heating of the glue, as explained previously).

6.4.2 Module #0'

The gluing of this new module 0, so called Mod #0', was made since Mars 28^{th} to June 1^{st} 2001. Therefore, it took slightly more than two months, what already indicates that we found far less problems for this Mod #0' than respect to Mod #0. For Mod #0' we used two different glues: UV curing glue NOA 61, and siliconic RTV 3145. NOA 61 was intended to be used for 50 subunits out of the 400 included in the whole module, although due to some problems, we could only supply 43 subunits properly glued with NOA 61 to the operators in charge of mounting the modules. Thus, the remaining 357 subunits were glued with RTV 3145.

The APDs used for this gluing were already delivered by producers with a

convex Epoxy layer, thus, being the centre of the epoxy window higher than the sides (see figure 6.14).

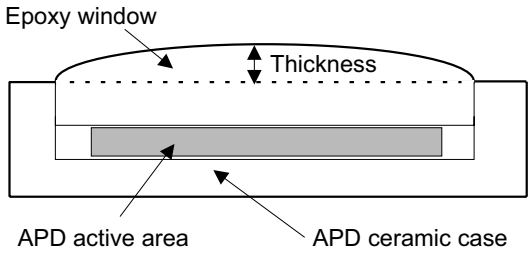

Figure 6.14: *Convex epoxy window profiles for recently delivered Hamamatsu APDs.*

NOA 61

The problems observed with this glue were mainly two: the appearance of cracks in the glue layer, and the mechanical adhesion. We are going to explain both problems in detail.

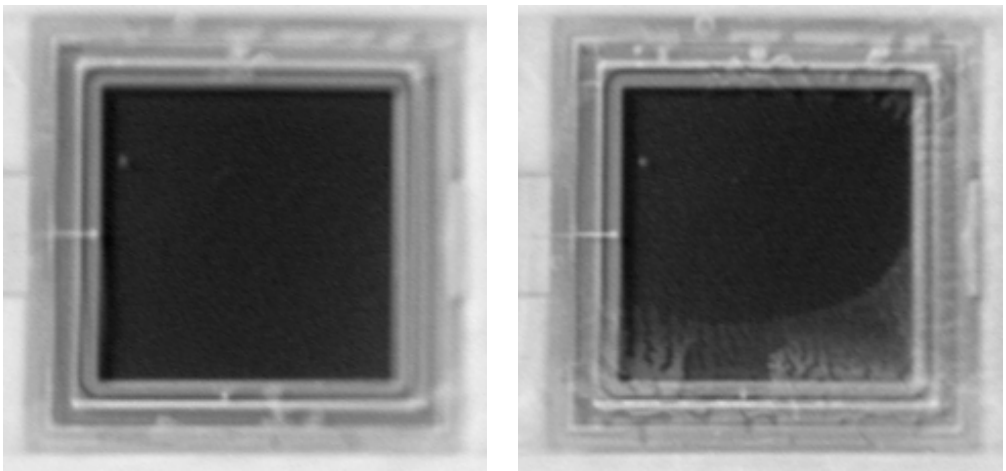

(a) 10 min after gluing (b) 20 min after gluing

Figure 6.15: *Pictures showing the evolution of the gluing of an APD to a PWO crystal using NOA 61.*

We observed that the glue layer was suffering changes during the minutes following irradiation even if the irradiation was long enough to provide good mechanical adhesion (when ungluing some of these APDs we found the glue to be completely cured). Figure 6.15 represents an APD glued to a crystal with NOA 61 10 minutes after gluing (a) and 10 minutes later (b). As we can see, in this short period of time, cracks appeared in the lower part of the APD. We suspect these cracks correspond to regions not well attached to any of the two surfaces (crystal or APD), and this means that we have air gaps in between crystal and APD, what strongly affects D/E ratio.

Normally, this glue (if well cured) does not provide inconvenients related to adhesion, however, for the gluing of Mod #0' we employed not only the lamp previously described, but also a second one, less powerful, provided by Marco Montecchi from INFN-ENEA/Rome RC. The mechanical adhesion problems were always found for the gluings performed with the second lamp.

As mentioned above, our initial plan was to glue 1/8 of the whole Mod #0' with NOA 61 (50 subunits), thus from those gluings performed we could observe: 30 out of 50 showing cracks presence (see figure 6.15), and 7 out of 50 presenting a poor mechanical adhesion (capsules were slightly moving when trying to rotate them on PWO rear face). As the techniques to correctly glue with NOA 61 were clearly not controlled, we decided to keep the 30 gluings presenting cracks as they were, and we planned to unglue only the 7 moving ones. However, this resulted in a more complicated task than we thought, since in 3 cases, even if the capsule frames were not well attached to crystals (that is why they were moving), the center of the APDs were well sticked to them. This caused the breaking of the three crystals, and even more: the crystal pieces remaining on the APDs made its cleaning so complex that at the end one of the capsules was destroyed.

To conclude, we tried to glue 50 subunits with NOA 61, from which: i) 43 could be finally accepted in spite of the presence of unexpected cracks on glue layer, and ii) 7 were unglued due to mechanical adhesion problems (breaking 3 crystals and 1 capsule). Finally these 7 subunits were recomposed with 3 new crystals and 1 capsule and were reglued with RTV 3145.

RTV 3145

Thanks to the APD convex epoxy layer and to the viscosity of RTV 3145, this glue has always given bubble-free gluings, as illustrates figure 6.16. In this figure we show two photographs of gluings performed during Module 0' gluing task. As we can see, no bubble can be detected by eye in the APD sensitive region (black area), although they do appear in the lateral sides for the two photographs. This is a consequence of the flow experimented by bubbles during the gluing that is induced by convex APD profiles. In any case, bubbles out of the sensitive region do not yield any problem for us.

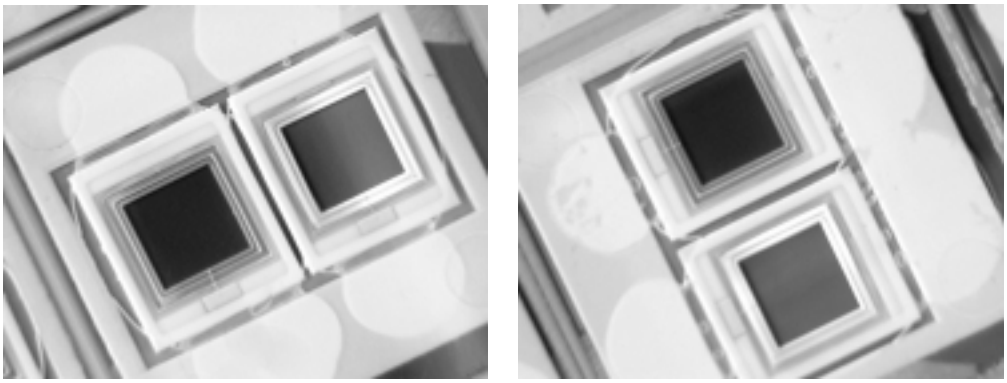

Figure 6.16: *Pictures showing two gluings performed for Module 0' using RTV 3145.*

As mentioned above, we initially intended to glue 350 subunits with RTV 3145. At the end we had to glue 7 more due to NOA 61 problems reported above. Therefore, we can present the results for these 357 subunits glued with RTV 3145: Only 2 out of the 357 were presenting problems in APD sensitive region due to small spots which could not be identified as bubbles but probably as an impurity which entered in the syringe used to dispense the glue. In any case, as the quality of the gluing for these 2 subunits was not as expected, we proceeded to unglue them. The ungluing was easy since this glue is not rigid after curing due to its siliconic consistency. After that, we cleaned the capsules and reglued them with no major problem. In addition, capsules were proved later to be in working conditions, therefore, this confirms that the ungluing and cleaning manipulations did not damage them.

We can conclude that the rate of successful gluings (no bubbles, impurities or cracks) is extremely better for RTV 3145 than for any other glue used for

Mod #0 or Mod #0' (355 out of 357, i.e. more than 99%). Besides, its harmless manipulation and short curing time are two more arguments in favour of the final choice of this glue.

Chapter 7

TEST-BEAM RESULTS

In this chapter we will present several important results achieved during last year testbeams. Firstable, we will describe the results from the tests performed during spring 2000 at PSI [a] which illustrate that uniformity parameters measured at CERN Regional Centre laboratory are in good agreement with the same parameters measured in beam conditions, i.e. excitation produced by high-energy particles, the crystals mounted in the final alveoles, readout performed with APDs, optical coupling performed with glue, etc. This result confirms we can trust on uniformity measurements performed at CERN RC laboratory with classical Light Yield benches or ACCOS devices.

Later, we are going to show the results achieved during summer 2000 test beam at H4 facility (CERN) which studied the performances of two PWO matrices under beam conditions. We will focus on the energy resolution achieved for the crystals used in this test, and will correlate results to their uniformity parameters. As we shall see, arguments used in chapter 5 to justify the importance of having a uniform light collection along crystal length in order to achieve an optimum energy resolution, will be confirmed with these results.

[a] Paul Scherrer Institute, Villigen (Switzerland).

7.1 Testing validity of uniformity curves at PSI

As was explained in previous chapter 4, the longitudinal uniformity of $PbWO_4$ crystals can be measured in the CERN RC laboratory in two ways: Using the classical benches or ACCOS devices. Both systems differ in several things, as for example the presence of a tyvek wrapping or an optical contact between crystal and PMT on classical benches (both are absent in ACCOS devices), but also have some important and basic common things: they both use PMT (photomultiplier tubes) readout and also both are based on the excitation produced by a radioactive source that is moved along crystal length.

In the final configuration, we will use an APD readout (see section 6.1) for PWO crystals, which will be enclosed into an alveolar structure. APDs do not cover the whole rear face of crystals, thus light collected with APDs and PMTs (which do cover the whole rear face) could be different. In order to understand these possible differences we must compare the light collection profiles measured for a number of crystals using both readout systems. However, APDs need a much larger deposit of energy on the crystal in order to have measurable signals, thus demanding the use of high-energy particles.

The differences induced in the light collection by several crystal wrappings and by the two different geometry readout systems (APDs vs. PMTs) will be analyzed in this section for twenty BTCP [b] barrel crystals. These results have been already reported elsewhere [46].

7.1.1 Description of the setup

The measurements performed at PSI were made using the π-1 area, where protons and pions of different energies are available. In the chosen configuration, we were getting around 14000 protons of 405 MeV/c per spill, and the beam size was $\sim 20 \times 20$ cm^2. Such a beam section allows to measure one full-size PWO crystal in a single run. Protons with momentum 405 MeV/c are stopping within 1 cm in lead tungstate, thus, by placing the crystals vertically as in our configuration (see figure 7.1), the protons release all their energy well

[b] Bogoroditsk Techno Chemical Plant.

at the middle of the crystal.

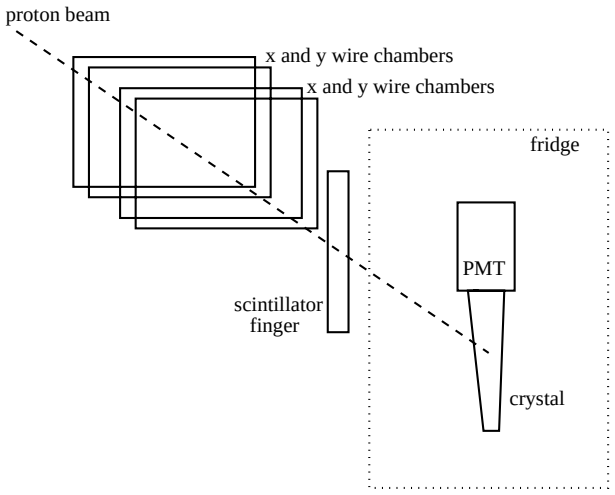

Figure 7.1: *Sketch of the setup used at PSI test beam.*

As stated above, crystals were positioned vertically (rear face upside), in a dark box where temperature was kept at 18°C. We also employed two pairs of wire chambers in order to reconstruct the position of the incoming protons. Besides, a scintillation finger counter with dimensions very close to crystals was placed $\sim$ 10 cm in front of it, being used as a trigger (see figure 7.1).

The measurements with APD readout were performed using capsules very close to final ones. These twin APD capsules were glued to crystals using Dow Corning RTV 3145 as optical glue. In this manner, the effective readout surface was $\sim$ 8% of crystal rear face. For the measurements with APDs we used the finger counter as trigger. The wrappings used with APD measurements at PSI were Tyvek, Mylar and Alveole. In addition, we measured five crystals into a submodule alveolar structure, which is the final configuration.

A photomultiplier tube (PMT) was also employed at PSI to perform measurements, since we wanted to understand better the differences induced in light collection with both readout systems: APDs and PMTs. In fact, we used the same PMT employed in B3, in order to minimise the differences between measurements. Crystals were coupled to PMT with the same optical grease used in B3 (Rhodorsil Silicones "*Pâte* 7"), and, as PMT has a photocathode window large enough, the sensitive surface for the readout was in this case 100% of rear face. For the measurements with PMT, the signal-to-noise ratio was too high, thus we used the crystal signal itself to trigger data. In the case of PMT measurements at PSI we used only a tyvek envelope to wrap the

crystals.

7.1.2 Comparison of Uniformities

For the comparisons we used 20 barrel crystals, 18 of which were belonging to Batch 9 and 2 to Batch 6 (review table 5.1). The two crystals from Batch 6 were intially too positive and hence, they were lapped at CERN RC on face D, in order to uniformize their light collection (as described in chapter 5). The crystals from Batch 9 were all presenting the surface state as delivered by BTCP producers: 2 were presenting all faces completely polished and 16 were treated according to method defined in chapter 5. In this group of 16 crystals, we included 2 with a very negative longitudinal light collection profile, 12 relatively flat, and 2 very negative. Summarizing, we had twenty crystals of which:

- 2 were lapped at CERN RC (Fnuf $\sim 0\frac{\%}{X_0}$),
- 2 were completely polished at BTCP (Fnuf $\gtrsim 1.2\frac{\%}{X_0}$),
- 2 treated with standard method at BTCP, and providing a very negative light collection profile (Fnuf < -0.35$\frac{\%}{X_0}$),
- 12 treated with standard method at BTCP, and providing a flat light collection profile (-0.35$\frac{\%}{X_0}$ < Fnuf < 0.35$\frac{\%}{X_0}$),
- 2 treated with standard method at BTCP, and providing a very positive light collection profile (Fnuf > 0.35$\frac{\%}{X_0}$).

All the twenty crystals were measured with tyvek wrapping in both APD and PMT readout configurations. Besides, with APD readout, we performed measurements on six crystals wrapped with mylar and alveola. In these conditions we can perform the following comparisons:

PMT vs. APD readout at PSI beam conditions

Firstable we wanted to understand the effects on the light collection curve induced by using APD and PMT readout in the same conditions. As stated above, APD measurements can only be performed when an important amount of light is emitted by the crystals, i.e. with large deposits of energy on the crystals. Therefore, the comparison of both readouts is only possible in high-energy particles beam conditions, which is our case now.

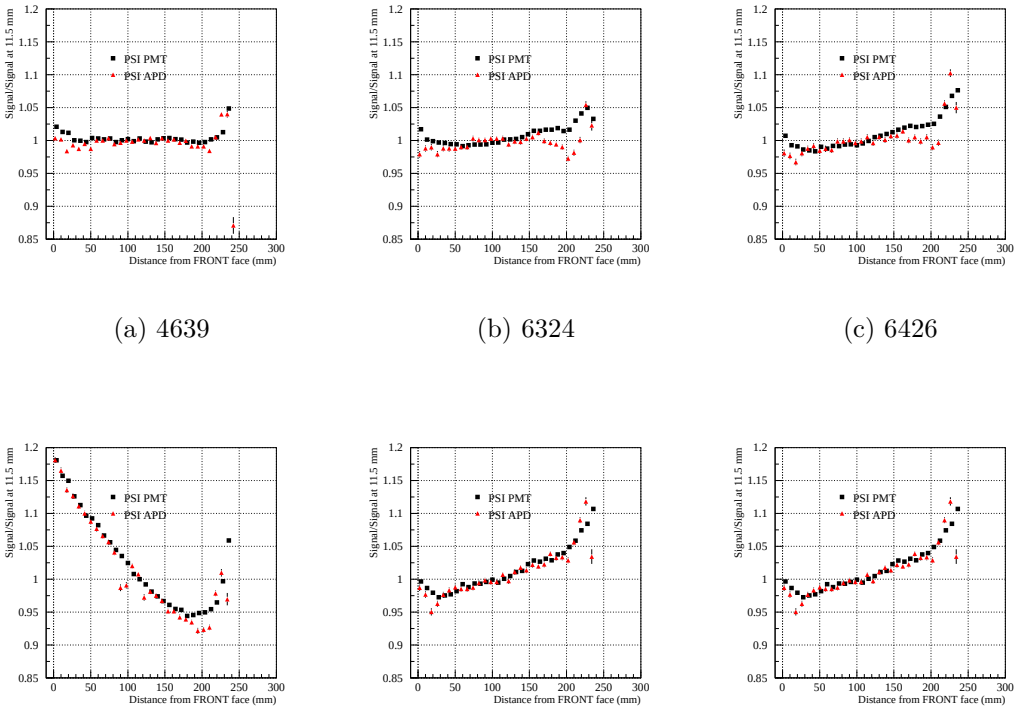

(a) 4639 (b) 6324 (c) 6426

(d) 6512 (e) 6689 (f) 6700

Figure 7.2: *Longitudinal light collection curves obtained with APD and PMT readout at PSI.*

Figure 7.2 depicts the uniformity profiles got for some of the twenty crystals used for this test, being the curves normalized to the Light Yield at 11.5 cm from Front end. The wrapping used for these measurements was a tyvek envelope. As we can see, the results are in excellent agreement, and we can only see systematic differences in the light collection at the two ends: light collected by APD use to be lower than light collected by PMT in the very first and very last centimeters of crystal. These differences in the non-uniformity

curves measured with both readouts configurations, which in any case are always within the 2-3% range, are believed to be due to geometrical reasons. The angular acceptances obtained with APD readout are reduced respect to the acceptances achieved with PMT readout, simply due to the percentage of rear face covered (∼8% for twin APD capsules vs. 100% for PMT). The different indices of refraction of the substances used to perform the optical contacts in both readout configurations could be another factor changing the angular acceptance. However, we believe that its influence is not that important, since both indices are very similar: in APD readout configuration we use optical glue RTV 3145 (n=1.49, as appears in table 6.1), and for the PMT readout we use Rhodorsil optical grease with a declared index of refraction n=1.5. Therefore, this lead us to think that the differences in the angular acceptances deduced from figure 7.2 are only due to geometrical differences in both configurations. A simple test performed with a mask reproducing the 2-APDs covering of the rear face placed on the PMT revealed [46] that uniformity curves obtained were very similar even in the crystal ends, thus confirming our hypothesis.

PMT readout at PSI vs. CERN RC Bench B3

Another test which we considered as very important was to verify that uniformity curves obtained with the two different crystal excitators considered were comparable. Thus we compared the light collection profiles of several crystals as measured with the ∼1.25 MeV gamma's emitted by the ^{60}Co source used in classical benches and the profiles measured for the same crystals using the protons beam as crystals excitator. In order to minimise the differences, we took the same PMT used at B3 to PSI, and also used the same optical grease (Rhodorsil) to perform the coupling between crystals and PMT. The resulting uniformity curves can be observed in figure 7.3.

As we can see in this figure, the curves agree very well specially in the Front part of the crystals, whereas the Rear part of the measurements performed in the classical bench B3 appear to be underestimated in most of cases. We believe this to be related to B3 tyvek ageing. As we already discussed in chapter 4, the ageing of the tyvek strongly decreases the sensitivity with which uniformity is measured in the rear part of the crystals in B3 (review plot 4.11-c). The variable ageing of the tyvek used for the measurements of these six crystals in B3, which was ranging from 15 days to more than 1 month, compared to the similar ageing of tyveks used when measuring at PSI, where

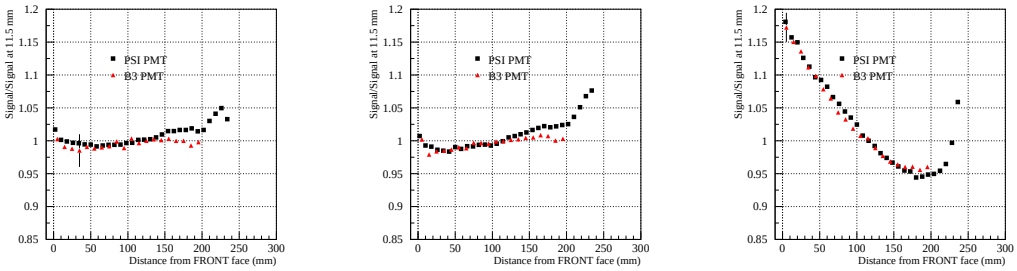

(a) 6324 (b) 6426 (c) 6512

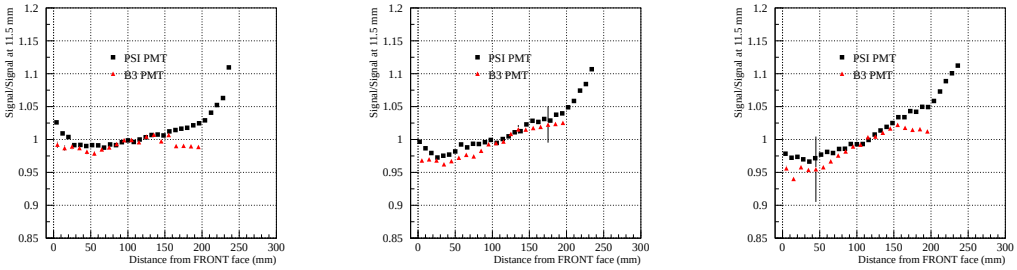

(d) 6679 (e) 6689 (f) 6700

Figure 7.3: *Longitudinal light collection curves obtained with PMT readout at PSI and at CERN RC with Bench 3.*

we used four tyveks specially made for this test short time before it started, explains why we find a good agreement in the uniformity curve at the rear end for certain crystals (B3 measurements made with a not too aged tyvek, e.g. 6512, 6689), whereas for some other crystals the disagreement can reach 2-3%[c] (the tyvek was aged in more than a month, e.g. 6679, 6700).

APD readout at PSI vs. CERN RC Bench B3

This comparison is specially interesting, since we compare very different things such as measurements with PMT at B3, with optical grease and ^{60}Co source as excitator (which is our standard method to measure crystals in Bench

[c] If we do not consider the last 2 or 3 centimeters of crystal where classical benches are usually unaccurate.

3) to measurements performed with PSI proton beam with APD readout and RTV 3145 as optical glue. Thus, we compare a situation very close to final one (PSI setup only differs in the wrapping used, which is tyvek instead of alveola) to the common situation that takes place at CERN RC laboratory when we measure with B3. As we mentioned in chapter 4, ACCOS devices are the ones used for large scale measurements and these machines are normalized to B3, which is our reference bench. This is why it is specially important for us to confirm that the agreement found in these two different configurations is satisfactory. The results are depicted in figure 7.4.

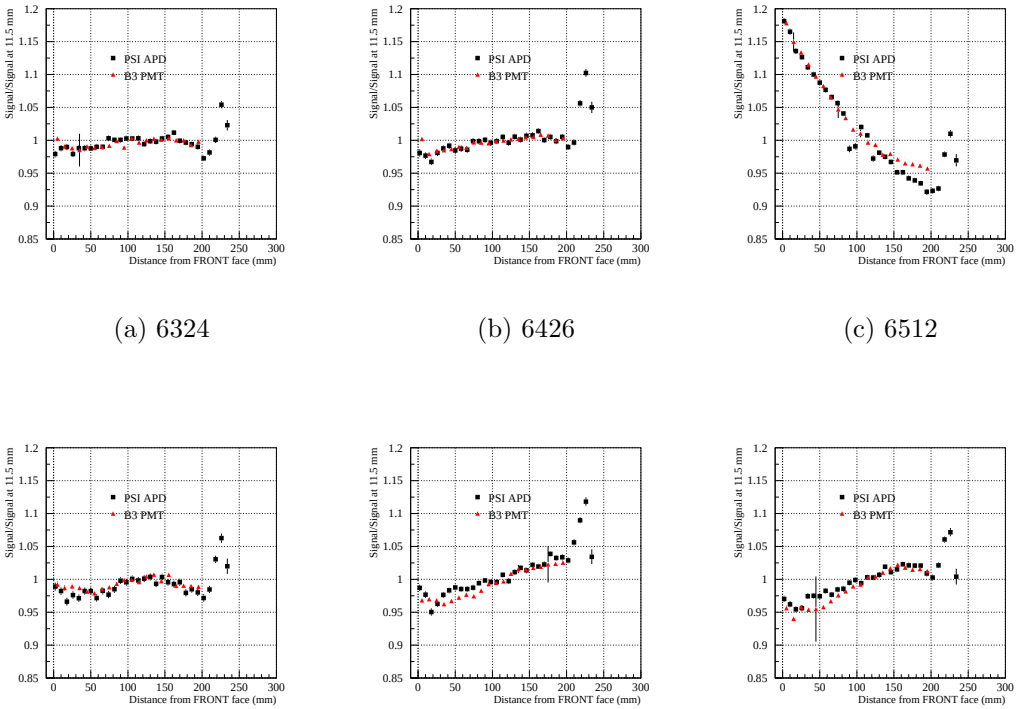

(a) 6324 (b) 6426 (c) 6512

(d) 6679 (e) 6689 (f) 6700

Figure 7.4: *Longitudinal light collection curves obtained with APD readout at PSI and at CERN RC with Bench 3.*

As we can observe for crystals 6324, 6426 and 6679, both curves are cuasi paralel, whereas for 6512 we observe some differences within 2% at the rear end and for 6700 and 6689 we observe also differences within 2% but at the front end in this case. In general we can consider that the agreement found in these two very different configurations is excellent.

APD readout at PSI vs. CERN RC ACCoCE 1

Apart from comparing measurements with PSI proton beam and APD readout with measurements performed in B3 in the classical way, we are also very interested in the correlation of the former data to ACCOS devices. This is depicted in figure 7.5.

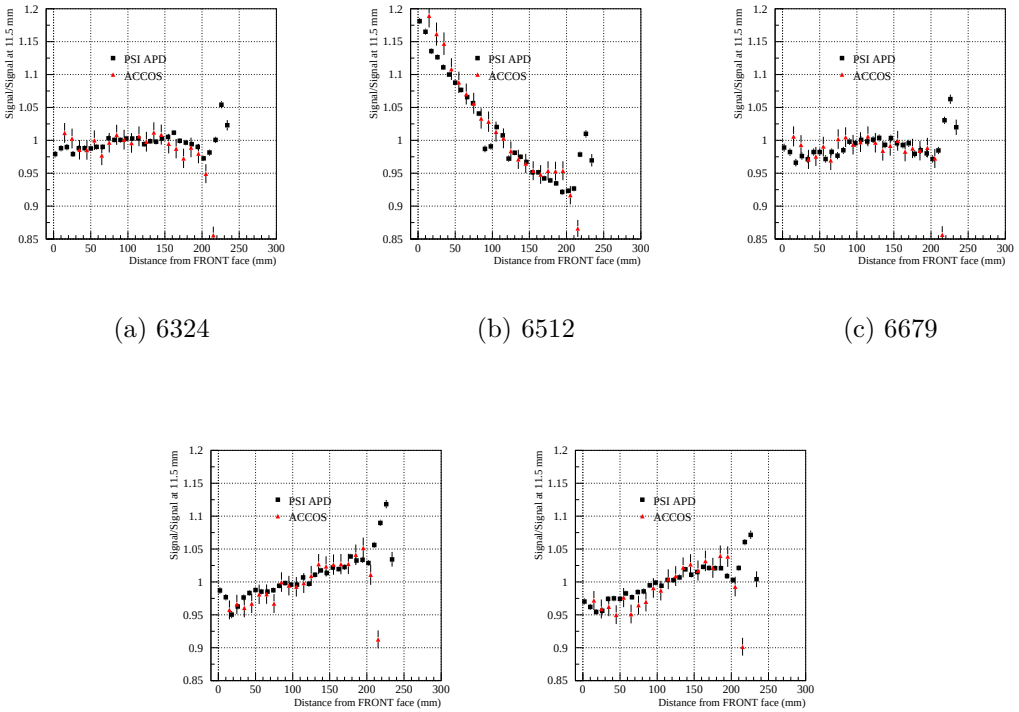

(a) 6324 (b) 6512 (c) 6679

(d) 6689 (e) 6700

Figure 7.5: *Longitudinal light collection curves obtained with APD readout at PSI and at CERN RC with ACCoCE 1.*

As we can see in this figure, the agreement is as expected (ACCOS devices are normalized to B3 data). Uniformities measured in these two situations are in excellent agreement for crystals 6324, 6679 and 6689, whereas small differences within 2% are observed for crystals 6512 and 6700. It is important to mention that ACCOS devices data at 21.5 cm from Front end is meaningless, thus it should not be taken into account to quantify differences between the two curves.

Different wrappings with APD readout at PSI

As we mentioned at the beginning of the section, when we initiated this test beam we were not only interested in studying the influences in the light collection induced by the different possible readout configurations, but also the ones induced by the different wrappings. Figure 7.6 shows that the light collection uniformities measured with different wrappings are, within errors, the same (please note the different scale respect to previous comparison plots showed).

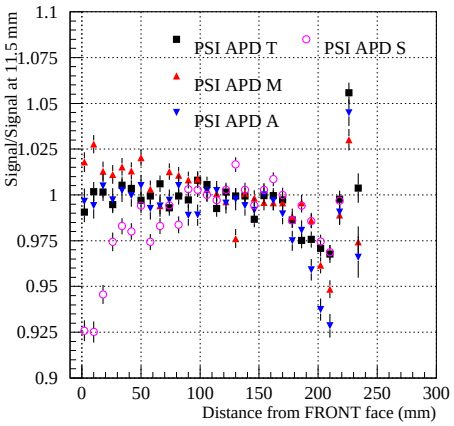

Figure 7.6: *Longitudinal light collection curves obtained with different wrappings (T=Tyvek; M=Mylar; A=Alveole; S=Submodule) for crystal 6326 with APD readout at PSI.*

We can observe in this figure that the agreement is quite good between Tyvek, Mylar and Alveole, whereas in the case of submodules, the difference is $\sim 3\%$ (not considering first 3 cm). This is specially surprising, since single crystal alveolar structures used for all the measurements showed here were cutted from 10-crystals alveolar submodule structures. Thus, the difference between alveola and submodule clearly illustrated in figure 7.6, already indicates that it must be another difference between submodule measurements and the rest (several hypothesis are given below). For the first three wrappings we could also extract information related to the relative light yield measured respect to tyvek envelope. Thus, we could construct table 7.1.

In this table, we can see that in beam conditions we find a ratio Mylar/Tyvek close to 0.8, and in the case of Alveole/Tyvek, it is $\sim$0.6, while the

Table 7.1: *Relative Light Yield measured for five crystals with different wrappings using APD readout at PSI.*

Crystal Number	**Mylar/Tyvek**	**Alveole/Tyvek**	**Alveole/Mylar**
6512	0.82	0.72	0.88
6694	0.71	0.56	0.78
4648	0.83	0.61	0.74
6655	0.73	0.60	0.83
6700	0.76	0.64	0.84
Average	*0.77 ± 0.12*	*0.63 ± 0.10*	*0.81 ± 0.10*

classical benches use to yield a ratio Mylar/Tyvek and Alveole/Tyvek close to 90%. In any case it must be stated that these results in beam conditions are entirely confirming results obtained in precedent PSI test beam campaings [47]. Taking into account that all the wrappings used here were in good conditions, we can only think of the APD readout lower angular acceptance as an explanation for the different ratios of Mylar and Alveole respect to Tyvek found at PSI and CERN RC.

In order to better understand the differences between submodule and the rest of wrappings appearing in figure 7.6, we will illustrate the light collection profiles obtained with both Tyvek and Submodular wrappings in the case of APD readout at PSI (see figure 7.7). In this figure we can observe that there are some sistematical differences in the Front part, typically within 3% when not considering very first or last centimeters. The reason for this is not clear. As mentioned above, we believe that submodule configuration was somehow different respect to others, since single alveolas were cutted from alveolar submodule structure, so no difference should be expected between them, fact that is denied by figure 7.6. We do believe that the reason for this could be a change in the setup introduced when measuring the submodules. Submodules contain 10 crystals, thus it means close to 15 Kg in total. In consequence, we had to adapt a special system to fix this weight, which finally could only be a tool which was holding the submodule in such a way that crystals were rotated 180° respect to setup sketched in figure 7.1. Therefore, we have two hypothesis for the differences observed in figure 7.7 related to this rotation:

a) It could be due to a misalignment between the finger counter used as trigger and the crystal, produced because submodule structure had to be measured upside-down respect to all the rest of measurements reported here, or

b) As crystals were having the front face upwards now, it could happen that the pressure of them on the reflectant piece inserted in the inner part of the alveolar structure facing crystals Front face is further reduced, thus de-

creasing the amount of light reflected at the crystals Front face, and thus the light collected at the photodetector.

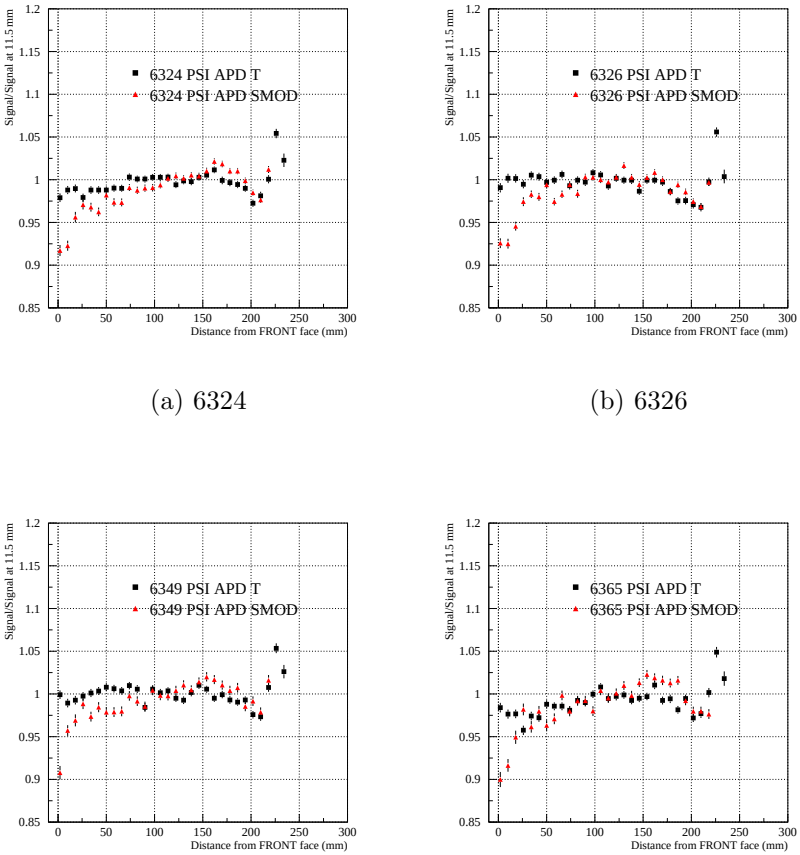

(a) 6324 (b) 6326

(c) 6349 (d) 6365

Figure 7.7: *Longitudinal light collection curves obtained with APD readout at PSI using Tyvek wrapping and Alveolar Submodule structure.*

Front and Rear NUF comparisons

In the previous sections of this chapter we have illustrated how do the uniformity curves look like under different readout configurations and wrappings. As all these uniformity curves are available, we can also perform comparison of uniformity parameters Front and Rear NUF, which are calculated from light collection curves as defined in chapter 4 (review equations 4.10 to 4.12 and related discussion).

All the data we can use for this comparison is presented in table 7.2. In this table, we present Fnuf and Rnuf for the twenty crystals used in the test, indicating the readout (APD or PMT), the setup (B3 or ACCOS) and the wrapping (T=Tyvek, M=Mylar and A=Alveole) employed. When no setup is indicated, we are referring to PSI data (columns 2, 3, 4, 5, 8 and 9). Crystals 4648 and 4639 belong to Batch 6 whereas the rest of crystals belong to Batch 9, being 6505 and 6512 the two completely polished by producers.

Using data from table 7.2, we can construct plots to compare uniformities as depicted in figure 7.8 and 7.9. In both figures we can see that for every plot a linear fit is overimposed to data together with the diagonal line given by $y = x$, so we can easily distinguish by eye how good the correlations are.

The slope of the linear fits are very close to 1 for all plots in figure 7.8, thus revealing the good agreeement between the compared data. The slope the most different to 1 is given by the comparison between ACCoCE 1 and APD readout at PSI (d), but it is in a great part due to the two most positive crystals (completely polished). We must take into account that thanks to the complex uniformity task undertaken at CERN RC, all the crystals accepted for the final detector will have a Fnuf within $\pm 0.35 \frac{\%}{X_0}$ (review equation 5.3 and corresponding section) as measured with ACCOS devices. If we focus on this region when can observe that the correlations showed in figure 7.8 are all excellent. This makes us to be confident about the uniformisation task made at CERN RC, which is based on uniformity parameters measured in lab conditions with ACCOS devices.

If we analyze plots on figure 7.9, where Rnuf values measured at CERN RC with ACCoCE 1 are compared to values measured at PSI with PMT (a) and APD (b) readout, we can see that the correlation is not as good as in the case of Fnuf (figure 7.8). However, we must notice one thing:

As mentioned in previous sections of this chapter, and also in chapter 4, the ageing of the tyveks strongly affects to the uniformity measured in the rear part of the crystals in the classical bench B3 (review plot 4.11-c). As ACCOS devices are calibrated respect to B3, it can be understood that correlations respect to ACCoCE 1 Rnuf are not excellent. However, this can be accepted, as Rnuf acceptable limits are much larger than Fnuf ones, since it has a lower influence on the resolution of the calorimeter (review section 5.2).

Table 7.2: *Summary of Uniformity parameters Fnuf and Rnuf obtained for the 20 crystals used in this test.*

Crystal	**Fnuf APD T** *(%/X_0)*	**Fnuf APD M** *(%/X_0)*	**Fnuf APD A** *(%/X_0)*	**Fnuf PMT T** *(%/X_0)*	**Fnuf B3** *(%/X_0)*	**Fnuf ACCoCE1** *(%/X_0)*	**Rnuf APD T** *(%/X_0)*	**Rnuf PMT T** *(%/X_0)*	**Rnuf B3** *(%/X_0)*	**Rnuf ACCoCE1** *(%/X_0)*
6512	1.288	1.293	1.468	1.256	1.336	1.490	0.832	0.619	0.481	0.475
6694	0.709	0.571	0.533	0.454	0.504	0.752	0.785	0.590	0.432	0.461
6655	-0.235	0.077	-0.044	-0.134	-0.274	-0.380	-0.131	-0.413	-0.058	-0.334
6700	-0.335	-0.425	-0.491	-0.332	-0.574	-0.848	-0.175	-0.575	-0.105	-0.344
6326	0.028	0.125	0.027	-0.048	-0.101	0.215	0.227	0.078	0.161	0.396
4648	-0.001	-0.070	-0.067	-0.076	-0.086	0.025	0.050	-0.170	0.227	-0.208
6689	-0.267	-	-	-0.265	-0.393	-0.551	-0.374	-0.433	-0.277	-0.468
6679	-0.309	-	-	-0.194	-0.168	-0.427	0.231	-0.255	0.169	0.160
4639	-0.111	-	-	-0.011	-0.155	0.065	0.098	0.034	0.287	-0.231
6514	0.119	-	-	0.294	0.121	0.477	0.336	0.352	0.507	0.465
6505	1.105	-	-	1.290	1.190	1.570	0.900	0.451	0.695	0.439
6349	-0.058	-	-	-0.023	-0.133	0.239	-0.032	-0.361	-0.046	-0.064
6365	-0.301	-	-	0.013	-0.148	0.073	0.065	-0.025	-0.010	0.199
6324	-0.213	-	-	-0.049	-0.120	-0.006	0.061	-0.212	0.023	0.357
6394	-0.169	-	-	-0.092	-0.094	0.170	0.245	-0.248	-0.019	0.101
6426	-0.193	-	-	-0.144	-0.173	-0.024	-0.016	-0.266	-0.031	-0.346
6424	-0.126	-	-	-0.171	-0.177	-0.068	-0.169	-0.450	-0.056	-0.188
6423	-0.143	-	-	-0.081	-0.133	0.006	0.252	-0.120	0.222	0.217
6422	-0.184	-	-	-0.179	-0.289	-0.099	0.276	-0.146	0.035	0.065
6428	-0.287	-	-	-0.235	-0.259	-0.010	-0.006	-0.441	0.006	0.291

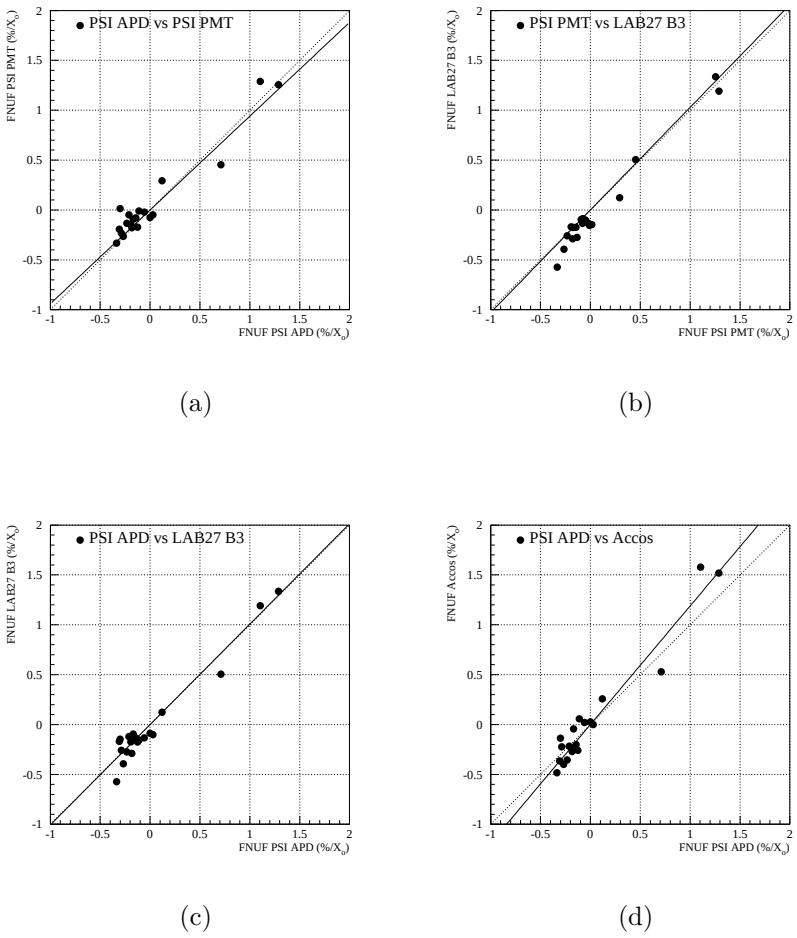

Figure 7.8: *Comparison of Front Non-Uniformities obtained between: (a) APD and PMT readout under PSI beam conditions; (b) PSI beam configuration and classical bench b3 configuration, both with PMT readout; (c) APD readout under PSI beam conditions and PMT readout at CERN RC classical bench B3; (d) APD readout under PSI beam conditions and PMT readout at CERN RC automatic device ACCoCE 1.*

7.1.3 Conclusions from this test

This exhaustive and extremely interesting test-beam shows that:

1. The geometrical differences between APD and PMT readout yield clear influences on the light collection curve obtained in beam conditions that

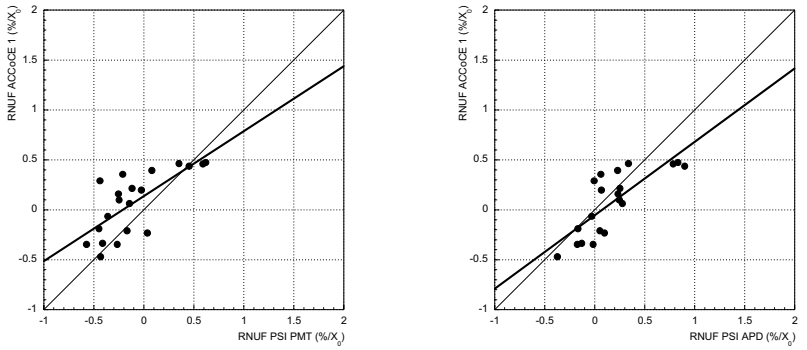

(a) (b)

Figure 7.9: *Comparison of Rear Non-Uniformities obtained between: (a) PMT readout under PSI beam conditions and PMT readout at CERN RC automatic device ACCoCE 1; (b) APD readout under PSI beam conditions and PMT readout at CERN RC automatic device ACCoCE 1.*

are mainly affecting the rear part. In this region, light collection with APD readout is underestimated in a 2-3% respect to PMT readout.

2. The tyvek ageing affecting B3 measurements produced an underestimation of the light collected in the crystals rear end respect to measurements performed at PSI with PMT readout with other less aged tyvek envelopes.

3. The lower angular acceptances induced by APD readout affecting light collected at rear end, and the tyvek ageing affecting B3 measurements at the same crystal region yield similar behaviors along the whole crystals length and thus the agreement between uniformities measured for tyvek wrapped crystals under PSI beam with APD readout and the ones measured at B3 with PMT readout is excellent (see figure 7.8-c).

4. The agreement between ACCoCE 1 uniformity data and APD readout at PSI with tyvek is also very good, as expected from precedent conclusion.

5. The disagreement observed at the front part of uniformity curves between submodule and the rest of wrappings is not well understood, although we believe it to be due to a different positioning.

6. Light yield ratio Alveole-to-Tyvek is not as high as in expected from laboratory measurements (0.63 ± 0.10).

This general very good agreement between data from CERN RC laboratories and data from PSI beam setup leads us to trust on the uniformisation task developed at CERN RC based on laboratory measurements.

7.2 Testing PWO matrices at H4 beam

As was mentioned in previous chapters, the very challenging performance needed for the light Higgs decay detection and the strict operation conditions expected for LHC, results in a demand of an excellent energy resolution to the CMS ECAL.

In section 2.4.1, we already discussed about the energy resolution expression and its related terms: stochastic term (a), noise term (b) and constant term (c). We also discussed in that section, and in section 5.2, about the parameters that could influence those terms. So, a can be influenced by fluctuations in the light collected at the photodetector (i.e. the Light Yield) and c is influenced by structural non-homogeneities in light collection (i.e. Front and Rear Non-Uniformity). Taking into account the last consideration, we justified the importance of the Uniformisation task in section 5.2 by showing simulations where strong non-uniformities in light collection were worsening the energy resolution.

In summer 2000, two matrices of 30 crystals each were tested with the H4 high-energy electron beam at CERN. One of the goals of these tests was to determine the performance of our detector in terms of energy resolution. Therefore, the matrices were exposed to high-energy particle beams of different energies. This allowed to construct the energy resolution plots, from which we could derive stochastic, constant and noise terms, according to equation 6.1.

In this section we are going to compare the resulting energy resolution parameters for the two matrices of crystals to its laboratory measurable related parameters (LY and Fnuf). In this manner we will demonstrate with real data what we justified with simulations in section 5.2: we will prove that a control on the non-uniformity of light collection reduces the constant term c, and thus the contribution to energy resolution. In addition, the weaker dependence of a with Light Yield will be also shown.

Detailed discussions about this test-beam, related to the setup, the comparisons shown here and some other interesting comparisons between LY laboratory measurements and LY test-beam data can be found elsewhere [48].

7.2.1 Description of the setup

For this test we used two matrices of 5×6 crystals with APD readout. The crystals were glued to final capsules with optical glue Dow Corning RTV 3145 (see chapter 6). Both matrices were composed of Type 6 crystals, grouped into three submodules (10 crystals each). The alveolar structures holding these submodules were the same used in the final detector configuration.

The first matrix was composed of 30 $PbWO_4$ crystals produced at the BTCP[d], and will be called from now onwards *Russian Proto 2000*. This matrix contained crystals from pre-production Batch 8 (see table 5.1), thus presenting lateral face D depolished to a roughness $\sim 0.35\mu$m to provide uniformity. The APDs used for this matrix were 1999 prototypes and thus, their performances were not the best: large gain dispersion for a given operating voltage. The high voltage for the Russian Proto 2000 APDs was at a relatively low gain (M$\sim$35). This matrix was installed at H4 area from May to June 2000.

The second matrix was composed of 30 $PbWO_4$ crystals produced at SIC[e], and will be called from now onwards *Chinese Proto 2000*. This matrix contained R&D crystals, which were not showing a depolished face since this SIC crystals use to present a higher absorption that opposes to focusing effect, providing uniform light collection curves without the need of a treatment. The APD readout used for this test was further improved respect to Russian Proto 2000, since APDs were corresponding to a more recent prototype. The high voltage for the Chinese Proto 2000 APDs was at gain M$\sim$50.

The program used on the test-beam of the two matrices were very similar. Chronologically, it was composed of:

[d]Bogoroditsk Techno-Chemical Plant, Bogoroditsk, RUSSIA.
[e]Shanghai Institute of Ceramics, Shanghai, CHINA.

1. First calibration of the matrices with 50 and 120 GeV electrons.
2. First energy scan at several beam energies with matrix central crystals.
3. Long irradiation with 120 GeV electrons on some crystals.
4. Second calibration of the matrices with 50 and 120 GeV electrons.
5. Second energy scan at several beam energies with matrix central crystals.

During the study of each matrix at H4, they were mounted on a computer controlled moving table. The trajectories of incoming electrons were measured with a set of wire chambers. With the standard collimators setup, the beam spot was $\sim 2\times2$ cm^2.

7.2.2 Energy Scan

As we already discussed in section 2.4.1, there is a parameter called *Moliere Radius* (R_M) which determines the radius of an infinite cylinder containing 90% of the shower energy. In the case of PWO, its R_M is 2.19 cm (review table 3.3). Our crystals have a transversal section that roughly can be considered to be ranging from 2.2×2.2 cm^2, at the front end, to 2.6×2.6 cm^2, at the rear end. The shower maximum region takes place at about $8X_0$ from front end, thus, we can assume that in this position, the transversal section is $\sim 2.3\times2.3$ cm^2. The biggest cylinder contained in the volume given by such a section has a radius of 1.15 cm, which is slightly more than half a R_M.

Therefore, we can understand that when high energy particles are pointed to the center of a PWO barrel crystal, only a fraction ranging between 70 and 80% of the shower is contained in that single crystal. When considering groups of 3×3 crystals, the shower containment increases to $\sim$ 95% of the total. In consequence, for the calculation of the energy resolution for a given crystal we will work with its 3×3 related matrix, for which we will calculate the sum of the energy deposited (Σ_9).

When considering not the sum of nine, but the single response of a crystal we get results which are very sensitive to the impact position, as depicted in

plots (a) and (b) from figure 7.10. This is obvious, since, when particles hit the PWO crystal at a position far from its center, there is a bigger chance for the electromagnetic shower to be partially developed in the closest lateral crystal. In this manner, the energy deposited in the original crystal will be lower, and thus also the ADC response (see plot (b) in this figure). However, if we do take into account the matrix of 3×3 crystals surrounding the central one, the situation is improved (see plot (d) in this figure), since the energy deposited into the lateral crystal is also taken into account. In any case, we can apply corrections for the impact position [48], which improve considerably the energy resolution in the case of Σ_1 energy distributions and a bit less the resolution of Σ_9 energy distributions (since it is intrinsically better).

Lets assume that we are working with 50 GeV electrons incoming into a given crystal, for which we want to calculate its related Σ_9. Lets numerate these 9 crystals from 1 to 9, the central one, in which the beam is impinging, being the 5^{th}. We will call c_i to the position of the ADC peak (pedestal substracted) obtained for crystal i when beam goes into central crystal 5, and we will call c'_i to the position of the ADC peak (pedestal substracted) obtained for crystal i when the 50 GeV electrons beam goes into it (in a different run, of course). We will denote k_i to the calibration factor for channel (crystal) i that converts ADC channels into Energy (in GeV) deposited. Then, for every non-pedestal event of the run in which 50 GeV electrons impinge into central crystal (5^{th}), we must perform the sum:

$$\sum_{i=1}^{9} \frac{c_5}{c'_i} c_i \tag{7.1}$$

which will give us the energy deposited in the nine crystals but expressed in ADC channels. By doing this with all non-pedestal events, we can construct a quasi-gaussian distribution from which we can extract mean value and sigma. The calibration of energy in ADC channels (k_5) can be performed now, taking into account that this Σ_9 peak corresponds to 50 GeV. Similarly, the sigma of the distribution, originally in ADC channels, can be converted into this crystal energy resolution at 50 GeV.

Using this method we have constructed the histogram (b) appearing in figure 7.11. In this figure we are comparing the energy distribution obtained, for two different crystals, when considering the sum of only one crystal (a) and when considering the sum of nine (b). As we can see, results are far less sensitive to leakage in the second case, the distribution being much closer to a perfect gaussian. Both Σ_1 and Σ_9 distributions were constructed taking into account the impact position correction mentioned above.

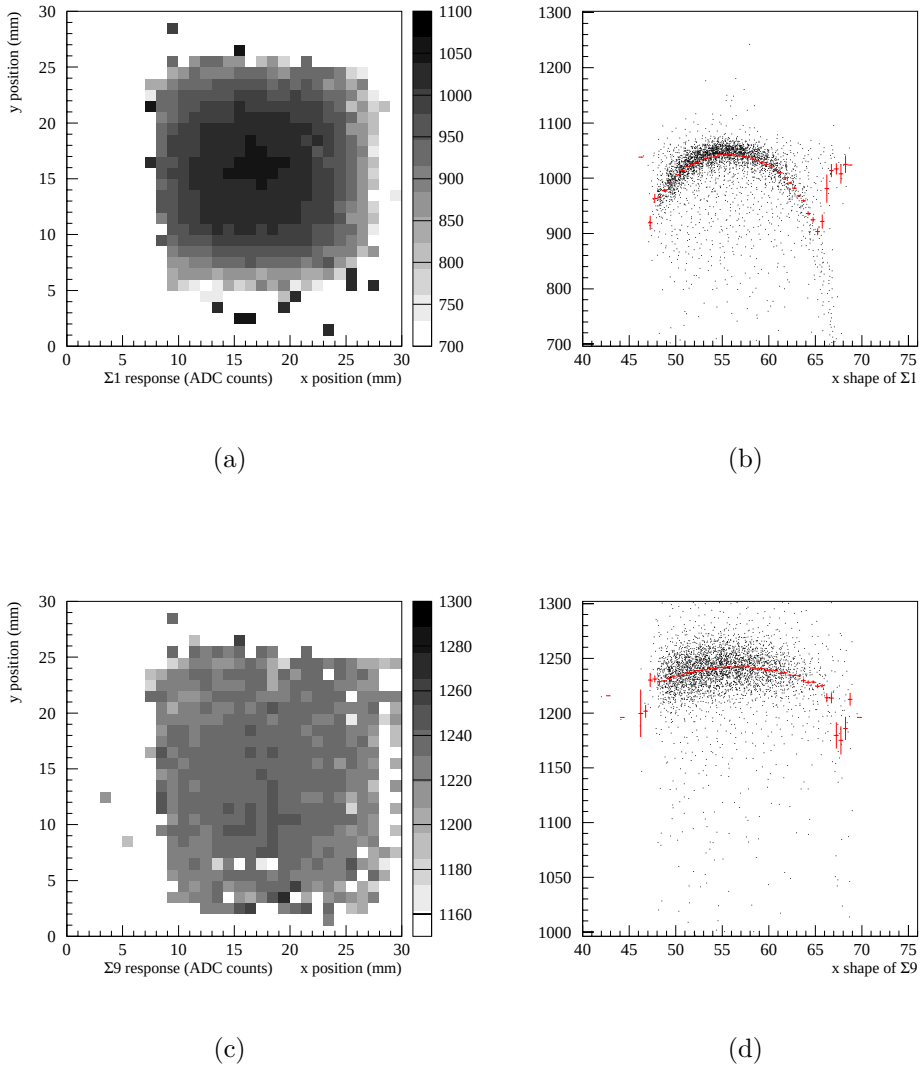

Figure 7.10: *Response of a crystal considering only the Σ_1 distribution as a function of x-y position (a) and as a function of x alone (b), and response of the same crystal when considering the Σ_9 distribution as a function of x-y position (c) and as a function of x alone (d).*

In this manner, we can obtain the energy resolution $\sigma(E)$ for all scanned energies, and also, for all crystals. Thus, we can construct plots like the ones showed in figure 7.12, where we do compare the energy resolution curve obtained in this way for a russian (a) and a chinese (b) crystal.

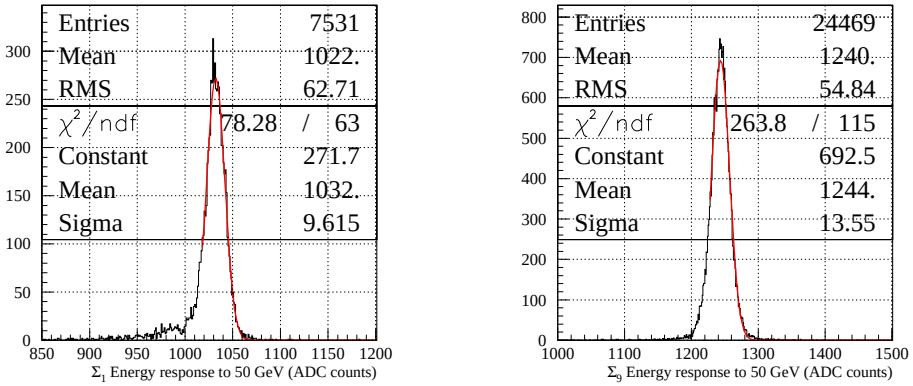

(a) (b)

Figure 7.11: Σ_1 *energy distribution after position correction (a) and* Σ_9 *energy distribution after position correction (b). Fits are performed with a gaussian function starting at* μ*-1.5*σ*. Both distributions correspond to different crystals.*

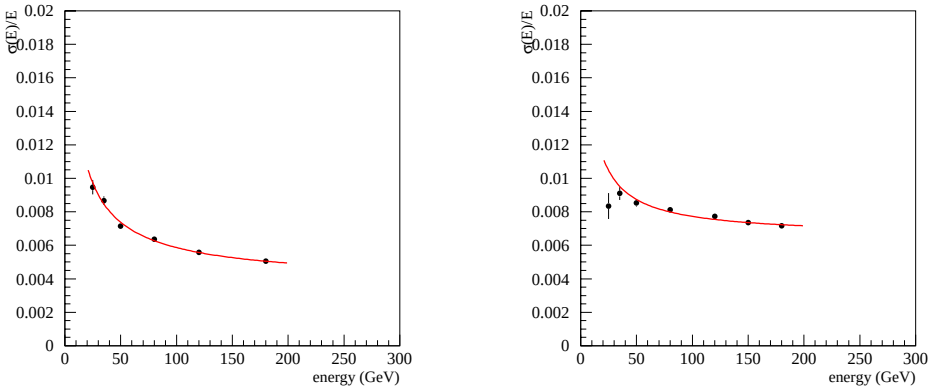

(a) (b)

Figure 7.12: *Energy resolution as a function of the beam energy for a russian crystal (a) and a chinese crystal (b). Fit is performed according to equation 6.1.*

These curves can be fitted with equation 6.1, where the noise term b can be set to zero, since it was already substracted from each point. In the case of this test we are describing, the fit was performed with all scanned energies

between 25 and 120 GeV. From this kind of fit, we can extract the energy resolution parameters given by the stochastic term and the constant term. The values for these parameters a and c were calculated for all the crystals (12) for which a sum of nine is feasible in a 5×6 crystals matrix after and before irradiation. They are shown in table 7.3.

Table 7.3: *Energy Resolution for the russian and chinese proto 2000 before and after irradiation.*

Russian Proto 2000				
	before Irradiation		*after Irradiation*	
Crystal	Constant Term	Stochastic Term	Constant Term	Stochastic Term
7	0.0041±0.0001	0.050±0.002	0.0044±0.0003	0.047±0.002
8	0.0042±0.0001	0.042±0.002	0.0045±0.0003	0.037±0.002
9	0.0042±0.0001	0.045±0.002	0.0046±0.0003	0.039±0.002
12	0.0036±0.0001	0.043±0.002	0.0025±0.0003	0.050±0.002
13	0.0041±0.0001	0.040±0.002	0.0036±0.0003	0.042±0.002
14	0.0038±0.0001	0.044±0.002	0.0043±0.0003	0.039±0.002
17	0.0032±0.0001	0.051±0.002	0.0036±0.0003	0.048±0.002
18	0.0044±0.0001	0.039±0.002	0.0043±0.0003	0.041±0.002
19	0.0043±0.0001	0.041±0.002	0.0040±0.0003	0.042±0.002
22	0.0036±0.0001	0.046±0.002	0.0033±0.0003	0.048±0.002
23	0.0037±0.0001	0.046±0.002	0.0035±0.0003	0.047±0.002
24	0.0049±0.0001	0.042±0.002	0.0038±0.0003	0.049±0.002
Chinese Proto 2000				
	before Irradiation		*after Irradiation*	
Crystal	Constant Term	Stochastic Term	Constant Term	Stochastic Term
7			0.0053±0.0001	0.041±0.002
12	0.0068±0.0001	0.038±0.002	0.0062±0.0001	0.043±0.002
13	0.0043±0.0001	0.042±0.002	0.0044±0.0001	0.038±0.002
17			0.0055±0.0001	0.036±0.002
19			0.0049±0.0001	0.041±0.002
22			0.0059±0.0001	0.046±0.002

The average values for a and b parameters calculated for the Russian Proto 2000 are the following:

$$a_{russian} = (4.41 \pm 0.03)\%/\sqrt{E(GeV)} \qquad c_{russian} = (4.01 \pm 0.03) \cdot 10^{-3}$$
$$a_{chinese} = (4.00 \pm 0.20)\%/\sqrt{E(GeV)} \qquad c_{chinese} = (5.60 \pm 1.00) \cdot 10^{-3}$$

and the corresponding values after irradiation are:

$$a_{russian} = (4.40 \pm 0.03)\%/\sqrt{E(GeV)} \qquad c_{russian} = (3.87 \pm 0.03) \cdot 10^{-3}$$
$$a_{chinese} = (4.10 \pm 0.20)\%/\sqrt{E(GeV)} \qquad c_{chinese} = (5.40 \pm 0.50) \cdot 10^{-3}$$

from which we can deduce that there is almost no variation of these energy resolution parameters after irradiation.

Using all data expressed in table 7.3 we can now perform the following comparisons:

Stochastic term versus LY

As we mentioned previously, the stochastic term is related to laboratory measurable crystal properties such as light yield. Therefore, it is very interesting to show the correlations between the a terms calculated for the two matrices object of this study and the LY measured at CERN RC with ACCOS machines. This is depicted in figure 7.13.

This plot includes the results after and before irradiation, in order to have more statistics. Assuming that a can be expressed as $\sqrt{F/N_{pe}}$ (as was explained in section 6.1) plus another contribution from the leakage, we can use the following equation to fit data points regarding the russian matrix:

$$a = \sqrt{\left(\sqrt{\frac{a_1}{\sqrt{LY}}}\right)^2 + (a_2)^2} \tag{7.2}$$

and thus, we get: a_1=0.117±0.002 when we fix a_2 to 0.02, and the LY is expressed in n_{pe}/MeV. As we can see, in figure 7.13, the chinese crystals, with higher LY, also follow the resulting fitted curve even if it was calculated only for russian crystals.

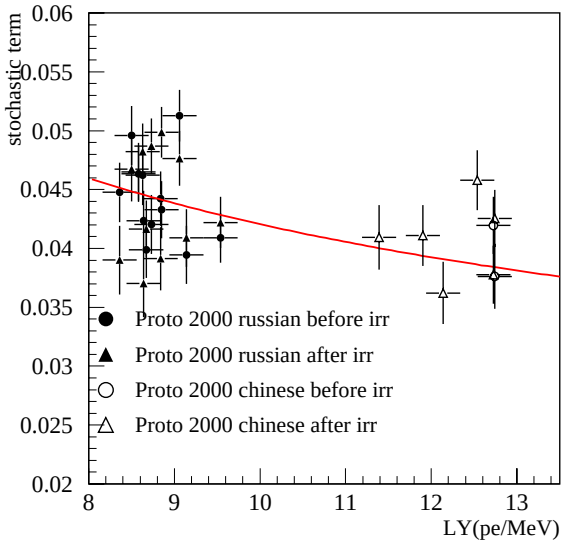

Figure 7.13: *Stochastic term calculated for russian and chinese crystals as a function of the Light Yield measured at CERN RC.*

Constant term versus Fnuf

As occurs with the stochastic term, the constant term c is related to laboratory measurable crystal properties such as Front Non-Uniformity. Figure 7.14-a shows the correlations between the c terms calculated for the russian and chinese crystals appearing in table 7.3 and the Fnuf measured at CERN RC with ACCOS machines.

As we can see, there is an overimposed fit performed with the following function:

$$c = \sqrt{(c_1)^2 + (c_2 \cdot Fnuf)^2} \tag{7.3}$$

where we assume a linear dependence of the constant term c with the Fnuf plus another contribution. If we express the Fnuf in its common units ($\%/X_0$), then we obtain: $c_1 = (0.40 \pm 0.01)\%$ and $c_2 = (0.68 \pm 0.23)\%$. As we can see, some chinese crystals with higher Fnuf values appear to be correlated to higher c values.

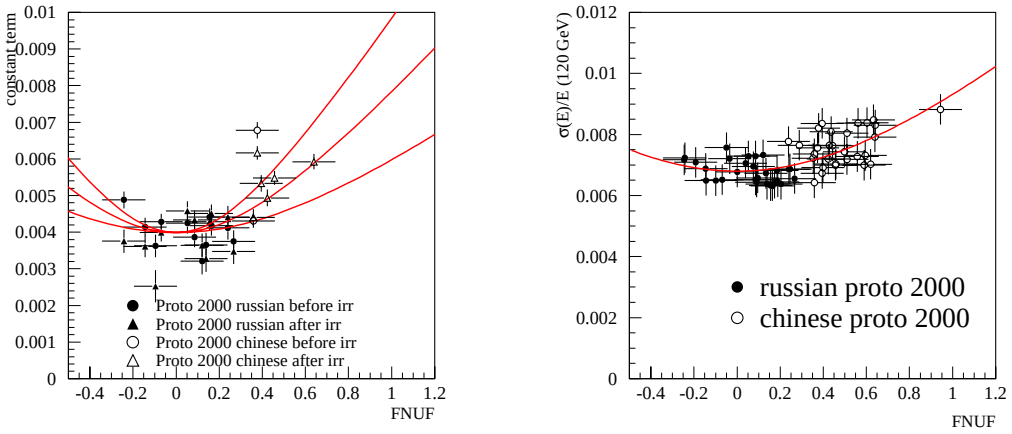

(a) (b)

Figure 7.14: *Constant term versus Front Non-Uniformity of russian and chinese crystals (a) and Σ_1 energy resolution at 120 GeV versus Front non-uniformity for all crystals in two matrices (b). Both fitted curves respond to equation 7.3.*

Unfortunately we do not have enough statistics for the SIC crystals since the energy scan was performed only with two crystals for the Chinese Proto 2000. Therefore, we have tried to complete this plot by using the Σ_1 energy resolution obtained for every crystal at 120 GeV. As was shown in figure 7.12, the stochastic term has a small influence on the energy resolution at 120 GeV, and thus, the main responsible for any change in $\sigma(E)$ at this energy will be strongly related to constant term c. In this manner, we have constructed plot (b) from figure 7.14. As we can see there is a clear correlation between the energy resolution at 120 GeV and the Fnuf measured with ACCOS machines at CERN RC, even if we know that when using the Σ_1 distribution, the non-containment fluctuations of the electromagnetic shower are larger than when using the Σ_9.

7.2.3 Conclusions from this test

This important test-beam performed at CERN H4 facility shows that:

1. Stochastic term a appears to be weakly correlated to Light Yield measured at CERN RC laboratory showing values slightly lower for chinese crystals, as they were also showing higher LY values (they were not presenting a depolished face). This smaller value for a term results in a slightly lower contribution of this term to energy resolution.

2. Stochastic term found for russian crystals is $a_{russian} = (4.41 \pm 0.03)$ $\%/\sqrt{E(GeV)}$, whereas its value for chinese crystals is $a_{chinese} = (4.00 \pm 0.20)$ $\%/\sqrt{E(GeV)}$. Both values appear to be not too sensitive to long irradiation (36 hours) with 120 GeV electrons.

3. Constant term is strongly correlated to Fnuf measured at CERN RC. Plots presented show that crystals with a very non-uniform light collection in their Front part do present higher values of c, thus having a major contribution to energy resolution. This was already indicated in section 5.2. Resulting correlation plots from this test-beam (figure 7.14) clearly confirm Monte Carlo simulations results showed in figure 5.1-(b), plot which was used for Fnuf limits definition. This evidences the importance of the uniformisation task undertaken at CERN RC.

4. Constant term found for russian crystals is $c_{russian} = (4.01 \pm 0.03) \cdot 10^{-3}$. In the case of chinese crystals, its value is $c_{chinese} = (5.60 \pm 1.00) \cdot 10^{-3}$, showing also both a weak variation after long irradiation (36 hours) with 120 GeV electrons.

5. Values obtained for stochastic and constant term appear to match reasonably well the CMS ECAL requirements explained in section 2.4.2. On one hand, stochastic terms obtained here for russian and chinese matrices are slightly higher than expected (stochastic term required: $a \lesssim 3$ %), whereas on the other hand, constant terms obtained verify the existing requirement ($c \lesssim 0.5$ %), at least for russian crystals.

Chapter 8

CONCLUSIONS

The homogeneous electromagnetic calorimeter of the CMS experiment will play an essential role in the potential discovery of a light Higgs boson ($m_H \leq 150$ GeV). This calorimeter, composed of ~ 80000 lead tungstate crystals ($PbWO_4$), must have an excellent performance in order to overcome the enormous background that characterizes the main observable decay channel of such a light Higgs: $H \rightarrow \gamma\gamma$. The optimum crystal performance requested are guaranteed thanks to the strict quality control undertaken at the Regional Centres.

A set of specifications in certain optical and dimensional crystal parameters constitute the framework of the quality control developed. In order to perform the measurements needed to compare those parameters with their corresponding specifications, two complex automatic systems (ACCOS devices) have been developed at the Regional Centres.

It has been shown that both CERN ACCOS devices can perform stable measurements, in a long term scale, of all required parameters. In addition, some complicated parameters related to light collection (Light Yield, Front Non-Uniformity and Rear Non-Uniformity) have been proved to be reliable when measured with ACCOS devices. This could be accomplished since the relative Light Yield measurements performed by ACCOS devices have been successfully calibrated according to classical Light Yield bench, the stability of which has also been proved.

We have shown that the uniformity of light collection along the lead tungstate crystals is of extreme importance to ensure the requested energy resolution parameters. This imposes certain acceptability limits to the measurements of Front and Rear Non-Uniformity performed with ACCOS devices. It has been proved that the procedure to uniformize the light collection in PWO crystals (based on the depolishing of a lateral face to a given degree of roughness) defined at CERN Regional Centre and later transferred to producers is a suitable technique, since it yields excellent results (few crystals must be corrected at CERN RC) and induces little Light Yield losses ($\sim 13\%$).

The importance of finding an adequate glue to perform the optical matching of the crystals to the chosen photodetectors (Avalanche Photodiodes or *APDs*) has been explained. The influence of the high radiation levels present at the CMS experiment, together with the high index of refraction needed to maximize the angular acceptance of photons outgoing the crystal constitute some of the many constraints that limit the choice of the glue. Some possible candidates have been analyzed, explaining their advantages and drawbacks. In addition, the gluing benches designed to ease the gluing operation and the quality control tools developed are described.

Finally, we present the results of two beam tests performed during last year in order to verify some critical aspects. In the former, the excellent agreement of the measured non-uniformity curves measured with ACCOS devices with the ones measured with APD readout in beam conditions (high energy particles hitting into PWO crystals) is proved. This confirms that the above mentioned calibration of ACCOS devices using the classical bench was completely successful. In the second beam test, we have analyzed the energy resolution of two crystal matrices. Among other things, thanks to this test, we have proved the influence of the non-uniformities in the light collection at the shower maximum region (4-13 X_0) on the energy resolution constant term. In addition, the observed energy resolutions have proved that our uniformization scheme and in particular our Front Non-Uniformity range was adequate for an acceptable contribution to the constant term of the energy resolution. This assures the validity of the complex uniformisation task accomplished at CERN RC.

Chapter 9

APPENDIX A: References Protocol

A special "references protocol" has been conceived in order to ease the stability verifications of all the devices implied in the quality control. It also allows continuous cross checking of those parameters measurable in more than one device. The crystals chosen to be references are seven Bogoroditsk-produced PWO crystals (see table 9.1).

Table 9.1: *Summary of references protocol used at CERN RC*

Barcode	**Engraved Number**	**Type of Reference**
33101000001649	5649	Fixed ACCoCE 1
33101000001611	5611	Fixed Bench 3
33101000001624	5624	Mobile
33101000001654	5654	Mobile
33101000001619	5619	Hidden
33101000001634	5634	Hidden
33101000001614	5614	Fixed Spectro

Two of these crystals are intended to be the **fixed references** of the two devices most widely used for the characterization of crystals up to now: ACCoCE 1 and Bench 3. Crystal 5611 is B3 fixed reference, whereas 5649 is ACCoCE 1 fixed reference. These crystals are measured very often on each machine: the one from ACCoCE 1 is never moved, being always placed in 1^{st}

pillar for every run performed in this machine. On the other hand, B3 fixed reference crystal is measured five times every night with a given tyvek wrapping. The day after, the mean value of these five measurements is calculated and introduced in the LabView-controlled acquisition program. It automatically calculates the ratio between this mean value and an historical averaged value which is assumed to be the Light Yield of crystal 5611 (9.8 pe/MeV), and uses this ratio to correct every measurement of non-reference crystals which is performed during the day. These non-reference crystals are measured using the same tyvek as fixed reference. In this way, the fluctuations in light yield measurements due to tyvek ageing are corrected. This tyveks are changed typically after $\sim$ 1 month, and replaced by another one built in the same way. Apart from these two crystals, another fixed reference has been chosen for the classical spectrophotometer (described later in the chapter). This crystal is 5614, and it is measured several times per week on this device.

Two other crystals are used as **mobile references**: 5624 and 5654. Every Monday one of them is mounted on ACCoCE 1 pillar number 19 whereas the other is sent to the Light Yield room in order to be measured in B3. During that week ACCoCE 1 crystal is measured on every run performed, whereas B3 crystal is measured once or twice. Then, when the following Monday arrives, the two crystals are interchanged: the one measured in B3 goes to ACCoCE 1 pillar 19, and viceversa. These two crystals are also used to crosscheck ACCOS devices and classical spectrophotometer transmission data.

Two more crystals are used as **hidden references**: 5619 and 5634. These crystals are kept in the darkness in between each measurement. These measurements are performed every 2-3 months in order to preserve its properties the most unchanged possible. They are used to verify at a long-term scale the fluctuations of ACCoCe 1, B3 and the spectrophotometer.

Chapter 10

RESUMEN EN CASTELLANO

Control de calidad y preparación de los cristales de PWO y otros componentes para la construcción del primer supermódulo del calorímetro electromagnético de CMS

El modelo estándard de Física de partículas describe las interacciones entre partículas denominadas electromagnética, débil y fuerte. En este modelo, la fuerza fuerte viene descrita por la Cromodinámica Cuántica (QCD), teoría en la cual ocho tipos diferentes de gluones actúan como portadores de dicha fuerza, que se ejerce entre quarks. Las otras dos fuerzas pueden describirse por la teoría electrodébil que, del mismo modo, está caracterizada por la existencia de varios portadores: uno neutro (Z^0) y dos cargados (W^+ y W^-).

Esta teoría electromagnética fue formulada a finales de los años 60 por Glashow, Salam y Weinberg y predijo, no solo la existencia de los bosones Z^0, W^+ y W^-, sino también la existencia de la corriente neutra débil. En 1973 se observaron por primera vez las corrientes neutras en el Centro Europeo de Investigaciones Nucleares (CERN), y diez años más tarde, la existencia de los tres bosones mencionados fue comprobada nuevamente en el CERN. Esto confirmaba la teoría electro-débil pero, sin embargo, el mecanismo que provoca que los portadores de fuerza difieran en masa (los bosones W y Z son masivos, mientras que el fotón no tiene masa) continúa siendo un misterio. El problema

puede resolverse mediante el denominado *mecanismo de Higgs* pero ello implica la existencia de una nueva partícula conocida como el bosón de Higgs (H^0) la cual no ha sido aún observada y de la que solo se sabe que presenta una masa en el rango: 100 GeV $< m_H <$ 1000 GeV. Actualmente, uno de los principales objetivos de los físicos de partículas de todo el mundo es el descubrimiento de dicho bosón.

El gran colisionador de hadrones (LHC, del inglés *Large Hadron Collider*) es un complejo acelerador que va a explorar la física que subyace a muy altas energías, con el objetivo último de encontrar el bosón de Higgs. El LHC está siendo construido en el CERN y entorno al año 2005 estará preparado para producir colisiones de protones a una energía en centro de masa de 14 TeV. Varios espectrómetros estarán instalados a lo largo del anillo de 27 Km del LHC. Uno de ellos, el *Compact Muon Solenoid* (CMS), presentará un calorímetro electromagnético (ECAL) compuesto por $\sim$ 80000 cristales centelleadores de tungstanato de plomo ($PbWO_4$).

La investigación sobre los cristales de tungstanato de plomo ha estado fundamentalmente motivada por la demanda de la física de altas energías de encontrar centelleadores que mejorasen las prestaciones de los centelleadores utilizados anteriormente. En concreto, las características requeridas eran: mejor resistencia a radiación para poder operar en ambientes hostiles como el LHC, más rápido mecanismo de centelleo para minimizar los tiempos de respuesta, alta densidad para permitir la compacidad de los detectores, y disponibilidad de materia prima y plantas de producción para minimizar costes. Son precisamente estos factores los que llevaron a la elección del $PbWO_4$ para el calorímetro electromagnético de CMS.

Este calorímetro electromagnético homogéneo va a jugar un papel esencial en el hipotético descubrimiento de un bosón de Higgs ligero ($m_H \leq 150$ GeV), cuyo principal canal de decaimiento viene dado por $H \rightarrow \gamma\gamma$. Este canal presenta un enorme background difotónico que solo puede ser contrarrestado con un calorímetro extremadamente preciso. Esta es la razón del complejo y detallado control de calidad al que son expuestos los cristales de $PbWO_4$ en

los Centros Regionales del ECAL de CMS[a].

Objetivos y estructura de la tesis

Este trabajo de tesis está principalmente fundamentado en el previamente mencionado control de calidad al que son sometidos los cristales de PWO del ECAL de CMS. Antes de explicar dicho control de calidad en detalle, se procede a describir en el Capítulo 2 lo que es el CERN y los principales objetivos del proyecto LHC. A continuación, en el mismo capítulo, se da una breve revisión al modelo estándard de física de partículas, al mecanismo Higgs y a los posibles canales de decaimiento del bosón de Higgs, centrándonos en las dificultades existentes en el canal $H \rightarrow \gamma\gamma$. Posteriormente se describen brevemente las diferentes partes que componen el detector CMS (desde dentro hacia afuera): el tracker interno, los calorímetros electromagnético y hadrónico, el imán superconductor y el sistema de muones. A continuación se dan unas breves nociones sobre calorimetría para luego adentrarnos en las complejidades del calorímetro electromagnético. Posteriormente, se discute el importante papel de los Centros Regionales del ECAL de CMS y los diferentes pasos que conforman el proceso de caracterización, pieza clave del control de calidad efectuado.

En el Capítulo 3 se realiza una detallada descripción de las propiedades de los cristales centelleadores de $PbWO_4$. Primeramente, se explican las razones que motivaron su elección como centelleador para el ECAL de CMS. Luego se comentan sus propiedades básicas, que a su vez se compararán con las de otros centelleadores usados comunmente en física de partículas. A continuación, se explican detalladamente los métodos de crecimiento de los cristales de PWO y sus propiedades centelleadoras y ópticas. Para terminar se describen las diferentes geometrías de los cristales usados en el Calorímetro Electromagnético de CMS y se discuten las especificaciones existentes para ciertos parámetros de vital importancia para el detector. Dichas especificaciones se refieren a parámetros dimensionales y ópticos de los cristales. Las especificaciones relacionadas con los parámetros dimensionales de los cristales deben ser muy precisas ya que debemos estar completamente seguros de que éstos son lo suficientemente pequeños como para poder insertarse en las estructuras alveolares que los sostendrán pero también deben ser lo suficientemente grandes como para minimizar el interespacio entre cristales en el detector final. Igualmente

[a]Existen dos Centros Regionales: el del CERN situado en Ginebra (Suiza) y el del INFN-ENEA situado en Roma (Italia).

precisas deben ser las especificaciones ópticas. Esto es debido a las óptimas prestaciones requeridas por el complicado canal de decaimiento $H \rightarrow \gamma\gamma$ y a los altos niveles de radiación presentes en el LHC. La medida de todos estos parámetros con los sistemas clásicos ralentizaría el control de calidad de manera excesiva. Es por esto que unos sistemas para el control automático de cristales denominados ACCOS (acrónimo que procede del inglés *Automatic Cristal COntrol System*) han sido contruidos en los Centros Regionales. Estos sistemas se describen en el capítulo siguiente.

En el Capítulo 4 se describe en detalle el procedimiento de caracterización de los cristales de tungstanato de plomo. Primero se realiza una descripción detallada de los diferentes sistemas de medida utilizados para dicha caracterización: los bancos clásicos (sistemas que generalmente sólo miden una característica de los cristales, e.g. transmisión o producción de luz) y los sistemas de control automático de cristales (ACCOS). Dichos sistemas realizan medidas de dimensiones, transmisión de luz (longitudinal y transversal) y tiempo de decaimiento de la luz de centelleo, medida a partir de la cual se puede deducir el *Light Yield* (número de fotoelectrones emitidos por MeV de energía incidente). Para terminar pondremos un énfasis especial en los estudios de estabilidad e intercalibración realizados para dichos sistemas.

La importancia de la uniformidad en la colección de luz y los métodos para conseguir dicha uniformidad son los principales aspectos desarrollados en el Capítulo 5. Primeramente se muestran los resultados de ciertas simulaciones que ilustran como la resolución en energía depende fuertemente de las heterogeneidades en la colección de luz. Posteriormente mostraremos que los cristales de PWO son naturalmente no-uniformes, requiriendo por ello un método de uniformización adecuado. A continuación, se decriben con precisión varias cosas: el método finalmente escogido, los resultados obtenidos tras su aplicación y las pérdidas en la producción de luz (*Light Yield*) que induce. Posteriormente se explica la existencia de un factor que afecta a la uniformidad y que era previamente desconocido. Dicho factor se conoce como el gradiente de transmisión transversal. Para terminar se discute la influencia del envoltorio de los cristales en el perfil de uniformidad medido.

En el Capítulo 6 se explican todos los aspectos relacionados con la extracción de luz de los cristales centelleadores de PWO. Primero se describen los fotodetectores utilizados, los denominados fotodetectores de avalancha (del inglés *Avalanche Photodiodes*, o APDs). Posteriormente nos centraremos en la importancia del pegamento óptico que unirá cristales y APDs. Se discuten

también los diferentes candidatos considerados, evaluando sus ventajas y sus inconvenientes, así como los diferentes útiles empleados para el pegado y los resultados obtenidos.

Para terminar, el Capítulo 7 presenta los resultados de dos diferentes tests en el haz realizados con los cristales de PWO. En el primero, mostraremos una comparación entre las curvas de uniformidad obtenidas en los laboratorios del Centro Regional del CERN y aquellas obtenidas en el PSI[b] en condiciones completemente diferentes (partículas de alta energía incidiendo en los cristales, lectura de la señal con APDs, etc.). En el segundo test en el haz se presentan los resultados obtenidos con dos matrices de cristales de PWO en el area H4 del CERN.

Resumen de los resultados

En este trabajo de tesis se ha demostrado que los dos sistemas ACCOS (llamados ACCoCE 1 y ACCoCE 2) realizan medidas estables de los parámetros requeridos. Por otro lado, cabe destacar que los sistemas ACCOS realizan medidas relativas del *Light Yield*. Es por ello, que este complicado parámetro debe ser correctamente normalizado respecto a los bancos clásicos de medida, cuyas medidas proporcionan valores absolutos del *Light Yield*. Gracias al demostrado éxito de esta calibración de ACCOS con los bancos clásicos, podemos concluir que las medidas realizadas por dichos sistemas ACCOS del *Light Yield* y de otros parámetros relacionados con la colección de luz a lo largo del cristal (la Front NUF y la Rear NUF[c]) son plenamente fiables.

Para mantener la resolución en energia en los márgenes requeridos, debemos reducir el rango de no-uniformidades aceptables, i.e. debemos reducirnos a aceptar solamente aquellos cristales con valores de Front y Rear NUF dentro de un intervalo predeterminado. La curva de colección de luz de un cristal resulta ser la contribución de dos efectos opuestos: la absorción y el efecto focalizador (inducido por el hecho de que las caras longitudinales del cristal no son paralelas). La excepcional calidad de los cristales recientemente producidos conlleva una reducción notable de la absorción de luz en su interior y, por tanto, el efecto focalizador resulta ser dominante. Ello provoca que los

[b] Paul Scherrer Institute, Villigen (Suiza).

[c] No-uniformidad de la colección de luz en la parte frontal (4-13 X_0) y en la parte trasera (13-22 X_0) del cristal, respectivamente.

cristales presenten curvas de colección de luz con parámetros Front y Rear NUF fuera del rango de aceptabilidad. Debido a esto, hemos tenido que establecer un procedimiento de uniformización de la colección de luz que está basado en el depulido de una de las caras longitudinales hasta un determinado valor de rugosidad, puesto que es el grado de rugosidad de dicha cara el que permite controlar la contribución del efecto focalizador a la colección de luz. Los resultados obtenidos para los parámetros Fnuf, Rnuf y Light Yield para los grupos de cristales 6, 7, 8 y 10 muestran que no solamente la técnica definida en el CERN y posteriormente transferida a los productores es válida, sino que también son válidos los tratamientos correctores aplicados en el Centro Regional del CERN. También se analizan en este trabajo de tesis, las pérdidas inducidas por dicho método de uniformización en la producción de luz *Light Yield*, las cuales resultan ser bastante débiles ($\sim 13\%$).

La elección del pegamento óptico que unirá cristales y fotodetectores es de gran importancia ya que dependerá de las propiedades del pegamento escogido el que las excelentes propiedades como centelleador de nuestros cristales sean plenamente aprovechadas. Por ejemplo, algunos aspectos que el pegamento debe satisfacer son los siguientes: a) debe presentar un índice de refracción elevado para maximizar la aceptancia angular de los fotones que inciden en la cara del cristal pegada al fotodetector, b) debe soportar los elevados niveles de radiación presentes en el espectrómetro CMS, c) debe presentar una absorción de la luz que lo atraviesa lo menor posible, por citar solo los más importantes. Del estudio comparativo de los diferentes candidatos considerados (14, en total) pudimos deducir que sólo tres de ellos eran adecuados para su uso en el ECAL de CMS. De los test realizados con estos tres candidatos finales (Histomount, RTV3145 y NOA61) se puede extraer como conclusión que el primero y el último presentan notables problemas que desaconsejan su elección. El Histomount se caracteriza por un tiempo de secado excesivamente largo así como por requerir el uso de complejos sistemas de seguridad debido al caracter tóxico de su disolvente. La evolución del pegamento NOA61 en las horas inmediatamente posteriores al pegado resulta ser díficil de predecir, lo cual supone un severo inconveniente para su elección. El candidato final es por tanto la silicona RTV3145 la cual presenta como único inconveniente unas propiedades ópticas ligeramente desfavorables respecto a los otros dos pegamentos comentados. En cualquier caso, los excelentes resultados obtenidos con el pegamento RTV3145 durante el pegado del Módulo 0', aconsejan su elección.

Los resultados de los dos tests en haz realizados durante el ultimo año para verificar algunos aspectos críticos de los cristales centelleadores de $PbWO_4$

son de gran importancia. Gracias al primero, realizado con el haz de protones disponible en el PSI pudimos comprobar el excelente acuerdo existente entre los perfiles de uniformidad de los cristales medidos en el laboratorio con los sistemas ACCOS[d] y los medidos con APDs como sistema de lectura en condiciones de test en el haz (partículas de alta energía incidiendo en los cristales de PWO). Teniendo en cuenta las grandes diferencias entre ambas configuraciones, estos resultados constituyen una rotunda confirmación de que las calibraciones de ACCOS usando los datos extraídos de los bancos clásicos son plenamente satisfactorias. En el segundo test, realizado con dos matrices de cristales expuestas al haz de electrones de alta energía disponible en el area H4 del CERN, hemos analizado la resolución en energía obtenida con estos cristales. Gracias a este test, hemos podido comprobar la influencia en el término constante de la resolución en energía causada por las no-uniformidades en la región de maxima deposición de energía de los cristales (4-13 X_0). Por otra parte, las resoluciones en energía deducidas de los datos adquiridos prueban que nuestro procedimiento de uniformización y, en particular, el rango de no-uniformidades en la parte frontal del cristal (Front NUF) establecido son adecuados para garantizar una contribución aceptable al término constante de la resolución en energía. Ello ratifica la validez del complejo y minucioso procedimiento de uniformización desarrollado en el Centro Regional del CERN.

[d]Sistemas caracterizados por el uso de tubos fotomultiplicadores para detectar la luz emitida por los cristales cuando éstos son excitados por una fuente de baja actividad de ^{22}Na.

Bibliography

[1] The LHC Study Group, *The Large Hadron Collider, Conceptual Design* , CERN/AC/95-05.

[2] M. Spira, P.M. Zerwas, *Electroweak Symmetry Breaking and Higgs Physics* , CERN-TH/97-379.

[3] CMS Technical Proposal, CERN/LHCC/94-38.

[4] The Tracker Project, CERN/LHCC/98-6.

[5] The Hadron Calorimeter Project, CERN/LHCC/97-31.

[6] The Muon Project, CERN/LHCC/97-32.

[7] C.W. Fabjan, *Calorimetry in High-Energy Physics*, CERN-EP/85-54.

[8] T.S. Virdee, *Calorimetry*, CMS Conference Report 1998/026.

[9] The Electromagnetic Calorimeter Project, CERN/LHCC/97-33.

[10] P.Lecoq, M.Schneegans, *A fast and radiation hard crystal calorimeter for the LHC*, Proceedings of Large Hadron Collider Workshop in Aachen (1990), Vol.III , CERN 90-10.

[11] The Crystal Clear Collaboration, *R&D proposal for the study of new fast and radiation hard scintillators for calorimetry at LHC*, CERN/DRDC P27/91-15 (1991).

[12] Etiennette Auffray, *These de doctorat de L'Universite de Paris VI*, 1995.

[13] William R. Leo, *Techniques for nuclear and particle physics experiments*, Berlin-Springer 1994.

[14] J.B. Birks, *The theory and practice of scintillation counting*, Oxford: Pergamon Press 1964.

[15] I.N. Shpinkov et al., *Optical functions and luminescence quantum yield of lead tungstate*, Phys. Stat. Sol. (a) *170*, 167 (1998).

[16] G. Blasse, *Heavy scintillators for scientific and industrial applications*, Proceedings of International Workshop CRYSTAL 2000, Chamonix (France), September 1992. (p. 85).

[17] A. Annenkov et al., *On the origin of the transmission damage in lead tungstate crystals under irradiation*, Phys. Stat. Sol (a) *170*, 47 (1998).

[18] P. Lecoq et al., *Lead Tungstate ($PbWO_4$) scintillators for LHC EM calorimetry*, Nucl. Instr. Meth. A 365 (1995) 291-298.

[19] Glenn F. Knoll, *Radiation detection and measurement; 2nd ed.*, New York Wiley 1989.

[20] A.N. Annekov et al., *Slow components and afterglow in PWO crystal scintillators*, Nucl. Instr. Meth. A 403 (1998) 302-312.

[21] S. Baccaro et al., *Optical properties of lead tungstate ($PbWO_4$ crystal for LHC em-calorimetry*, CMS TN/95-152.

[22] R. Chipaux, *Numerical formulae for the refractive index of lead tungstate*, CMS TN/95-184.

[23] E. Auffray et al., *Specifications for lead tungstate crystals preproduction*, CMS Note 98/038.

[24] M. Montecchi, *Proposal of a functional representation of the PWO transmittance spectrum*, CMS IN 2000/015.

[25] C. D'Ambrosio et al, *Low dose rate irradiation set-up for scintillating crystals*, Nucl. Instr. Meth. A 388 (1997) 119-126.

[26] G. Drobychev et al, *Studies and proposals for an Automatic Crystal COntrol System (ACCOS)*, CMS Note 97/036.

[27] G. Basti et al, *A proposal for an Automatic Crystals COntrol System*, CMS IN 97/033.

[28] J.M Le Goff et al., *C.R.I.S.T.A.L. / Concurrent Repository & Information System for Tracking Assembly and production Lifecycles. A data capture and production management tool for the assembly and construction of the CMS ECAL detector*, CMS Note 96/003.

[29] W.W. Moses, *A method to increase optical timing spectra measurement rates using a multi-hit TDC*, Nucl. Instr. Meth. A 336 (1993) 253-261.

[30] G. Drobychev et al, *ACCOS User Manual*, Internal Note available at CERN Regional Centre, 1998.

[31] B. Borgia et al, *Precise determination of the light yield of scintillating crystals*, CMS TN 96/079.

[32] C. D'Ambrosio et al, *A HMPT based set-up to characterize scintillating crystals*, Nucl. Instr. Meth. A 434 (1999) 387-398.

[33] C. D'Ambrosio et al, *Photon counting with a hybrid photomultiplier tube (HPMT)*, Nucl. Instr. Meth. A 338 (1994) 389-397.

[34] E. Auffray et al, *Performance of ACCOs, an Automatic Crystal quality Control system for the PWO crystal of the CMS calorimeter*, Nucl. Instr. Meth. A 456 (2001) 325-341.

[35] M. Schneegans, *Progress of the L3/BGO calorimeter*, Nucl. Instr. Meth. A 257 (1987) 528-537.

[36] D. Graham and C. Seez, *Simulation of Longitudinal Light Collection Uniformity in $PbWO_4$ crystals*, CMS Note 96/002.

[37] R. Wigmans, *Calorimetry - Energy Measurement in Particle Physics*, Oxford Science Publications 2000.

[38] G.J. Davies et al, *Development of a Uniformisation procedure of the $PbWO_4$ crystals of the CMS Electromagnetic Calorimeter*, CMS Note 01/004.

[39] P. Rivoallan, *Rapport de stage*, INSA Engineering Studies, Rennes, France, 1996.

[40] A. Annenkov et al, *Suppression of the radiation damage in lead tungstate scintillation crystal*, Nucl. Instr. Meth. A 426 (1999) 486-490.

[41] S. Paoletti et al, *Light Collection in $PbWO_4$ crystals*, Proceedings of International Workshop on Tungstate Crystals (p. 277), Roma (Italy), October 1998.

[42] M. Montecchi and Q. Ingram, *Study of some optical glues for the Compact Muon Solenoid at the Large Hadron Collider of CERN*, CMS Note 01/030.

[43] R. Chipaux, *Study of some optical glues in a LHC-like environment*, CMS TN/95-032.

[44] T. Kirn et al, *Absorption length, radiation hardness, and ageing of different optical glues*, CMS Note 99/003.

[45] M. Montecchi et al, *Tools for the inspection of PWO//APD gluing*, CMS Note 98/024.

[46] F. Cavallari et al, *Comparison of light yield Uniformities measured on the laboratory bench and in the testbeam for ECAL barrel crystals*, CMS Note 01/031.

[47] G. Davies et al, *Comparison of light yield Uniformities measured on the laboratory bench and in the testbeam for Pre-production ECAL barrel crystals*, CMS Note 00/014.

[48] F. Cavallari et al, *Test-beam results on the performance of two matrices of $PbWO_4$ crystals for the CMS ECAL and comparison with Laboratory measurements*, CMS Note 01/033.